AN ABSTRACT OF THE THESIS OF

Mary Ann Triska for the degree of Master of Science in Civil Engineering presented on April 29, 2010.

Title: Flexural Steel Anchorage Performance at Diagonal Crack Locations.

Abstract approved: _____

Christopher C. Higgins

Large numbers of reinforced concrete deck girder bridges that were constructed during the interstate system expansion of the 1950s have developed diagonal cracking in the stems. Compared to the present AASHTO-LRFD standards, the provisions of the 1950s allowed for higher shear stress in the concrete, thus reducing the amount of transverse steel required. Further, service loading has increased over time. When load-rating these structures, the current design specification check of tension reinforcement anchorage often controls the capacity of these bridges. This check compares the applied tensile force in the reinforcement to the tensile force available based on the reinforcement development length. The tensile force demand is controlled by the load-induced moment and shear, the number of stirrups, and the diagonal crack angle. However, the crack angle considered in the

design specification is commonly flatter then the angle of the vertically-oriented cracks generally noted in field inspections. The tensile force that can be developed in the flexural reinforcing steel depends on the diameter of the bar and the embedded length, however, little information is currently available regarding bond stresses developed with larger-diameter bars for full-size specimens in the presence of diagonal cracks.

Experimental data from realistic full-size specimens with anchorage of flexural bars interacting with diagonal cracks would enhance ratings methods for evaluation of existing bridges. Ultimately, improved understanding of the response of these bridge girders can help maintain the operational safety and freight mobility of the transportation system, thereby allowing optional use of available resources for repair or replacement of truly deficient bridges.

FLEXURAL STEEL ANCHORAGE PERFORMANCE AT DIAGONAL CRACK LOCATIONS

by

Mary Ann Triska

A THESIS

submitted to

Oregon State University

in partial fulfillment of

the requirements for the

degree of

Master of Science

Presented April 29, 2010

Commencement June 2010

Master of Science thesis of Mary Ann Triska presented on April 29, 2010

APPROVED:

Major Professor, representing Civil Engineering

Head of the School of Civil and Construction Engineering

Dean of the Graduate School

I understand that my thesis will become part of the permanent collection of Oregon State University libraries. My signature below authorizes release of my thesis to any reader upon request.

Mary Ann Triska, Author

ACKNOWLEDGEMENTS

I would like to extend my sincerest gratitude to Dr. Christopher Higgins for his assistance and guidance for the duration of my research project.

I gratefully acknowledge the Oregon Department of Transportation for funding this research project.

I appreciate the comments and feedback provided by my theses committee members: Dr. Michael Scott, Dr. Tonatiuh Rodriguez-Nikl, and Dr. Timothy Kennedy.

The construction and testing of the large-scale specimens would have been impossible if it were not for the assistance of my friends and co-workers: Josh Goodall, Jora Lehrman, Anthony Peressini, Scott Mersereau, Duncan Stark, Eric Goodall, Brandon Johnson, and Jake Goebel.

I am very thankful to my husband Josh for his understanding of my commitment to my project. Lastly, I would like to acknowledge the support of my parents, siblings, and extended family for showing sincere interest in my project.

TABLE OF CONTENTS

TABLE OF CONTENTS (Continued)

Page

TABLE OF CONTENTS (Continued)

Page

LIST OF FIGURES

LIST OF FIGURES (Continued)

LIST OF FIGURES (Continued)

LIST OF FIGURES (Continued)

LIST OF FIGURES (Continued)

LIST OF TABLES

LIST OF TABLES (Continued)

LIST OF APPENDICES

Page

LIST OF APPENDIX FIGURES

LIST OF APPENDIX FIGURES (Continued)

LIST OF APPENDIX FIGURES (Continued)

LIST OF APPENDIX FIGURES (Continued)

LIST OF APPENDIX FIGURES (Continued)

LIST OF APPENDIX FIGURES (Continued)

LIST OF APPENDIX FIGURES (Continued)

LIST OF APPENDIX FIGURES (Continued)

LIST OF APPENDIX TABLES

FLEXURAL STEEL ANCHORAGE PERFORMCANCE AT DIAGONAL CRACK LOCATIONS

1. INTRODUCTION

Large numbers of reinforced concrete deck girder (RCDG) bridges were constructed during the interstate system expansion of the 1950s and are approaching the end of their originally intended design lives. Over the last 60 years, service loading has increased in terms of volume and magnitude, thereby placing a higher demand on the system than originally envisioned. Compared to the present AASHTO-LRFD standards, the provisions of the 1950s allowed for higher shear stress in the concrete, thus reducing the amount of transverse steel required. The 1950s also saw the introduction and widespread use of standardized deformed reinforcing bars. Compared to proprietary reinforcing bars, standardized deformed bars were believed to provide adequate anchorage without the need for hooks and bends. As a consequence, designers terminated flexural steel without special detailing where it was no longer needed by calculation, while in the past, proprietary reinforcing bars would have been bent to ensure anchorage. Due to the combination of age, use, and what is now understood to be poor detailing, many RCDG bridges exhibit diagonal cracking in the stems. These cracks are sometimes associated with the flexural bar terminations and have been a cause of concern from some bridge engineers and owners. The interactions of the diagonal cracks at cutoff locations in existing bridges are not well known and improved understanding will enable evaluation of members to best reveal the load carrying capacity thereby maintaining the operational safety and freight mobility of the transportation system, thereby allowing optional use of available resources for repair or replacement of truly deficient bridges.

Since the early 2000s, Oregon State University has conducted a number of experimental tests of vintage RCDG bridge girders details (Higgins, *et al.* 2004). The typical specimen

was a T-shaped girder that was 7.92 m (26 ft) long, with a 356 x 1067 mm (14 x 42 in.) stem, and a 914 x 152 mm thick (36 x 6 in.) deck. The deck was placed in such a way as to test either T (positive moment) and IT (negative moment) conditions. The concrete strength and grade of transverse steel reasonably mimicked the materials used in the 1950s. In this previous study, it was thought that none of the T-beam specimens failed in anchorage, even those specimens that had cutoff details. The current research program made use of similar specimen proportions to test new specimens and also used some of the previous experimental data from the earlier test program to identify shear anchorage response.

Ultimately, this research intended to improve the understanding of the behavior of flexural steel anchorage in the presence of diagonal cracks in RCDG bridge girders with 1950s vintage details, and present analytical methods which adequately determine the capacity of these girders. To accomplish these goals, research methodology included a literature review, construction and laboratory testing of realistic full-scale T-beam bridge girder specimens to evaluate strength and behavior, and use of several analytical methods to assess capacity. A portion of the analysis included modeling the test specimens using the nonlinear finite element analysis program VecTor2, which is specifically designed for reinforced concrete.

2. BACKGROUND

Over the last 65 years, a number of test programs have attempted to quantify the factors that influence bond stress. Most tests were performed at small scale, using smaller size reinforcing bars, and concrete blocks. A few pullout and beam-end tests have been conducted using larger bars, but there has been a lack of research involving full-scale specimens using the most common size bars used in vintage RCDG bridges. This chapter includes a description of the anchorage failure mechanism, summaries of previous experimental research, a brief explanation of current design specifications and their history, a list of conclusions drawn from the literature, summary of research objectives based on the findings from the literature for the present test program.

2.1. Anchorage Concerns

Flexural reinforcement detailing of some vintage RCDG girders may be considered insufficient by the design standards of today. Prior to the development of standardized deformed rebar in the late 1940s, designers used hooks, bends, and transitions (such as extending positive moment steel from the bottom of the girder to the top) to ensure anchorage of the flexural steel. In continuous girders, this positive moment steel was commonly transitioned to become the negative moment steel over the piers. At the advent of the modern deformed bars, tests showed that the presence of deformations produced mechanical engagement with the surrounding concrete with greatly improved performance compared to that of the relatively weak chemical adhesion and friction relied upon from smooth or proprietary reinforcing steel. As a result, the design specifications were relaxed and allowed straight bars cutoffs in regions where they were no longer needed for flexural

capacity. Often the flexural bars were terminated near the quarter point of the girder. Today, AASHTO-LRFD requires these same bars to be detailed so as to prevent pullout and reduce stress concentrations within the cross-section.

There are two types of anchorage failures that occur when the tensile force demand in the flexural reinforcing steel exceeds the strength of the bond between the bar and the surrounding concrete: splitting anchorage and pullout anchorage. When sufficient force is applied to the deformed bar to break the chemical bond, the bar slips just enough to cause the deformations to bear on the concrete surface (Fig. 2.1a and b). As the bars slip, the concrete splits, and the stirrups are not able to resist splitting of the concrete. Splitting anchorage failures can be abrupt. Specimens containing principal reinforcement having little cover, such as IT-beams, are more likely to experience splitting anchorage failures. In contrast, pullout anchorage failures can be more ductile. For this failure mode, the beams are confined by the stirrups, so the cover concrete cannot split as the bars slip (Fig. 2.1c). Even as the bars slip, the demand in the bars can continue to increase to the point that the flexural bars may reach yield. Pullout anchorage failures are more likely in T-beams with transverse confinement provided by stirrups.

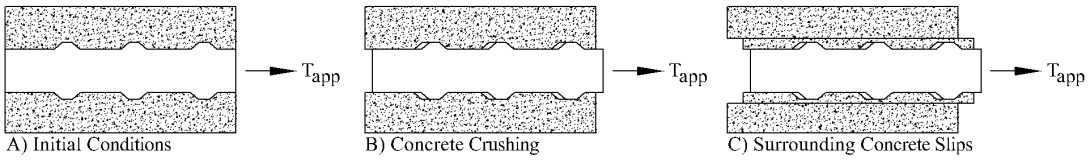

Fig. 2.1 – Pullout anchorage failure process

Stresses are transferred between the concrete and reinforcing steel through bond stress as illustrated in Fig. 2.2. Experimentally, bond stress is difficult to measure; a wide range of factors influence the bond stress, including bar size, concrete strength, concrete cover, and confinement provided by transverse reinforcement and at supports.

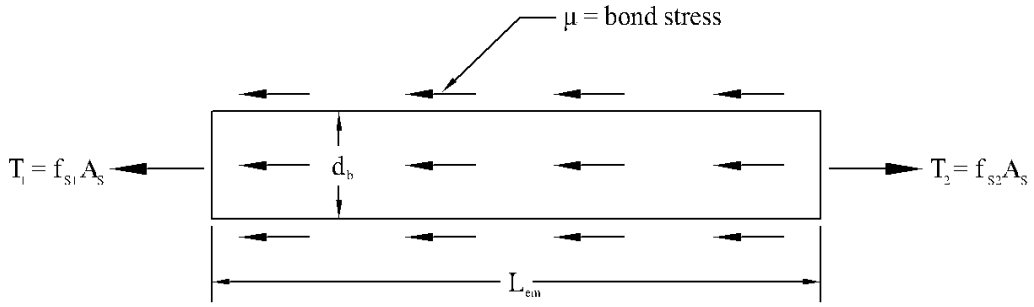

Fig. 2.2 – Forces acting on a segment of reinforcing steel

In theory, the average bond stress, μ_{avg}, over an incremental segment of reinforcement is:

$$\mu_{avg} = \frac{\Delta f_s d_b}{4 l_d} \qquad [2.1]$$

where Δf_s is the change in reinforcement stress over the length of the segment which may not exceed the yield strength f_y of the steel, d_b is the bar diameter, and l_d is the segment length.

The true bond stress, μ, maybe determined by taking l as a very small length, dx, such that:

$$\frac{df_s}{dx} = \frac{4\mu}{d_b} \qquad [2.2]$$

In this report, average bond stress is used in all calculations. The average bond stress is converted to the resistive tensile force, T_μ, by multiplying the average bond stress by the segment surface area, $\pi d_b l_{em}$, such that:

$$T_\mu = \mu_{avg} \pi d_b l_{em} \quad [2.3]$$

Bond stress may also be defined in terms of the minimum embedment length required to produce the yield stress in the reinforcing bar. If the average bond stress, μ_{avg}, is known from experiments, Eq [2.1] may be rewritten as:

$$l_d = \frac{f_y d_b}{4\mu_{avg}} \quad [2.4]$$

Eq. [2.4] is the basis for what modern design codes call “minimum development length.”

Wherever a crack is present, the bond stresses increase as shown in Fig. 2.3. Peak and average bond stress values reported in the literature vary greatly, with little information currently available regarding bond stresses of larger bars in full-size specimens in the presence of diagonal cracks.

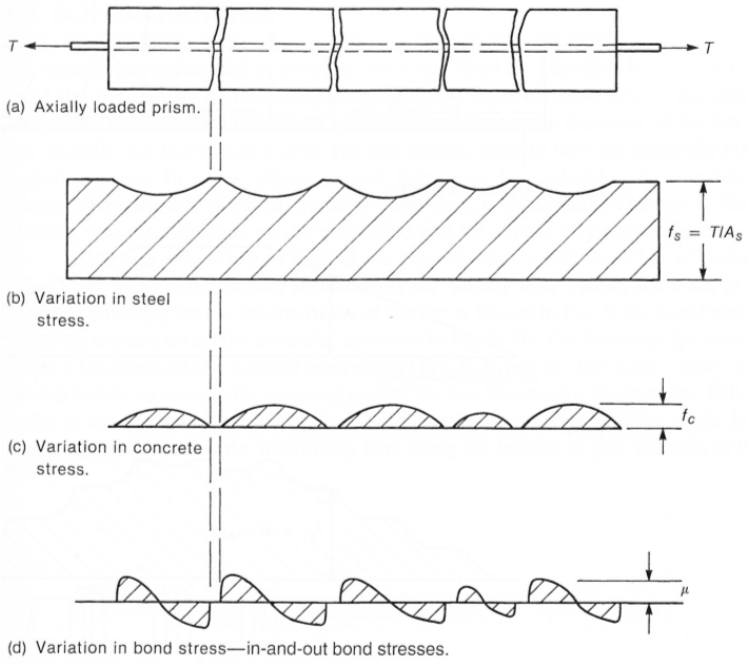

Fig. 2.3 – Bond stresses in a cracked prism (MacGregor and Wright 2005)

The AASHTO-LRFD Bridge Design Manual uses an implementation of Modified Compression Field Theory (MCFT) to determine the shear capacity at a section. The theory recognizes the interaction of shear and moment on the strength of a member. AASHTO-LRFD also considers the effect of diagonal cracking on the flexural steel tensile demand, *T*. As shown in Fig. 2.4, by summing moments around point A, the tensile demand is expressed as:

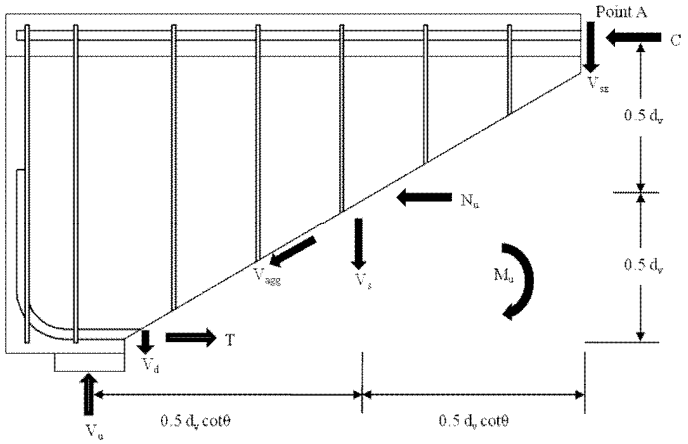

Fig. 2.4 – Internal forces in a diagonal cracked reinforced concrete section

$$T = \frac{M_u}{d_v} + 0.5N_u + (V_u - 0.5V_s - V_p)\cot\theta \qquad \text{AASHTO-LRFD 5.8.3.5-1} \qquad [2.5]$$

where M_u is the moment demand taken where the crack crosses the flexural steel; d_v is the effective section depth taken as 90% of *d; d* is the depth from the centroid of the flexural reinforcement to the top of the beam; N_u is the axial force contribution; V_u is the shear demand; V_s is the tensile force carried by the stirrups; V_p is the shear carried by the prestressing strands; and θ is the diagonal crack angle. Other labeled forces in Fig. 2.4 are: the force in the concrete compression zone, *C*; the dowel action of the flexural bars, V_d; the shear carried by the concrete compression zone, V_{cz}; and the shear carried by aggregate interlock, V_{agg}. In Fig. 2.4, the V_d and V_{agg} forces are difficult to measure, are small compared to the other forces, and their inclusion in the tensile demand equation reduces the tensile demand and thus are ignored.

The current AASHTO-LRFD design specification check of tension reinforcement anchorage can control the rating of some vintage RCDG bridges. The check compares the applied tensile force in the reinforcement (Eq. [2.5]) to the tensile force developed by the bond between the reinforcement and the concrete (Eq. [2.3]). However, the crack angle considered by AASHTO-LRFD is flatter than the steeper cracks angles generally noted in field inspections. This distinction may have a role in the actual capacity of these structures.

2.2. Literature Review

Mylrea (1948) wrote a paper summarizing the state of knowledge about bond and anchorage up to 1947. From pullout and beams tests, it was understood that bond stress was not uniformly distributed over the length of a bar. Further, the maximum bond stress in beam specimens was less than that of pullout specimens. Bond stress varies with concrete strength, but not directly. In uncracked sections, it may be assumed that the bond is perfectly uniform, the total steel stress varying directly with the moment. However, once the section cracks under heavy loading, high bond stress occurs near the cracks, with lower stress in between the cracks as shown in Fig. 2.3. As the slipping process proceeds, the bond stress at a particular point increases with bar movement, rapidly initially, then more slowly until the maximum bond stress is achieved at failure.

Clark (1949) conducted a number of beam and pullout tests to determine which type of deformed bar common in the 1940s developed the strongest bond. The specimens varied in bar size, embedment length and depth of concrete beneath the bar, and measured 203 x 457 x 1981 mm (8 x 18 x 78 in.). The largest bar investigated was a 28.6 mm (1-1/8 in.) square

bar. Clark recommended two changes to the ASTM 305-47T standard for deformed reinforcing bars that were eventually adopted in ASTM 305-50T and are still present in the standard today (ASTM 615/A615M-09b 2009). One change specified the deformation spacing; the other, the deformation height. For a 22.2 mm ($^{7}/_{8}$ in.) bar, average bond stress values were about 2.07-2.76 MPa (300-400 psi), while peak bond stresses at crack locations were about 4.83-6.20 MPa (700-900 psi).

Mains (1951) used strain gages inside the reinforcing steel to quantify how bond stresses vary along the length of plain and deformed reinforcing bars. Most of the beam specimens measured 203 x 318 x 1981 mm (8 x 12.5 x 78 in.) with either a straight or hooked No. 22 (No. 7) flexural bars. Both plain and non-ASTM 305-47T deformed bars were used. For the straight deformed bars, the maximum measure bond stress was 12.4 MPa (1800 psi), while the average bond stress calculated with code equations used at the time was 5.52 MPa (890 psi). The data showed that diagonal cracks caused increase in bar forces and consequently caused a local increase in bond stresses at the crack.

Doerr (1978) investigated the influence of transverse pressure on the bond stress-strain relationship by testing 25 cylinders equipped with a confining ring in pullout. Each 150 x 600 mm (5.91 x 23.6 in.) cylinder had a single No. 16 (No. 5) reinforcing bar embedded 500 mm (20.0 in.) into the concrete. Two strain gages measured the strain of the concrete and reinforcing bar. Each specimen was loaded in tension by pulling on the extended bar ends and the transverse pressure was varied from 0 – 15 MPa (0 – 2175 psi). From the

data, Doerr concluded that the bond stress $\tau(x)$ along the length of the bar could be calculated as:

$$\tau(x) = -\frac{1}{u}\frac{dP(x)}{dx} \qquad [2.6]$$

where u is the bar diameter, and $P(x)$ is the force at a point x along the length of the bar.

Losberg and Olsson (1979) systematically tested standard and altered Swedish reinforcing bars to determine which characteristics of reinforcing bars reduce splitting failures while maximizing bond. Diameter of bar, height of lug, inclination of lug, and distance between lugs were varied. Pullout tests established the lower limit of maximum bond without splitting failure while beam-end tests allowed realistic splitting failures to occur. Ring pullout tests were used to directly measure splitting force. The data showed that lug height and spacing made a negligible contribution to splitting failures. Splitting failures were more likely to occur with increased lug inclination rather than with transverse lugs. The amount of transverse reinforcement crossing the splitting surface greatly influenced the force developed in the reinforcing steel.

Reynods and Beeby (1982) investigated the effect of transverse steel on bond stresses in lap splices. They noted, in 100 x 200 x 1220 mm (3.94 x 7.87 x 48.0 in.) beam tests using No. 16 (0.63 in dia.) flexural bars and No. 8 (0.32 in dia.) stirrups that the increase in bond strength resulting from the transverse confinement depended on lap splice location. When the splice is in a constant moment region, the increase in bond strength is very little, since the stirrups are not fully engaged. However, in regions with diagonal shear cracks and the transverse steel is near yield, the increase in bond strength is significant.

Soroushian, *et al*. (1991) reported the results of a test program investigating the slipping behavior of beam-column connections. Block specimens with No. 13 (No. 4) stirrups and No. 25 (No. 8) anchor bars projecting from the block were tested in a pullout. Specimens varied in concrete strength and quantity of transverse reinforcement. Specimens with little or no transverse reinforcement failed in a brittle, splitting fashion. In contrast, the specimens with dense transverse reinforcement had ductile, pullout failures. The peak bond stress of the confined specimens was about twice that of the unconfined specimens. Also, the confined failure specimens had much high slip values when compared to the unconfined specimens. Peak bond stress and post-peak bond stress increased with concrete compressive strength. Bond stress, τ_1, in MPa, maybe calculated by:

$$\tau_1 = (20 - d_b / 4)\sqrt{f_c^{'} / 30} \qquad [2.7]$$

where the bar diameter, d_b (mm), and concrete strength, f_c, (MPa). For the typical specimen in this test program, bond stress is predicted to be about 9.91 MPa (1.44 ksi).

Malvar (1992) tested 12 specimens to investigate the local bond stress-slip characteristics of No. 19 (No. 6) reinforcing bars subjected to transverse confinement pressure. Each 76.2 x 102 mm (3 x 4 in.) cylinder had a single No. 19 (No. 6) bar and was confined by a steel ring. The angle of lug inclination was varied. By increasing the confinement stress from 3.45 – 31.0 MPa (500 – 4500 psi) the bond stress increased from about 11.4 – 19.3 MPa (1.65 – 2.80 ksi). Comparing pre-crack and post-cracked conditions, it was noted that confinement stress is crucial to ensuring an adequate bond after cracking has occurred.

Darwin, *et al*. (1996), using experimental test results from 199 specimens conducted by various researchers, statically showed that the ACI 318-95 design equations overestimated development and lap splice lengths. Never adopted, the proposed design equation is:

$$\frac{l_d}{d_b} = \frac{\dfrac{f_y}{\phi f_c^{'1/4}} - 2130\left(0.1\dfrac{c_M}{c_m} + 0.9\right)}{80.2\left(\dfrac{c + K_{tr}}{d_b}\right)} \qquad [2.8]$$

where f_y is longitudinal steel yield strength (psi); $f_c^{'}$ is concrete strength (psi); and ϕ is a factor of safety. The term c, taking into account concrete cover, is determined as:

$$c = \left(c_m + 0.5d_b\right)\left(0.1\frac{c_M}{c_m} + 0.9\right) \qquad [2.9]$$

where c_m and c_M are the minimum and maximum values of c_b or c_s. c_b is the bottom cover (in) and c_s is the minimum of one-half of the clear spacing between bars (in) or one-quarter of the side cover of the reinforcing bars (in). Lastly, the transverse reinforcement index is defined as:

$$K_{tr} = \frac{34.5 t_d A_{tr}}{sn} \qquad [2.10]$$

where t_d = ($0.72d_b$ + 0.28), represents the effect of bar size on the confining steel force; A_{tr} is cross-sectional area of transverse reinforcement (in^2); s is transverse reinforcement spacing (in); and n is the number of bars being developed.

Using Eq. [2.8], the development length of the typical specimen used in this experimental program is 1.17 m (46.7 in.), compared to the ACI 318-08 required value of 1.55 m (61.1 in.) as calculated in Section *5.3.1 Design Codes and Response 2000 Comparisons.*

Abrishami and Mitchell (1996) researched the effect compression has on bond strength from a series of pullout and push-in tests using No. 25 (No. 8) and No. 35 (No. 11) bars. Of the specimens which failed in pullout, the average bond stress was reported as 5.86 MPa (0.85 ksi). For specimens subjected only to pullout, the ratio of maximum to average bond stress was about 1.37. Specimens tested in both pullout and push-in had a ratio of 1.10.

Jeppsson and Thelandersson (2003) investigated the effect of debonded longitudinal reinforcement on shear capacity. Six small beam specimens with 6 mm stirrups and No. 10 (No. 3) flexural reinforcement were constructed with plastic pipe surrounding the majority of the flexural bars. Compared to a control specimen, the 80 percent reduction in bond only reduced the shear capacity by 33 percent, verifying that relatively little embedment length produces high bond stress.

Harajli (2004) conducted small beam tests using both normal and high strength concrete. It was noted that except for short development lengths, using $f_c'^{1/4}$ correlated much better for both concrete types than when correlating the data using $f_c'^{1/2}$.

Goodall (2010) reported an average bond stress value for vintage RCDG IT-beam specimens failing in shear-anchorage as 3.76 MPa (0.510 ksi). These specimens were similar in design to the T-beam specimens described in this thesis and were tested concurrently at Oregon State University.

Table 2.1 summarizes the average and peak bond stress values reported in the literature review documents. The value reported using Eq. [2.8] developed by Darwin, *et al*. considers the material and geometric properties of the present test program design specimen. The average bond stress value is 3.45 MPa (0.500 ksi).

Table 2.1 – Reported Bond Stress Values in Literature

Data Source	**μ_{avg} (MPa) [ksi]**	**μ_{max} (MPa) [ksi]**
Clark	2.07-2.76 [0.300-0.400]	4.83-6.20 [0.700-0.900]
Mains	2.31-6.14 [0.335-0.890]	-
Darwin, *et al*.	3.52 [0.510]	-
Goodall	3.76 [0.545]	-
Soroushian, *et al*.	-	9.91 [1.437]

2.3. Design Specification Review

An examination of the historical and the current design specifications for determining bond strength was conducted to compare the methods used to design vintage RCDG bridges to current methods. Documents reviewed were the Standard Specification for Highway Bridges published by the American Association of State Highway Officials (AASHO 1953), ACI 318 published by the American Concrete Institute (ACI 318-08), and the 2005 AASHTO-LRFD Bridge Design Manual published by the American Association of Highway and Transportation Officials (AASHTO-LRFD).

2.3.1. AASHO Allowable Stress Design

When vintage RCDG bridges girders were designed in the 1950s, AASHO used allowable stress design to design reinforced concrete structures (AASHO 1953). The applied bond stress, *u*, between concrete and reinforcing bars in beams was calculated as:

$$u = \frac{V}{jdZ_o} \qquad \text{AASHO Sec. 3.7.3.(c)} \quad [2.11]$$

where V is the total shear at section, jd is the arm of the resisting couple, and Z_o is the sum of perimeters of bars in one set. The code requires that the allowable bond stress subjected to the flexural reinforcement be limited to:

$$u = 0.10\, f_c^{'} \le 350\, psi \qquad \text{AASHO Sec. 3.4.12} \quad [2.12]$$

Starting in 1973, the AASHTO limiting bond stress equation considered bar diameter, d_b:

$$u = \frac{4.8\sqrt{f_c^{'}}}{d_b} \le 500\, psi \qquad [2.13]$$

The allowable stress method assumes that all the flexural reinforcing bars are equally sharing the stress, however as discussed in Section *4.4 Bond Stress*, this is not always true.

2.3.2. AASHTO-LRFD Bridge Design Specifications

Since the 1970s, an ideological shift has occurred to produce the modern day design provisions for guarding against anchorage failures. The practice of limiting bond stress in allowable stress design was replaced by the minimum development length provision required by load and resistant factor design (LRFD). The minimum development length is defined as the embedment length required to produce yield stress in the reinforcing bar. To make a comparison between modern and historical codes, the development length may be

converted to an average bond stress using Eq. [2.1]. The pertinent, current design specifications are summarized as follows.

For straight No. 36 (No. 11), and smaller bars, the minimum development length is:

$$l_{db} = \frac{1.25 A_b f_y}{\sqrt{f_c'}} \qquad \text{AASHTO-LRFD Sec. 5.11.2.1.1} \qquad [2.14]$$

but no less than $0.4 d_b f_y$. A_b, is the bar area (in^2), f_y is the steel yield strength (ksi), f_c' is the concrete strength (ksi), and d_b is the bar diameter (in.).

For No. 36 (No. 11) and smaller hooked reinforcing bars, the development length is:

$$l_{hb} = \frac{38.0 d_b}{\sqrt{f_c'}} \qquad \text{AASHTO-LRFD 5.11.2.4-1} \qquad [2.15]$$

and shall exceed $8 d_b$ or 6 inches, whichever is greater.

2.3.3. ACI 318 American Building Code for Structural Concrete

When vintage RCDG bridges girders were designed in the 1950s, ACI also required that reinforced concrete structures be designed using allowed stress design as described previously. (ACI 1956) Similar to Eq. [2.11], the applied bond stress, u, between concrete and reinforcing bars in beams was calculated as:

$$u = \frac{V}{\Sigma o j d} \qquad \text{ACI 318-56 Sec 901} \qquad [2.16]$$

where $\sum o$ is the sum of perimeters of bars in one set, j is the ratio of the distance between centroid of compression and centroid of tension to the beam depth, d. Like the contemporary AASHO code, the upper limit for bond stress was controlled by Eq. [2.12].

Like the AASHTO specification, ACI 318 shifted from allowed stress design to strength design. The current ACI 318-08 methods for determining minimum development are similar to the AASHTO-LRFD design equations.

Chapter 12.2 of ACI 318-08 describes two methods for determining the minimum development length of a straight reinforcing bar. In the simple method, for No. 22 (No. 7) and larger bars:

$$l_d = \frac{f_y \psi_t \psi_e \lambda}{20\sqrt{f_c'}} d_b \qquad \text{ACI 318-08 Sec. 12.2.2} \quad [2.17]$$

where f_y is the reinforcing bar yield strength (psi); d_b is the bar diameter (in.), and f_c' is the concrete strength (psi). Modification factors ψ_t, ψ_e, and λ consider concrete depth below the bar, the type of bar, and the type of concrete, respectively.

The complex ACI 318-08 method considers the effects of stirrups confinement and concrete cover:

$$l_b = \frac{3}{40} \frac{f_y}{\sqrt{f_c'}} \frac{\psi_t \psi_e \lambda}{\frac{c_b + K_{tr}}{d_b}} d_b \qquad \text{ACI 318-08 12.1} \quad [2.18]$$

The term $(c_b+K_{tr})/d_b$ need not be taken larger than 2.5. When this term is less than 2.5, splitting failures are likely, while pullout failures are more likely when the term is greater than 2.5 (ACI 2008). c_b *is* the lesser of the side cover measured to the center of the bar, the bottom cover measured to the center of the bar, or half of the center-to-center adjacent bar spacing (in). The transverse reinforcement index, K_{tr}, is defined by:

$$K_{tr} = \frac{A_{tr} f_{yt}}{1500sn} \qquad \text{ACI 318-08 12.2} \qquad [2.19]$$

where A_{tr} is the area of transverse reinforcement (in^2), f_{yt}, is the stirrup yield strength (psi), s is the stirrup spacing (in.), and the number of bars being developed along the plain of splitting is n. K_{tr} may be taken as zero for a conservative design.

For No. 36 (No.11) and smaller hooked bars, the development length is the greater of:

$$l_{dh} = \frac{0.02\psi_e \lambda f_y}{\sqrt{f_c'}} d_b \qquad \text{ACI 318-08 Sec. 12.5.2} \qquad [2.20]$$

$$l_{dh} \geq 8d_b \; or \; 6'' \qquad \text{ACI 318-08 Sec. 12.5.1} \qquad [2.21]$$

ACI 318-08 Section 12.5.3 describes various reduction factors which may be taken depending on cover and transverse reinforcement which are not reported here, since these factors do not apply to the present test specimens. ACI 318-08 specifies that the design moment curve be shifted a distance, d, to the right of left (whichever produces the maximum effect) to account for effect of diagonal cracks.

2.4. Conclusions

Based on the literature and design specification reviews, several conclusions about bond stress behavior are made:

- Most experiments do not adequately represent realistic member sizes or details. Pullout and beam end tests do not account for the effects of shear, especially at diagonally-cracked locations where bond stress demands are expected to be higher.

Generally, these tests are at a small scale, using flexural bars sizes which are smaller than those used in bridges.

- Historically, design codes have attempted to conservatively limit bond stresses. Since most data are developed from smaller bars, more information about the bond stress of specimens with larger bars is critical to assess the adequacy of present design specifications for evaluation of existing members with large size bars.
- Transverse reinforcement and concrete cover significantly increase bond stress at failure. This may be an important consideration for evaluating positive and negative moment regions of continuous bridge girders.

2.5. Research Objective

The objectives of this research are to:

- Investigate the role of idealized diagonal cracks near flexural cutoff locations on the behavior and strength of vintage RC girders in positive moment regions.
- Use test data to develop methods to rate existing bridges for flexural anchorage requirements around cutoff locations.

The effects of existing diagonal cracks on the bond of flexural reinforcing bars are not well understood. Diagonal cracks occurring during service level loading do not necessarily imply those cracks cause ultimate failure of the structure. The geometric and material properties of the girder greatly influence the behavior of the structure including: the type and location of anchorage details, the amount of transverse reinforcement, and the compressive strength of the concrete. The effect of a diagonal crack on anchorage response

depends on its overall relationship to the other section properties of the girder and loading. In the laboratory, the geometric and material properties can be precisely controlled and the response of the specimens can be measured. Measured bond stress along developing cutoff bars, the impact of design specification minimum development length, and influence of a preformed crack can be analyzed for their effect on the ultimate specimen behavior. Modified Compression Field Theory (MCFT) can be compared to tests results involving variable amounts of transverse reinforcement to investigate the influence of transverse reinforcement on tensile bar demand. Ultimately, improved understanding of the response of these bridge girders can help bridge inspectors and owners more efficiently and accurately identify potential issues, thereby allowing optional use of available resources for repair, replacement, or posting of truly deficient bridges.

3. EXPERIMENTAL SETUP

This chapter describes the design of the experimental setup, construction, testing protocol, and instrumentation used to characterize the performance of large size RC girders with diagonal cracks intersecting flexural reinforcing steel near cutoff locations. Four specimens were used in the test program and each of these had a similar geometry, with a varying number of flexural reinforcing bars and varying preformed crack orientation. Fig. 3.1 illustrates the specimen naming convention used in this study.

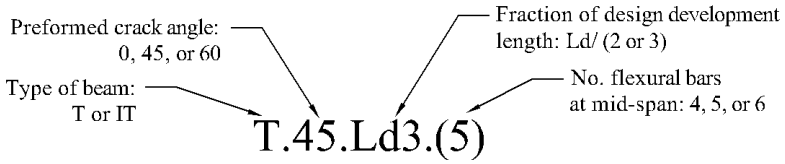

Fig. 3.1 – Specimen naming convention

3.1. Design Capacity

There are three likely failure modes for the specimens: “shear”, “flexure”, or “anchorage”. The goal of the design analysis was to identify the controlling shear-moment interaction point and then determine if the location had shear and moment capacities greater than the corresponding anchorage capacity.

3.1.1. Development Length Determination

The first step in designing the specimens was to determine the length of the cutoff bar past the preformed crack compared to the specified minimum development length. The minimum development length was determined using the AASHTO-LRFD Bridge Design Manual Design and ACI 318-08. Nominal material properties, representative of the specimens, were used: flexural bar steel yield strength of 472 MPA (68,500 psi), transverse

steel yield strength of 350 MPA (50,700 psi), and concrete strength of 24.1 MPa (3500 psi).

Following the procedures detailed in Section *2.3.2 AASHTO-LRFD Bridge Design Specifications*, the AASHTO-LRFD minimum development length was determined for a straight bar to be 1.81 m (71.4 in.) and for a hooked bar to be 726 mm (28.6 in.). As described in Section *2.3.3 ACI 318 American Building Code for Structural Concrete*, ACI 318-08 has two methods for determining the development length of straight bars. According to the simple method, the design minimum development length is computed as 2.07 m (81.6 in.). Assuming all of the specimens had transverse steel spaced at 254 mm (10 in.) and had a c_b of 54.6 mm (2.15 in.), the more detailed ACI 318-08 method produced a minimum development length of 1.55 m (61.1 in.). The development length of a hooked bar was determined as 829 m (32.6 in.). For a straight bar, the complex method produced a development length that is 75% of the simplified length.

At the time the test specimens in the present work were designed, it was thought that previous vintage T-beam specimens with a cutoff detail tested at Oregon State University did not exhibit anchorage failures. These specimens had a development length about one-half of that recommend by AASHTO-LRFD or 76.2 cm (30 in.). To ensure that an anchorage failure occurred in the present T-beam specimens, the embedment length was reduced to one-third the minimum development length required by the complicated ACI 318-08 method. Therefore, the cutoff bar embedment length past the preformed crack was

designed to be 0.52 m (20.3 in.). Further analysis, described in Section *3.1.4 Determining Likelihood of an Anchorage Failure*, justifies the use of this short development length.

3.1.2. Design Bond Stress Determination

Comparing the experimental bond stress values reported by other researchers as reported in Table 2.1, both the ACI 318-08 and AASHTO–LRFD design codes conservatively under-estimate the experimentally measured average bond stress quantities. In fact, based on the design analysis, the bond stress values inherent in the design codes will more likely predict an anchorage failure. Therefore, the bond stress value used to design the specimens was taken as the average bond stress of the literature review data, or 3.45 MPa (0.500 ksi)

3.1.3. MCFT Section Analysis Approach Using Response 2000

Response 2000 (R2K) is a free computer program, available on the Internet, developed by Evan Bentz and Michael Collins at the University of Toronto. (See http://www.ecf.utoronto.ca/~bentz/r2k.htm). The program performs a two-dimensional, non-linear sectional analysis for concrete beams and columns and assesses load-deformation response. R2K provides an easy-to-use input and output graphic user interface. For this investigation, the outputs of interest are the tensile demand on the flexural reinforcement and the AASHTO-99 shear-moment interaction diagram based on Modified Compression Field Theory (MCFT) as described in the AASHTO-LRFD Bridge Design Manual. R2K provides the predicted capacity for the specified moment-shear ratio. This was the value that was compared with the measured capacity of the T-beams specimens. The test specimens were analyzed at key cross-sections using R2K along the

development length of the cutoff bars, near the support, and an effective depth distance, d_v, from the loading point as described subsequently in Section*3.1.4 Determining Likelihood of an Anchorage Failure*.

3.1.4. Determining Likelihood of an Anchorage Failure

An anchorage failure was predicted to occur if the tensile demand calculated in Eq. [2.5] exceeded the resistive tensile force determined from Eq. [2.3]. The crack angle determined from AASHTO-LRFD method analysis was not used in determining likelihood of anchorage failure, for two reasons. First, AASHTO-LRFD predicts crack angles to be between 18° and 38° for specimens with at least minimum transverse reinforcement. Crack angles observed in field inspections are steeper than these values. Second, over the majority of the length of each specimen, the relatively shallow crack angles could not physically fit on the specimen in the present loading scheme. Given these two conditions, a Microsoft Excel macro program was written to search for the most likely crack angle-applied shear combination which satisfies Eq. [2.5] when limited by Eq. [2.3].

Summarized in the flowchart in Fig. 3.2, the macro works as follows: Inputs are required for the material properties, beam geometry, and locations of flexural and shear reinforcement. At 25.4 mm (1 in.) increments along the span, the effective area of flexural steel was determined using a linear method to interpolate strength gained along the developing bar. Hooked bar development lengths were determined using the AASHTO-LRFD method. For purposes of this analysis, the maximum average bond stress of a straight No. 36 (No. 11) bar was assumed to be 3.45 MPa (0.500 ksi) resulting in a

development length of 1.23 m (48.3 in.). In the end support regions, bond strength was increased by a factor of 1.3 over the 45° projection length along the straight bar (Higgins, *et al*. 2004). The effective shear depth per AASHTO-LRFD is determined for the effective flexural steel area. Based on the effective area of flexural steel at each increment along the span, Eq. [2.3] is used to determine the maximum tensile capacity at that section.

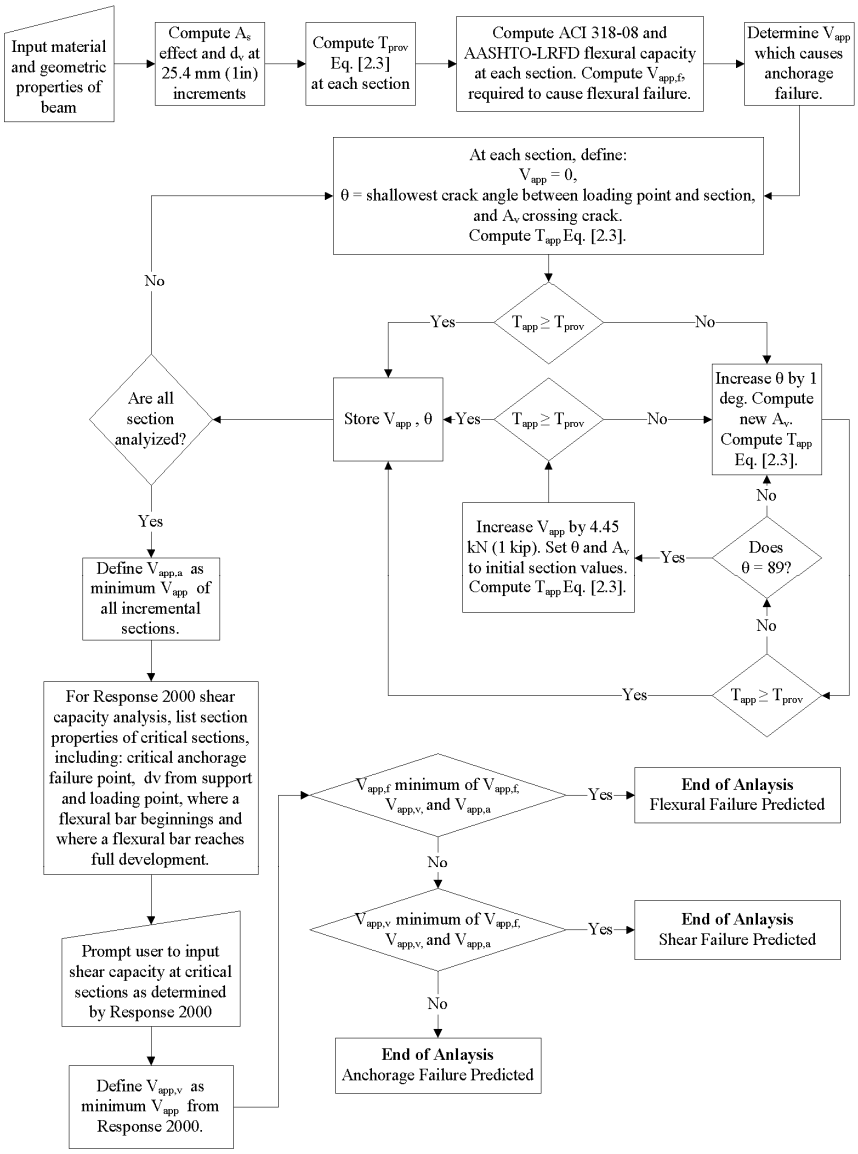

Fig. 3.2 – Failure load and mode solution procedure using Excel Macro

Satisfying Eq. [2.5] is an iterative process. Starting at the support location, the applied shear is defined as 4.45 kN (1 kip) and the crack angle is defined as the shallowest crack angle which can exist between the loading point and the section in question. The number of stirrups that cross the diagonal crack is calculated. If Eq. [2.5] is not satisfied by the given applied shear-crack angle combination, the angle is increased by 1 degree. If Eq. [2.5] is not satisfied when the crack angle is 89°, the applied shear value is increased by 4.45 kN (1 kip). The process continues until an applied shear value and corresponding crack angle are reported for every 25.4 mm (1 in.) increment of the beam.

An additional feature of the macro helps the user decide if the critical anchorage failure location is also the critical failure location when also considering shear and flexure. The program automatically calculates the flexural capacity of each section specified by ACI 318-08 and AASHTO-LRFD design specifications. The moment capacity is converted to a shear load that would produce the computed moment based on the given shear-moment ratio of the applied loading. Similarly, the shear capacity as determined by ACI 318-08 and AASHTO-LRFD is also calculated. The methods for calculating the code specified shear and moment capacities are presented in Appendix D and Appendix E, respectively. The user is prompted to input R2K predicted shear capacities at the critical locations. These locations include: where anchorage failure is identified in the above procedure; d_v from the support and loading point; where a flexural bar begins; and where a flexural bar reaches full development.

The applied shear at which anchorage failure may occur and the R2K predicted shear capacity and the equivalent shear to produce moment capacity are shown in Fig. 3.3. In the figure, only capacities for cross-sections on the under-reinforced section of the beam are shown and the equivalent shear to produce moment failure is not shown when the value is above 2224 kN (500 kips) for clarity. If the shear required to produce anchorage failure is below the shear strength and shear to produce moment failure, then an anchorage failure is most likely to control. The predicted shear at anchorage failure is compared to the actual shear at failure using experimental bond stresses and material properties are summarized in Table 3.1 and described in Section *4 Experimental Results.* Note that using this experimental bond stress, the predicted failure load indicates the point at which the flexural steel begins to slip, not when the specimens will no longer accept an increase in load.

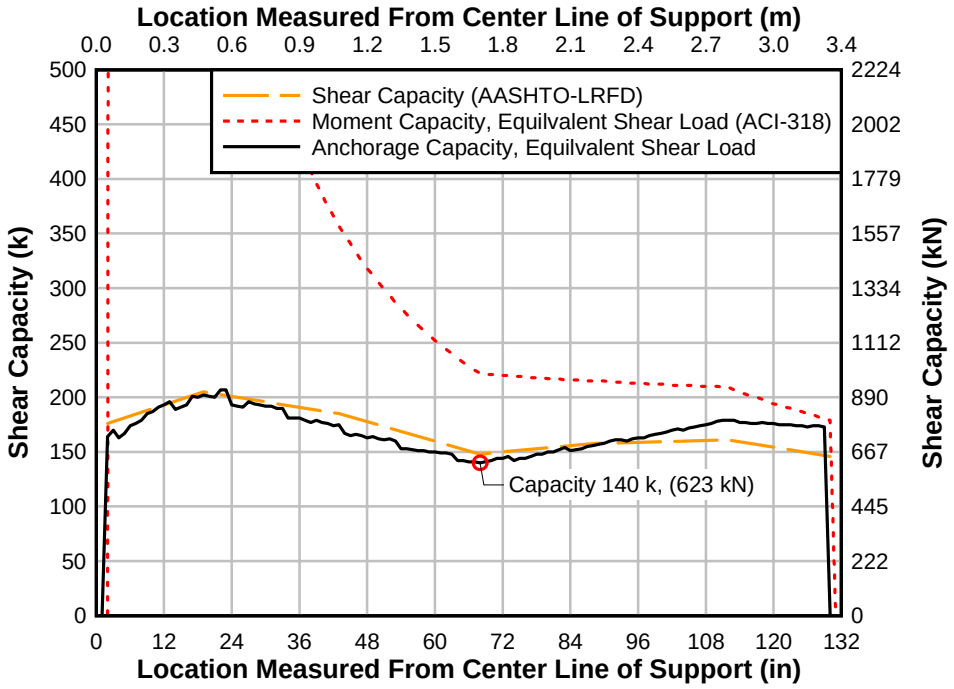

Fig. 3.3 - Example Macro capacity and mode prediction for Specimen T.45.Ld3.(4)

Table 3.1 – Comparison of Predicted to Actual Applied Shear at Anchorage Failure

Specimen	V_{PRED} at Max. μ_{avg} (kN) [kips]	V_{APP} (kN) [kips]	V_{DL} (kN) [kips]	V_{EXP} (kN) [kips]	V_{EXP} / V_{PRED}
T.45.Ld3.(4)	453.7 [102.0]	497.7 [111.9]	12.9 [2.9]	510.6 [114.8]	1.12
T.45Ld3.(5)	622.7 [140.0]	661.0 [148.6]	13.9 [3.1]	674.9 [151.7]	1.08
T.60.Ld3.(5)	622.7 [140.0]	685.0 [154.0]	16.6 [3.7]	701.6 [157.7]	1.13
T.0.Ld3.(5)	622.7 [140.0]	686.8 [154.4]	13.3 [3.0]	700.1 [157.4]	1.13

3.2. Specimen Description

3.2.1. Specimen Geometry

All of the test specimens were designed based on previous vintage RCDG T-beam tests at the Oregon State University (Higgins, *et al*. 2004). Each specimen is 7.92 m (26 ft) long, with a 356 x 1067 mm (14 x 42 in.) stem, and a 914 x 152 mm (36 x 6 in.) deck. To ensure failure of the beams where instrumentation was concentrated, half of the beam was over-reinforced with stirrups spaced at 152 mm (6 in.) and hooked flexural reinforcement extending past the support. The under-reinforced portion of each beam had stirrups spaced at 254 mm (10 in.). The No. 36 (No. 11) flexural steel was arranged in two layers, located 68.6 and 162 mm (2.70 and 6.45 in.) from the bottom of the beam. Each beam had two cutoff bars in the top layer, two hook bars in the bottom layer, and a straight bar extending the full length of the beam in the bottom layer for specimens with five flexural bars. Two No. 36 (No. 11) bars were used as compression reinforcement to facilitate construction. The elevation and cross-section of each specimen are shown in Figs.3.4 Fig. 3.4to 3.7.

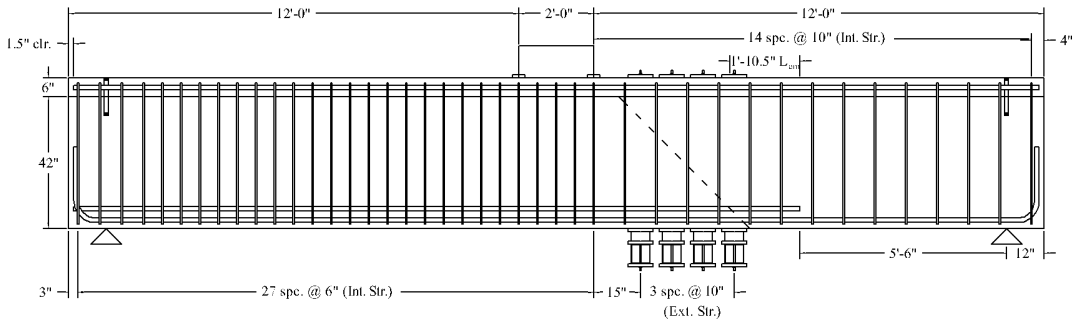

Fig. 3.4 – Elevation of specimens T.45.Ld3.(4) and T.45.Ld3.(5)

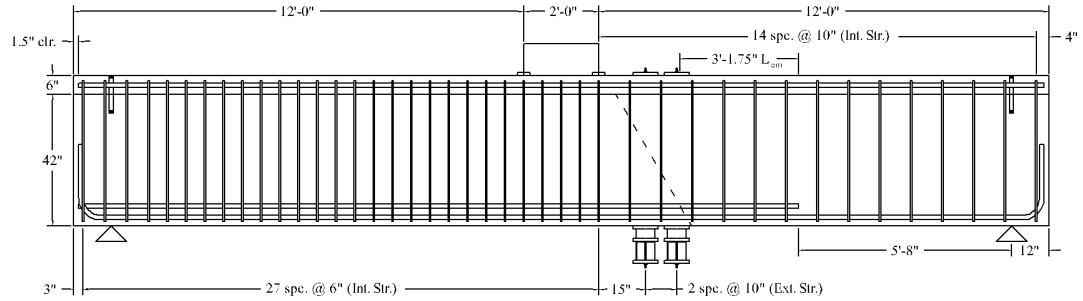

Fig. 3.5 – Elevation of specimen T.60.Ld3.(5)

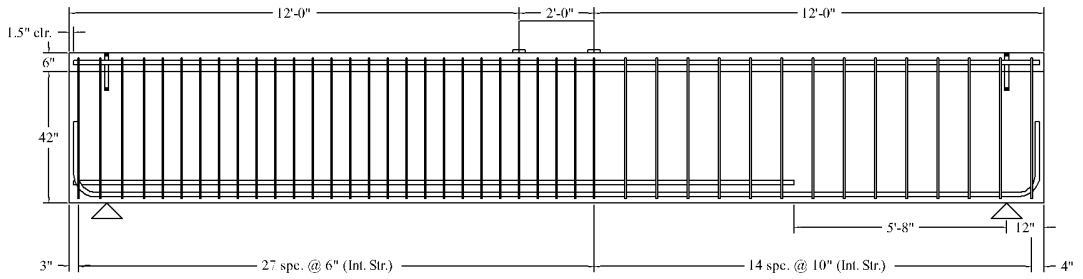

Fig. 3.6 – Elevation of specimen T.0.Ld3.(5)

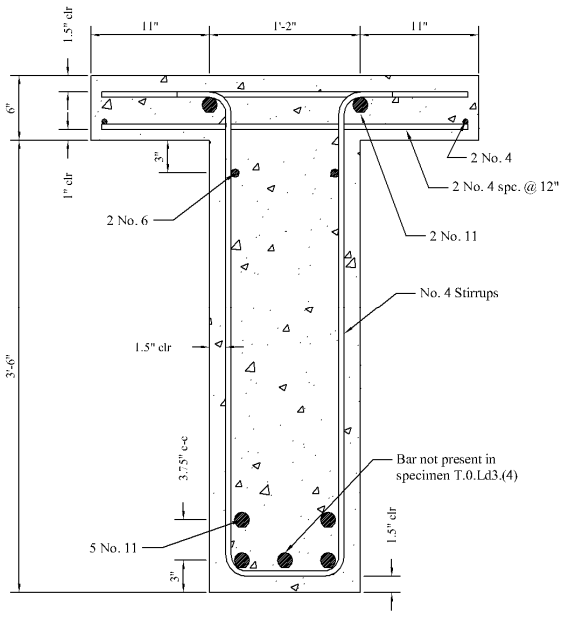

Fig. 3.7 – Typical specimen cross-section

It was intended that the cutoff bars extend past the preformed diagonal crack about one third of the development length specified by ACI 318-08 (for the No. 36 Gr. 420 (No. 11 Gr. 60) reinforcing bar). The specimen cutoff bars were shorter than in similar T-beam specimens tested in previous Oregon State University experimental programs (Higgins, *et al*. 2004). Specimen T.45.Ld3.(4) had a cutoff bar length as described above. However, for specimen T.45.Ld3(5), the instrumentation access box shifted during the concrete placement, resulting in a development length 50.8 mm (2 in.) shorter than originally intended. Therefore, specimens T.60.Ld3.(5) and T.0.Ld3.(5) were constructed with a shorter development length to allow more direct comparison with the results of specimen T.45.Ld3.(5).

Three preformed crack angles were investigated: 0°, 45°, and 60°. Preliminary analysis of the first two specimens, T.45.Ld3.(4) and T.45.Ld3.(5), showed that an anchorage failure would most likely occur when a crack angle of 45° developed with cutoff bars extending one third the ideal development length past the crack. The preformed crack angles for specimens T.60.Ld3.(5) and T.0.Ld3.(5) were then selected after the first two specimens were tested. For the initial specimens, the preformed crack was not the eventual failure crack. At failure, as the cutoff bars slipped through the concrete, new cracks formed at progressively steeper angles. Therefore, the T.60.Ld3.(5) was designed to investigate what happens when these progressively steeper cracks meet an existing weak plane. During testing, the 60° preformed crack was not mobilized at failure. To provide a control specimen without an initial preformed crack specimen T.0.Ld3.(5) was designed.

During service level loading, external stirrups, as shown in Fig. 3.8, were added and removed as described in Section *3.4 Loading Scheme* to examine the effect of varying amounts of transverse reinforcement on the tensile force carried by the flexural steel at the preformed diagonal crack location. It is only possible to determine the tensile force carried by the flexural steel using Eq. [2.5] when the crack angle and force in the shear reinforcement is known. Therefore, external stirrups were not deployed for specimen T.0.Ld3.(5).

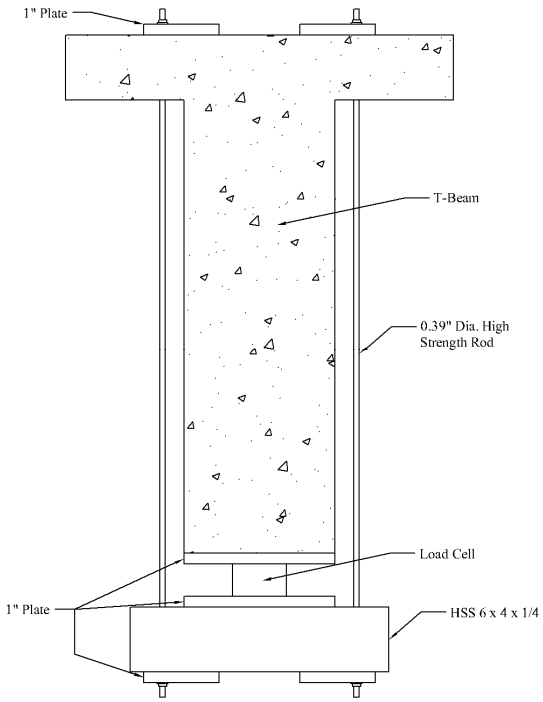

Fig. 3.8 – External stirrup setup

3.2.2. Specimen Construction

The reinforcement cage was assembled after strain gages were applied to the stirrups and flexural bars. To increase the likelihood of gage operation after exposure to water and vibration during the concrete casting process, the strain gages were waterproofed and the leads were tied to the reinforcement. The preformed crack was constructed from a piece of 1.59 mm ($^1/_{16}$ in.) thick polycarbonate sheet. The polycarbonate sheet extended all the way to the stirrups and was attached at these locations to maintain the crack geometry as shown in Fig. 3.9. Also shown in Fig. 3.9, a box constructed of wood allowed access to the strain gage leads and to the ends of the cutoff bars for later instrumentation.

Fig. 3.9 – Example of specimen geometry prior to concrete placement

3.3. Material Properties

Each specimen required approximately 4.59 m^3 (6 yd^3) of concrete which was provided by a local ready-mix supplier. The concrete design was based on the typical AASH0 “Class A”, 21 MPa (3000 psi) mix used in 1950s era bridges and has been used in previous research on similar sized specimens at Oregon State University. Standard slump tests were conducted and water added to achieve a 127 mm (5 in.) slump. The actual concrete compressive strengths were determined from 152 x 305 mm (6 x 12 in.) cylinders in accordance to ASTM C39M/C 39M-09a and ASTM C617-09a. Cylinders were tested on days 7, 14, and 28 when applicable. Average test day concrete strengths are reported in Table 3.2.

Table 3.2 – Average Test Day Specimen Concrete Strength

Specimen	Concrete Age (days)	Concrete Strength, f_c' (MPa) [psi]
T.45.Ld3.(4)	21	21.82 [3165]
T.45.Ld3.(5)	30	22.77 [3303]
T.60.Ld3.(5)	26	23.57 [3418]
T.0.Ld3.(5)	21	24.39 [3538]

All of the reinforcing steel was provided by a local rebar fabricator. The Gr. 276 (Gr. 40) No. 13 (No. 4) open internal stirrups were made from the steel heat with the lowest yield-stress available. All of the remaining internal steel was ASTM A706 Gr. 420 (Gr. 60). The material properties of the internal stirrups and flexural reinforcement were determined in accordance with ASTM E8-09a as reported in Table 3.3. The material properties of the external stirrups determined during a previous test program are also reported in Table 3.3 (Howell 2009).

Table 3.3 – Average Reinforcing Steel Properties

Reinforcement Type	Bar Dia. (mm) [in.]	Grade (MPa) [ksi]	f_y (MPa) [ksi]	f_u MPa) [ksi]
Internal Stirrups	12.7 [0.50]	280 [40]	369 [53.5]	583 [84.6]
Flexural	35.8 [1.41]	420 [60]	494 [71.7]	722 [105
External Stirrup Rod	9.9 [0.39]	N/A	581 [84.3]	672 [90.2]

The transverse reinforcing steel used in the test specimens reasonably approximates the Gr. 276 (Gr. 40) A305 steel available in the 1950s. Unfortunately, No. 36 (No. 11) reinforcing bars are not commonly commercially available in Gr. 276 (Gr. 40) steel, only in Gr. 420 (Gr. 60) steel.

3.4. Loading Scheme

All of the specimens were tested in the Structural Engineering Research Laboratory at Oregon State University. A reaction frame constructed on the strong floor allowed for four-point loading as shown in Fig. 3.10. A 224 kN (500 kip) servo-hydraulic actuator applied load to each specimen. Illustrated in Fig. 3.10, the steel loading shoe distributed the actuator force via two 102 mm (4 in.)-wide plates space 610 mm (24 in.) apart, centered about the middle of the specimen. Both loading plates were leveled and adhered to the specimen using hydrostone to ensure uniform application of the load across the plates. The specimens were leveled in the transverse and longitudinal directions, and were assumed to be perfectly straight and flat. Initial support settlements and midspan displacements were set to 0 mm (0 in.). Similarly, all other displacement sensors, strain gages, and load cells were set to zero.

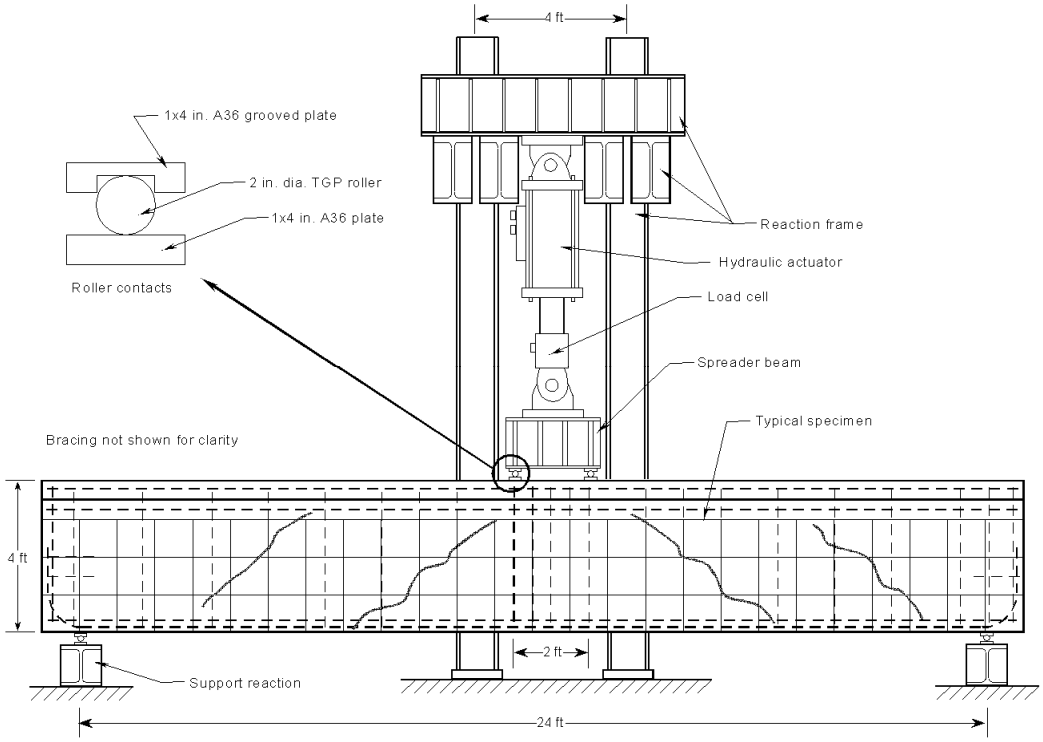

Fig. 3.10 – Four-point load configuration used for specimen testing

A series of cyclic tests without load reversals were performed on each specimen. Each load step increased the peak load by 111 or 222 kN (25 or 50 kips) from the previous load cycle as summarized in Table 3.4. The load was applied at a rate of 4.45 kN/sec (1 kip/sec). At each new load step, the load was reduced by 111 kN (25 kips) so cracks could be marked on the beam without creep effects.

Table 3.4 – Typical Load Cycle Pattern

Load Step	
(kN)	**(kips)**
0 – 111	0 – 25
22.2 – 222	5 – 50
22.2 – 334	5 – 75
22.2 – 445	5 – 100
22.2 – 667	5 – 150
22.2 – 890	5 – 200
22.2 –1112	5 – 250
22.2 – 1334	5 – 300
22.2 – to Failure	5 – to Failure

The loading cycle at each level was repeated for three reasons: to initiate any cracking of the specimen at that load level, to establish the load behavior of the specimen at the particular cracked condition (herein called baseline), and to investigate the effect of additional transverse reinforcement (external stirrups). The baseline test was used to make a direct comparison between the specimen with and without external stirrups throughout the load cycle. For specimen T.45.Ld3.(4), external stirrups were used at the 445 and 667 kN (100 and 150 kip) load cycles. For T.45.Ld3.(5) and T.60.Ld3.(5), external stirrups were used at the 445, 667, and 890 kN (100, 150, and 200 kip) load cycles.

3.5. Instrumentation

A variety of instruments were used on the interior and exterior of the specimens as described in the subsequent subsections. Data from all instruments were sampled every 0.25 seconds.

3.5.1. Internal Sensor Array

Internal strain gages served three purposes. Gages were applied on each stirrup leg at the mid-height of the stirrups and wherever the preformed crack crossed a stirrup in order to determine the tensile force carried by each stirrup at those locations. Specimens T.45.Ld3.(4) and T.45.Ld3.(5) had gages applied to a total of 13 stirrups. Since the force carried by the stirrups between the end of the cutoff and the support was negligible, those stirrups received no gages in specimens T.60.Ld3.(5) and T.0.Ld3.(5).

To determine the tensile force and bond stress distribution in the flexural bars, each bar had five strain gages. Three gages were between the end of the bar and where the preformed crack crossed the bar. Two gages were between the preformed crack and midspan.

A set of eight strain gages were used to determine the dowel action (reinforcing steel shear transfer) at the location where the preformed crack crossed the flexural bars in specimens T.45.Ld3.(4) and T.45.Ld3.(5). In specimens T.60.Ld3.(5) and T.0.Ld3.(5), the dowel action gages were located the same distance from the end of the cutoff bar as in the first two specimens. Only one flexural bar received these gages. In specimens T.45.Ld3.(5), T.60.Ld3.(5), and T.0.Ld3.(5), the gages were located on the bottom layer straight bar. Specimen T.45.Ld3.(4) had the gages on the west hooked bar. Fig. 3.11 shows the typical arrangement and labeling convention of the dowel action gages.

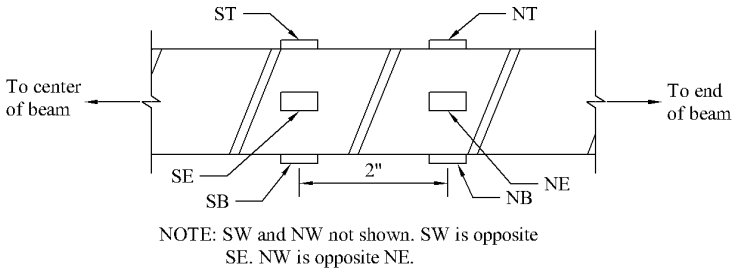

Fig. 3.11 – Dowel action strain gages locations

Fig. 3.12 shows the strain gage locations for specimens T.45.Ld3.(4) and T.45.Ld3.(5). Similarly, Fig. 3.13 illustrates the strain gage location for specimens T.60.Ld3.(5) and T.0.Ld3.(5). Appendix A gives further information about how each gage was labeled, and summarizes the data gathered from each gage.

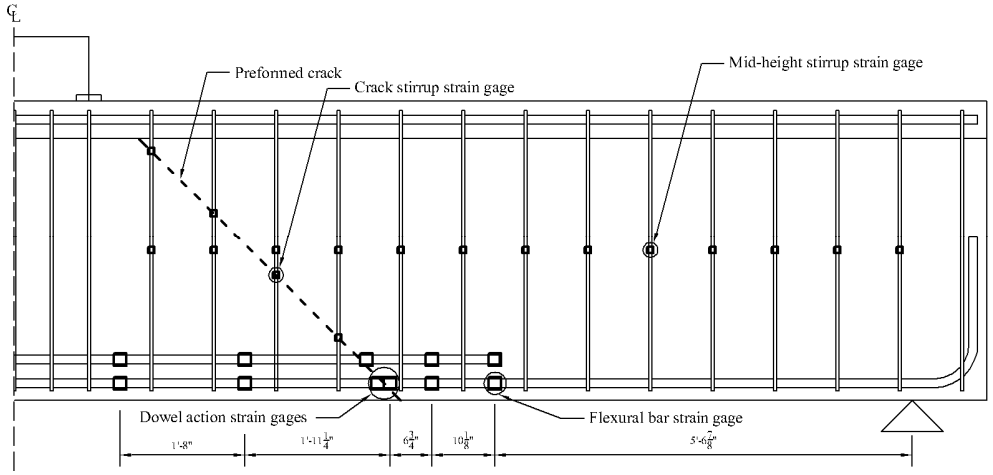

Fig. 3.12 – Specimens T.45.Ld3.(4) and T.45.Ld3.(5) internal sensor array

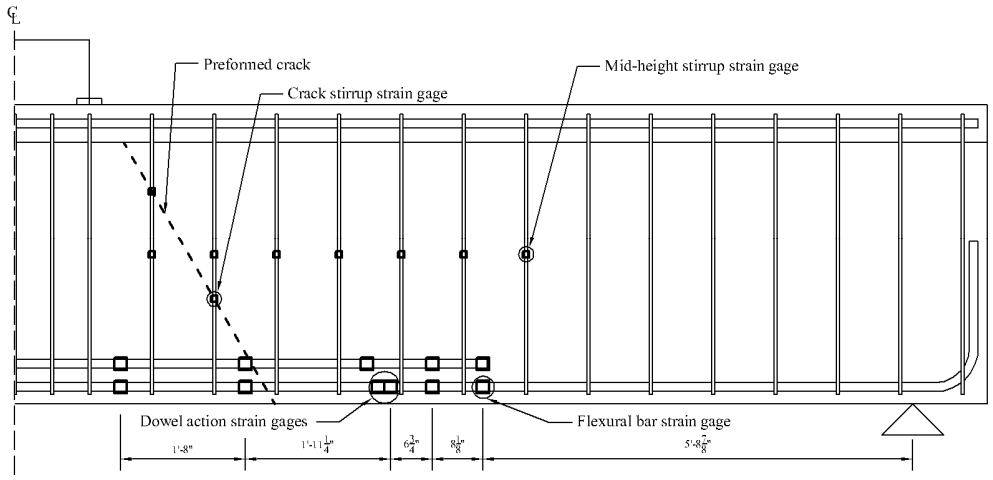

Fig. 3.13 – Specimens T.60.Ld3.(5) and T.0.Ld3.(5) internal sensor array

3.5.2. External Sensor Array

Although load cells were used to determine the force carried by the external stirrups, strain gages were also applied to each high-strength steel rod as shown in Fig. 3.8.

As shown in Fig. 3.14, six strain gages were applied in the concrete compression zone near the preformed crack. The strain information was used to determine the amount of shear carried by the concrete. Each gage was applied to a smooth surface which had been ground and prepared with an epoxy resin sub-base to fill any imperfections in the surface of the concrete. Specimen T.0.45.Ld3.(5) did not have any concrete compression zone gages.

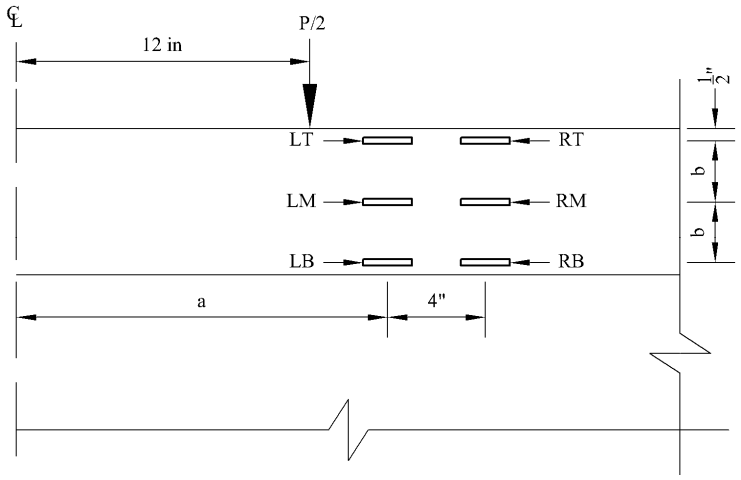

SPECIMEN	a (in)	b (in)
T.45.Ld3.(4)	15.50	1.50
T.45.Ld3.(5)	18.50	2.50
T.60.Ld3.(5)	12.25	2.50

Fig. 3.14 – Concrete compression zone strain gages locations

Pairs of displacement sensors with a range of 12.7 mm (0.5 in.) were used to measure the shear over regions of the beam. As the cracks opened, the top sensor would measure elongation, while the bottom sensor would measure contraction. There were a total of three regions instrumented as shown in Fig. 3.15. All of the gages were located on the northwest side of the beam.

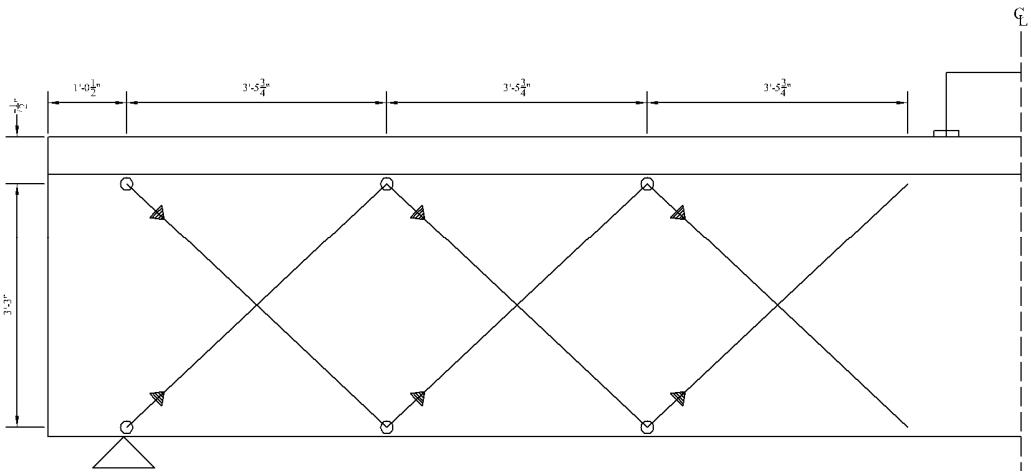

Fig. 3.15 – Typical external displacement sensor array

To measure midspan displacement, two 127 mm (5 in.) stroke displacement sensors were attached to opposite sides of the stem at midspan using threaded studs glued into holes drilled 38.1 mm (1.5 in.) from the bottom of the beam.

Displacement sensors were placed under each corner of the specimen to measure the support settlement. Each 12.7 mm (0.5 in.) stroke sensor was attached to a stand resting on the floor. As photographed in Fig. 3.16, a piece of small aluminum angle, adhered to the beam surface, provided a level surface for the sensor to rest upon.

Fig. 3.16 – Typical vertical displacement sensor to measure support settlement

To measure the relative slip between the cutoff bar and the surrounding concrete, a 12.7 mm (0.5 in.) stroke displacement sensor was placed at the end of each cutoff bar. In specimens T.45.Ld3.(4) and T.45.Ld3.(5), each instrument was anchored to a peg exposed in the instrument access box. Wood blocks were used to bridge the gap between the peg and center of the cutoff bar if necessary, as pictured in Fig. 3.17a. For specimens

T.60.Ld3.(5) and T.0.Ld3.(5), the exposed peg did not have sufficient length to attach to a sensor. Therefore, each sensor was glued to the box via a wood spacer, such that the instrument contacted the center of the cutoff bar. As photographed in Fig. 3.17b, an additional sensor was added to measure the movement of the crack which formed between the box and the surrounding concrete. The horizontal movement at the crack was later subtracted from the relative movement of the cutoff bar and the concrete.

a) Specimens T.45.Ld3.(4) and T.45.Ld3(5)

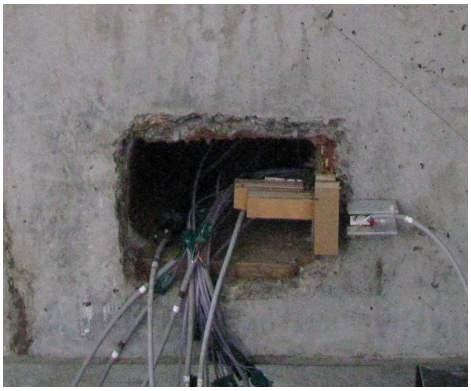

b) Specimens T.60.Ld3.(5) and T.0.Ld3(5)

Fig. 3.17 – Typical anchorage slip sensor installation

Lastly, displacement sensors were used to track the change in crack width of select cracks on the northwest side of the beam. For all of the tests, the preformed crack had two instruments straddling the crack. Specimens T.45.Ld3.(5) and T.0.Ld3.(5) had two instruments at the preformed crack location, with two addition sensors crossing the major crack which developed extending from the loading plate to the end of the cutoff bar.

4. EXPERIMENTAL RESULTS

Given the definition of anchorage failures in Section *2.1 Anchorage Concerns*, based on the crack patterns, cutoff bar slippage, and load versus midspan displacement behavior at failure, all the specimens exhibited pullout anchorage failures. All of the failures were ductile and exhibited signs of distress prior to failure. The applied shear at failure, the observed failure crack angle, and the as-built preformed diagonal crack angle are reported in Table. 4.1. Shear forces reported in Table 4.1 include the applied shear on the specimen from the actuator, V_{APP}, the shear force from the beam self-weight acting at the failure plane, V_{DL}, and the total shear force, V_{EXP}. Assuming the unit weight of reinforced concrete is 23.6 kN/m^3 (150 lb/ft^3), V_{DL} was estimated by computing the weight of concrete acting on the diagonally cracked failure plane. Where applicable, the as-built preformed diagonal crack angle was used for comparative analyses, not the design crack angle.

Table 4.1 – Summary of Specimen Condition at Failure

Specimen	**V_{APP} (kN) [kips]**	**V_{DL} (kN) [kips]**	**V_{EXP} (kN) [kips]**	**As Built Crack Angle**	**Failure Crack Angle**	**Anchorage Failure Type**
T.45.Ld3.(4)	497.7 [111.9]	12.9 [2.9]	510.6 [114.8]	45	36	Pullout
T.45.Ld3.(5)	661.0 [148.6]	13.9 [3.1]	674.9 [151.7]	45	33	Pullout
T.60.Ld3.(5)	685.0 [154.0]	16.6 [3.7]	701.6 [157.7]	70	49	Pullout
T.0.Ld3.(5)	686.8 [154.4]	13.3 [3.0]	700.1 [157.4]	-	35	Pullout

4.1. Displacement Results

4.1.1. Load-Deformation Response of Specimens

The load-deformation responses for all specimens were similar as seen in Figs.4.1 to 4.4. The deformation reported is the average midspan displacement less the average support settlement. In the standard cyclic tests, each specimen exhibited softening following the 222 kN (50 kip) load cycle. At failure, the applied load was maintained as deformation rapidly increased. The apparent ductility was not due to reinforcing steel yielding (as discussed later), but due to slip of the cutoff bars.

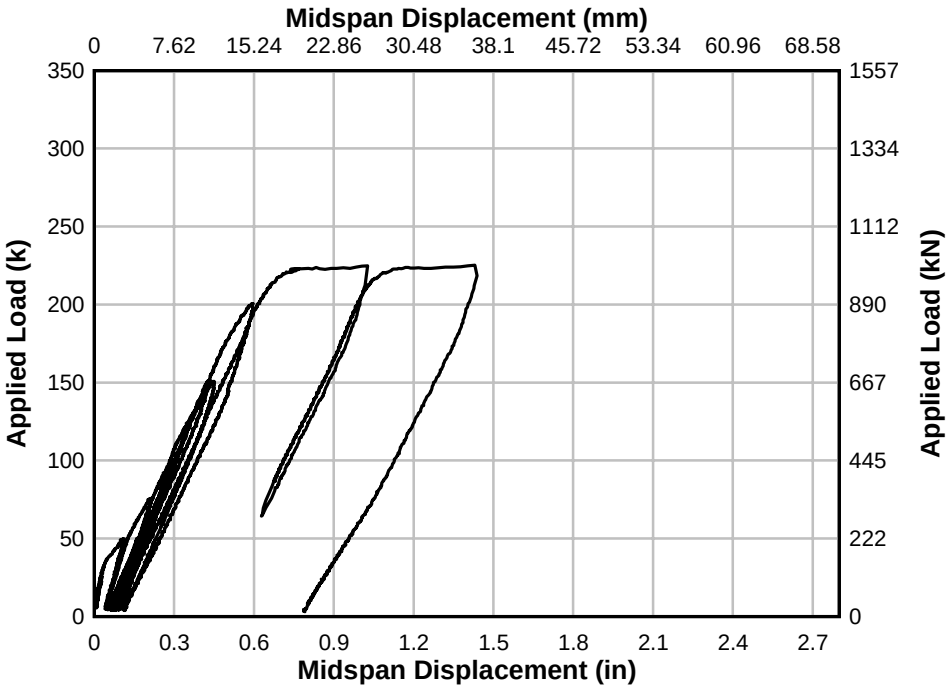

Fig. 4.1 – Specimen T.45.Ld3.(4) load-displacement plot at midspan

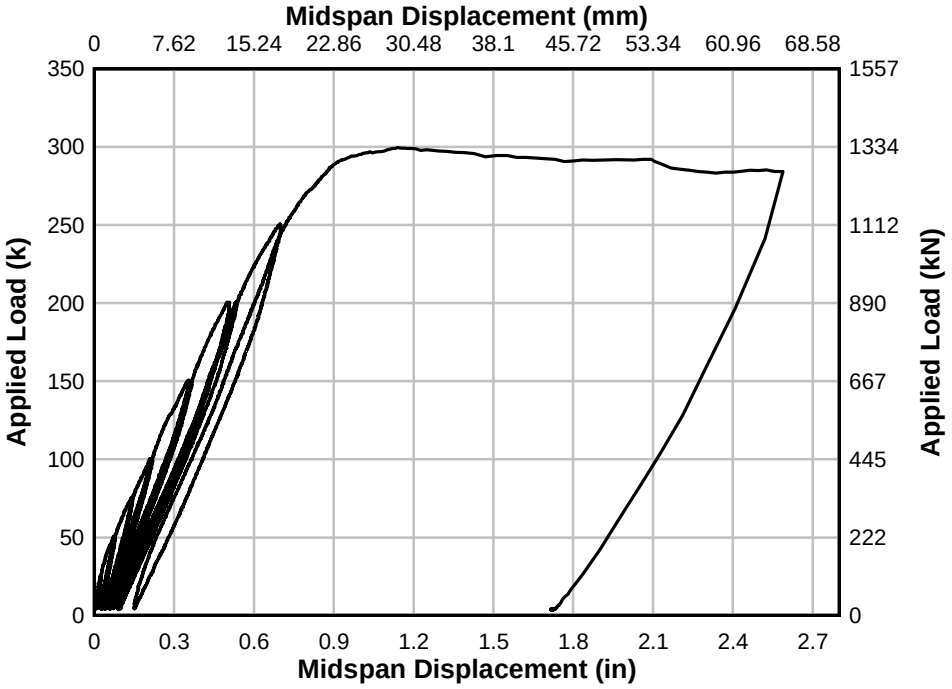

Fig. 4.2 – Specimen T.45.Ld3.(5) load-displacement plot at midspan

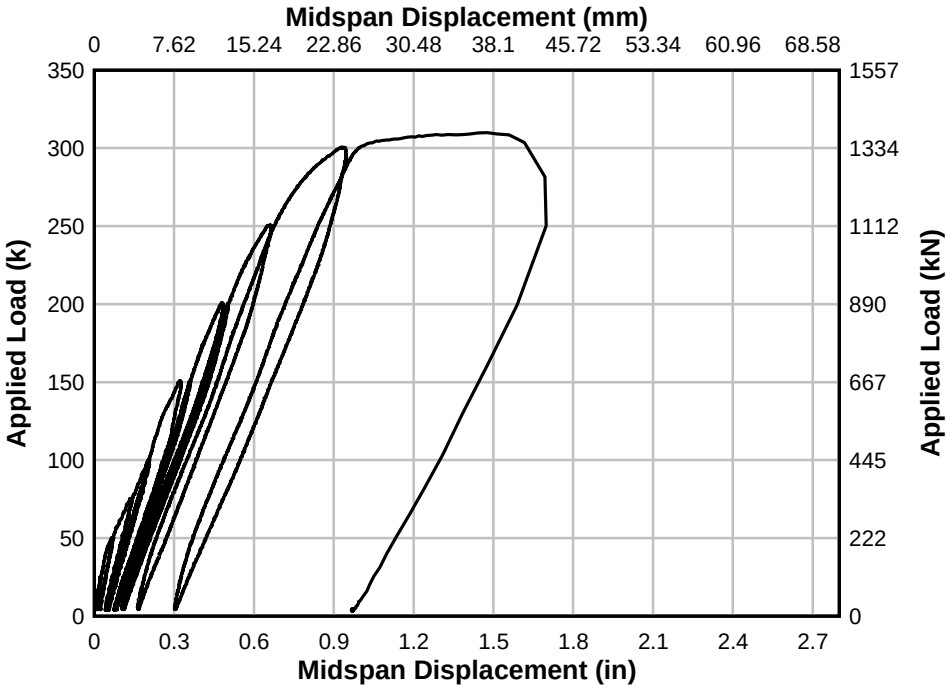

Fig. 4.3 – Specimen T.60.Ld3.(5) load-displacement plot at midspan

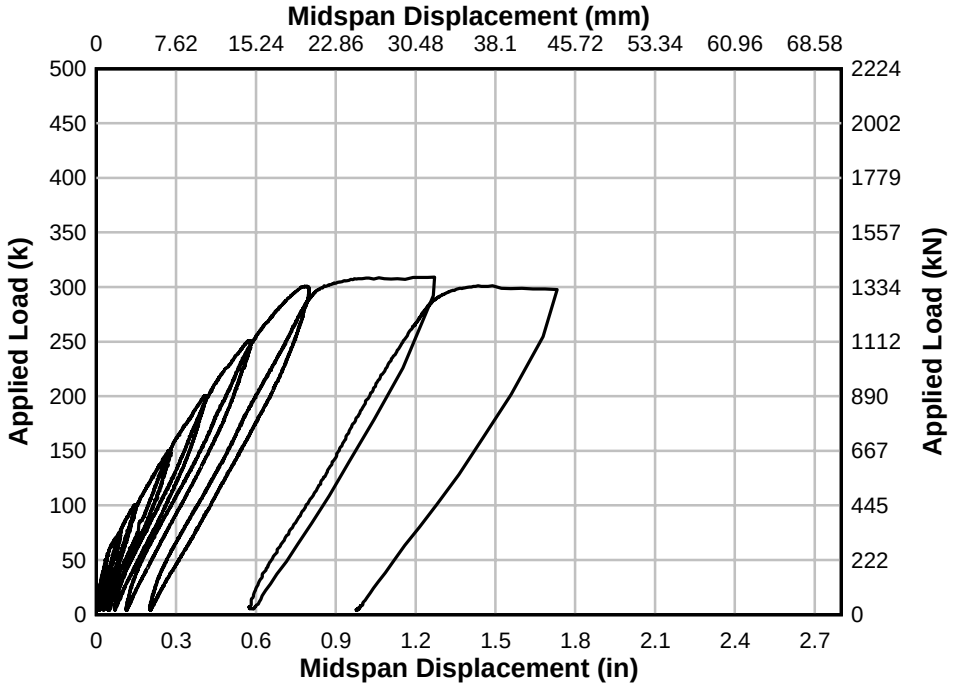

Fig. 4.4 – Specimen T.0.Ld3.(5) load-displacement plot at midspan

4.1.2. Crack Growth in Specimens

Crack growth was monitored throughout the test. At each new load level, the applied load was reduced by 111 kN (25 kip) after achieving the target amplitude. This allowed new cracks to be traced without producing creep deformations in the specimen. The crack map records are shown in Fig. 4.5. Photographs were taken after mapping cracks. In all cases, the crack that extended from the loading plate to the end of the cutoff bars caused failure as shown in Figs. 4.6 to 4.9

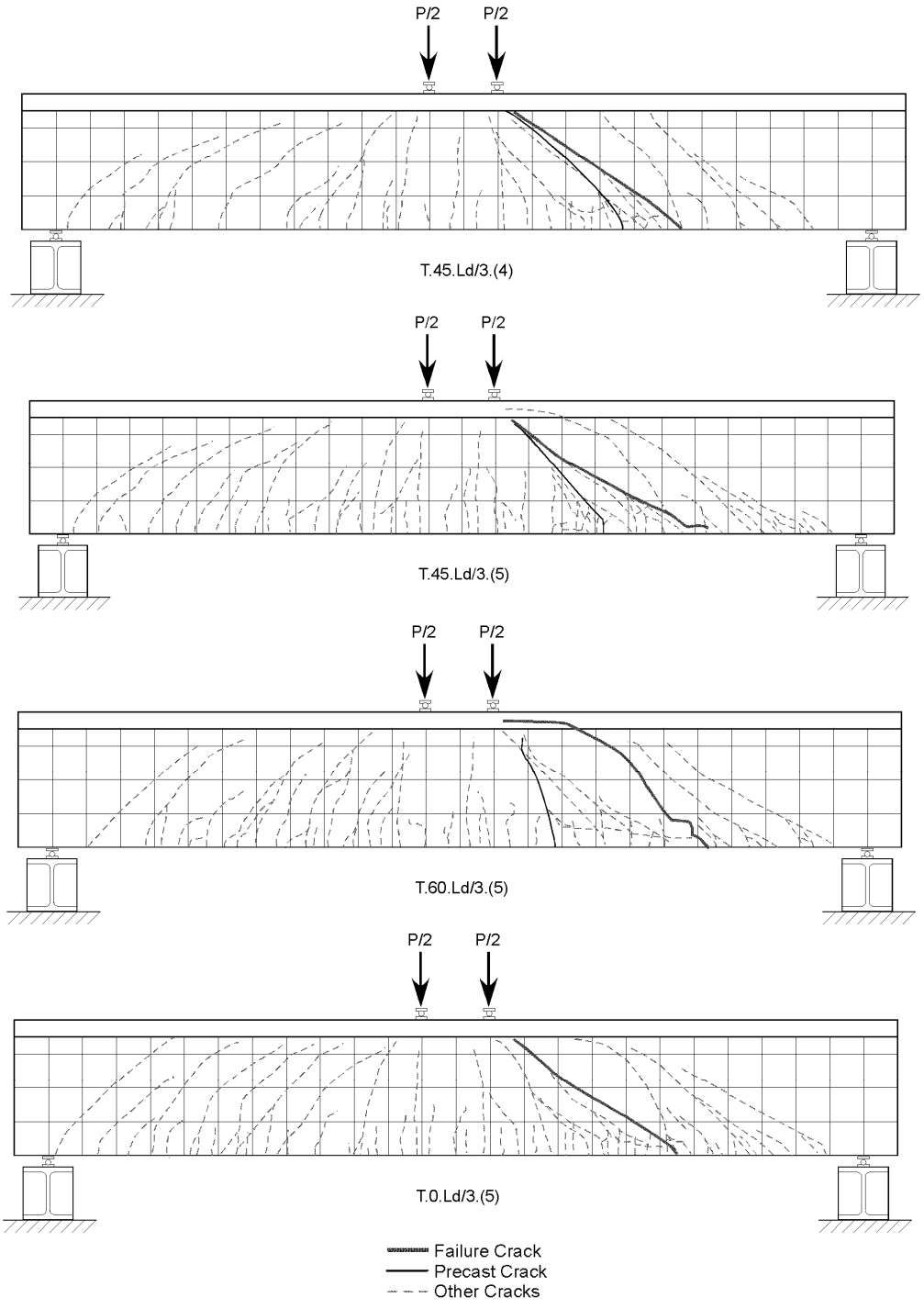

Fig. 4.5 – Failure crack maps

Fig. 4.6 – Specimen T.45.Ld3.(4) digital photograph at failure

Fig. 4.7 – Specimen T.45.Ld3.(5) digital photograph at failure

Fig. 4.8 – Specimen T.60.Ld3.(5) digital photograph at failure

Fig. 4.9 – Specimen T.0.Ld3.(5) digital photograph at failure

Just prior to failure, the largest diagonal crack in each of the specimens extended from the loading plate to the end of the cutoff bars. As the cutoff bars slipped, additional diagonal cracks formed while some of the existing cracks propagated. All of these diagonal cracks were steeper (more vertical) than the failure diagonal crack and were closer to midspan. Evidence of this diagonal crack evolution at failure was preserved in digital videos taken during testing.

Starting at the 445 kN (100 kip) load cycle, cracks along the anchorage zone of the cutoff bars started to form as shown in Fig. 4.10. These cracks were characterized by periodic vertical cracks extending from the location of the cutoff bar to the bottom soffit of the beam stem. The vertical cracks were connected by primary horizontal cracks at the level of the cutoff bar. As the applied load increased, the extent and density of the anchorage cracks increased.

Fig. 4.10 – Typical anchorage cracking caused by slip of the cutoff bars

4.1.3. Anchorage Slip Response of Specimens

All load-cutoff bar slip plots are reported in Appendix A. An example load-cutoff bar slip response is shown in Fig. 4.11 for specimen T.45.Ld3.(4). As seen here, at early stages of loading the permanent slip in the cutoff bars was less than 0.25 mm (0.01in.) for each specimen. As loads increased toward failure, the cutoff bars slipped and upon unloading residual slips was observed. At failure, large slip was observed, with as much as 12.7 mm (0.5 in.) (the limit of the instrumentation), as the additional load increased only moderately. This behavior was typical of all of the specimens.

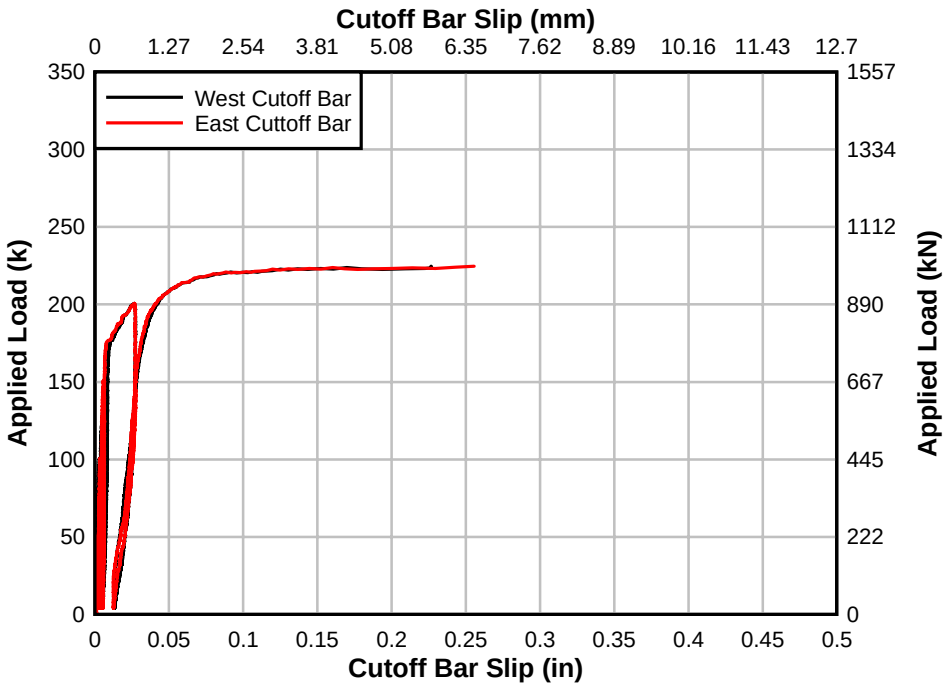

Fig. 4.11 – Typical load-cutoff bar slip plot (specimen T.45.Ld3.(4))

4.2. Shear Transfer

Shear carried by an internal or external stirrup leg, V_s, was calculated by converting measured strain, ε, to stirrup force:

$$V_s = A_v E_s \varepsilon_s \quad [4.1]$$

where E is the modulus of elasticity of the transverse steel (ksi), and A_v is the cross-section of one stirrup leg (in^2). Appendix B and Appendix C describe how the concrete compression zone shear transfer and dowel action were calculated, respectively.

4.2.1. Standard Test Comparison

The measured internal shear carried by the stirrups, concrete compression zone, and dowel action across the as build preformed crack for applied shears at various load levels for specimens T.45.Ld3.(4), T.45.Ld3.(5), and T.0.Ld3.(5) are shown in Figs.4.12 to 4.14. For specimen T.0,Ld3.(5), only the stirrups crossing what became the failure diagonal crack were used in the comparison as shown in Fig. 4.15. For graphs with multiple internal shear measurements, the line displayed is the cumulative value. In all cases, the stirrups carried the majority of the applied shear throughout the test and at failure. Sources of shear not accounted for include concrete shear and dowel action where strain gages were broken, and aggregate interlock, in the case of specimen T.0.Ld3.(5) Further, specimen T.0.Ld3.(5) carried relatively low load in the stirrups crossing the dominant crack before the crack appeared. Similarly, for specimen T.60.Ld3.(5), about one third of the applied shear is not accounted for since the 70° as built preformed crack was at no time the dominant crack. For the 45° specimens, most of the applied shear was accounted for since the failure crack in both cases was closer to 45° at about 35° and the failure crack did not become dominant until late in the test.

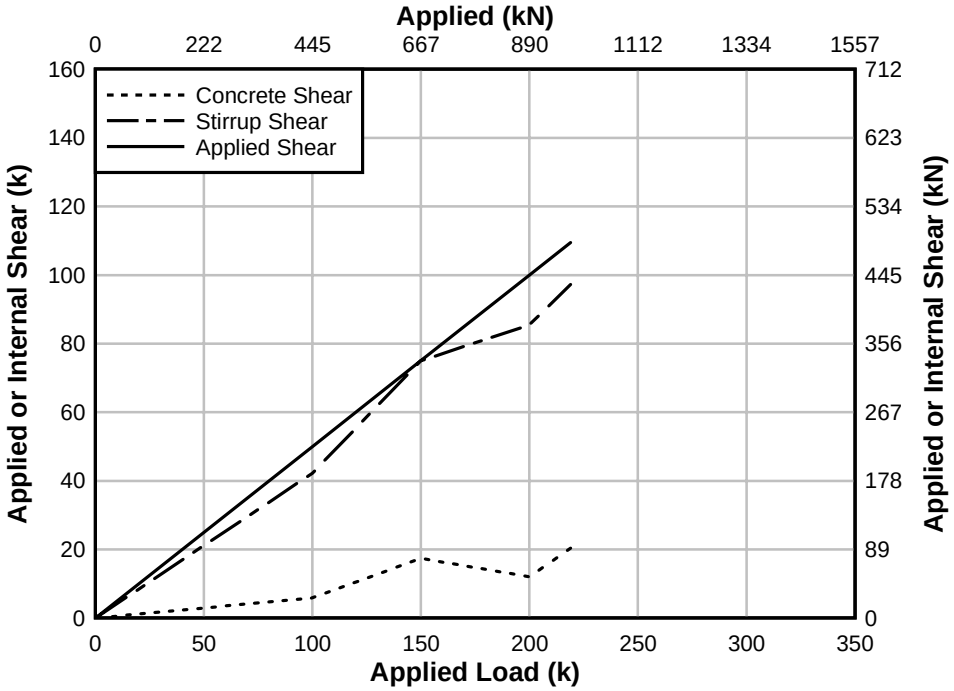

Fig. 4.12 – Specimen T.45.Ld3.(4) internal and applied shear comparison

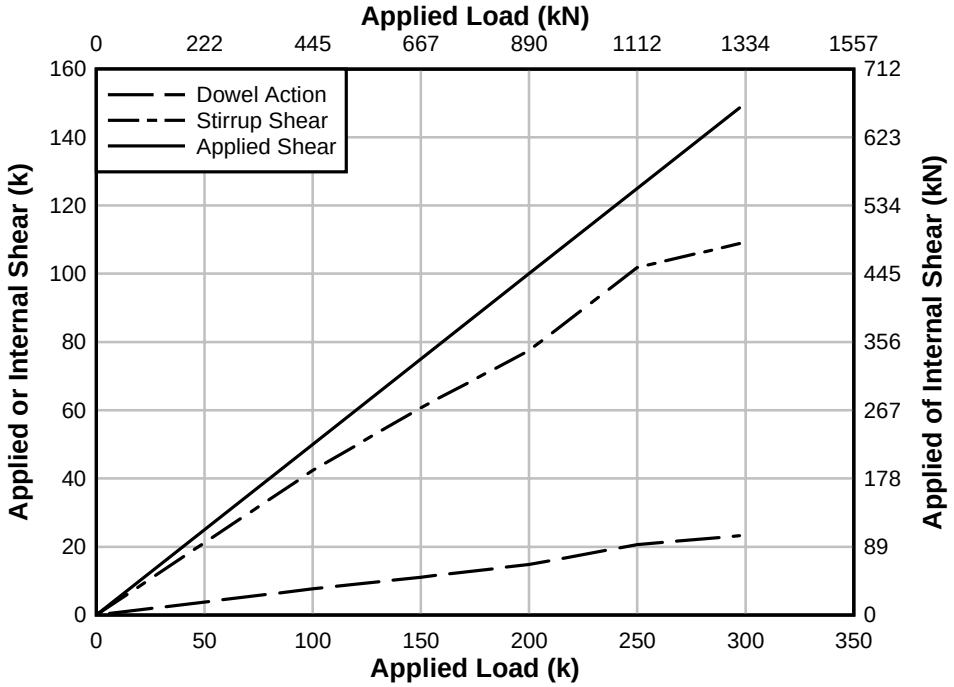

Fig. 4.13 – Specimen T.45.Ld3.(5) internal and applied shear comparison

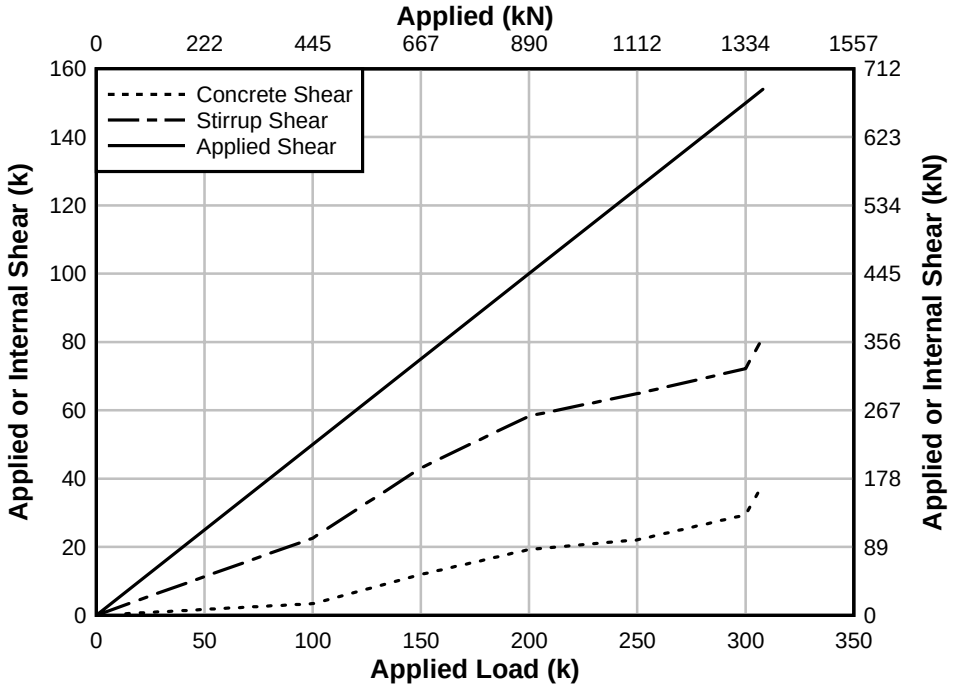

Fig. 4.14 – Specimen T.60.Ld3.(5) internal and applied shear comparison

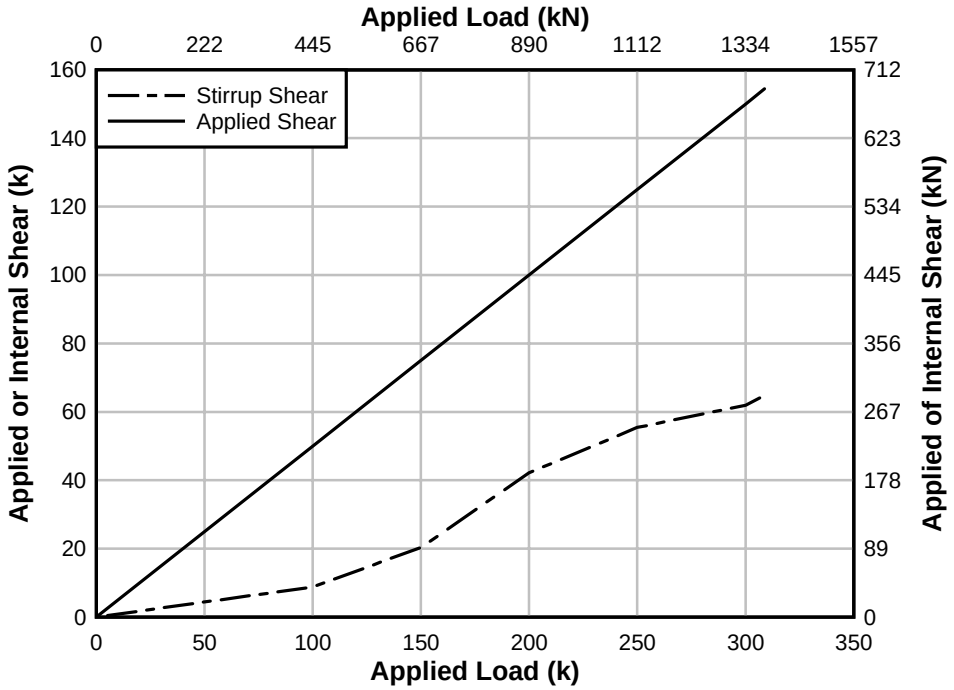

Fig. 4.15 – Specimen T.0.Ld3.(5) internal and applied shear comparison

4.2.2. Baseline and External Stirrup Test Comparison

The amount of shear carried by the stirrups that crossed the preformed crack in specimens T.45.Ld3.(4), T.45.Ld3.(5), and T.60.Ld3.(5) are shown in Figs. 4.16 to 4.18. When comparing the amount of shear carried by the internal stirrups during the baseline tests to the internal and external stirrups during the complimentary external stirrup load cycle, the internal stirrups carried slightly less force when the external stirrups were engaged. The total stirrup forces during the external stirrup tests were always more than during the baseline test. The changes in concrete compression zone shear transfer and dowel action are not included in the comparison as the concrete compression gage readings were influenced by local compression stress from the external stirrup top transfer plates.

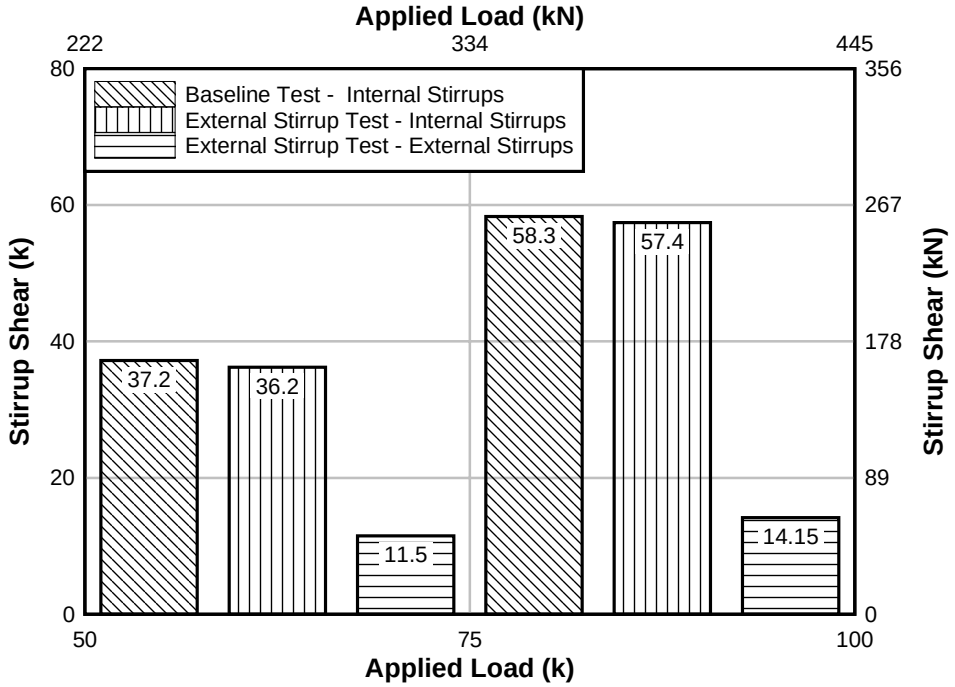

Fig. 4.16 – Specimen T.45.Ld3.(4) baseline and external stirrup tests shear transfer comparison

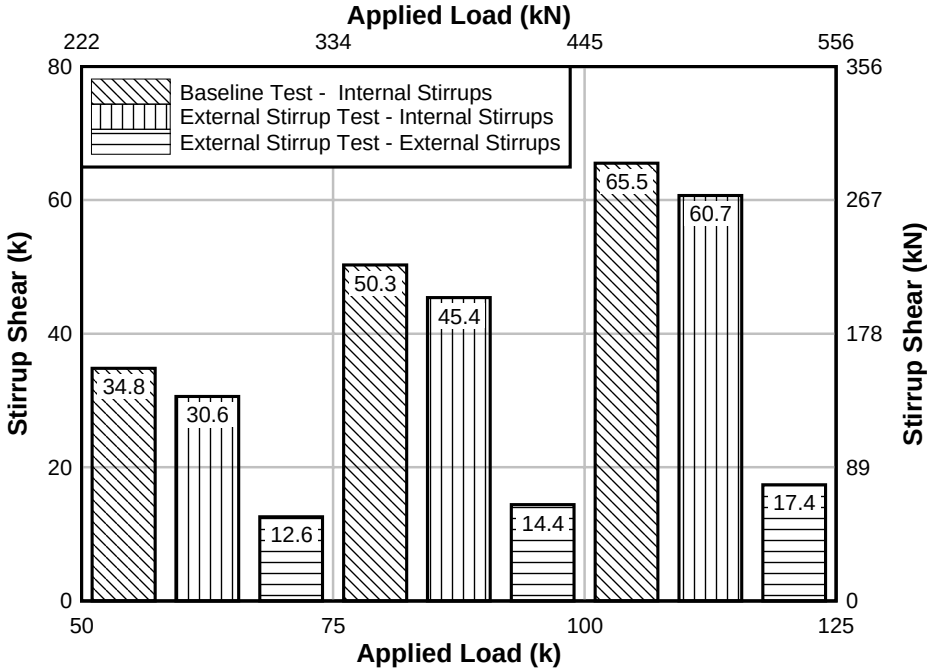

Fig. 4.17 – Specimen T.45.Ld3.(5) baseline and external stirrup tests shear transfer comparison

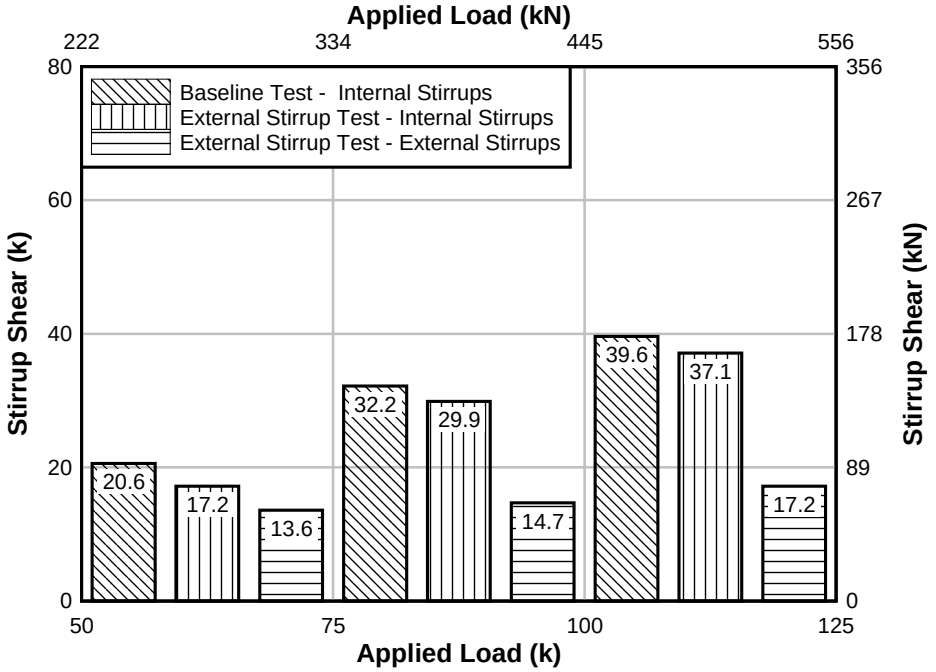

Fig. 4.18 – Specimen T.60.Ld3.(5) baseline and external stirrup tests shear transfer comparison

4.3. AASHTO-LRFD Tensile Capacity

Tension carried by the flexural reinforcement, T, at any particular point along the length of the bar was calculated by converting the measured strain, ε_s, to force as:

$$T = A_s E_s \varepsilon_s \qquad [4.2]$$

where E_s is the modulus of elasticity of the flexural steel (ksi), and A_s is the cross-sectional area of the bar (in^2).

4.3.1. Standard Test Comparison

The predicted AASHTO-LRFD tensile capacity of the flexural reinforcing at the preformed crack location using Eq. [2.5] was compared with the measured tension force flexural steel for specimens T.45.Ld3.(4), T.45.Ld3.(5), and T.60.Ld3.(5) as seen in Fig. 4.19. In all cases, AASHTO-LRFD overestimated the tensile capacity.

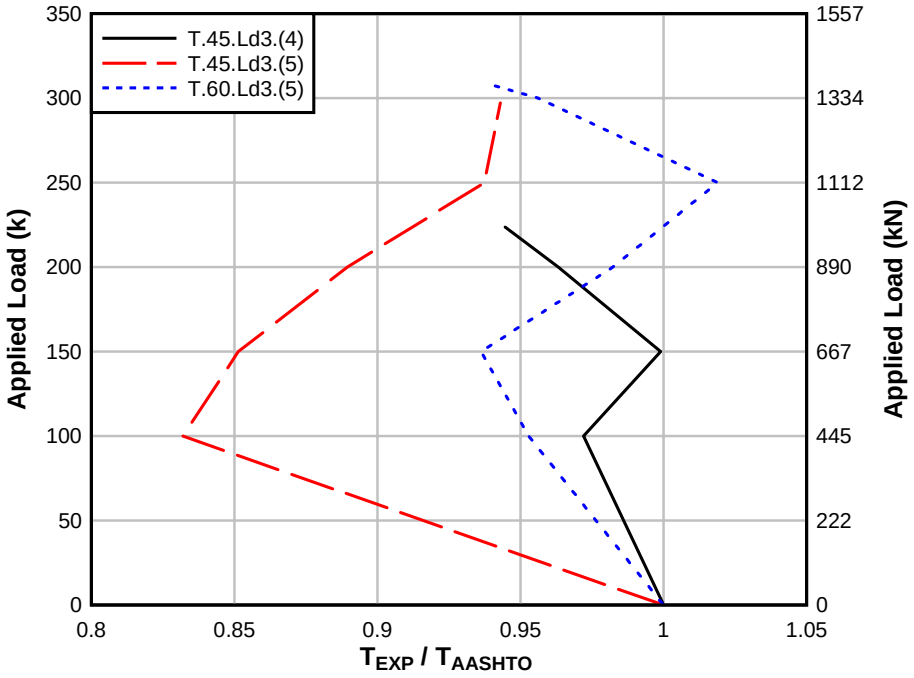

Fig. 4.19 – Comparison of predicted AASHTO-LRFD tensile capacity to actual capacity

The tensile demands in the flexural reinforcing steel of the five bar specimens over the entire load history are shown in Fig. 4.20. This figure shows the that the tensile demand for specimen T.45.Ld3.(5), T.60.Ld3.(5) and T.0.Ld3.(5) is similar during the entire load history. The three specimens had similar specimen geometry and material properties except for orientation of the preformed diagonal crack. The similarity of the data indicates the preformed crack has little influence on the overall behavior of the structure.

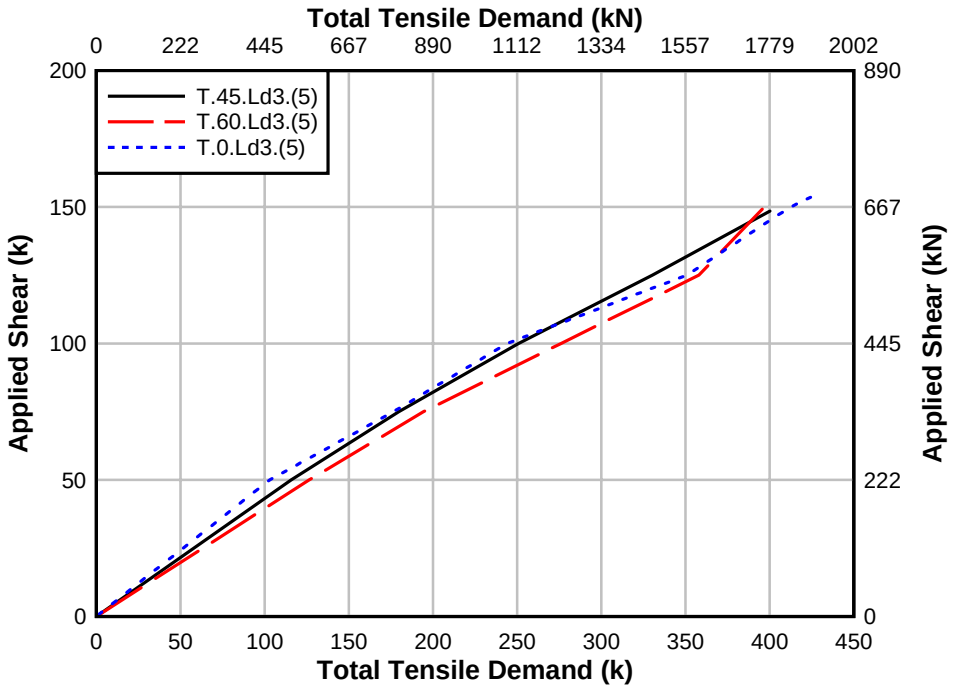

Fig. 4.20 – Comparison of total tensile force carried by five bar specimens

The tensile forces carried in the fully anchored bars and cutoff bars were not the same at coincident instrument locations along the span. The typical distribution of force in the fully anchored and developing flexural bars is shown in Fig. 4.21. As seen in this figure, the

cutoff bar carried a noticeably lower tensile force at the coincident locations. The difference between the fully anchored and developing bars decreased toward midspan.

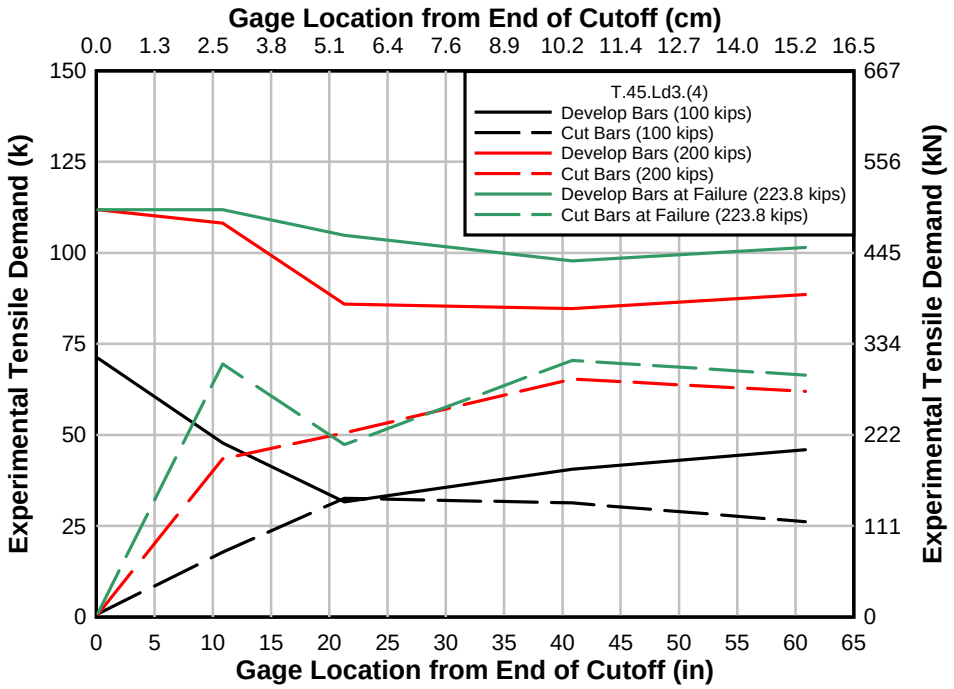

Fig. 4.21 – Comparison of distribution of tensile force among flexural reinforcing bars (specimen T.45.Ld3.(4))

4.3.2. Baseline and External Stirrup Test Comparison

The external stirrups were centered between the internal stirrups crossing the preformed crack, increasing the shear reinforcement at the preformed crack location by about 30 percent. This did not significantly change the experimental tensile demand on the flexural reinforcing bars at the preformed crack location as seen in Table 4.2. Generally, the experimental tension decreased by only about 4.44 kN (1 kip). However, the AASHTO-LRFD predicted demand is reduced in the presence of external stirrups. Therefore, the ratio

of the experimental tensile force to the predicted is closer to 1.0 for the external stirrup tests than in the baseline test as shown in Figs. 4.22 to 4.24.

Table 4.2 – Comparison of Tensile Forces in Flexural Bars with and without External Stirrups

Specimen	Applied Shear (kN) [kips]	No External Stirrups		External Stirrups		Tension Decreased Y/N
		AASHTO (kN) [kips]	Measured (kN) [kips]	AASHTO (kN) [kips]	Measured (kN) [kips]	
T.45.Ld3.(4)	222.4 [50]	621.8 [139.8]	604.9 [136.0]	598.3 [134.5]	605.4 [136.1]	N
	333.6 [75]	926.5 [208.3]	934.5 [210.1]	897.6 [201.8]	928.7 [208.8]	Y
T.45.Ld3.(5)	222.4 [50]	621.8 [139.8]	524.4 [117.9]	603.1 [135.6]	533.3 [119.9]	N
	333.6 [75]	936.7 [210.6]	814.9 [183.2]	869.1 [195.4]	817.5 [183.8]	N
	444.8 [100]	1252.6 [281.6]	1129.8 [254.0]	1225.0 [275.4]	1128.0 [253.6]	Y
T.60.Ld3.(5)	222.4 [50]	643.2 [144.6]	621.4 [139.7]	636.1 [143.0]	616.9 [138.7]	Y
	333.6 [75]	965.2 [217.0]	927.0 [208.3]	956.3 [215.0]	922.1 [207.3]	Y
	444.8 [100]	1278.4 [287.4]	1282.8 [288.4]	1266.4 [284.7]	1277.5 [287.2]	Y

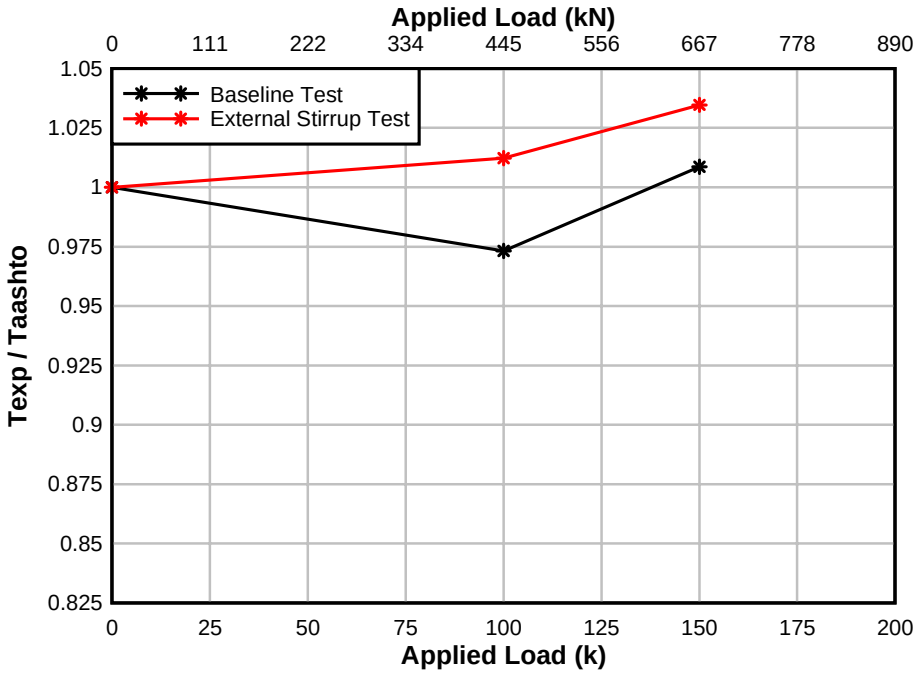

Fig. 4.22 – Specimen T.45.Ld3.(4) comparison of tensile forces when external stirrups were and were not present

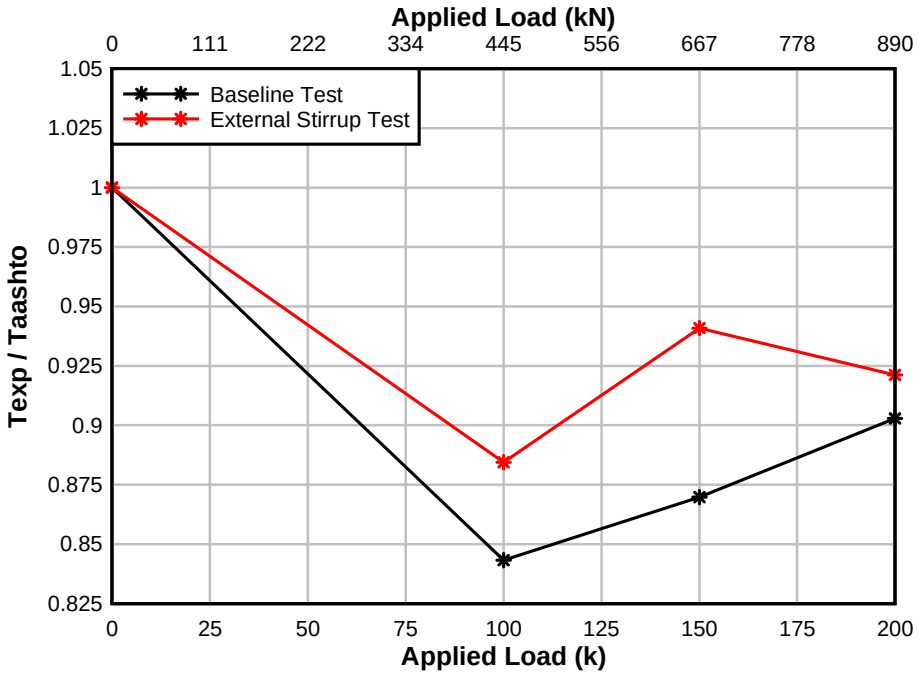

Fig. 4.23 – Specimen T.45.Ld3.(5) comparison of tensile forces when external stirrups were and were not present

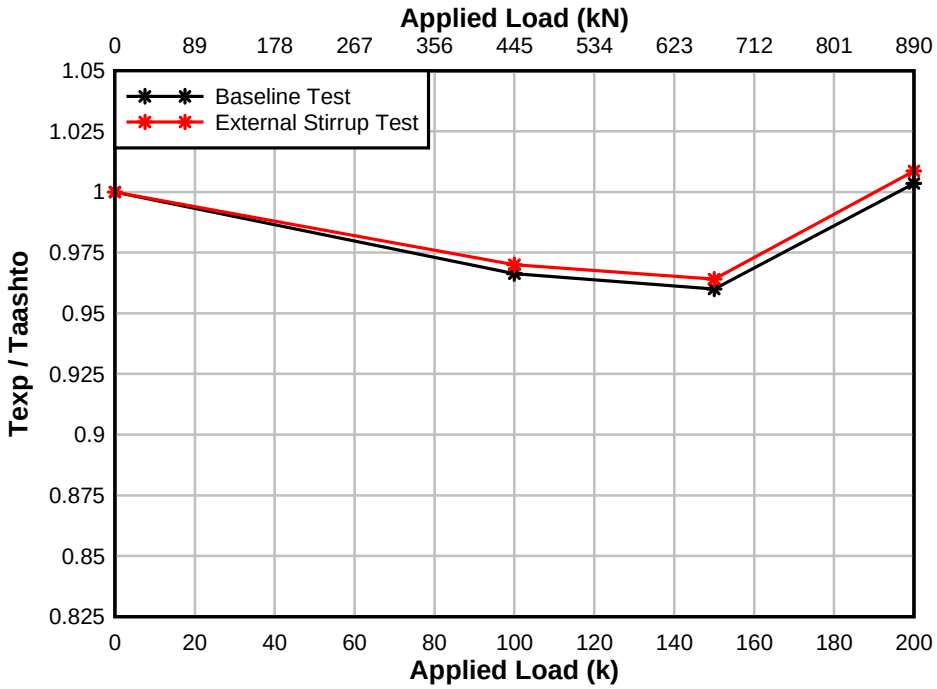

Fig. 4.24 – Specimen T.60.Ld3.(5) comparison of tensile forces when external stirrups were and were not present

4.4. Bond Stress

Using Eq. [2.1] the average and peak bond stress values for each cutoff bar in each specimen were determined and reported in Table 4.3. The average bond stress was taken as the average measurement from all of the strain gages between the end of the cutoff bars and the preformed crack. The peak bond stress was taken as the maximum bond stress value along the cutoff bars. For T.0.Ld3.(5), which did not have a crack, the bond stresses were determined using the first three sets of cutoff bar strain gages.

Table 4.3 – Summary of Peak and Average Bond Stresses (μ_{max} and μ_{avg}) in Cutoff Bars

Specimen	Cutoff Bars			Anchored Bars
	Bar	μ_{avg} (MPa) [ksi]	μ_{max} (MPa) [ksi]	μ_{avg} (MPa) [ksi]
T.45.Ld3.(4)	1	3.86 [0.560]	7.92 [1.149]	1.93 [0.280]
	2	5.05 [0.732]	12.05 [1.748]	
T.45.Ld3.(5)	1	7.57 [1.098]	19.43 [2.818]	1.98 [0.287]
	2	5.75 [0.834]	9.31 [1.964]	
T.60.Ld3.(5)	1	5.14 [0.745]	6.12 [0.887]	1.87 [0.271]
	2	5.97 [0.866]	6.41 [0.930]	
T.0.Ld3.(5)	1	7.72 [1.120]	8.62 [1.250]	2.05 [0.298]
Average		5.87 [0.851]	10.58 [1.535]	49.8 [0.284]

Average bond stress versus cutoff bar slip for each cutoff bar of each specimen is presented in Figs. 4.25 to 4.28. The responses of the different specimens were all slightly different. Generally, the maximum bond stress was achieved prior to member failure. However, in cases where data was available for both cutoff bars, the maximum bond stress does not necessarily occur concurrently or at the same slip value.

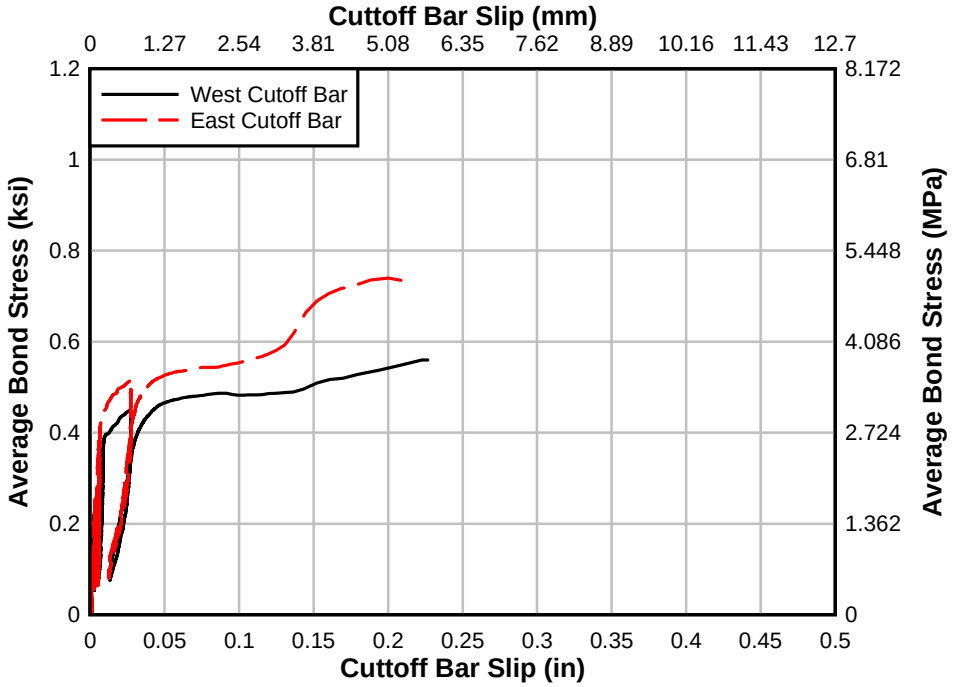

Fig. 4.25 – Specimen T.45.Ld3.(4) Bond stress-cutoff bar slip comparison

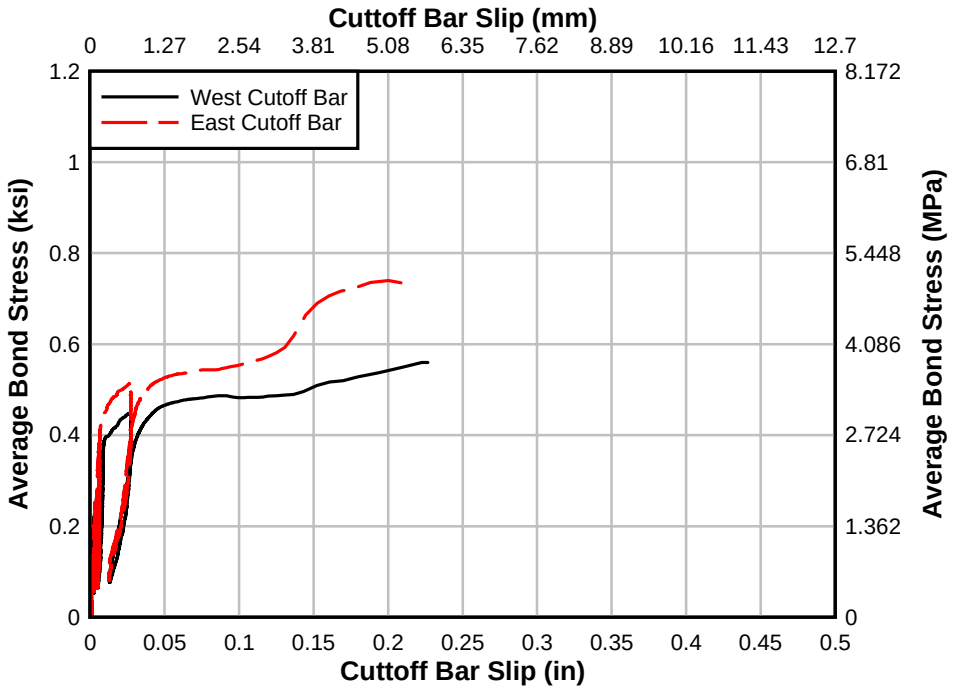

Fig. 4.26 – Specimen T.45.Ld3.(5) Bond stress-cutoff bar slip comparison

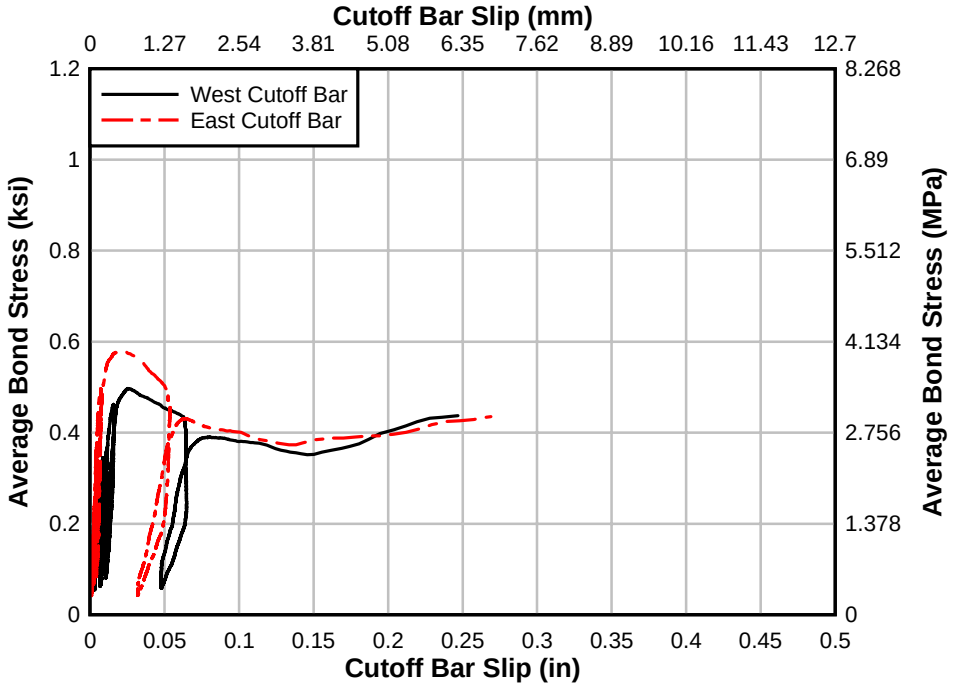

Fig. 4.27 – Specimen T.60.Ld3.(5) Bond stress-cutoff bar slip comparison

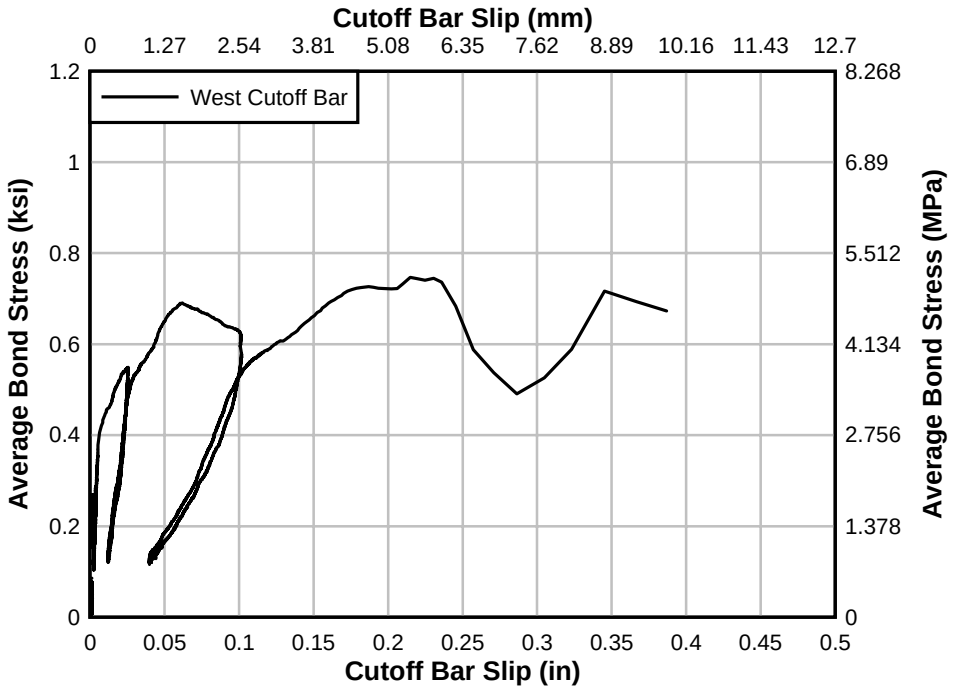

Fig. 4.28 – Specimen T.0.Ld3.(5) Bond stress-cutoff bar slip comparison

5. ANALYTICAL METHODS

Chapter 5 describes the methods used to analyze the experimental data. The experimental bond stress results were compared to present design specifications and archival literature sources. Similarly, the failure mechanism of the present specimens was compared to historical data. Nonlinear finite element analyses were performed and results were compared to the experimental results.

5.1. Experimental Bond Stress Analysis

The data showed that for a given location and loading, the tension carried by the cutoff and anchored bars was not equal. Therefore, a modification factor or tensile ratio, T_{ratio}, was applied to the tensile force of the cutoff bars before calculating the average bond stress. The T_{ratio} is defined as:

$$T_{ratio} = \frac{T_{cutoff}}{T_{anchored}} \quad [5.1]$$

where T_{cutoff} is the tensile demand on the cutoff bars per bar and $T_{anchored}$ is the tensile demand on the anchored bars per bar.

The T_{ratio} was calculated for all reinforcing steel with strain gages at points between the preformed crack and the end of the cutoff bar. A linear regression of the one-sided, 97.5% lower-confidence limit for these points is shown in Fig. 5.1. The R^2 correlation is 0.8054, which is reasonable for using the data to determine the effective bond strength at a given length of embedment. From the regression line, the maximum tensile force, $T_{97.5CL}$, for the cutoff bar is computed as:

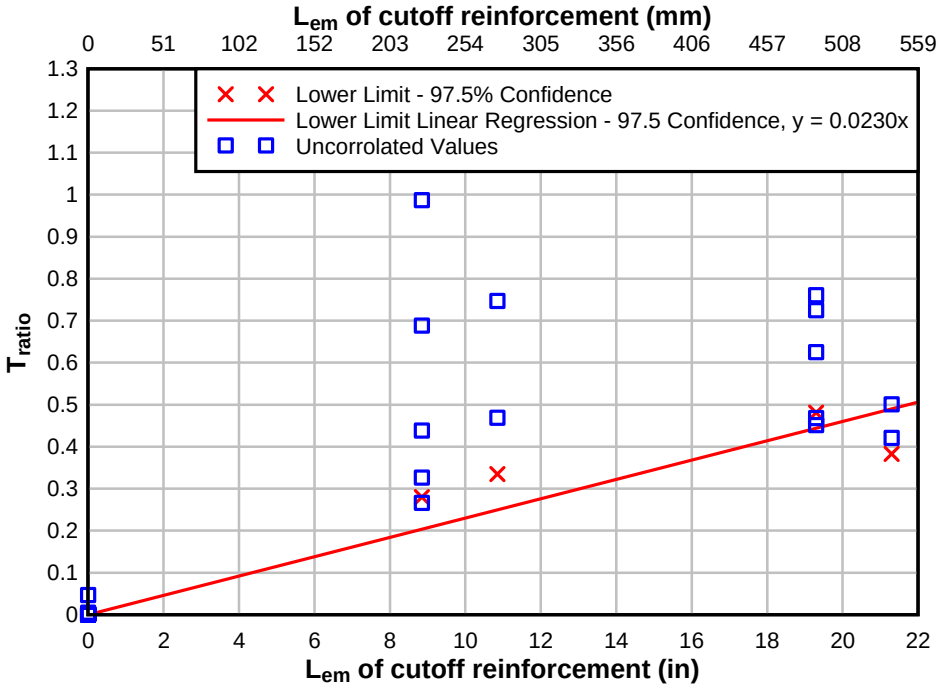

Fig. 5.1 – T_{ratio} analysis of the development of tension in cutoff reinforcement

$$T_{97.5CL} = 0.0230 l_{em} A_s f_y \quad [5.2]$$

where l_{em} is the length of embedment of the cutoff bar (in.), A_s is the bar cross-sectional area (in^2), and f_y is the flexural reinforcement yield strength (ksi). Eq. [5.2] must be limited by the full yield strength to indicate the bar is fully developed. Additionally, Eq. [5.2] may be converted to a maximum, permissible average bond stress, μ_{avg}, by:

$$\mu_{avg} = 0.00574 f_y d_b \quad [5.3]$$

where f_y is the flexural reinforcement yield strength (ksi), and d_b is the bar diameter (in.). Using the measured material properties for the test specimens, the average bond stress is 4.01 MPa (0.581 ksi) and the development length is 1.10 m (43.3 in).

5.2. Non-Linear Finite Element Analysis

The finite element method (FEM) has become a useful tool to structural engineers to analyze and predict behavior of complex structures. Successful implementation of the FEM relies on realistically representing the geometry, boundary conditions, and materials of the structure and validation of results with experimental findings.

5.2.1. Non-linear Finite Element Analysis Using VecTor2

Reinforced concrete can be a difficult material to model due to quasi-brittle and anisotropic properties and including realistic steel reinforcement interactions adds an additional degree of complexity. Such FEM analyses were under taken using a program called VecTor2. VecTor2 v6.0 is the core application of a suite of programs used for finite element analysis under development at the University of Toronto since 1990. VecTor2 is a two-dimensional, membrane, nonlinear finite element analysis program specifically intended for reinforced concrete structural modeling. Loadings schemes are static, cyclic or thermal. Two analytical models are used for predicting the results of rectangular reinforced concrete elements, Modified Compression Filed Theory (MCFT) (Vecchio and Collins, 1986) and the Disturbed Stress Field Model (DSFM) (Vecchio, 2000). The preprocessor, FormWorks v2.0 includes a graphical user interface for assigning structural geometry and material properties, an automatic mesh generator and bandwidth reducer, and produces VecTor2 input files. The postprocessor, Augustus v5.0.6 uses a graphical user interface to display the deflected shape, the crack patterns, and the stress-strain distribution in the elements.

VecTor2 uses low-order planar triangular, rectangular, and quadrilateral elements. Reinforcing steel can be modeled as either discrete or smeared. Linear truss bar elements model discrete reinforcement, with non-dimensional link or contact elements attaching the reinforcement to the concrete. The non-dimensional elements may be used to model bond-slip behavior. Alternatively, when modeled as smeared reinforcement, each element is modeled with a mixture of concrete and reinforcement material properties.

VecTor2 uses constitutive models for the concrete and steel reinforcement which account for second-order effects particular to reinforced concrete, including: compression softening, tension stiffening, tension softening, and tension splitting. Other reinforced concrete behaviors modeled by VecTor2 include: concrete dilation and confinement, bond slip, crack shear deformations, reinforcement dowel action, reinforcement buckling, and crack propagation. Default VecTor2 material and behavioral models were used to model the concrete and reinforcing steel. Appendix F, gives a brief description of each model. Further information for all models supported by VecTor2 are reported in the VecTor2 and FormWorks Manual (2002).

One of six models may be used to estimate the bond behavior between the concrete and the reinforcement. Each model uses a series of reference bond-slip and bond stress values, for both the unconfined (splitting failure) and confined (pullout failure) cases. When the anticipated confinement pressure is somewhere between the unconfined and confined cases, a confinement pressure coefficient, β, is used to linearly interpolate between the unconfined and confined cases, where β is defined as:

$$\beta = \frac{\sigma}{7.5} \qquad 0 \le \beta \le 1 \qquad \text{(in MPa)} \qquad [5.3]$$

where σ is the anticipated confinement pressure in MPa.

The “perfectly bonded” model assigns a large stiffness and strength to prevent deformation between the concrete and reinforcement elements. The “hooked bar” model consists of an ascending branch and sustained plateau at 22 MPa (3.19 ksi) of bond stress. The Fujii model is best suited when the expected failure is splitting. The Eligehausen, Gan, and Harajli models consider both the unconfined and confined cases. The Eligeausen and Gan models use the same model for a confined cases, and for the unconfined case, the models have the same peak bond stress. The Harajli predicts a higher confined bond stress, and for the unconfined case, the bond stress is zero after the peak bond stress has occurred. Fig. 5.2 compares the Eligehausen, Gan, and Harajli models using the material properties of

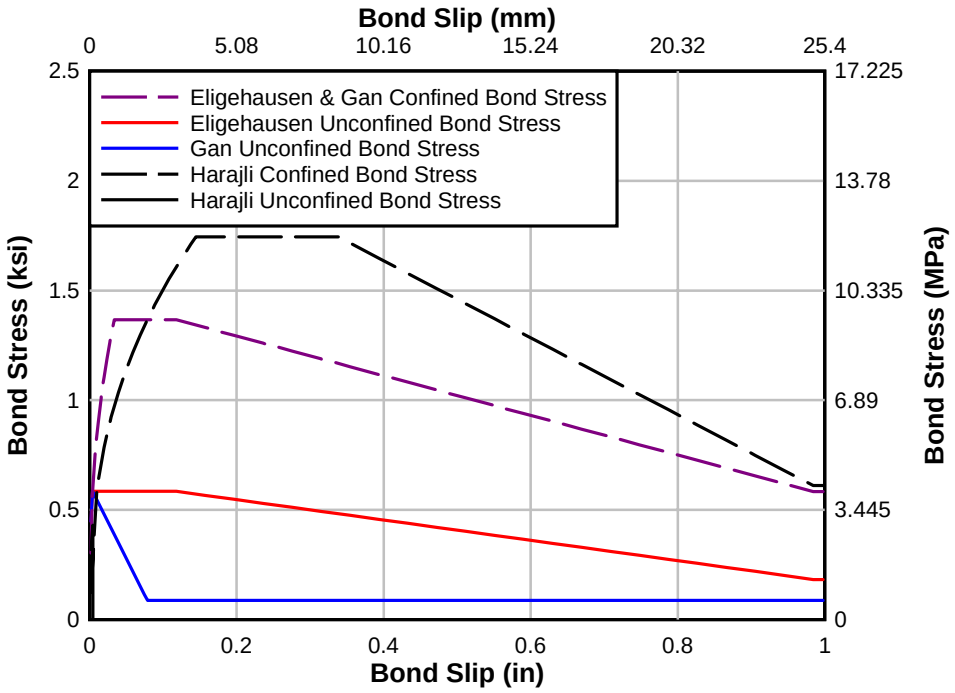

Fig. 5.2 – Eligehausen, Gan, and Harajli bond stress-slip response

5.2.2. The Finite Element Model and Trial Analysis

Due to the asymmetry of the reinforcement details, the full geometry of the T-beam specimens was modeled. In the experiment, both supports were friction rollers. However, to provide sufficient boundary conditions, one support was modeled as a pin and the other a roller. The pin support was modeled by constraining one node in the x and y directions, while the roller support was modeled by constraining one node in only the y-direction. Difference out of plane thicknesses were assigned for the deck and stem portions of the T-beam. The concrete was modeled with rectangular and triangular elements. All reinforcement was modeled discretely using truss elements. Except for the cutoff bars, the reinforcement was assumed to be perfectly bonded to the concrete. Non-dimensional

contact elements were used to connect the cutoff bar truss elements to the concrete elements to more accurately describe the bond behavior. In specimens with preformed cracks, the crack was modeled as a 2 mm (0.079 in.) gap between two adjacent regions in the stem. The as-build preformed diagonal crack angle was used. The deck was left as continuous. Using the automatic mesh generator, the element aspect ratio was limited to 1.5.

The number of rectangular and triangular elements representing the concrete, the number of truss elements representing the reinforcement, and the number of contact elements representing bond for each specimens are shown in Table 5.1. VecTor2 limits the number of elements to 6000 and the number of nodes to 5200. The finite element model for each of the specimens is shown in Figs. 5.3 to 5.6.

Table 5.1 – Number of Elements in Each Finite Element Model

Specimen	Number of Elements				
	Rectangular	Triangular	Truss	Contact	Total
T.45.Ld3.(4)	1643	602	1152	80	3477
T.45.Ld3.(5)	1643	602	1152	80	3477
T.60.Ld3.(5)	1690	349	1079	82	2091
T.0.Ld3.(5)	1630	270	1048	76	3024

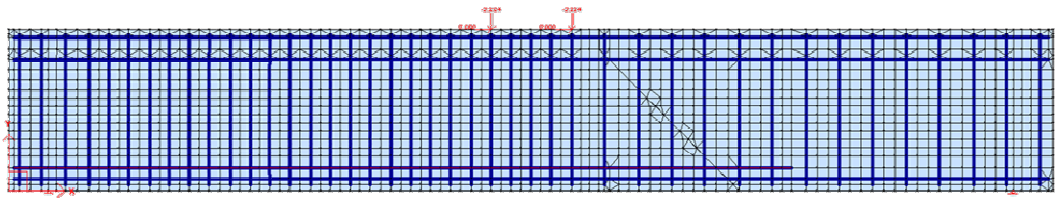

Fig. 5.3 – Specimen T.45.Ld3.(4) finite element model

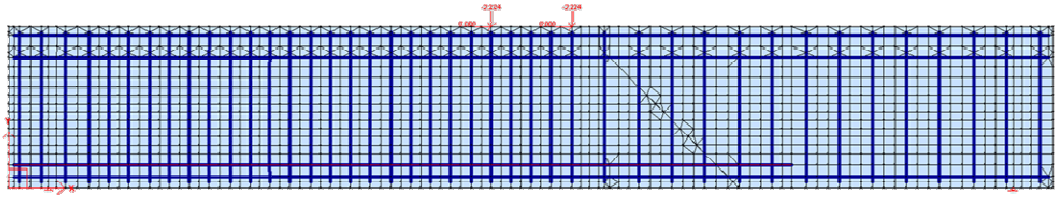

Fig. 5.4 – Specimen T.45.Ld3.(5) finite element model

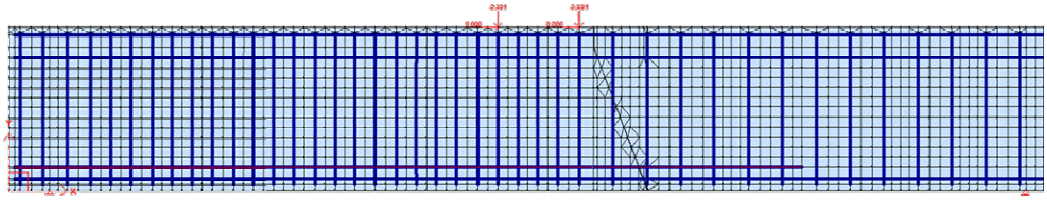

Fig. 5.5 – Specimen T.60.Ld3.(5) finite element model

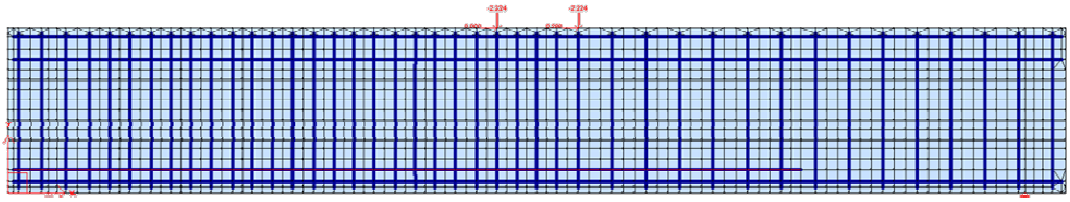

Fig. 5.6 – Specimen T.0.Ld3.(5) finite element model

Material properties were defined using the results from material testing as described in Section *3.3 Material Properties*. All of the derivative concrete material properties except for f_c' were determined by VecTor2. The steel elastic modulus, E_s, was taken as 200,000 MPa (29000 ksi), and the strain harding modulus, E_{sh}, was assumed to be 20,000 MPa (2900 ksi).

Three trial analyses were conducted to determine which analysis options best captured the experimental response. These parameters were the bond model, mesh size, and load step size.

A confinement pressure coefficient study was also conducted to establish a value for β in Eq. [5.3] that reasonably approximated the experimental bond stress values using specimen T.45.Ld3.(4) for the calibration. The predicted load-displacement for each trial is shown in Fig. 5.7 and Table 5.2 summarizes the β values and corresponding peak bond stress for each test trial analysis. VecTor2 reports the average reinforcement stress for each element. Using Eq. [2.1], taking l_d as the distance between midpoint of the element in question and the end of the cutoff, the bond stress for each element between the preformed crack and the end of the cutoff was determined. The reported bond stress from VecTor2 is the average of all of the points calculated. The experimental bond stress value was defined as the average of the bond stress values reported for specimen T.45.Ld3.(4) as reported in Table 4.3 was 4.45 MPa (0.646 ksi). At high β values, both the bond stress and failure load were overestimated and at low β values the bond stress and failure load were under-estimated. For the trials investigated, a β value of 0.140 most reasonably predicted the experimental load-displacement behavior, bond stress with a bias of 0.95, and failure load with a bias of 0.97. Even though using a β value of 0.10 predicted a more accurate bond stress with a bias of 1.02, the β value of 0.140 was used for the remainder of the analyses as the theoretical stirrup pressure is a practical means of estimating the β value and the results are conservative and still reasonable. The Eligehausen bond stress model, was used for the study.

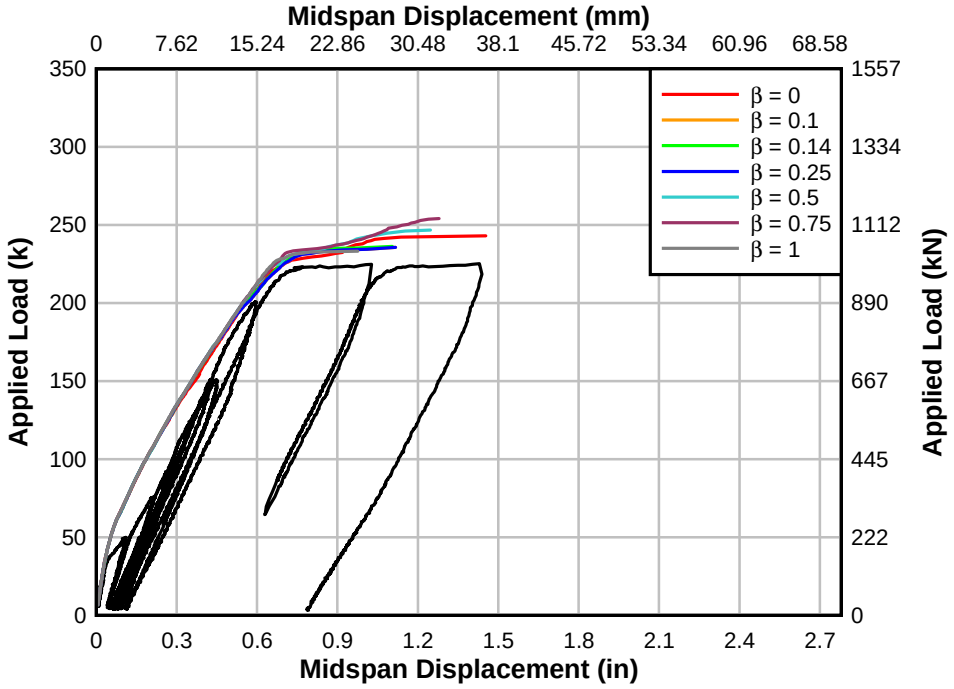

Fig. 5.7 – Predicted load-deformation response for different β values (specimen T.45.Ld3.(4))

Table 5.2 – Predicted Bond Stress and Ultimate Capacities for Different β Values

β	Bond Stress		Shear at Failure	
	μ (MPa) [ksi]	Bias μ_{EXP}/μ_P	V_P (kN) [kips]	Bias V_{EXP}/V_P
0.000	4.08 [0.592]	1.09	540.4 [121.5]	0.94
0.100	4.36 [0.633]	1.02	525.8 [118.2]	0.97
0.140	4.71 [0.683]	0.95	525.3 [118.1]	0.97
0.250	4.72 [0.685]	0.94	525.8 [118.2]	0.97
0.500	5.09 [0.738]	0.88	548.9 [123.4]	0.93
0.750	5.54 [0.804]	0.80	565.3 [127.1]	0.90
1.00	6.03 [0.875]	0.74	518.6 [116.6]	0.98

A convergence study was performed using h-refinement. Using the automatic mesh option provided in FormWorks, five mesh sizes were investigated: 55 mm (2.16 in.), 70 mm (2.76 in.), 75 mm (2.95 in.), 100 mm (3.94 in.), and 200 mm (7.87 in.). In all cases, the initial

stiffness of the specimen was the same. However, at high loads, the ultimate capacity and ultimate displacement varied. Further, when using small mesh sizes, the smallest of the elements at the cutoff location were very small compared to the nearby elements. As a consequence, an almost vertical crack at the cutoff location was the cause of failure. For these reasons, a 75 mm (2.95 in.) mesh size was selected for the reminder of the analysis. Knowing that the mesh size was more critical for the specimens with preformed cracks, the mesh size study was conducted using specimen T.45.Ld3.(4). The results of the convergence trials are shown in Fig. 5.8. Similarly, the required computing time as a function of the number of element in the model is presented in Fig. 5.9. Generally, the number of elements was proportional to the required computation time.

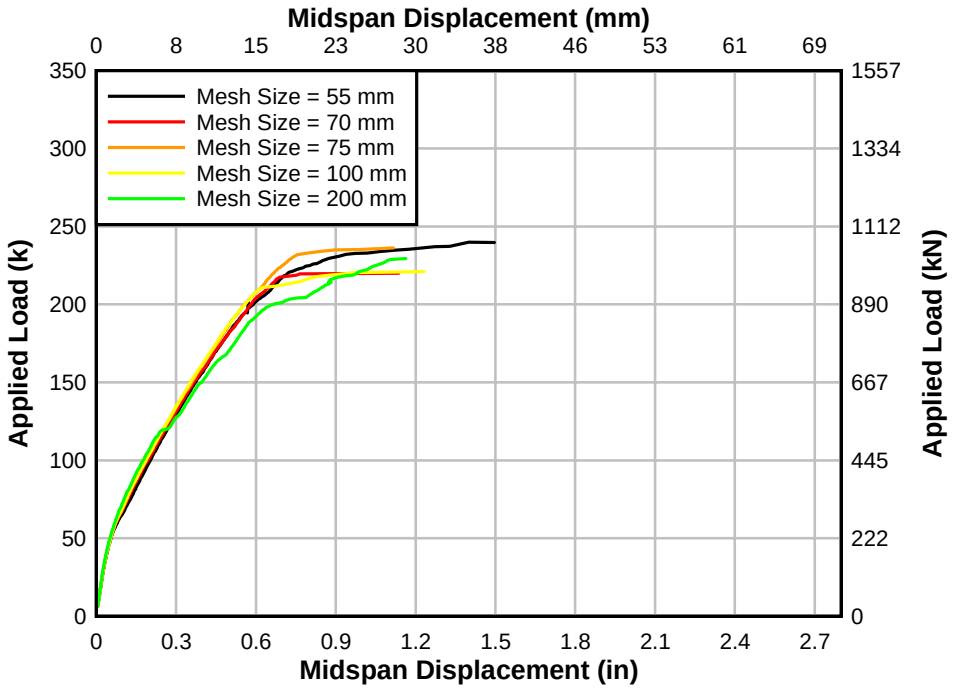

Fig. 5.8 – Predicted load-deformation response for different finite element mesh sizes (specimen T.45.Ld3.(4))

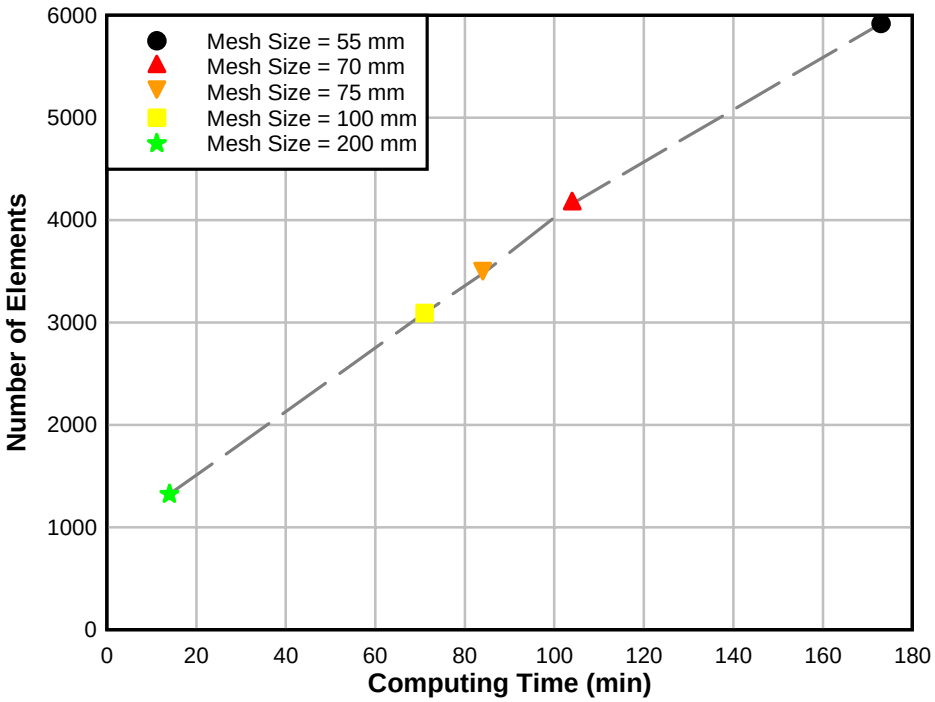

Fig. 5.9 – Computing time for different mesh sizes (specimen T.45.Ld3.(4))

All analyses were force controlled. It was observed that different load step sizes affected the behavior near failure. Five load step sizes were investigated: 2.2 kN (0.5 kip), 3.3 kN (0.75 kip), 4.5 kN (1 kip), 22.5 kN (5 kips), and 45 kN (10 kips). Using the two largest load steps and the two smallest load steps, the ultimate load appeared to converge. The 4.5 kN (1 kip) trial predicted the lowest ultimate capacity. The 2.2 kN (0.5 kip) and 3.3 kN (0.75 kip) load step converged more closely to the experimental capacity as shown in Fig. 5.10. Therefore, a load step size step of 2.2 kN (0.75 kip) was used for the remainder of the analyses.

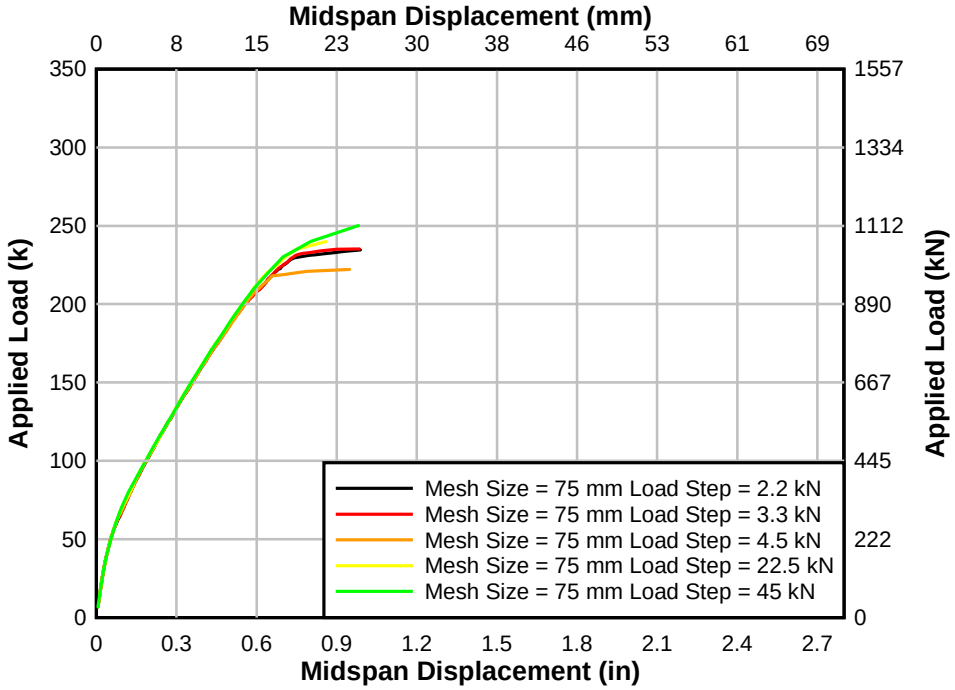

Fig. 5.10 – Predict load-deformation response for different load step sizes (specimen T.45.Ld3.(4))

5.2.3. Non-Linear Finite Element Analysis Results

After selecting the confinement pressure coefficient, the mesh size, and the load step size, further force controlled analyses were conducted using combinations of monotonic/cyclic load increments, using bonded/not bonded elements, and modeling and not modeling the preformed crack. Table 5.3 reports the parameters used in each analysis. The ultimate capacities predicted by VecTor2 are shown in Fig. 5.11.

Table 5.3 – Finite Element Analysis Series

#	Loading	Bonded Elements	Preformed Crack
1	Monotonic	Yes	Yes
2	Monotonic	No	Yes
3	Monotonic	Yes	No
4	Cyclic	Yes	Yes

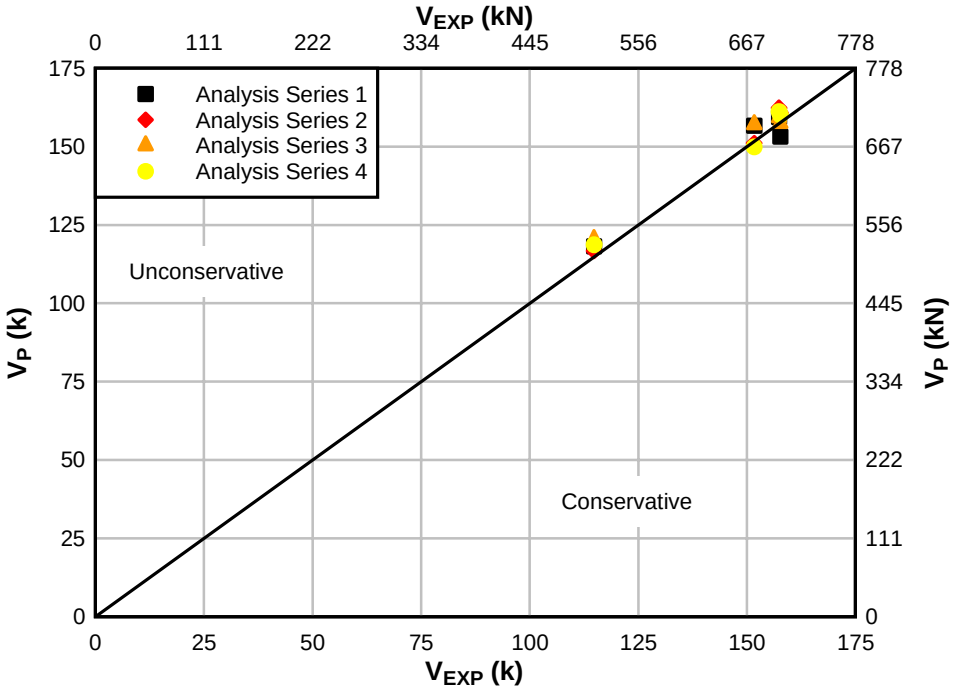

Fig. 5.11 – VecTor2 NLFEA ultimate shear strength prediction results

Generally, VecTor2 slightly over-predicted the ultimate capacity, with low values for the standard deviation and the coefficient of variation. The prediction biases, standard deviations, and the coefficients of variation for each analysis series are reported in Table 5.4. The analysis series rank order results according to standard deviation are shown in Fig. 5.12. In terms of ultimate capacity, each series has a similar bias and coefficient of variation values. Analysis series 2 most accurately matched the experimental results with a predicted bias of 0.96 and a coefficient of variation of 1.47.

Table 5.4 – VecTor2 Finite Element Analysis Prediction Results

Analysis Series	Specimen	V_{EXP} (kN) [kips]	V_P (kN) [kips]	Bias V_{EXP}/V_p	Mean Bias	STD Bias	COV [%]
VecTor2 NLFEA #1	T.45.Ld3.(4)	510.6 [114.8]	525.8 [118.2]	0.97	0.97	0.028	2.85
	T.45.Ld3.(5)	674.9 [151.7]	697.0 [156.7]	0.97			
	T.60.Ld3.(5)	701.6 [157.7]	681.4 [153.2]	1.03			
	T.0.Ld3.(5)	700.1 [157.4]	709.0 [159.4]	0.99			
VecTor2 NLFEA #2	T.45.Ld3.(4)	510.6 [114.8]	519.1 [116.7]	0.98	0.96	0.014	1.47
	T.45.Ld3.(5)	674.9 [151.7]	672.1 [151.1]	1.00			
	T.60.Ld3.(5)	701.6 [157.7]	715.2 [160.8]	0.98			
	T.0.Ld3.(5)	700.1 [157.4]	722.4 [162.4]	0.97			
VecTor2 NLFEA #3	T.45.Ld3.(4)	510.6 [114.8]	535.5 [120.4]	0.95	0.95	0.021	2.20
	T.45.Ld3.(5)	674.9 [151.7]	698.8 [157.1]	0.97			
	T.60.Ld3.(5)	701.6 [157.7]	700.6 [157.5]	1.00			
	T.0.Ld3.(5)	700.1 [157.4]	709.0 [159.4]	0.99			
VecTor2 NLFEA #4	T.45.Ld3.(4)	510.6 [114.8]	528.0 [118.7]	0.97	0.96	0.019	1.96
	T.45.Ld3.(5)	674.9 [151.7]	666.8 [149.9]	1.01			
	T.60.Ld3.(5)	701.6 [157.7]	712.1 [160.1]	0.99			
	T.0.Ld3.(5)	700.1 [157.4]	717.0 [161.2]	0.98			

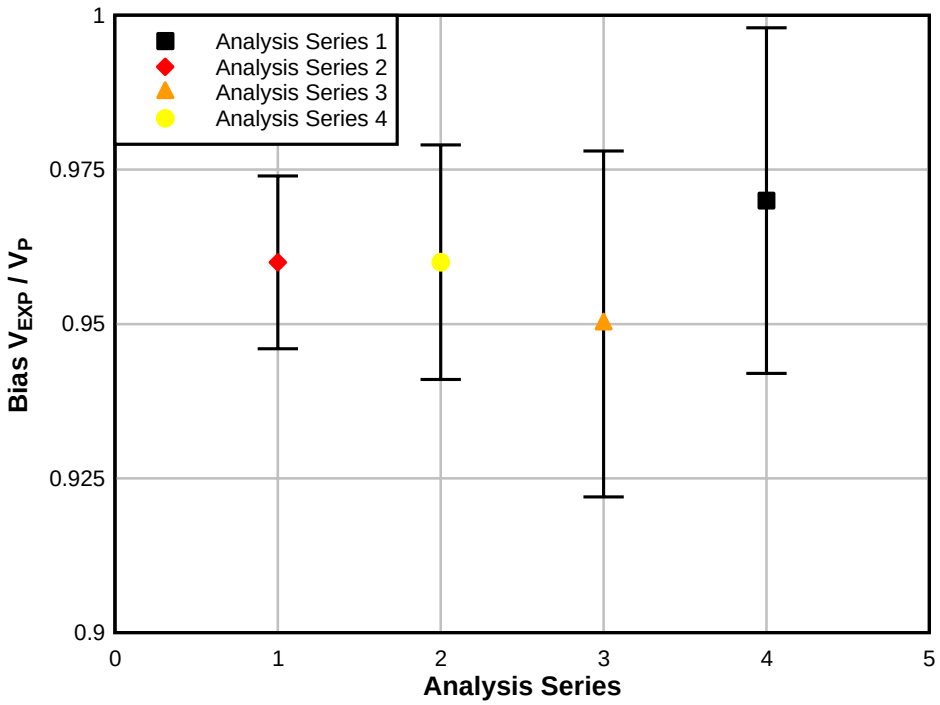

Fig. 5.12 – VecTor2 NLFEA ultimate shear strength prediction results

5.2.3.1. Load Deflection Response

The experimental and finite element analysis predicted load-displacement curves for analysis series 1 are shown in Figs. 5.13 to 5.16. For specimen T.0.Ld3.(5), without a preformed crack, VecTor2 predicted the stiffness well at low services levels (below 155 kN (35 kips)). For the specimens with preformed cracks, VecTor2 predicted a gradual softening response compared to the observed stiffening response. This is due to the presence of the diagonal crack not being well captured in the predicted behavior.

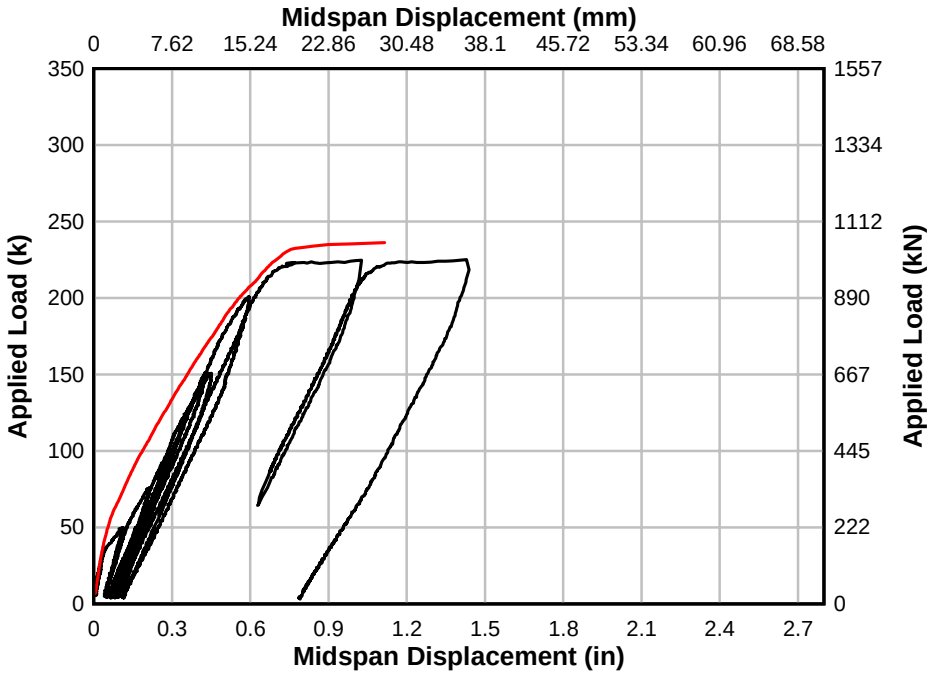

Fig. 5.13 – Predicted and experimental load-deformation of specimen T.45.Ld3.(4), monotonic analysis

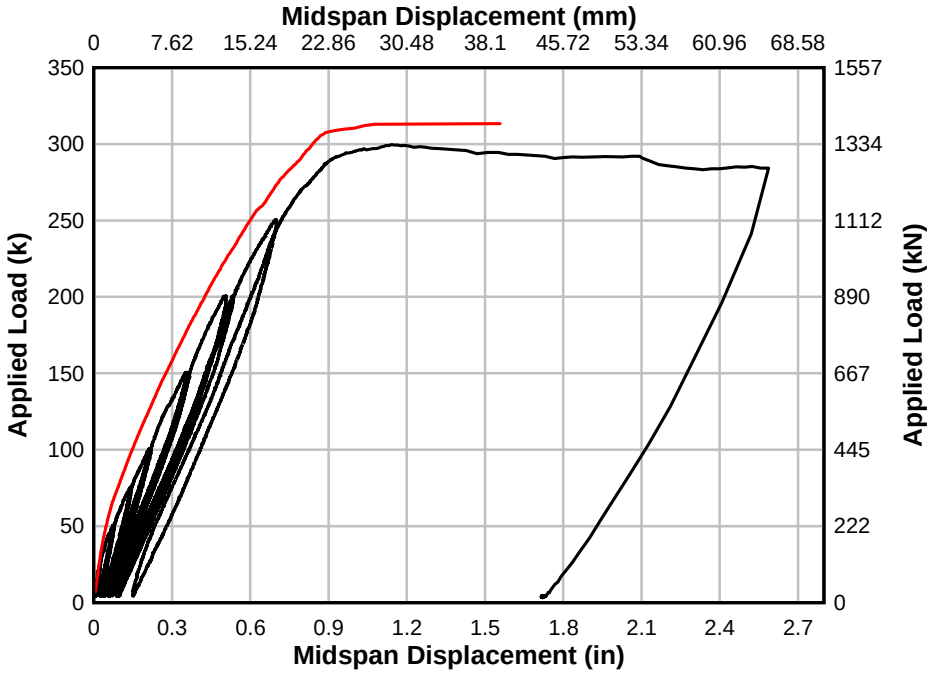

Fig. 5.14 – Predicted and experimental load-deformation of specimen T.45.Ld3.(5), monotonic analysis

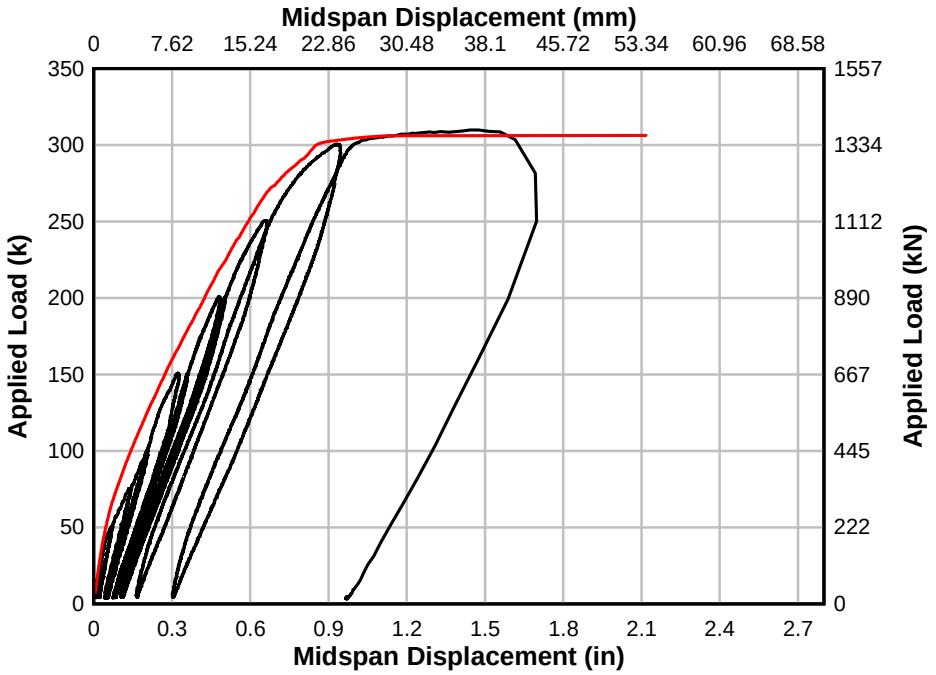

Fig. 5.15 – Predicted and experimental load-deformation of specimen T.60.Ld3.(5), monotonic analysis

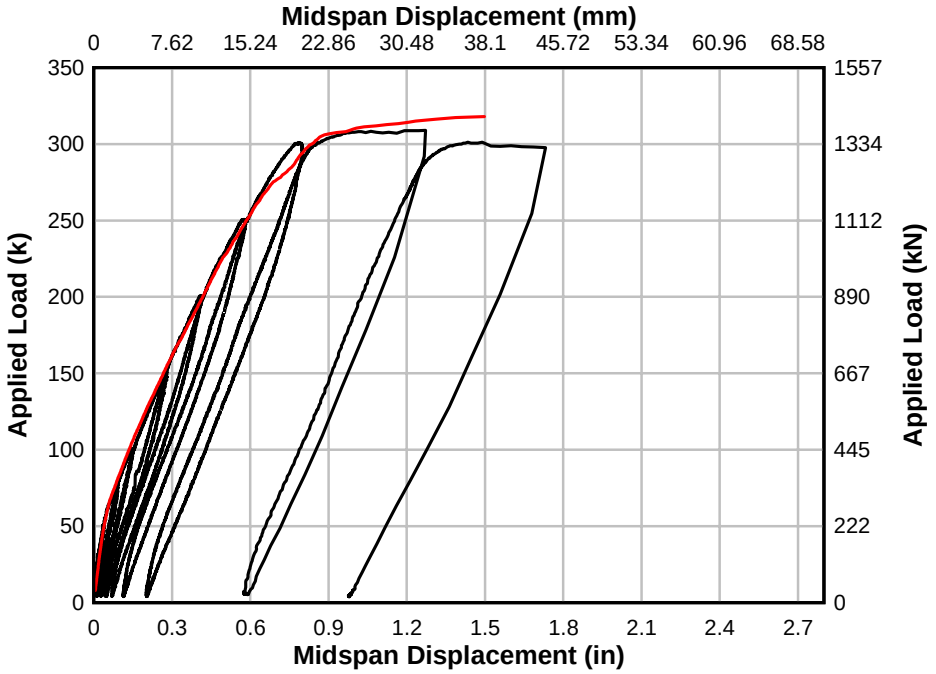

Fig. 5.16 – Predicted and experimental load-deformation of specimen T.0.Ld3.(5), monotonic analysis

To reflex the cyclic loading protocol used during the experimental testing, a cyclic finite element analysis was conducted. The loads were increased by 222 kN (50 kips) after each loading – unloading cycle. Except for specimen T.45.Ld3.(5), the load step size was 3.33 kN (0.75 kips). The results of specimen T.45.Ld3.(5) would not load into the Augustus postprocessor using a cyclic load step of 3.33 kN (0.75 kip), so the load step was increased to 4.45 kN (1 kip). Generally, cyclic loading did not significantly affect the predicted capacity or behavior of the load-displacement curves shown in Figs. 5.17 to 5.20. While loading to 1334 kN (300 kips), the finite element analysis for specimen T.45.Ld3.(4) terminated at 1056 kN (237.5 kips). The failure load was reported as 1056 kN (237.5 kips), not the peak load of 1112 kN (250 kips).

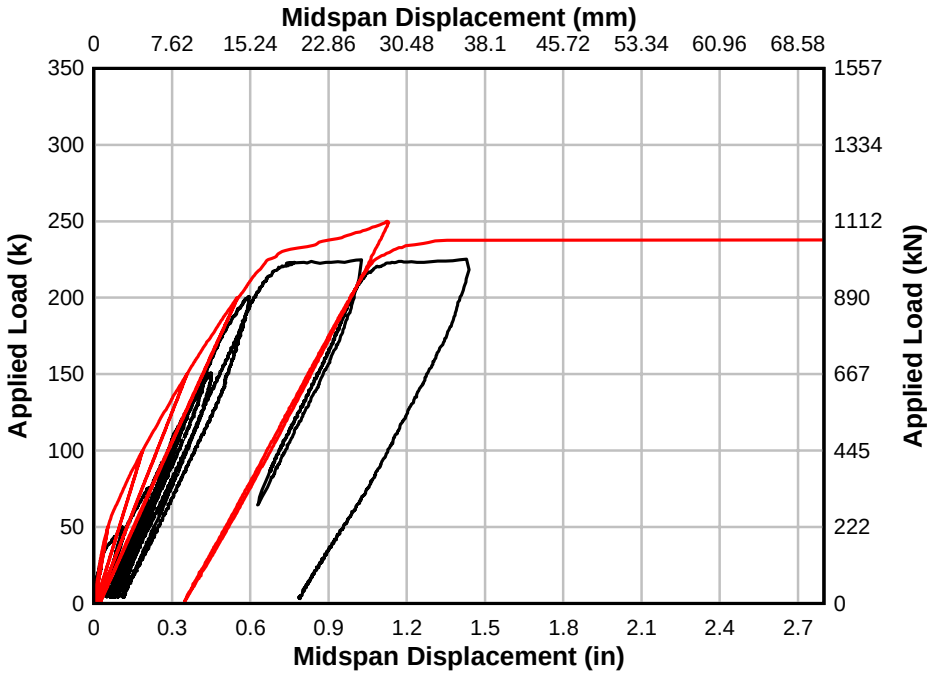

Fig. 5.17 – Predicted and experimental load-deformation of specimen T.45.Ld3.(4), cyclic analysis

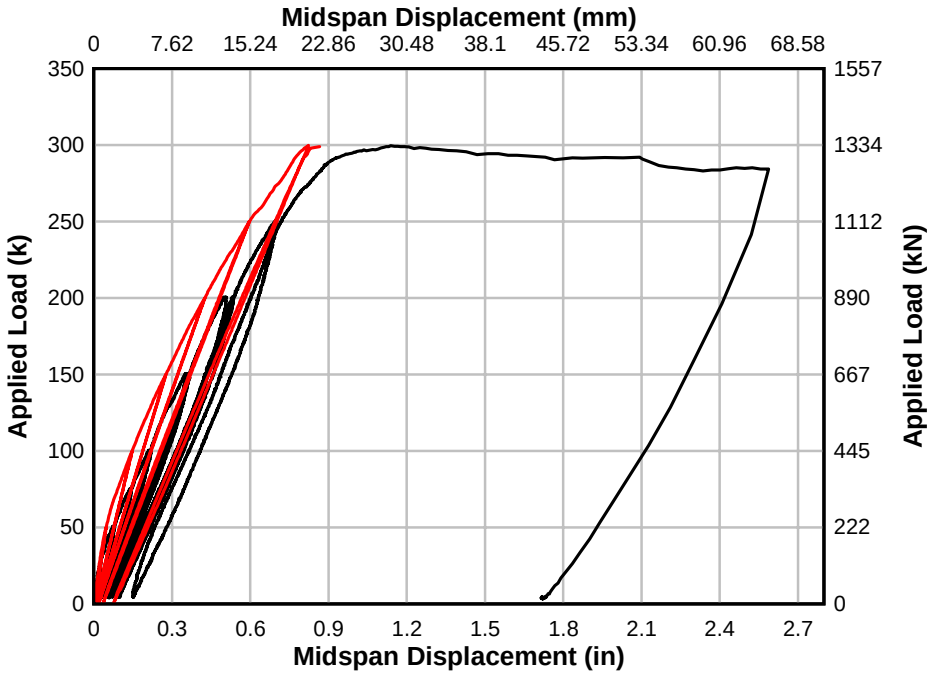

Fig. 5.18 – Predicted and experimental load-deformation of specimen T.45.Ld3.(5), cyclic analysis

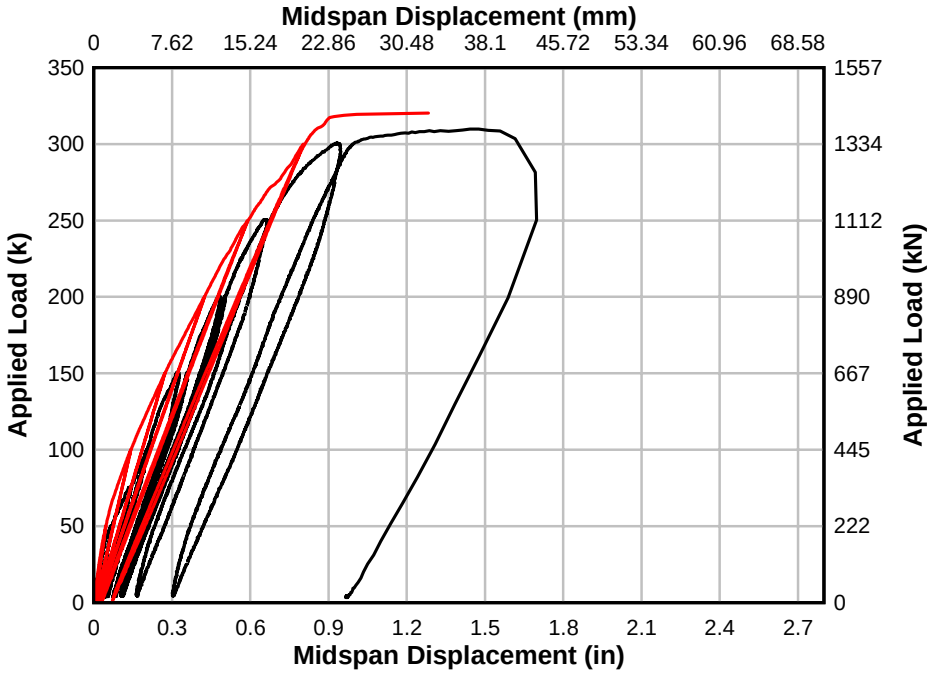

Fig. 5.19 – Predicted and experimental load-deformation of specimen T.60.Ld3.(5), cyclic analysis

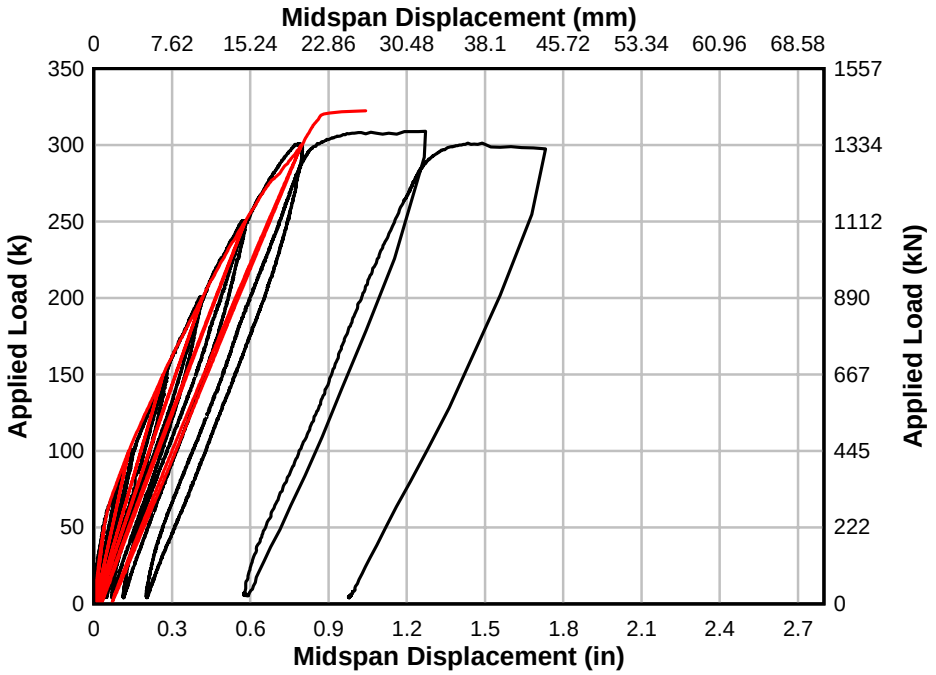

Fig. 5.20 – Predicted and experimental load-deformation of specimen T.0.Ld3.(5), cyclic analysis

The cyclic analyses, the predict load capacity bias was 0.96, with a standard deviation of 0.019. The backbone of the cyclic load-displacement curve matched the monotonic load-displacement curve. However, the predicted plastic displacement offsets following each load cycles were underestimated in all cases. Unfortunately, the computation time for the cyclic analyses was much as 545 minutes compared to the maximum of 176 minutes to complete a monotonic analysis as shown in Fig. 5.21. Generally, it was observed that monotonic finite element analysis was sufficient to predict the T-beam specimen behavior given the similarities in predicted behavior, and the length of time required to compute the results.

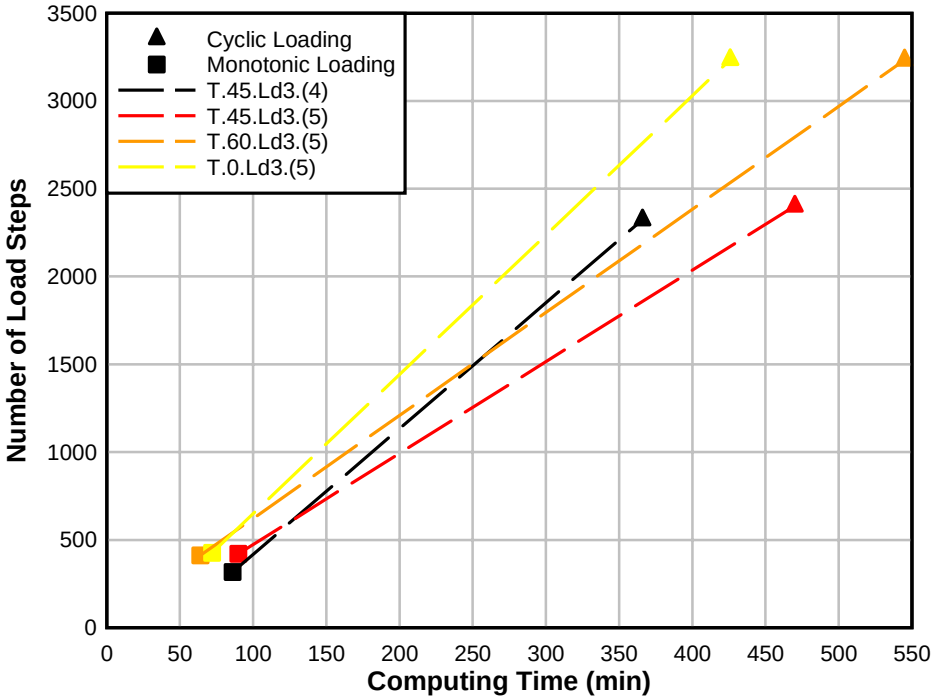

Fig. 5.21 – Computation time for monotonic and cyclic analyses

Generally, the overall load-displacement results for the analysis series using perfectly bonded elements (series 2) and not modeling the preformed crack (series 3) were similar to analysis series 1. Therefore, the load-displacements plots are not shown. However, for analysis series 2 specimen T.0.Ld3.(5), and analysis series 3 specimen T.45.Ld3.(4), VecTor2 predicted a stiffer load-displacement response then in analysis series 1.

5.2.3.2. Crack Patterns

The experimental and VecTor2 predicted crack patterns for analysis series 1 correlated well as seen in Figs. 5.22 to 5.25. Both the location and height of vertical cracks near midspan and the locations of the characteristic diagonal cracks were reasonably predicted.

When the specimens were modeled without preformed cracks, the predicted crack patterns were similar to those of analysis series 1. However, when all of the reinforcement was assumed to be perfectly bonded, the characteristic diagonal crack appeared at the end of the cutoff with no major diagonal cracks occurring between midspan and the end of the cutoff. VecTor2 also reasonably captured the characteristic anchorage cracking which occurred along the cutoff bars as explained in Section *4.1.3 Anchorage Slip Response of Specimens*.

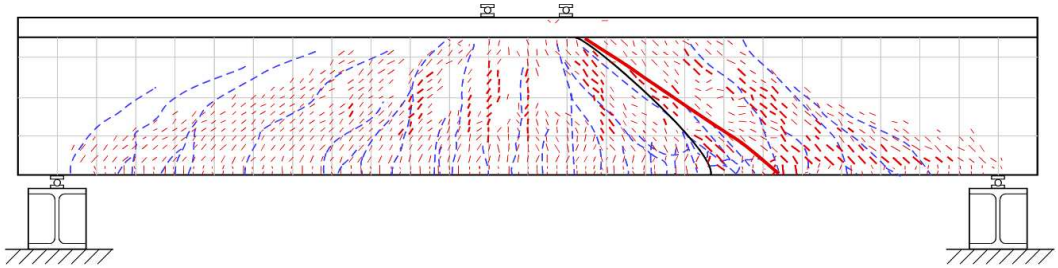

Fig. 5.22 – Specimen T.45.Ld3.(4) experimental and VecTor2 predicted crack pattern

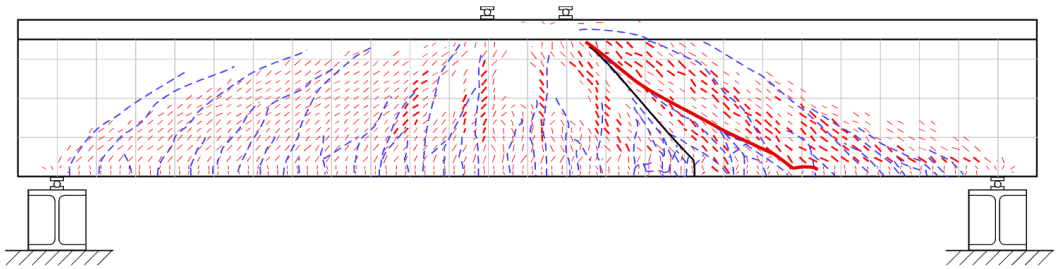

Fig. 5.23 – Specimen T.45.Ld3.(5) experimental and VecTor2 predicted crack pattern

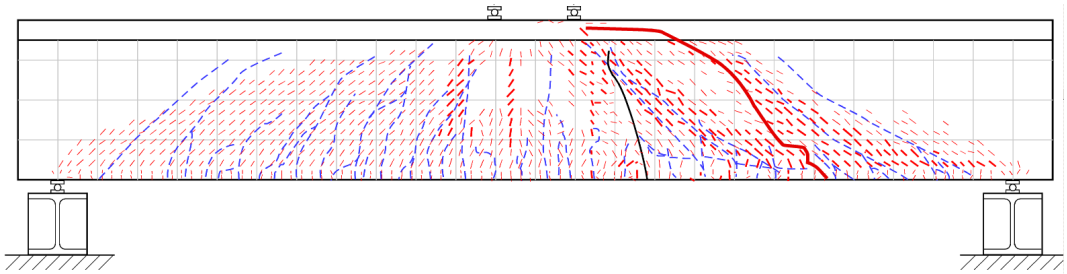

Fig. 5.24 – Specimen T.60.Ld3.(5) experimental and VecTor2 predicted crack pattern

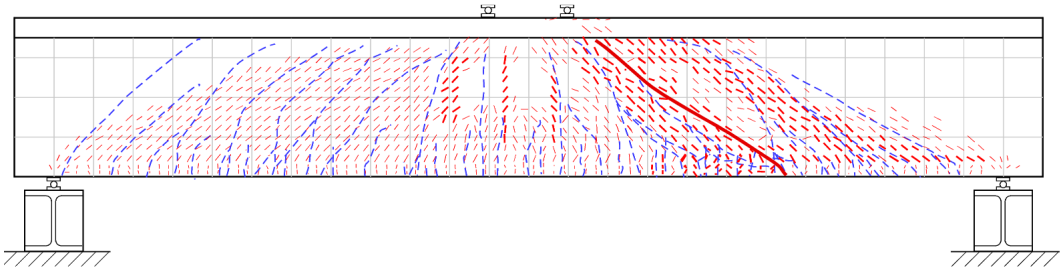

Fig. 5.25 – Specimen T.0.Ld3.(5) experimental and VecTor2 predicted crack pattern

5.2.3.3. Steel Reinforcement Stress Distribution Converted to Bond Stress

For analysis series 1 and 2, the predicted average bond stress, μ_{avg}, for the cutoff bars for each specimen was determined using the method described in Section *5.2.1 Non-Linear Finite Element Analysis Using VecTor2*. In Table 5.5, the average predicted bond stresses are compared to the average experimental bond stress of 5.87 MPa (0.851 ksi) reported in Table 4.3. The peak average bond stress occurred prior to failure. Based on the observed variability, the FEM analyses using the Eligehausen bond stress model predicted a bond stress value closer to the experimental value. The steel reinforcement stress distributions are shown in Figs. 5.26 to 5.29 and were used to determine the bond stress for analysis series 1.

Table 5.5 – Comparison of Experimental and VecTor2 Predicted Cutoff Bar Bond Stress

Analysis Series	Specimen	μ_P (MPa) [ksi]	Bias μ_{EXP}/μ_P	Mean	STD	COV (%)
1	T.45.Ld3.(4)	4.71 [0.683]	1.25	1.16	0.149	12.9
	T.45.Ld3.(5)	5.02 [0.728]	1.17			
	T.60.Ld3.(5)	6.18 [0.897]	0.95			
	T.0.Ld3.(5)	4.58 [0.664]	1.28			
2	T.45.Ld3.(4)	9.45 [1.37]	0.62	0.62	0.076	12.2
	T.45.Ld3.(5)	8.27 [1.20]	0.71			
	T.60.Ld3.(5)	11.2 [1.62]	0.52			
	T.0.Ld3.(5)	9.31 [1.35]	0.63			

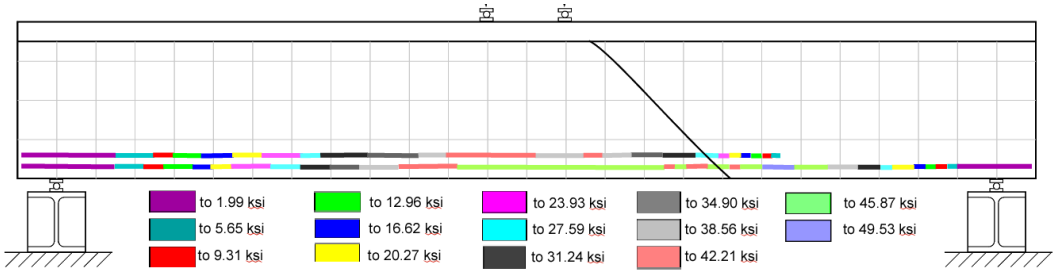

Fig. 5.26 – Specimen T.45.Ld3.(4) predicted steel reinforcement stresses at 182 kips

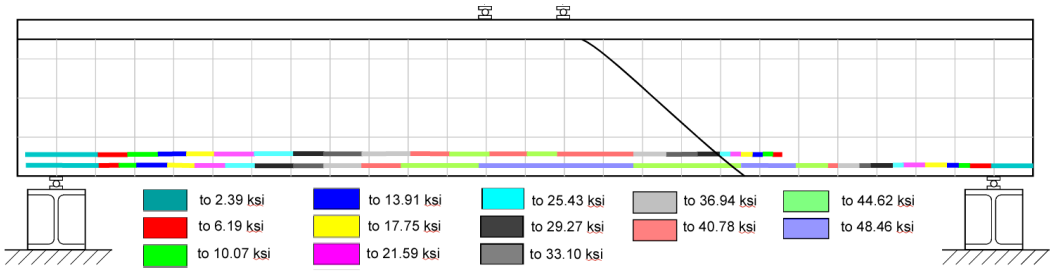

Fig. 5.27 – Specimen T.45.Ld3.(5) predicted steel reinforcement stresses at 234 kips

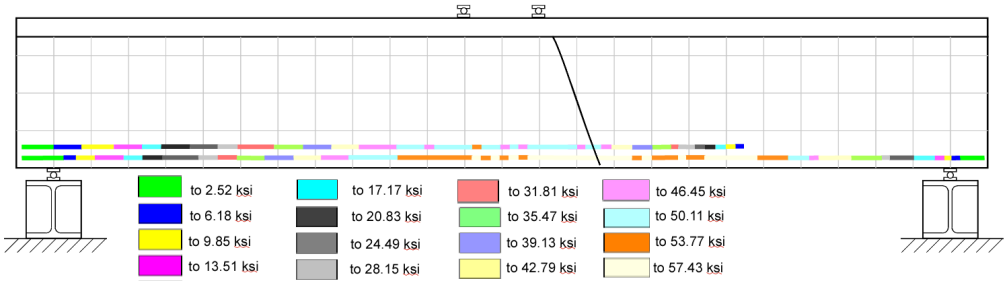

Fig. 5.28 – Specimen T.60.Ld3.(5) predicted steel reinforcement stresses at 274 kips

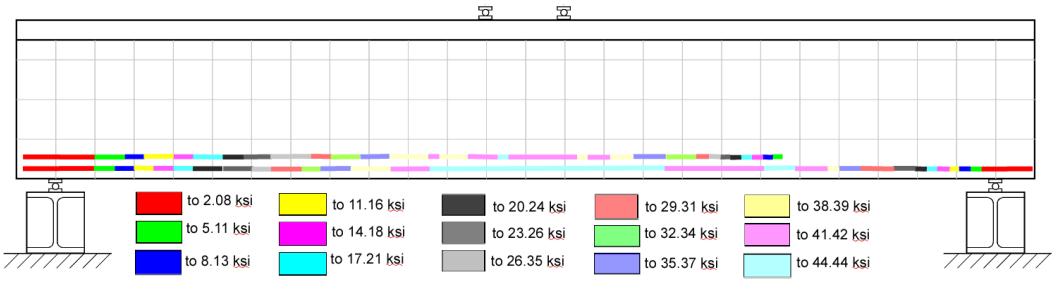

Fig. 5.29 – SpecimenT.0.Ld3.(5) predicted steel reinforcement stresses at 228 kips

5.2.4. VecTor2 Non-Linear Finite Element Analysis Conclusions

Based on the results and comparisons between the different series of non-linear finite element analyses using VecTor2 and experimental results, the following conclusions are presented:

- Non-linear finite element analyses provided good correlation with experimental results for overall member load -displacement response and average bond stress values. For a model with discrete reinforcement, a preformed crack, and bond elements loaded monotonically, a mean predicted bias of 0.97 with a coefficient of variation of 2.85% was obtained.
- The predicted crack patterns from the nonlinear finite element analyses agreed well with experimental observations. However, the failure shear cracks were not necessarily coincident.
- Generally, conducting a cyclic load analysis to take into account the hysteretic response of concrete, reinforcing steel, and bond did not significantly improve the analysis results, but significantly increased computation time.
- The use of contact elements and the Eligehausen bond-slip model reasonable predicted the experimental average bond stress. Assuming the bond between the concrete and reinforcement to be perfect results in unrealistically high bond stress values and ultimate capacities. Like in the experiment, the peak average bond stress was not coincidence with failure.

5.3. Comparative Analysis

The comparative analysis consists of two parts: evaluating the design specifications, and evaluating previous Oregon State University experimental results in light of the data gather during the current test program.

5.3.1. Design Codes and Response 2000 Comparisons

The specified minimum development lengths calculated for straight and hooked bars using the actual material properties of each specimen reported in Tables 5.6 and 5.7. In all cases, actual development was greater than the length of bar used past the preformed crack tip for design of the specimens. The specified minimum development lengths are less than the 97.5% confidence limit development length of 1.10 m (43.3 in.).

Table 5.6 – Comparison of Specified Minimum Development Length for Straight Bars

Specimen	**f_c (MPa) [psi]**	**f_y (MPa) [ksi]**	**AASHTO (mm) [in]**	**ACI-318 (mm) [in]**	
				Simplified	**Complex**
T.45.Ld3.(4)	21.8 [3165]	494 [71.7]	1996 [78.6]	2281 [89.8]	1686 [66.4]
T.45Ld3.(5)	22.8 [3302]		1953 [76.9]	2235 [88.0]	1651 [65.0]
T.60.Ld3.(5)	23.6 [3418]		1920 [75.6]	2197 [86.5]	1623 [63.9]
T.0.Ld3.(5)	24.4 [3538]		1887 [74.3]	2159 [85.0]	1595 [62.8]

Table 5.7 – Comparison of Specified Minimum Development Length for Hooked Bars

Specimen	**f_c (MPa) [psi]**	**f_y (MPa) [ksi]**	**AASHTO (mm) [in]**	**ACI-318 (mm) [in]**
T.45.Ld3.(4)	21.8 [3165]	494 [71.7]	765 [30.1]	912 [35.9]
T.45Ld3.(5)	22.8 [3302]		749 [29.5]	894 [35.2]
T.60.Ld3.(5)	23.6 [3418]		737 [29.0]	879 [34.6]
T.0.Ld3.(5)	24.4 [3538]		724 [28.5]	864 [34.0]

Appendix D describes the ACI 318-08 and AASHTO-LRFD methods for calculating nominal shear capacities. The critical and predicted shear capacities for all of the tests specimens are shown in Table 5.8. Even though the specimens failed in a ductile anchorage mode, the applied shear at failure was approximately the same as the critical shear capacity predicted by R2K. For all of the specimens, the predicted critical shear location was located at the end of the cutoff bars. Therefore, as the cutoff bars slipped, the critical failure mode and location became a "shear" failure at the ends of the cutoff bars.

Table 5.8 – Comparison of Experimental Shear Capacity to Predicted Capacity for Different Methods

Specimen	**ACI-318 (kN) [kips]**	**AASHTO (kN) [kips]**	**Response 2000 (kN) [kips]**	**V_{APP} at Failure (kN) [kips]**	**V_{APP}/ V_{R2K}**
T.45.Ld3.(4)	717.5 [161.3]	461.7 [103.8]	495.1 [111.3]	510.6 [114.8]	1.03
T.45Ld3.(5)	730.4 [164.2]	640.1 [143.9]	659.2 [148.2]	674.9 [151.7]	1.02
T.60.Ld3.(5)	735.7 [165.4]	640.5 [144.0]	660.1 [148.4]	701.6 [157.7]	1.06
T.0.Ld3.(5)	741.5 [166.7]	640.5 [144.0]	659.6 [148.3]	700.1 [157.4]	1.06

Appendix E describes the ACI 318-08 and AASHTO-LRFD methods for calculating nominal moment capacities. The critical and predicted moment capacities for all of the test specimens are shown in Table 5.9. Since the specimens failed in anchorage, the predicted moment capacity is higher than the failure moment. The specimens were designed to have a ductile, tension controlled failure. The top bars were assumed not to act as compression steel since closed stirrups were not used to prevent buckling of the top bars. Therefore, both the ACI 318-08 and AASHTO-LRFD methods report the same moment capacity.

Table 5.9 – Comparison of Moment Recorded at Failure to Predicted Capacity

Specimen	**ACI-318 and AASHTO (MN-m) [k-ft]**	**M_{APP} at Failure (MN-m) [k-ft]**
T.45.Ld3.(4)	22.4 [1532.9]	17.4 [1193.6]
T.45Ld3.(5)	27.9 [1912.3]	23.1 [1585.1]
T.60.Ld3.(5)	28.0 [1916.7]	24.0 [1642.7]
T.0.Ld3.(5)	28.0 [1920.9]	24.0 [1646.9]

ACI 318-08 and AASHTO-LRFD have difference approaches to account for the increase in tensile demand in the flexural bars in shear regions where diagonal cracks may be present. The AASHTO-LRFD approach was described in Section *2.1 Anchorage Concerns*. ACI 318-08 Section 12.10.3 requires that the flexural reinforcement extend a distance d or $12d_b$ past the point at which the reinforcement is no longer needed for moment resistance to account for shifts in maximum loading and for the effects of diagonal cracking. Therefore, assuming a single point loading, the increase in tensile demand is:

$$T_{add,ACI} = \frac{Vd}{jd} \qquad [5.4]$$

The portion of Eq. [2.5] which may be considered as additional tensile demand caused by a diagonal crack is:

$$T_{add,AASHTO} = (V_u - 0.5V_s)\cot\theta \qquad [5.5]$$

Assuming that j in Eq. [5.4] is equal to 0.9 such that jd will be equal to d_v, the ACI 318-08 and AASHTO-LRFD methods of determining tensile capacity can be graphically compared as shown in Fig. 5.30. ACI 318-08 assumes that the diagonal crack angle which

forms is 45°, and ignores the effects of the transverse reinforcement. Therefore, the several combinations of stirrup quantities and crack angles were used to solve Eq. [5.5]. For crack angles less than or equal to 45°, then ACI 318-08 overestimates the tensile demand. However, for crack angles greater than 45°, then the tensile demand maybe underestimated at high load levels.

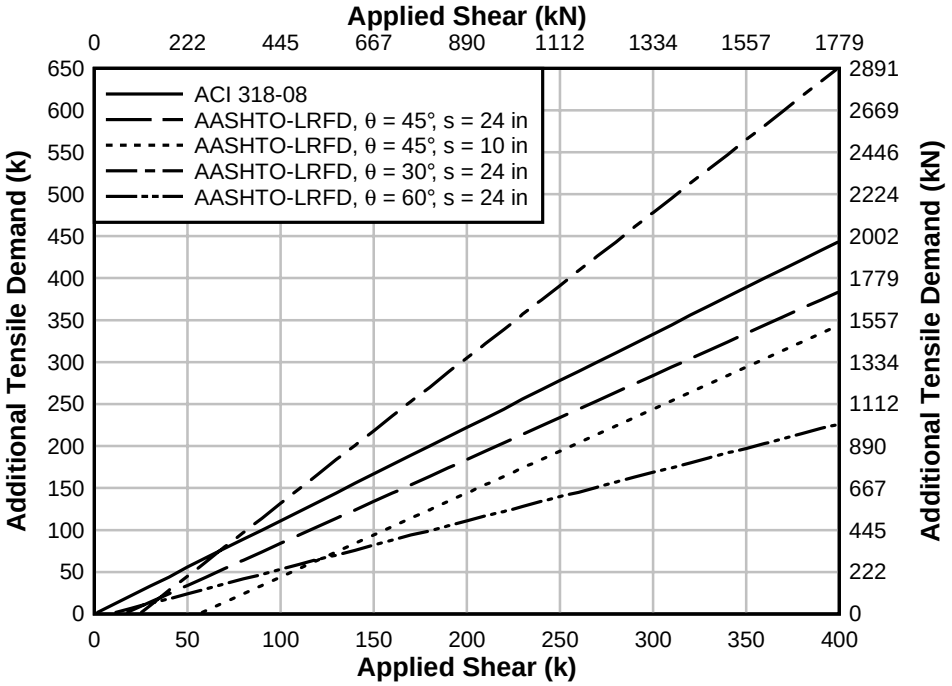

Fig. 5.30 – Comparison of additional tensile demand in flexural steel at diagonal cracks for ACI and AASHTO-LRFD

5.3.2. Comparing Bond Stress Results to Design Codes and Literature

The average bond stress values were higher than those contained in the ACI 318-08 and AASHTO-LRFD (after converting minimum development length to average bond stress). However measured bond stress values were within the limits reported by others in the literature as described in Table. 2.1. The various methods of calculating development

length in the design specifications and literature are shown graphically in Fig 5.31. Where applicable, the average material properties and geometry were used to determine the development length. When only average bond stress values were reported, the development length was determined using Eq. [2.4]. On average, the design specifications overestimate the development length by about 170 percent.

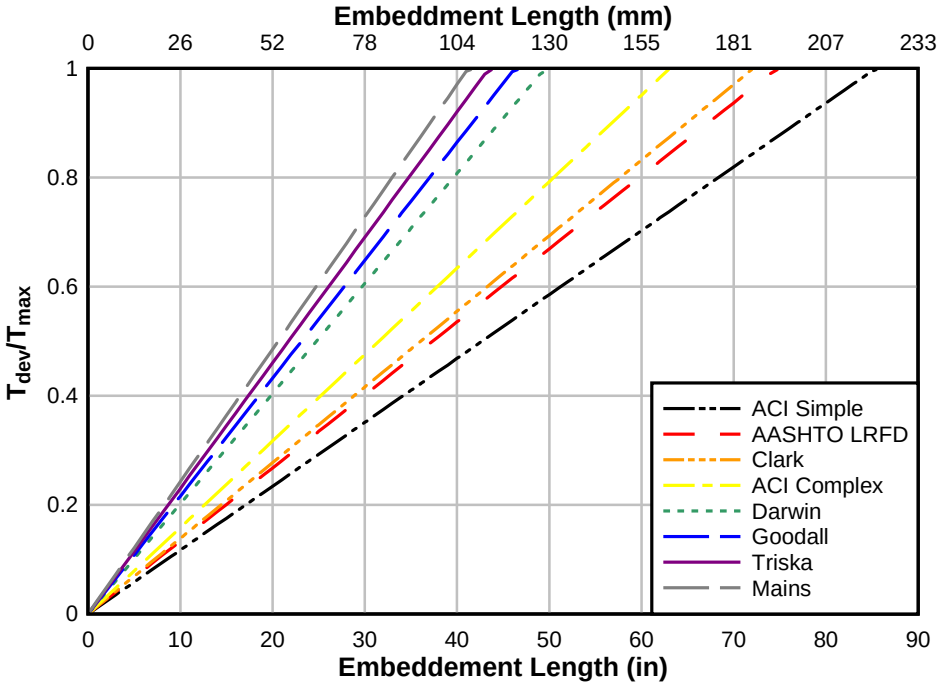

Fig. 5.31 – Comparison of literature, design specification, and experimental development lengths

5.3.3. Comparing Test Results to Previous Large-Size Experimental Results

In the early 2000s, a series of vintage RCDG bridge girders were tested to evaluate shear capacity (Higgins, *et al.* 2004). Both IT- and T-beam configurations were investigated. At the time, it was concluded that most of the T-beam specimens failed in shear-moment interaction and several in flexure. However, several specimens were re-evaluated based on

the findings of the present work and it was concluded that three of the archival T-beams were susceptible to anchorage failures associated with diagonal cracking. There are two reasons for this conclusion: data comparison and analysis using the Excel design macro.

Specimen 8T12-B3, 8T12-B4, and 9T12-B4 were the three archival T-beams susceptible to anchorage failure. The failure photos and load-deformation responses for each specimen are shown in Figs. 5.32 to 5.34. Specimens 8T12-B4 and 9T12-B4 had cutoff details similar to the specimens T.45.Ld.3(5), T.60.Ld3.(5), and T.0.Ld3.(5) with the major differences in the specimens being that the older specimens had longer cutoff bars, wider stirrup spacing, and no hooked bars. Specimen 8T12-B3 had 6 straight bars and no cutoffs. Mostly likely, specimen 8T12-B4 failed in anchorage. Like the specimens in this report, the failure of specimen 8T12-B4 was ductile and characteristic anchorage cracks were observed near the bottom soffit in the anchorage zone. Although the load-deformation response of specimen 8T12-B3 was less ductile the 8T12-B4, cracks were observed in the anchorage zone near the support. Even through the macro analysis described in the subsequent paragraphs predicted an anchorage failure for specimen 9T12-B4, the experimental results do not agree. The failure diagonal crack bypassed the cutoff region entirely, with only minor diagonal cracking between midspan and the end of the cutoff. It is likely that 9T12-B4 did not fail in anchorage.

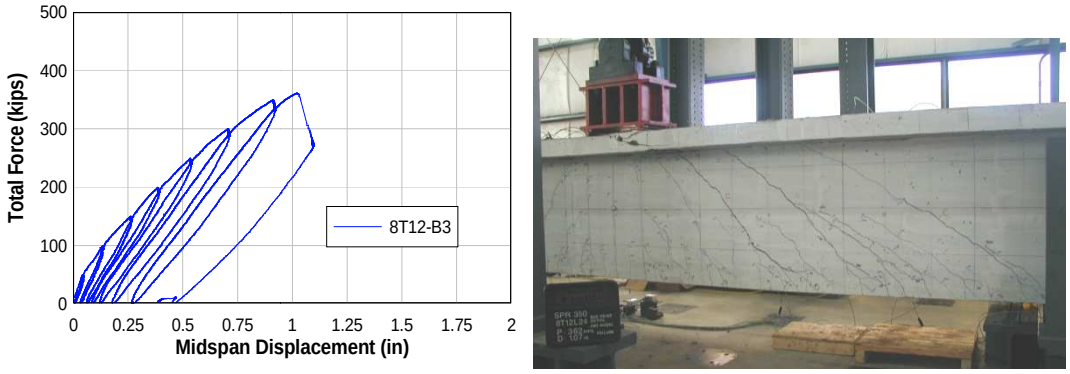

Fig. 5.32 – Specimen 8T12-B3 load-deflection plot and failure photo (Higgins, *et al.* 2004)

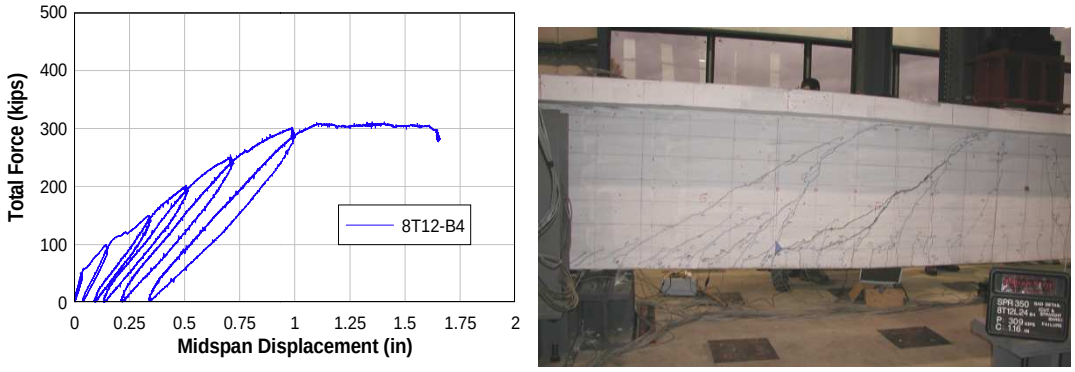

Fig. 5.33 – Specimen 8T12-B4 load-deflection plot and failure photo (Higgins, *et al.* 2004)

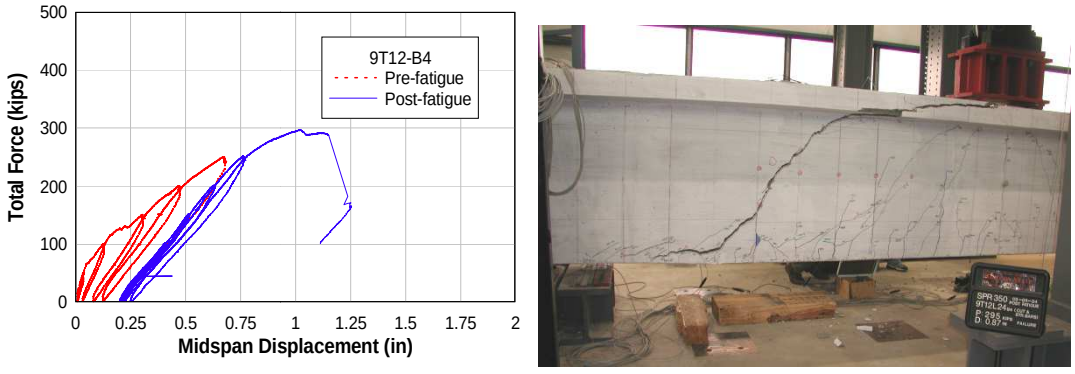

Fig. 5.34 – Specimen 9T12-B4 load-deflection plot and failure photo (Higgins, *et al.*2004)

Secondly, the Excel macro used to design the specimens for the current research was also used to evaluate 13 likely specimens from the SPR 350 program (Higgins, *et al.* 2004). The reported material properties in the archival report were used in the analysis. The macro analysis inputs and outputs from the investigation are described in Tables 5.10 to 5.12. To evaluate the capacity of the specimens the 97.5 percent confidence limit average bond stress values were used. The bond stress value used for the T-beams was 4.01 MPa (0.581 ksi) as reported in Section *5.1 Experimental Bond Stress Analysis*. Goodall reported the bond stress value for IT-beams as 3.76 MPa (0.545 ksi) (2010). The mean bias and the standard deviation for the T-beam specimens and the IT-beams specimens are reported in Table 5.13.

Table 5.10 – Comparative Analysis Macro Inputs: Material Properties

Test Program	**Specimen**	**f'_c (MPa) [ksi]**	**f_y (MPa) [ksi]**	**f_{yv} (MPa) [ksi]**
SPR 350	1T6	30.1 [4370]	463.3 [67.2]	349.6 [50.7]
	1IT6	32.9 [4775]	463.3 [67.2]	
	2T10	23.2 [3360]	540.5 [78.4]	
	2IT10	22.7 [3290]	578.4 [83.9]	
	2IT12	24.6 [3575]	588.1 [85.3]	
	5IT12-B4	28.5 [4130]	457.8 [66.4]	
	6T10	28.9 [4195]	448.8 [65.1]	
	7T12	29.7 [4310]	486.1 [70.5]	
	7IT12	28.7 [4165]	503.3 [73.0]	
	8IT12	33.4 [4840]	500.5 [72.6]	
	8T12-B3	31.5 [4570]	447.4 [64.9]	
	8T12-B4	32.6 [4725]	454.3 [65.4]	
	9T12-B4	33.8 [4910]	438.5 [63.6]	
Goodall	IT.45.Ld/2	27.0 [3918]	494.3 [71.7]	368.8 [53.5]
	IT.60.Ld/2	26.6 [3862]		
	IT.45.Ld/2 (5)	24.8 [3603]		
	IT.60.Ld/2 (5+19)	25.3 [3664]		
Triska	T.45.Ld/3.(4)	21.8 [3165]	494.3 [71.7]	368.8 [53.5]
	T.45.Ld/3.(5)	22.8 [3302]		
	T.60.Ld/3.(5)	23.6 [3417]		
	T.0.Ld/3.(5)	24.4 [3538]		

Table 5.11 – Comparative Analysis Inputs: Beam Geometry

Test Program	Specimen	Span (m) [ft]	s (mm) [in]	No. Bars			Cutoff Location (m) [in]
				Hook	Straight	Cutoff	
SPR 350	1T6	7.32 [24]	152.4 [6]	3	3	0	-
	1IT6	7.32 [24]	152.4 [6]	0	6	0	
	2T10	7.32 [24]	254.0 [10]	3	3	0	
	2IT10	7.32 [24]	254.0 [10]	0	6	0	
	2IT12	7.32 [24]	304.8 [12]	0	6	0	
	5IT12-B4	6.58 [21.6]	304.8 [12]	0	6	0	
	6T10	7.32 [24]	254.0 [10]	3	3	0	
	7T12	6.58 [21.6]	304.8 [12]	3	3	0	
	7IT12	6.58 [21.6]	304.8 [12]	0	6	0	
	8IT12	6.70 [22]	304.8 [12]	0	4	2	1.22 [48]
	8T12-B3	7.32 [24]	304.8 [12]	0	6	0	-
	8T12-B4	7.32 [24]	304.8 [12]	0	3	2	1.52 [60]
	9T12-B4						
Goodall	IT.45.Ld/2	6.58 [21.6]	304.8 [12]	2	2	2	1.02 [40]
	IT.60.Ld/2			2	2	2	1.52 [60]
	IT.45.Ld/2 (5)		254.0 [10]	2	1	2	1.02 [40]
	IT.60.Ld/2 (5+19)						
Triska	T.45.Ld/3.(4)	7.32 [24]	254.0 [10]	2	0	2	1.68 [66.2]
	T.45.Ld/3.(5)			2	1	2	1.73 [68.2]
	T.60.Ld/3.(5)			2	1	2	
	T.0.Ld/3.(5)			2	1	2	

Table 5.12 – Comparative Analysis Macro Outputs

Test Program	Specimen	Failure Mode		V_{app} (kN) [kips]		Bias V_{exp}/V_p
		Test	Macro	Experimental	Predicted	
SPR 350	1T6	Flexure	Flexure	918.5 [206.5]	897.6 [201.8]	1.02
	1IT6	Flexure	Flexure	1049.7 [236.0]	869.1 [195.4]	1.21
	2T10	Shear	Shear	913.2 [205.3]	944.3 [212.3]	0.97
	2IT10	Anch.	Anch.	913.2 [205.3]	858.5 [193.0]	1.06
	2IT12	Anch.	Anch.	817.5 [183.8]	782.8 [176.0]	1.04
	5IT12-B4	Shear	Shear	918.5 [206.5]	962.1 [216.3]	0.95
	6T10	Flexure	Shear	935.8 [210.4]	930.5 [209.2]	1.00
	7T12	Shear	Shear	963.0 [216.5]	958.5 [215.5]	1.00
	7IT12	Shear	Shear	909.2 [204.4]	964.8 [216.9]	0.94
	8IT12	Shear	Anch.	827.8 [186.1]	836.2 [188.0]	0.99
	8T12-B3	Shear	Anch.	818.0 [183.9]	765.0 [172.0]	1.07
	8T12-B4	Shear	Anch.	706.8 [158.9]	640.5 [144.0]	1.10
	9T12-B4	Shear	Anch.	682.8 [153.5]	613.8 [138.0]	1.11
Goodall	IT.45.Ld/2	Shear	Shear	1022.6 [225.4]	926.1 [208.2]	1.08
	IT.60.Ld/2	Shear	Anch.	780.2 [175.4]	840.7 [189.0]	0.93
	IT.45.Ld/2 (5)	Anch.	Anch.	798.4 [179.5]	774.0 [174.0]	1.03
	IT.60.Ld/2 (5+19)	Anch.	Anch.	810.4 [182.2]	769.5 [173.0]	1.05
Triska	T.45.Ld/3.(4)	Anch.	Anch.	497.7 [111.9]	453.7 [102.0]	1.10
	T.45.Ld/3.(5)	Anch.	Anch.	661.0 [148.6]	622.7 [140.0]	1.06
	T.60.Ld/3.(5)	Anch.	Anch.	685.0 [154.0]	622.7 [140.0]	1.10
	T.0.Ld/3.(5)	Anch.	Anch.	686.8 [154.1]	622.7 [140.0]	1.10

Table 5.13 – Macro Analysis Failure Applied Load Predicted Results Statistic Analysis

Beam Type	Bias Mean	Bias STD
T	1.06	0.050
IT	1.03	0.083

Of the 21 specimens investigated, the program inaccurately reported the failure mode for six specimens as shown in Table 5.12. Five of the six specimens were said to have failed in shear, but the macro predicted an anchorage failure. One specimen failed in flexure, but

was predicted to fail in shear. As described previously, it is likely specimens 8T12-B3, 8T12-B4, and 9T12-B4 were influenced by or failed in anchorage. Similarly, specimen 8IT12 had six flexural bars, two of which were cutoff, may have been influenced by anchorage. For specimen 8IT12, the macro predicted that the critical anchorage failure would occur near the support, not the cutoff location.

The predicted difference in critical failure shear between the three possible failure modes for specimen 6T10 is less than 22.4 kN (5 kips). With the prediction window so narrow, it is possible that overlapping of the failure modes could influence outcomes due to material or analytical variability.

Lastly, specimen IT.60.Ld2 actually failed in shear at the preformed crack while an anchorage failure was predicted. Both the predict anchorage and shear capacities were greater than the failure capacity.

Partial safety factors were calculated. If the results of the comparative analysis are assumed to be normally distributed, the probability of over-predicting the experimental strength (V_{exp}/V_p <1) with the Macro method depends on the outcome uncertainties and bias as seen in Table 5.14 and the type of beam (T or IT) being evaluated. Although the bias of the T-beam data is further from one when compared to the IT data, the standard deviation is less for the T-beam data as reported in Table 5.13. This is particularly clear, when the data reported in Table 5.14 is shown with the confidence interval bands as in Fig. 5.35.

Further, the T-beam data requires a higher safety factor, showing that the comparative analysis results more accurately predicts T-beam failure results than IT-beams.

Table 5.14 – Confidence Intervals with Corresponding Resistance Factors

Confidence Interval	Partial Safety ϕ	
	T-Beam	IT-Beam
95%	0.98	0.89
99%	0.94	0.84

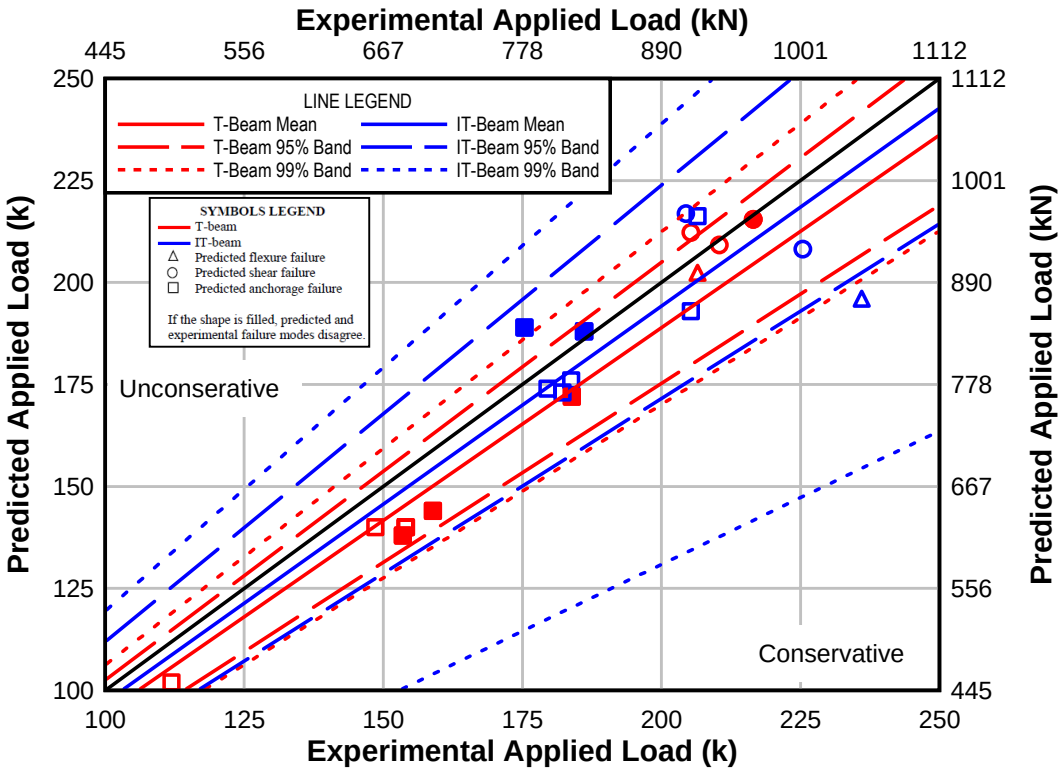

Fig. 5.35 – Macro analysis failure applied load predicted results bias analysis

6. CONCLUSIONS

The objectives of this research were to provide bridge inspectors and rating engineers with tools to evaluate vintage reinforced concrete deck girder bridges containing diagonal cracks interacting with flexural reinforcing steel bar cutoffs. To meet these objectives, four large size specimens were designed, constructed, and tested to failure. Three specimens were constructed with a plastic preformed diagonal crack, which eliminated aggregate interlock. Two preformed diagonal cracks were at 45° and one was at 60°, both common crack angles observed in the field. The fourth specimen did not have a preformed crack, but contained similar reinforcing details. The cutoff bar location began about one-third the minimum development length (as defined by ACI 318-08 specification) away from where the 45° crack crosses the flexural reinforcing bars. Data were collected to assess the shear and flexural tensile forces at various locations, to verify design specification analysis methods and to assist in the development of a new model for assessing anchorages in the presence of diagonal cracks. Conclusions based on the analytical and experimental results provide the framework for field inspection recommendations and evaluation, while suggestions for further research are described in the following sections.

6.1. Analytical Conclusions

The accurate prediction of beam capacity and failure mode requires analyzing sections along the length of the specimen, not just those sections which appear to be the intuitive weak points: at diagonal crack locations, at the support, near the loading point, and along the length of the developing bars. The shear, flexural, and anchorage capacities must all be checked at each section. An anchorage failure will occur when the tensile bar demand is

greater than the force that the reinforcing bar-concrete interface can resist and occurs at some load level less than the shear and flexural capacities.

The data showed that the required tensile demands at a diagonal crack location, as specified in the AASHTO-LRFD specification are reasonable. The additional demands in the flexural bars require coincident load effects rather than maximums applied simultaneously. Except at low load levels, the total shear crossing the preformed crack, as determined from the internal stirrup tensile force, dowel action, and concrete compression zone shear transfer, reasonably equaled the shear applied to the section.

Non-linear finite element analysis using VecTor2 predicted the ultimate capacities and load-deformation behavior of the specimens quite well. The presence or absence of a modeled preformed crack did not significantly change which characteristic diagonal crack caused failure. However, the bond-slip relationship of the cutoff affected the bond stress in the reinforcement and the failure diagonal crack.

6.2. Experimental Conclusions

The four T-beam specimens that are a part of this thesis showed that the presence of a preformed crack does not necessarily affect the failure mode of the specimens. Further, the presence of a diagonal crack crossing a partially developed bar at service level conditions may not necessarily weaken the structure. Although the preformed crack causes an initial increase in bond stress near the crack, as the failure crack develops the peak bond stress moves. The location of the failure crack and the failure mode depends on other more

predicable geometric properties, such as cutoff location, number of flexural reinforcing bars, and stirrup spacing, rather than highly variable cracks which can develop during service level conditions.

6.3. Recommendations

The crack patterns observed in each of the specimens near the cutoff bar location gives field inspectors examples of what kind of damage to look for prior to a possible anchorage failure. Although fully described in Section *4.1.2 Crack Growth in Specimens* with photos, it is recommended that inspectors look for a grouping of vertical and horizontal cracks near the beam soffit at the level of the flexural reinforcing steel and focus on those locations that are near cutoff locations shown in available structural drawings. Distress of this type will be indicative of anchorage slip and must be followed up with additional scrutiny.

6.4. Additional Research

The primary focus of this thesis project was to investigate flexural anchorage failures and interaction with diagonal cracks in vintage RCDG specimens. As such, several future analytical and experimental projects which might further define the anchorage failure program are suggested:

Further non-linear finite element analysis may be conducted using VecTor2. More work may be done to increase the accuracy of the bond predictions. Alternate methods of modeling cracks observed in the field may be investigated. Development of a finite

element model which reproduces the experimental results of other experimental tests programs performed at Oregon State University including FRP repairs may be explored.

Although the experimental program made an attempt to recreate vintage RCDG girders, not every possible parameter could be considered with four specimens. As such, future research projects could investigate the effects of the following:

- Influence of cutoffs in deep beams (a/d <1).
- Performance of bond under repeated loading to determine possible deterioration from bond fatigue.

BIBLIOGRAPHY

Abrishami, H., & Mitchell, D. (1996) Analysis of bond stress distributions in pullout specimens. *Journal of Structural Engineering*, 122 (3), 255-261.

American Concrete Institute (1956) Building code requirements for reinforced concrete (ACI 318-56). *ACI Manual of Concrete Practice*, Farmington Hills, Michigan, 927, 949.

American Concrete Institute (2008) 318-08/318R-08: Building Code Requirements for Structural Concrete and Commentary. *ACI Manual of Concrete Practice*, Farmington Hills, Michigan.

AASHO (1953) Standard specifications for highway bridges, 6th Edition, *American Association of State Highway Officials*, Washington, DC, 182, 238.

AASHO (1973) Standard specifications for highway bridges, *American Association of State Highway Officials*, Washington, DC, 57-58,93.

AASHTO (2005) AASHTO LRFD bridge design specifications, 3rd edition with 2005 interims, *American Association of State Highway and Transportation Officials*.

ASTM A305-50T (1950) Minimum requirements for the deformations of deformed steel bars for concrete reinforcement. *ASTM International*, 218-220.

ASTM A615/A615M-09b (2009) Standard specification for deformed and plain carbon-steel bars for concrete reinforcement. *ASTM International*.

ASTM C39/C39M-09a (2009) Standard test method for compressive strength of cylindrical concrete specimens. *ASTM International*

ASTM C617-09a (2009) Standard practice for capping cylindrical concrete specimens. *ASTM International*.

ASTM E8/E8M-09a (2009) Standard test methods for tension testing of metallic materials. *ASTM International*.

Bentz, E., (2000). Response-2000: Reinforced Concrete Sectional Analysis using the Modified Compression Field Theory (Version 1.0.5) [Computer software]. University of Toronto

Clark, A. P. (1949) Bond of concrete reinforcing bars. *Journal of the American Concrete Institute Proceedings*, 21 (3), 161-184.

Darwin, D., Zou, J., Tholen, M., & Idun, E. (1996) Development length criteria: for conventional and high relative rib area reinforcing bars. *ACI Structural Journal*, 93 (3), 1-13.

Doerr, K. (1978) Bond behavior of ribbed reinforcement under transversal pressure. *Nonlinear behavior of reinforced concrete spatial: contributions to IASS symposium* (pp. 13-24) Dusseldorf, Germany: International Association for Shell Structures.

Goodall, J. K. (2010). *Influence of diagonal cracks of negative moment flexural anchorage performance in reinforced concrete bridge girders.* Unpublished masters thesis, Oregon State University.

Harajli M. H. (2004) Comparison of bond strength of steel bars in normal- and high-strength concrete. *Journal of Materials in Civil Engineering*, 16 (4), 365-374.

Higgins, C., Miller, T., Rosowsky, D. V., Yim, S.C., Potisuk, T., Daniels, T. K., Nicholas, B.S., Robelo, M. J., et al. (2004) *SPR 350 Assessment Methodology for Diagonally Cracked Reinforced Concrete Deck Girder.* Salem, Oregon: Oregon Department of Transportation.

Howell, D., (2009) *Shear repair methods for conventionally reinforced concrete girders and deep beams*. PhD dissertation, Oregon State University.

Jeppsson, J., & Thelandersson, S. (2003) Behavior of reinforced concrete beams with loss of bond at longitudinal reinforcement. *Journal of Structural Engineering*, 129 (10), 1376-1383.

Losberg, A., & Olsson, P. (1979) Bond failure of deformed reinforcing bars based on the longitudinal splitting effect of the bars. *ACI Journal Symposium Paper*, 5-18.

MacGregor, J. G., & Wright, J. K. (2005) *Reinforced concrete mechanics and design.* Upper Saddle River, New Jersey: Pearson Prentice Hall.

Mains, R. M (1951) Measurement of the distribution of tensile and bond stresses along reinforcing bars. *Journal of the American Concrete Institute*, 48 (3) 225-252.

Malvar, J. (1992) Bond of reinforcement under controlled confinement. *ACI Materials Journal*, 89 (6), 593-601.

Microsoft Corporation (2006) Microsoft Office Excel 2007 [Computer software]

Mylrea, T. D. (1948) Bond and anchorage. *Journal of the American Concrete Institute Proceedings*, 44 (3), 521-552.

Reynolds, G. C., & Beeby, A. W. (1982). Bond strength of deformed bars. In P. Bartos (Ed.) *Bond in concrete*, (pp. 434-445). London: Applied Science Publishers.

Senturk, A. E. (2008) *Experimental and analytical evaluation of conventionally reinforced deck-girder bridge bent caps with vintage details*. PhD dissertation, Oregon State University.

Soroushian, P., Choi, K. B., Park, G., & Aslani, F. (1991) Bond of deformed bars to concrete: effects of confinement and strength of concrete. *ACI Materials Journal*, 88 (3), 161-168.

Sherwood, E.G. (2008) *One-way shear behaviour of large, lightly-reinforced concrete beams and slabs.* PhD dissertation, University of Toronto.

Vecchio, F. J. (2000) Disturbed stress field model for reinforced concrete: formulation. *ASCE Journal of Structural Engineering*, 126 (9), 1070-1077.

Vecchio, F. J., and Collins, M. P. (1986) The modified compression field theory for reinforced concrete elements subjected to shear. *ACI Journal*, 83 (2), 219-231.

Vecchio, F. J., and Wong, P. (2002) *VecTor2 and Formworks Manual.* Toronto, Ontario, Canada: Department of Civil Engineering, University of Toronto.

APPENDECIES

APPENDIX A – EXPERIMENTAL DATA

Appendix A describes the labeling of each instrument used for each specimen, with illustrations. Section *3.5 Instrumentation* defines the purpose of each instrument. The functionality of each gage at failure is provided. Plots are provided of selected data.

Midspan Displacement: Midspan displacement was measured using a displacement sensor attached to each side of the stem at midspan. The instrument on the west side of the beam was “Midspan W” and the instrument on the east side of the beam was “Midspan E.”

Support Settlement: A displacement sensor was located at each of the four corners of the specimen to measure the support settlement. The instruments were identified by two letters. The fist letter (N or S) noted the north or south side of the beam. The second letter (W or E) noted the west or east side of the specimen.

Cutoff Bar Slippage: A displacement sensor was located at the end of each cutoff bar. The instrument on the west cutoff bar was “Cutoff Bar Slippage W” and the instrument on the east cutoff bar was “Cutoff Bar Slippage E.”

Crack Width Sensors: Displacement sensors were used to track the change in crack width of select cracks on the northwest side of the beam. All four specimens had two instruments straddling the preformed crack and were labeled as “Preformed Crack Top: or “Preformed Crack Bottom.” “Top” referred to the narrower portion of the crack near the top of the beam, with “Bottom” noting the wider portion of the crack near the bottom of the beam.

Additional, specimens T.60.Ld3.(5) and T.0.Ld3.(5) had two instruments crossing the dominate crack location which developed extending from the loading plate to the end of the cutoff bar. The labeling conversion was similar; accept the crack was identified as "Dominate" instead of "Preformed."

Diagonal Displacement Potentiometers: Six displacement sensors measured the displacement of the beam over a region. The instrument was anchored to one point on the specimen, and a wire attached to the instrument was strung to a second anchor point. Each instrument was identified by these numbered anchor points. For example, the sensor connecting points 1 and 4 was label "1-4", as shown in Fig. A.1.

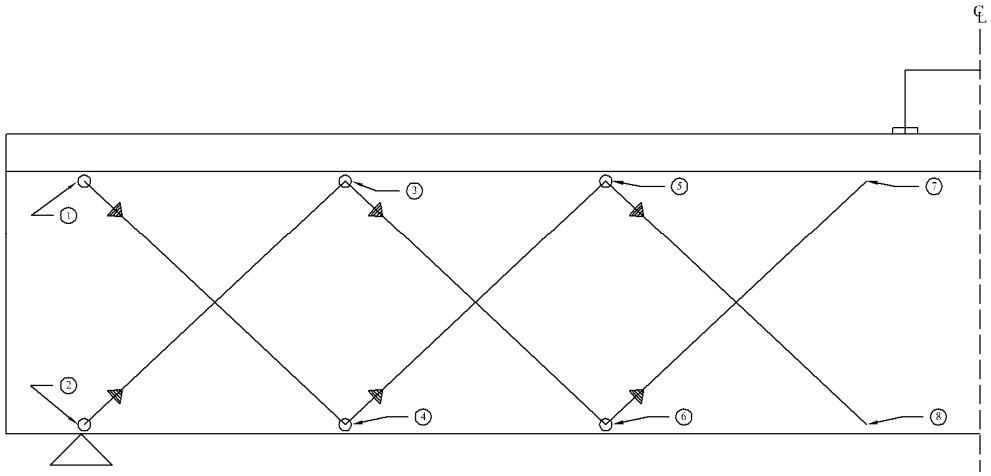

Fig. A.1 – Typical external displacement sensor array labeling conversion

Flexural Bar Stain Gages: Each flexural bar had five strain gages. Each gage was identified by the words "Flexural Bar" followed by two numbers. The first number signified the location as taken from the end of the cutoff bar, as shown in Fig. A.2 to A.4. The second number identified the bar as located in cross-section shown in Fig. A.5.

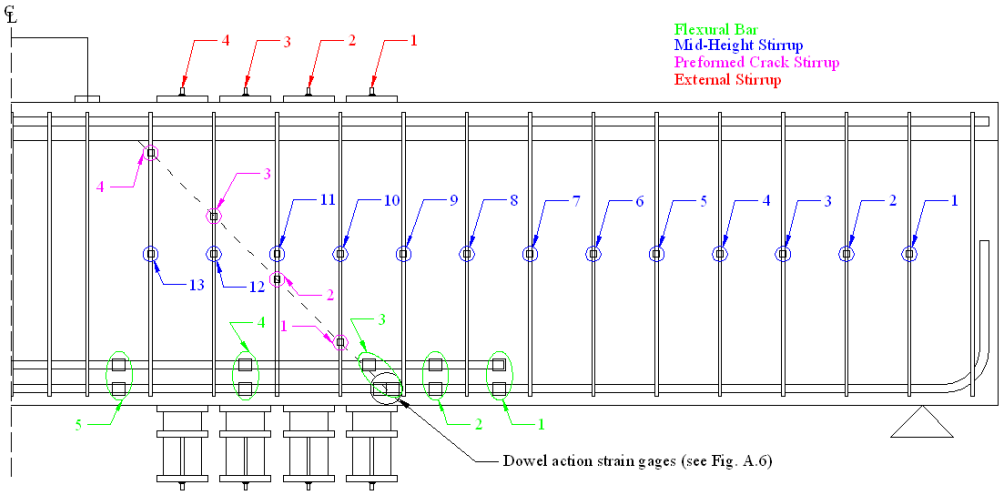

Fig. A.2 – Specimens T.45.Ld3.(4) and T.45.Ld3.(5) strain gage labeling convention

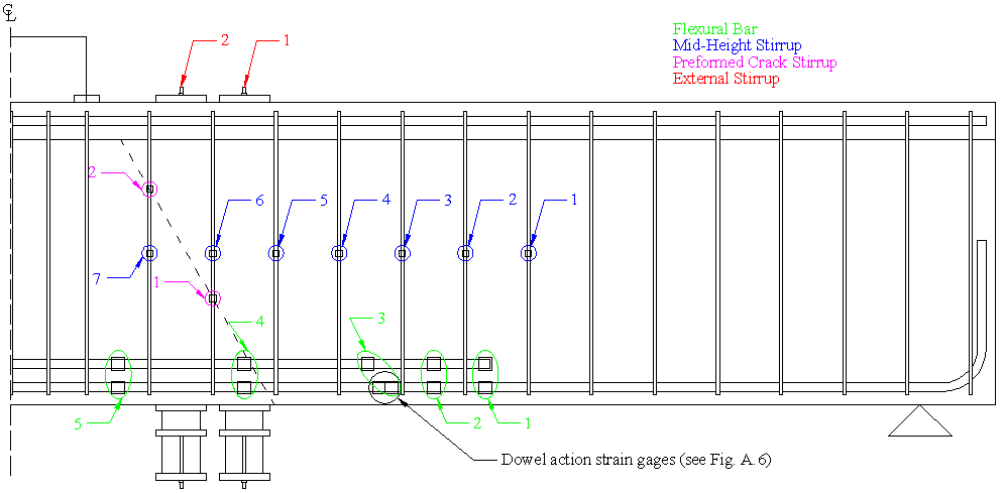

Fig. A.3 – Specimen T.60.Ld3.(5) strain gage labeling convention

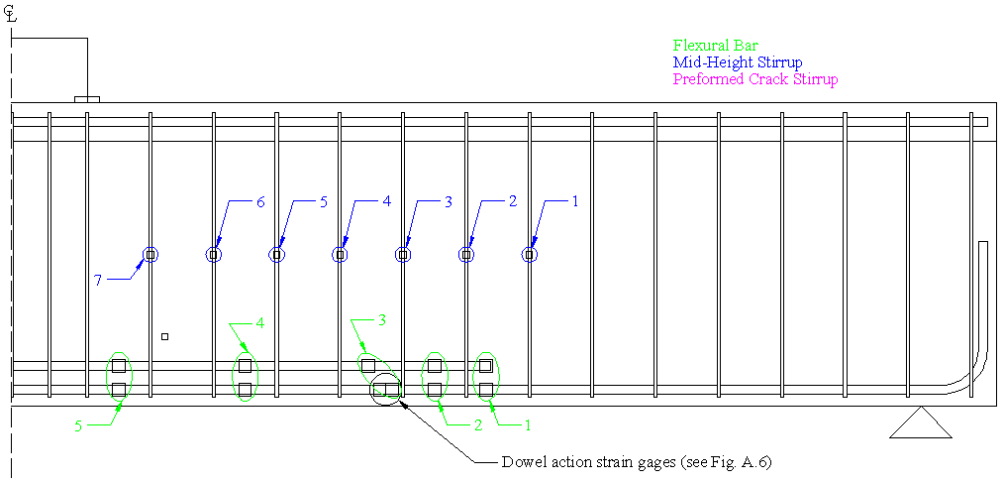

Fig. A.4 – Specimen T.0.Ld3.(5) strain gage labeling contention

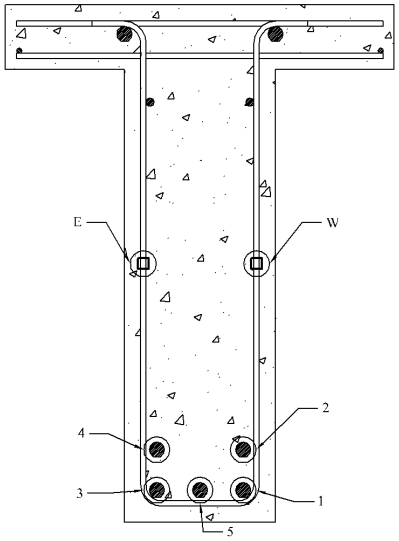

Fig. A.5 – Typical cross-section of specimens strain gage labeling convention

Dowel Action Strain Gages: One flexural bar received a set of eight strain gages used to determine the dowel action (reinforcing steel shear transfer) at the location where the preformed crack crossed the flexural bars. In specimens T.45.Ld3.(5), T.60.Ld3.(5), and

T.0.Ld3.(5), the gages were located on the bottom layer straight bar. Specimen T.45.Ld3.(4) had the gages on the west hooked bar. Fig. A.6 shows the typical arrangement and labeling convention of the dowel action gages.

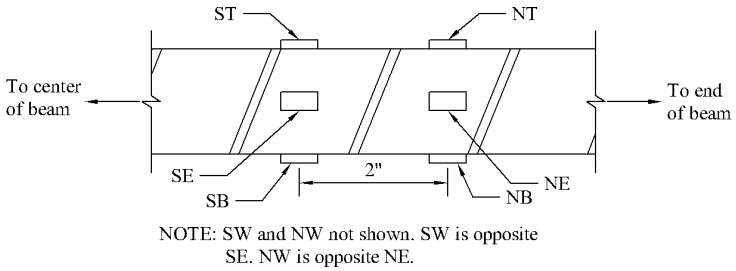

Fig. A.6 – Dowel action strain gages locations

Concrete Compression Zone Strain Gages: Six strain gages were applied in the concrete compression zone near the preformed crack. Specimen T.0.45.Ld3.(5) did not have any concrete compression zone gages. Fig. A.7 shows the typical arrangement and labeling convention of the concrete compression zone gages.

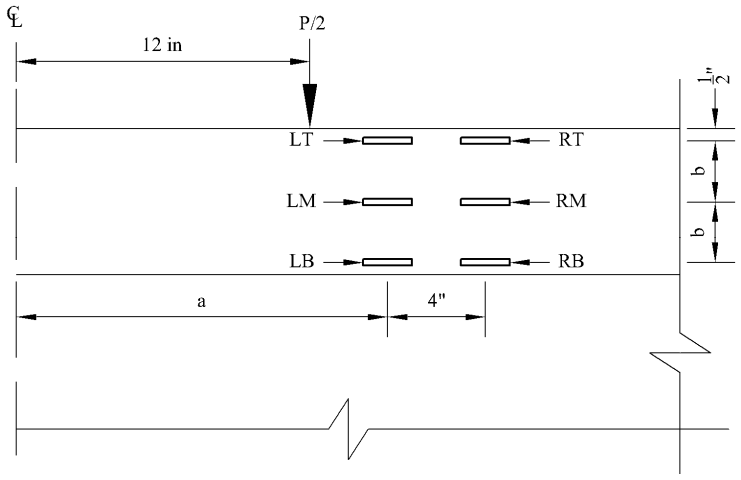

SPECIMEN	a (in)	b (in)
T.45.Ld3.(4)	15.50	1.50
T.45.Ld3.(5)	18.50	2.50
T.60.Ld3.(5)	12.25	2.50

Fig. A.7 – Concrete compression zone strain gages locations

Mid-Height Stirrup Strain Gages: Strain gages were applied on each stirrup leg at the mid-height of the stirrup. Each gage was identified by the word “Stirrup” followed by a number and letter. The number identified the stirrup, with 1 being the stirrup closest to the support as shown in Figs. A.2 to. A.4. The letter (W or E) identified the stirrup leg as shown in the cross-section in Fig. A.5. Specimens T.45.Ld3.(4) and T.45.Ld3.(5) had gages applied to a total of 13 stirrups. Specimens T.60.Ld3.(5) and T.0.Ld3.(5) and 7 stirrups instrumented.

Preformed Crack Stirrup: Strain gages were applied on each stirrup leg wherever the preformed crack crossed a stirrup. Each gage was identified by the words “Crack Stirrup” followed by a number and letter. The number identified the stirrup, with 1 being the stirrup closest to the support as shown in Figs. A.2 to A.4. The letter (W or E) identified the stirrup leg as depicted in the cross-section in Fig. A.5. Specimen T.0.Ld3.(5) did not have any preformed crack stirrup gages.

External Stirrup Strain Gages: As part of the external stirrup set, strain gages were applied to each high-strength steel rod near mid-height. Each gage was identified by the words “External Stirrup” followed by a number and letter. The number identified the stirrup, with 1 being the stirrup closest to the support as shown in Figs. A.2 to A.4. The letter (W or E) identified the stirrup leg as depicted in the cross-section in Fig. A.5.

Load Cells: Each external stirrup setup at a load cell. Load cells were label numerically, with 1 being closest to the end of the cutoff as shown in Figs. A.2 and A.3. Specimen T.0.Ld3.(5) did not have any load cells.

Figs. A.8 to A.148 are graphs showing the data collected by the instrumentation. The failure load cycle, and last baseline and external stirrup load cycles are reported. For specimen T.45.Ld3.(4) the final baseline and external stirrup load cycles reached a load of 667 kN (150 kips). Specimens T.45.Ld3.(5) and T.60.Ld3.(5) had a peak load of 890 kN (200 kips) during the final load cycle. Table A.1 serves as a table of contents for the data plots.

Table A.1 – Data Plot Table of Contents

Graph	**T.45.Ld3.(4)**	**T.45.Ld3.(5)**	**T.60.Ld3.(5)**	**T.0.Ld3.(5)**
Midspan[a] Displacement	124	139	154	169
Cutoff Bar Slippage	125	140	155	169
Crack Width	126	141	156	169
Diagonal Displacement	127	142	157	170
Flexural Bars Location 1	128	143	158	170
Flexural Bars Location 2	129	144	159	170
Flexural Bars Location 3	130	145	160	171
Flexural Bars Location 4	131	146	161	171
Flexural Bars Location 5	132	147	162	171
Dowel Action	133	148	163	172
Concrete Compression Zone	134	149	164	N/A
West Mid-Height Stirrups	135	150	165	172
East Mid-Height Stirrups	136	151	166	172
Preformed Crack Stirrups	137	152	167	N/A
External Stirrups	138	153	168	N/A

[a] Midspan displacement is the average of the two midspan displacements less the average of the four support settlement displacement.

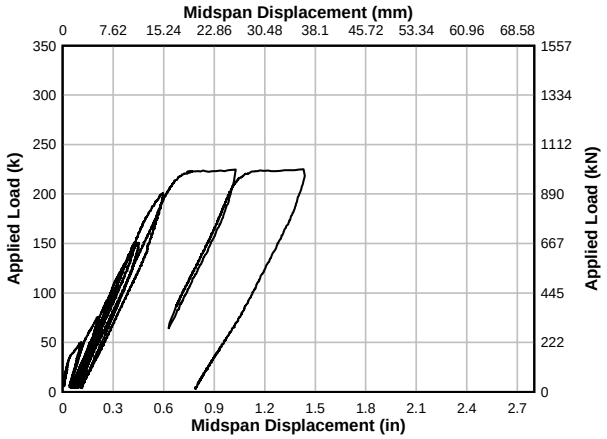

Fig. A.8 – Specimen T.45.Ld3.(4) load-midspan displacement (failure test)

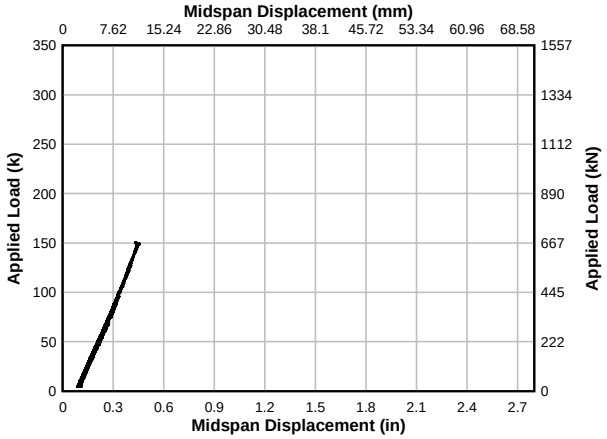

Fig. A.9 – Specimen T.45.Ld3.(4) load-midspan displacement (baseline test)

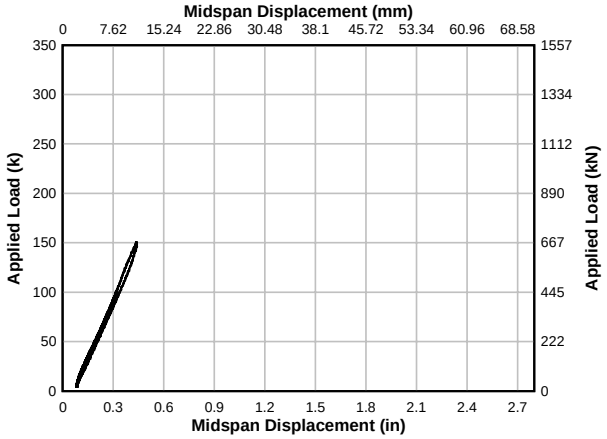

Fig. A.10 – Specimen T.45.Ld3.(4) load-midspan displacement (ext. stirrup test)

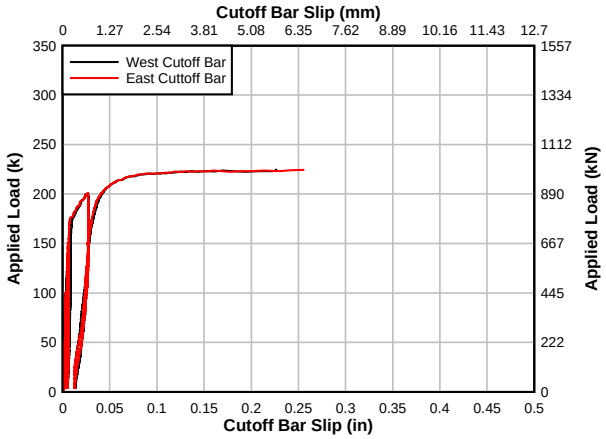

Fig. A.11 – Specimen T.45.Ld3.(4) load-cutoff bar slip (failure test)

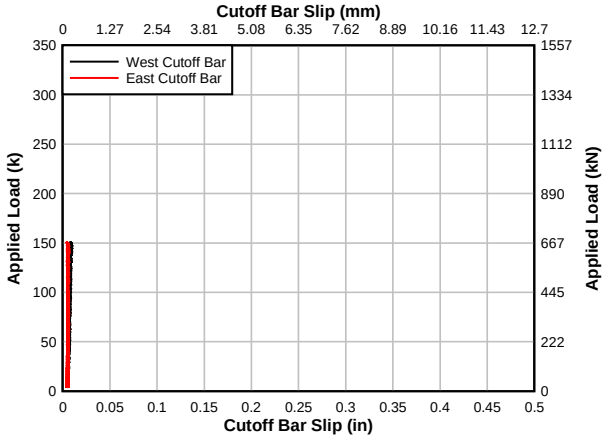

Fig. A.12 – Specimen T.45.Ld3.(4) load-cutoff bar slip (baseline test)

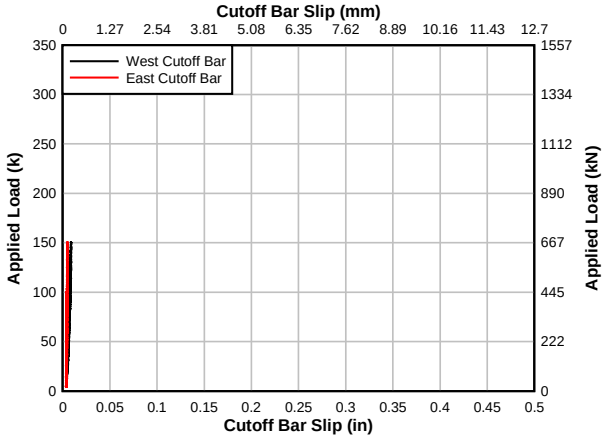

Fig. A.13 – Specimen T.45.Ld3.(4) load-cutoff bar slip (ext. stirrup test)

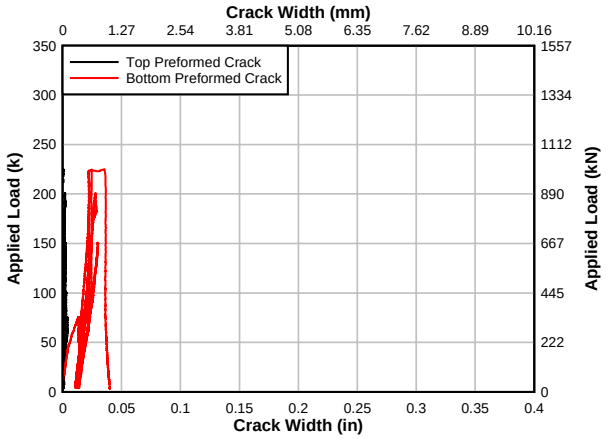

Fig. A.14 – Specimen T.45.Ld3.(4) load-preformed crack width (failure test)

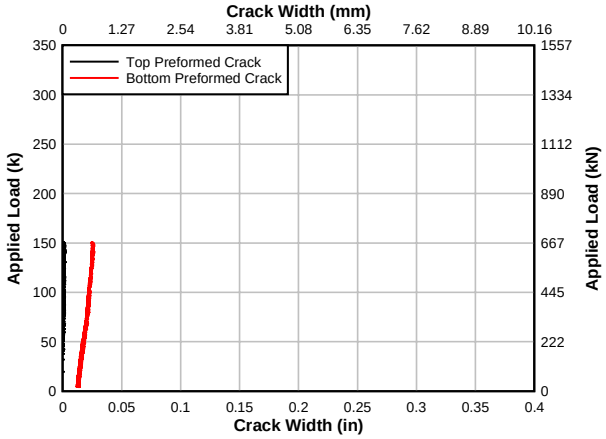

Fig. A.15 – Specimen T.45.Ld3.(4) load-preformed crack width (baseline test)

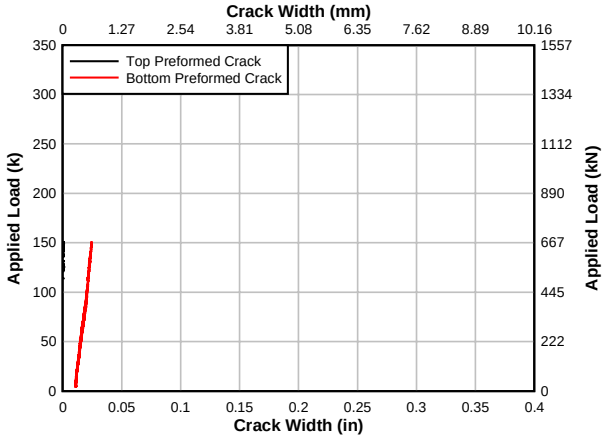

Fig. A.16 – Specimen T.45.Ld3.(4) load-preformed crack width (ext. stirrup test)

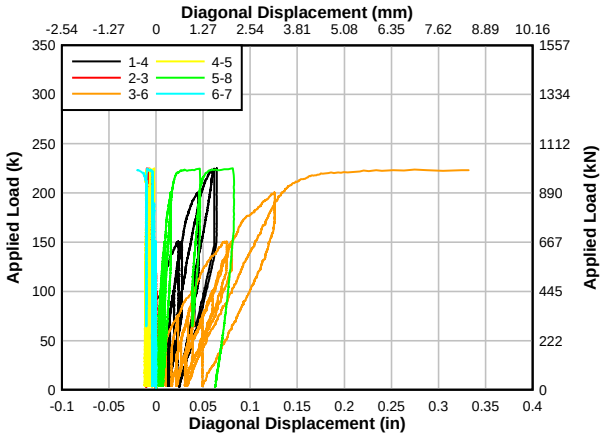

Fig. A.17 – Specimen T.45.Ld3.(4) load-diagonal displacement (failure test)

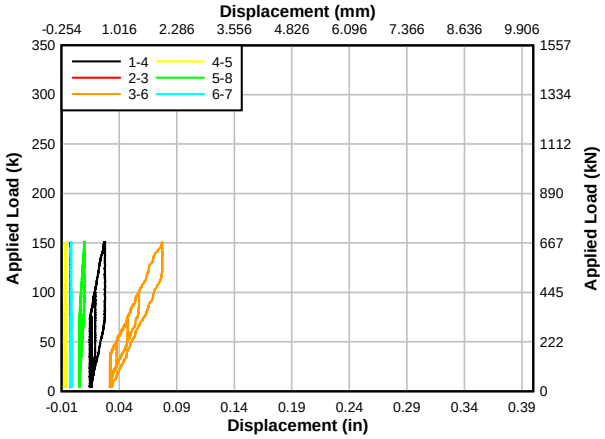

Fig. A.18 – Specimen T.45.Ld3.(4) load-diagonal displacement (baseline test)

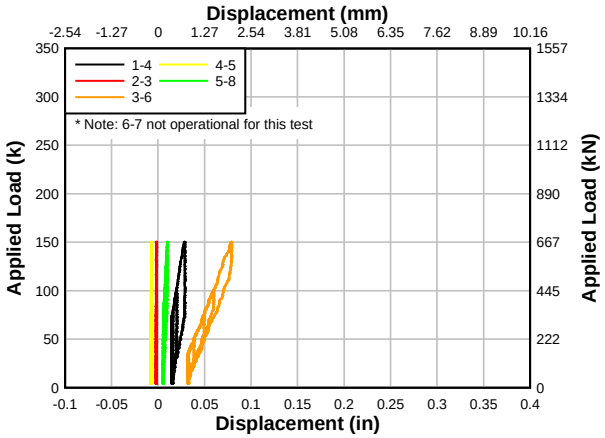

Fig. A.19 – Specimen T.45.Ld3.(4) load-diagonal displacement (ext. stirrup test)

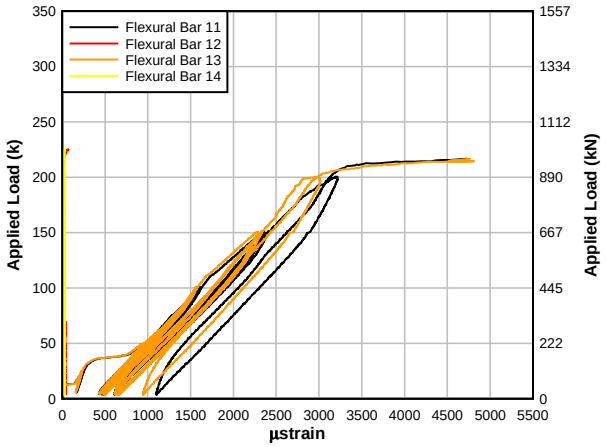

Fig. A.20 – Specimen T.45.Ld3.(4) load-flexural bar location 1 strain (failure test)

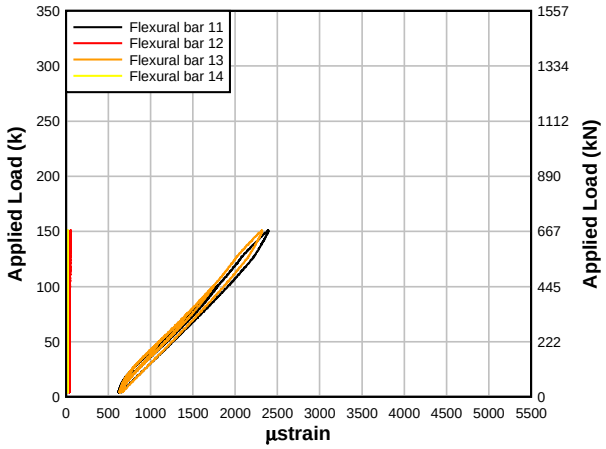

Fig. A.21 – Specimen T.45.Ld3.(4) load-flexural bar location 1 strain (baseline test)

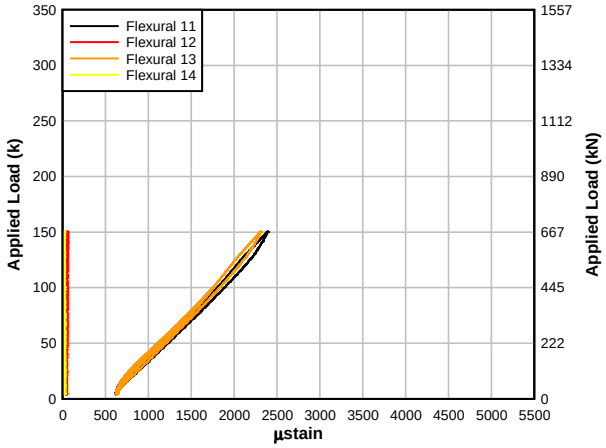

Fig. A.22 – Specimen T.45.Ld3.(4) load-flexural bar location 1 strain (ext. stirrup test)

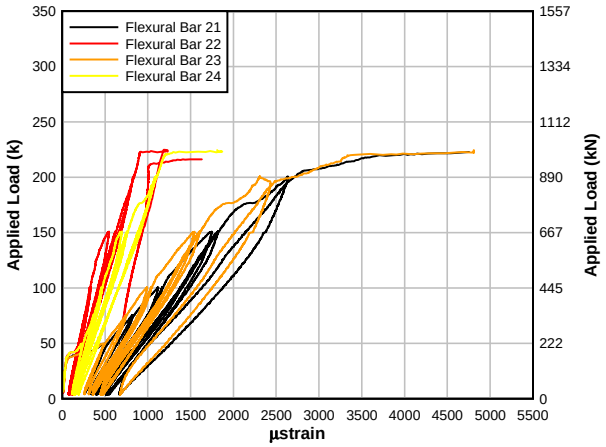

Fig. A.23 – Specimen T.45.Ld3.(4) load-flexural bar location 2 strain (failure test)

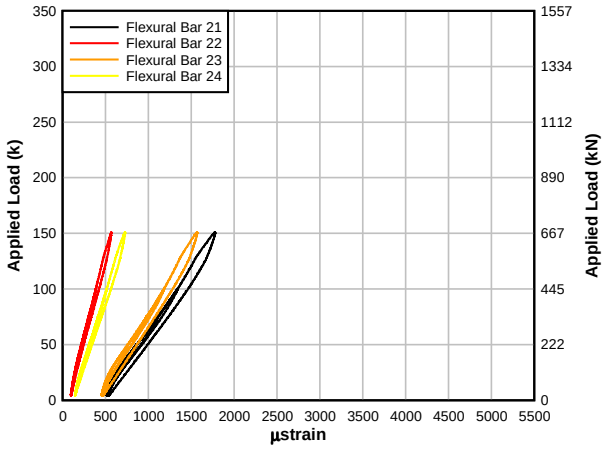

Fig. A.24 – Specimen T.45.Ld3.(4) load-flexural bar location 2 strain (baseline test)

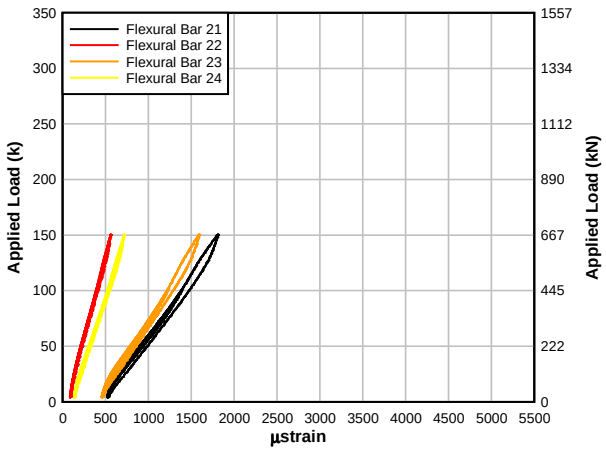

Fig. A.25 – Specimen T.45.Ld3.(4) load-flexural bar location 2 strain (ext. stirrup test)

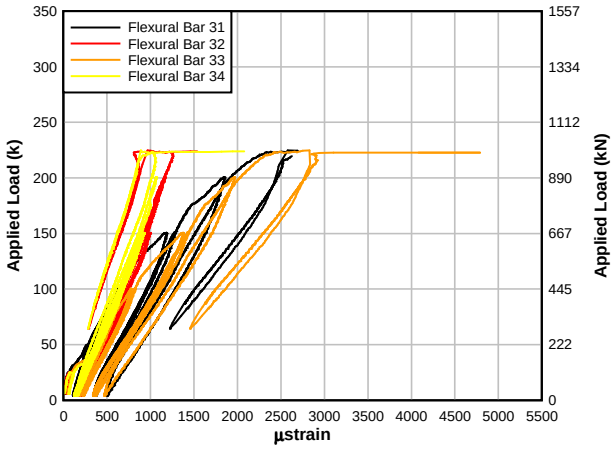

Fig. A.26 – Specimen T.45.Ld3.(4) load-flexural bar location 3 strain (failure test)

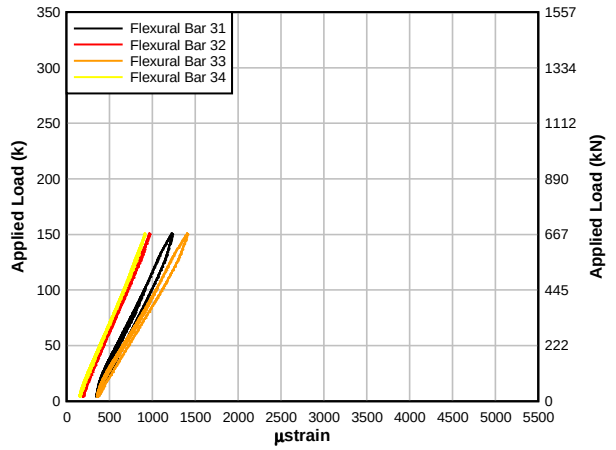

Fig. A.27 – Specimen T.45.Ld3.(4) load-flexural bar location 3 strain (baseline test)

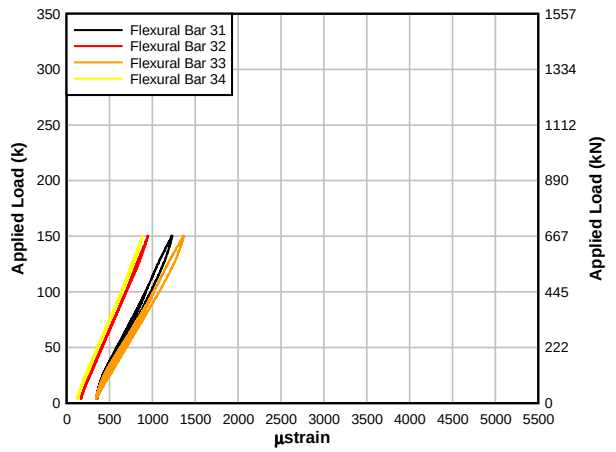

Fig. A.28 – Specimen T.45.Ld3.(4) load-flexural bar location 3 strain (ext. stirrup test)

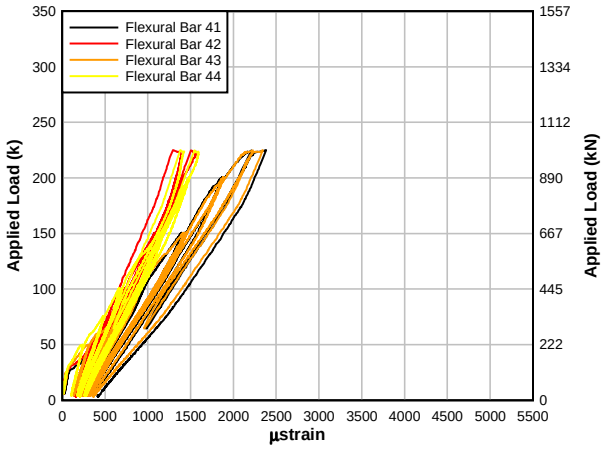

Fig. A.29 – Specimen T.45.Ld3.(4) load-flexural bar location 4 strain (failure test)

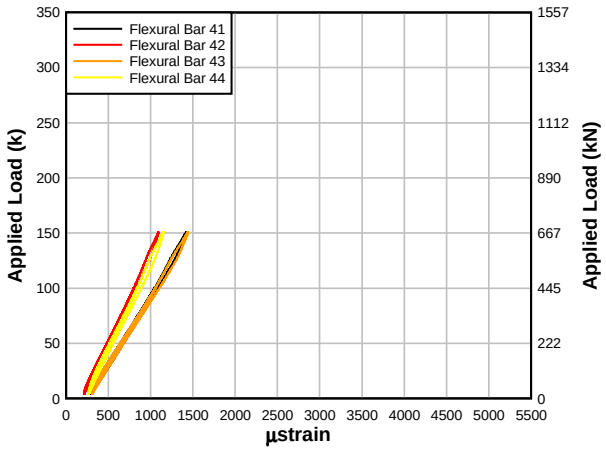

Fig. A.30 – Specimen T.45.Ld3.(4) load-flexural bar location 4 strain (baseline test)

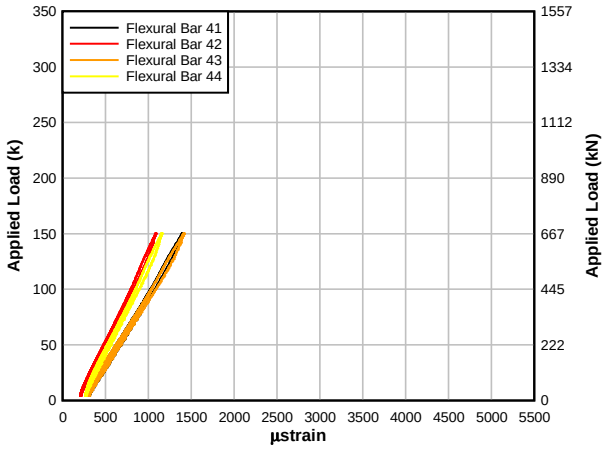

Fig. A.31 – Specimen T.45.Ld3.(4) load-flexural bar location 4 strain (ext. stirrup test)

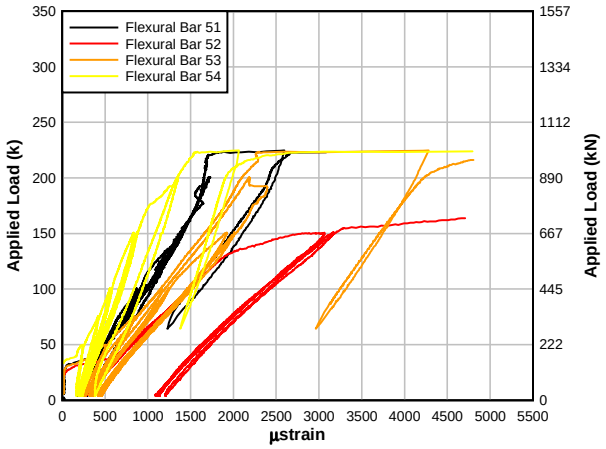

Fig. A.32 – Specimen T.45.Ld3.(4) load-flexural bar location 5 strain (failure test)

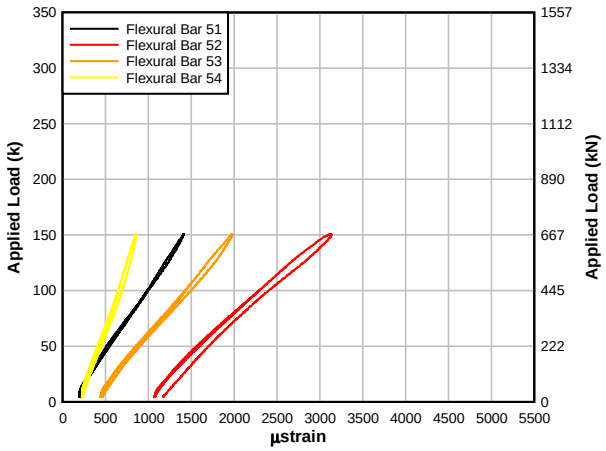

Fig. A.33 – Specimen T.45.Ld3.(4) load-flexural bar location 5 strain (baseline test)

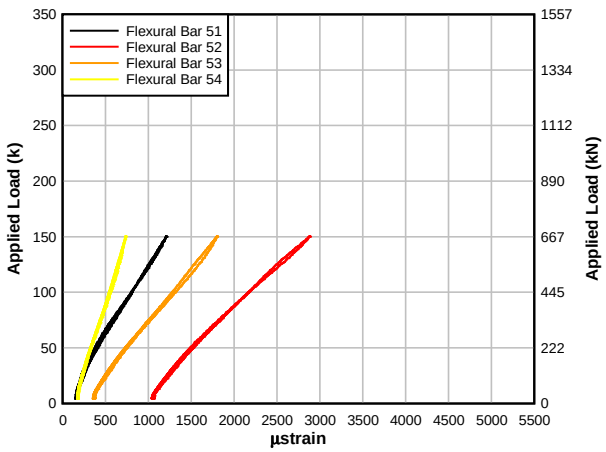

Fig. A.34 – Specimen T.45.Ld3.(4) load-flexural bar location 5 strain (ext. stirrup test)

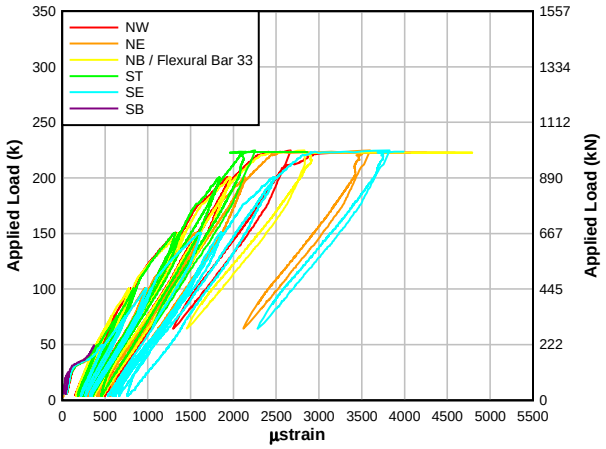

Fig. A.35 – Specimen T.45.Ld3.(4) load-dowel action stain (failure test)

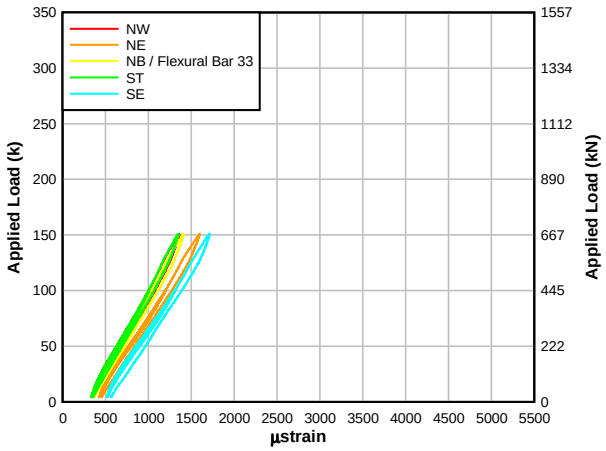

Fig. A.36 – Specimen T.45.Ld3.(4) load-dowel action stain (baseline test)

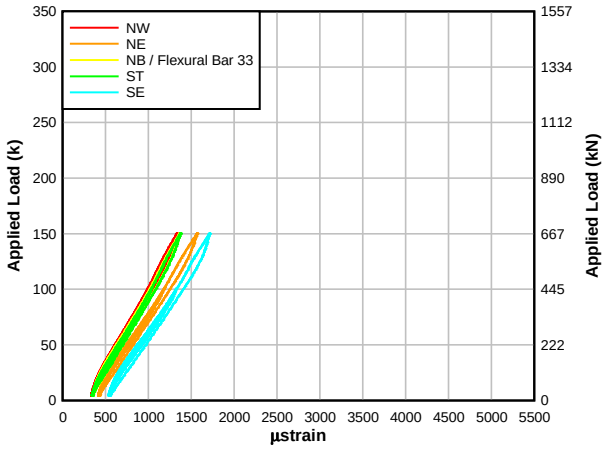

Fig. A.37 – Specimen T.45.Ld3.(4) load-dowel action stain (ext. stirrup test)

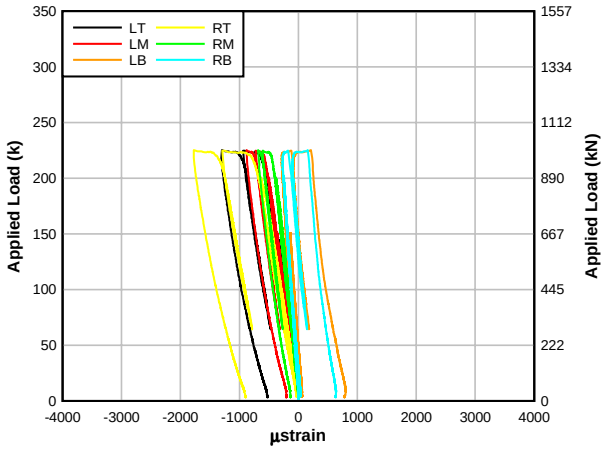

Fig. A.38 – Specimen T.45.Ld3.(4) load-concrete compression zone stain (failure test)

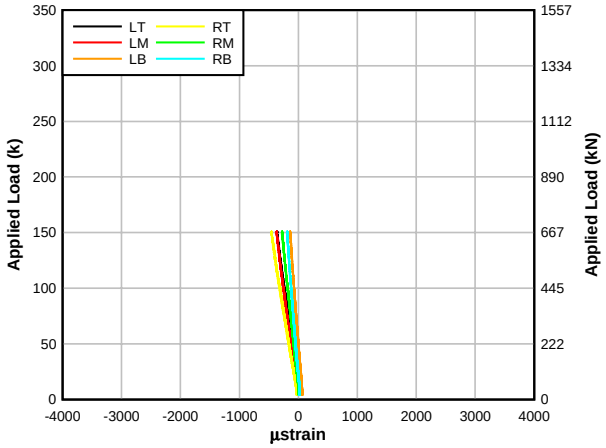

Fig. A.39 – Specimen T.45.Ld3.(4) load-concrete compression zone stain (baseline test)

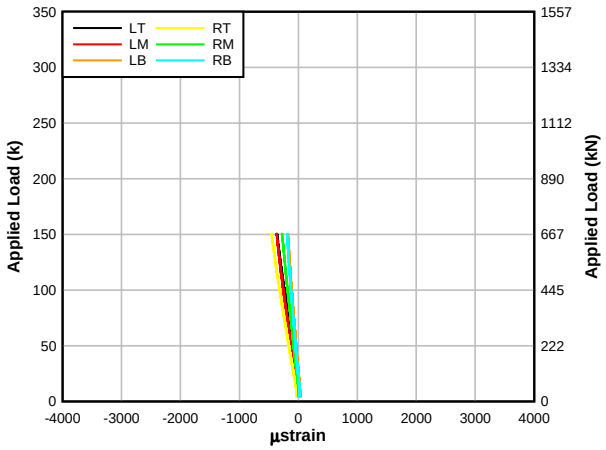

Fig. A.40 – Specimen T.45.Ld3.(4) load-concrete compression zone stain (ext. stirrup test)

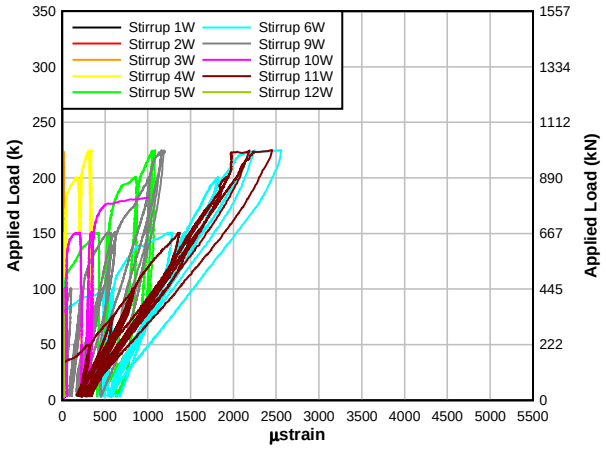

Fig. A.41 – Specimen T.45.Ld3.(4) load-west mid-height stirrup stain (failure test)

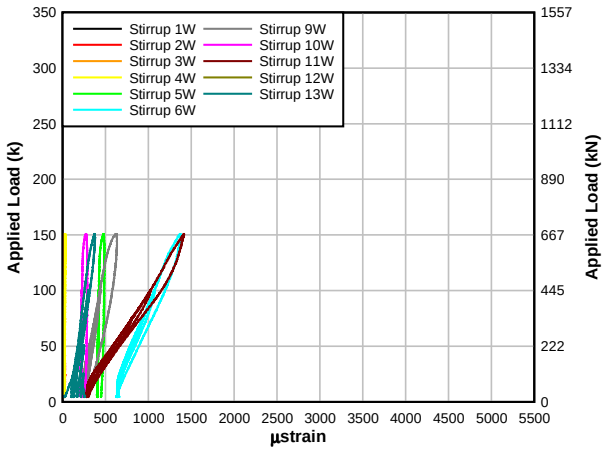

Fig. A.42 – Specimen T.45.Ld3.(4) load-west mid-height stirrup stain (baseline test)

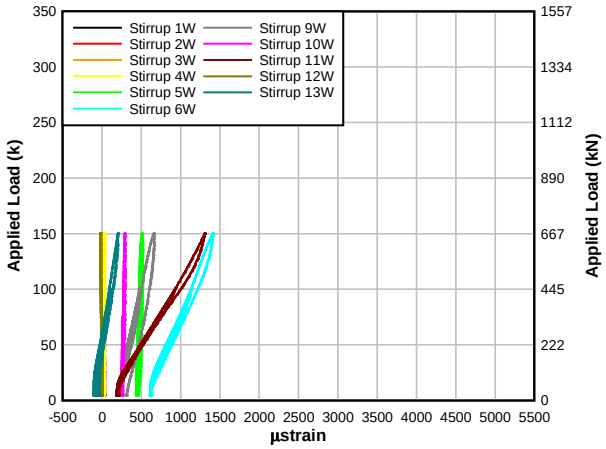

Fig. A.43 – Specimen T.45.Ld3.(4) load-west mid-height stirrup stain (ext. stirrup test)

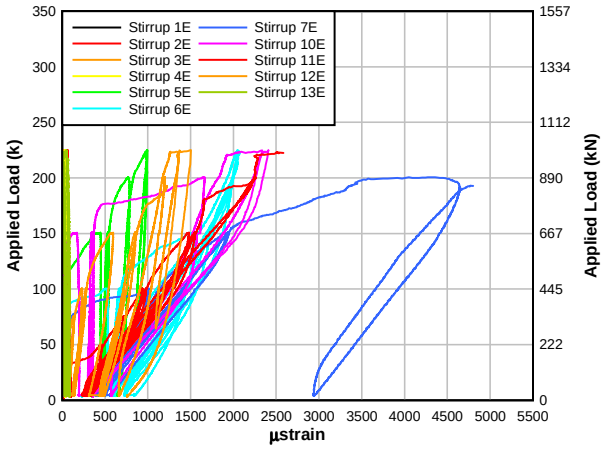

Fig. A.44 – Specimen T.45.Ld3.(4) load-east mid-height stirrup stain (failure test)

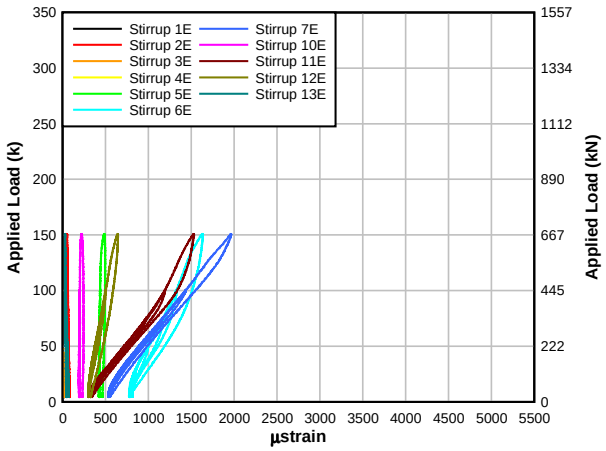

Fig. A.45 – Specimen T.45.Ld3.(4) load-east mid-height stirrup stain (baseline test)

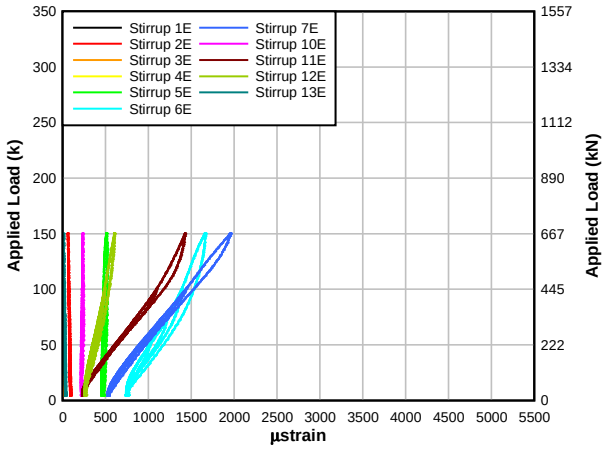

Fig. A.46 – Specimen T.45.Ld3.(4) load-east mid-height stirrup stain (ext. stirrup test)

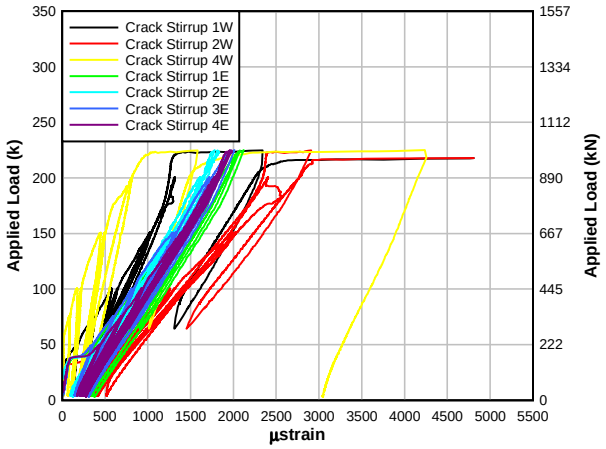

Fig. A.47 – Specimen T.45.Ld3.(4) load-preformed crack stirrup stain (failure test)

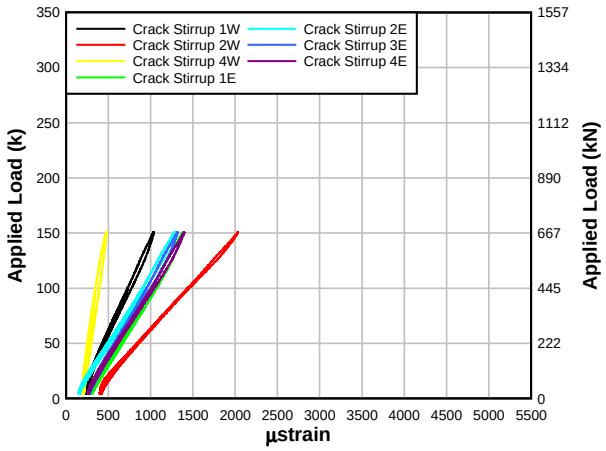

Fig. A.48 – Specimen T.45.Ld3.(4) load-preformed crack stirrup stain (baseline test)

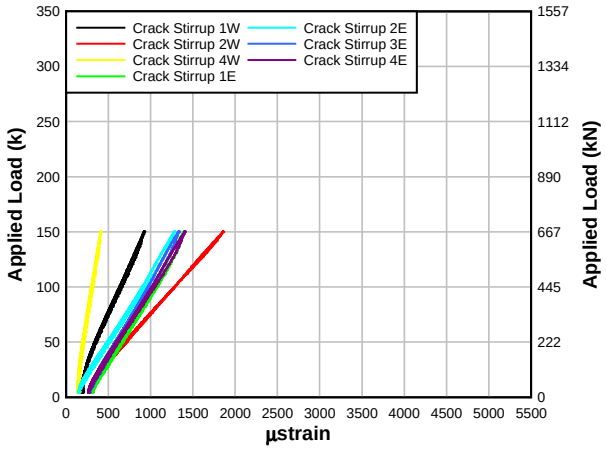

Fig. E .49 – Specimen T.45.Ld3.(4) load-preformed crack stirrup stain (ext. stirrup test)

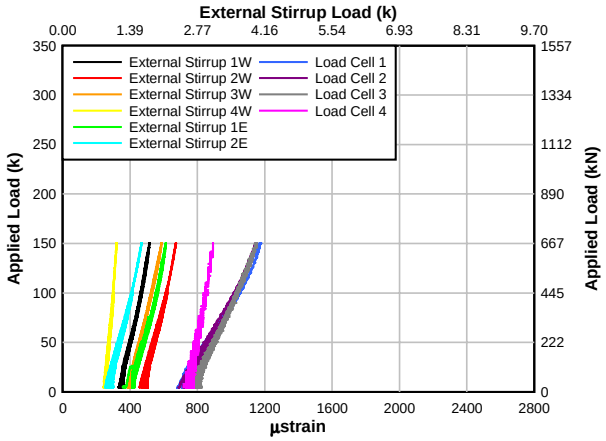

Fig. A.50 – Specimen T.45.Ld3.(4) load-external stirrup strain/load (ext. stirrup test)

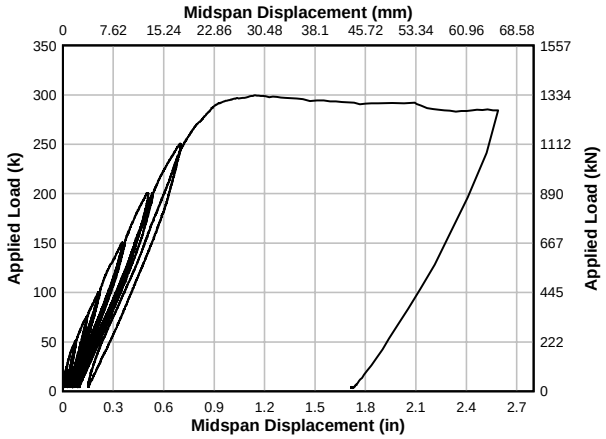

Fig. A.51 – Specimen T.45.Ld3.(5) load-midspan displacement (failure test)

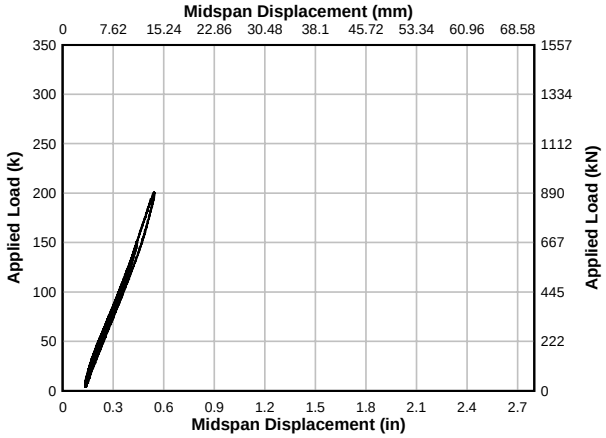

Fig. A.52 – Specimen T.45.Ld3.(5) load-midspan displacement (baseline test)

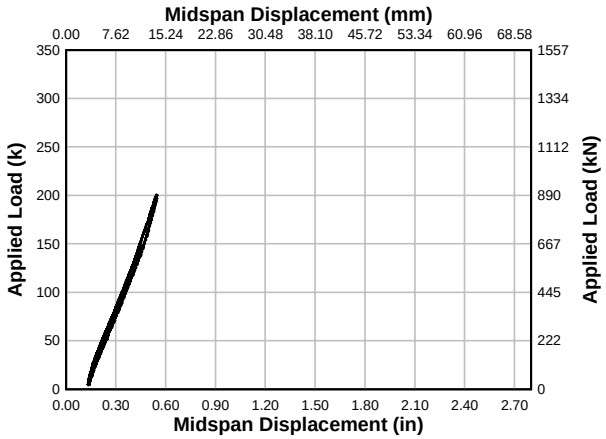

Fig. A.53 – Specimen T.45.Ld3.(5) load-midspan displacement (ext. stirrup test)

Fig. A.54 – Specimen T.45.Ld3.(5) load-cutoff bar slip (failure test)

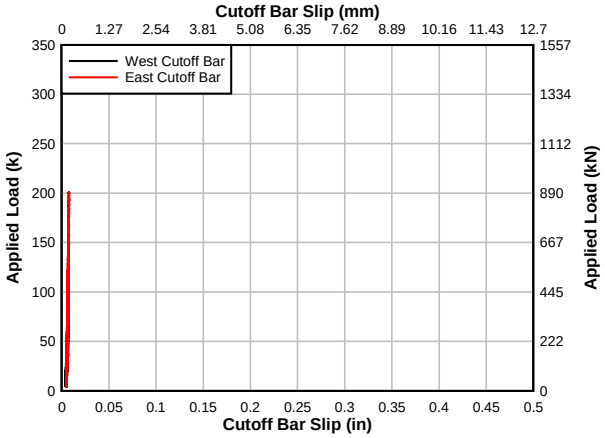

Fig. A.55 – Specimen T.45.Ld3.(5) load-cutoff bar slip (baseline test)

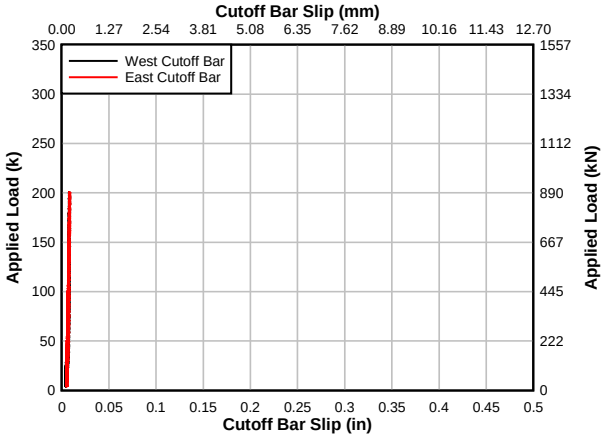

Fig. A.56 – Specimen T.45.Ld3.(5) load-cutoff bar slip (ext. stirrup test)

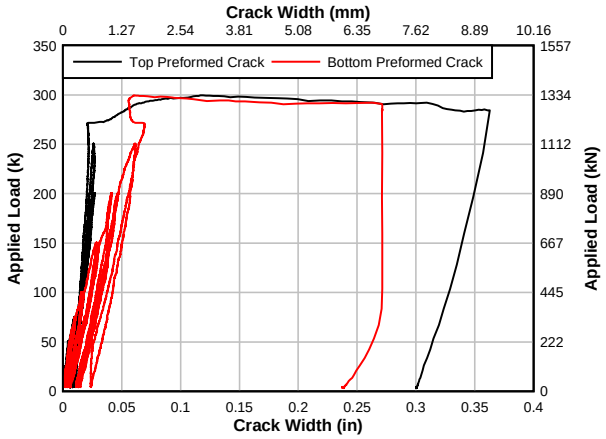

Fig. A.57 – Specimen T.45.Ld3.(5) load-preformed crack width (failure test)

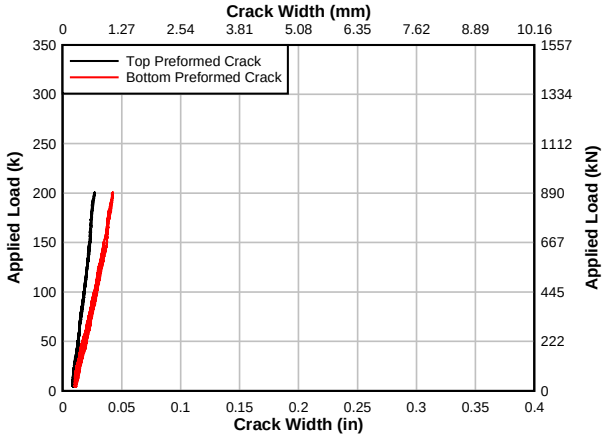

Fig. A.58 – Specimen T.45.Ld3.(5) load-preformed crack width (baseline test)

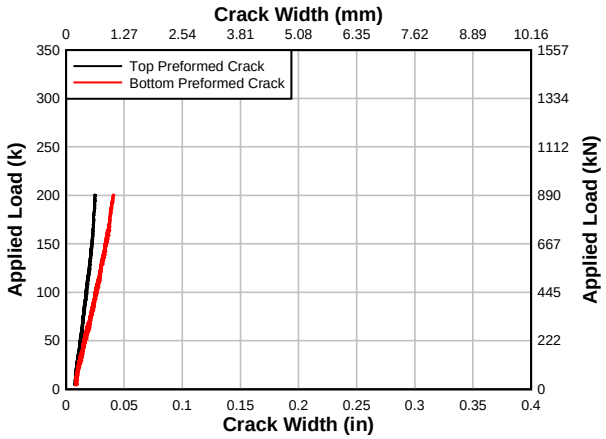

Fig. A.59 – Specimen T.45.Ld3.(5) load-preformed crack width (ext. stirrup test)

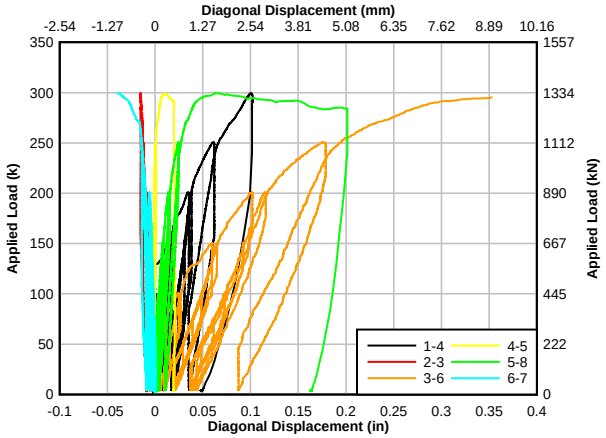

Fig. A.60 – Specimen T.45.Ld3.(5) load-diagonal displacement (failure test)

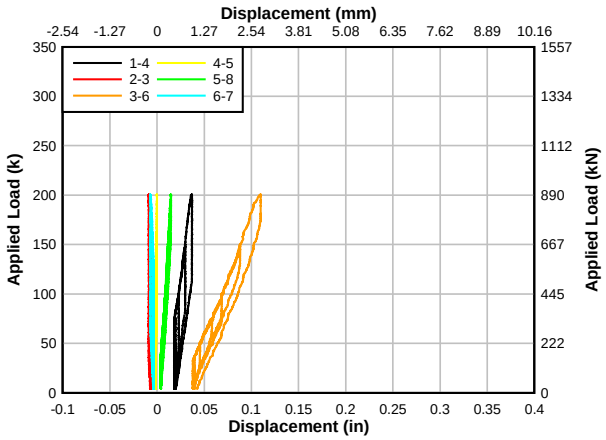

Fig. A.61 – Specimen T.45.Ld3.(5) load-diagonal displacement (baseline test)

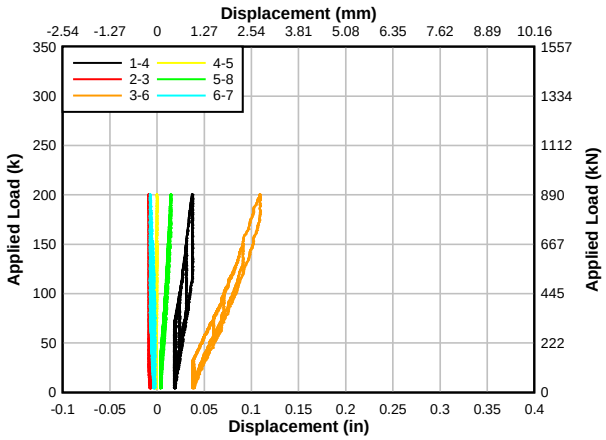

Fig. A.62 – Specimen T.45.Ld3.(5) load-diagonal displacement (ext. stirrup test)

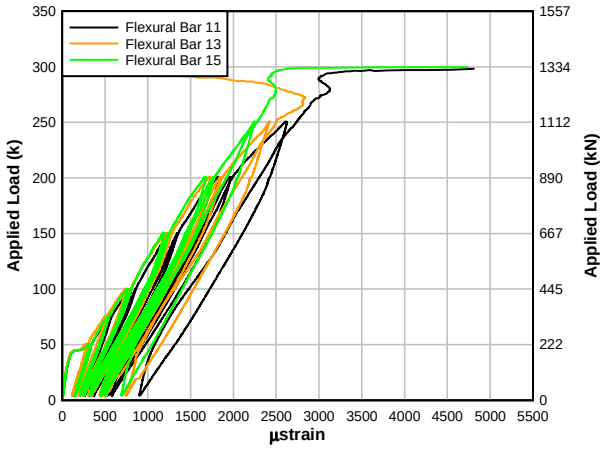

Fig. A.63 – Specimen T.45.Ld3.(5) load – flexural bar location 1 strain (failure test)

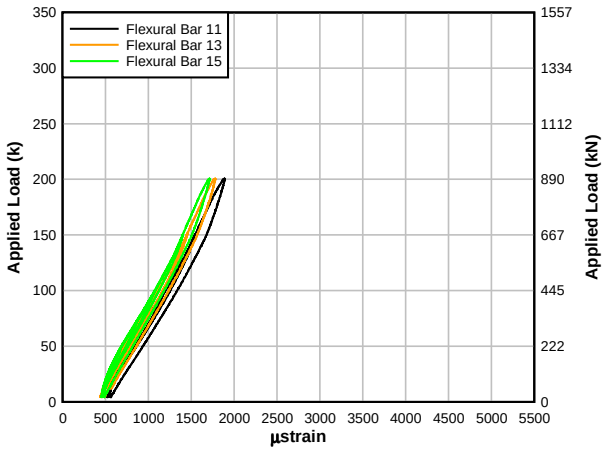

Fig. A.64 – Specimen T.45.Ld3.(5) load-flexural bar location 1 strain (baseline test)

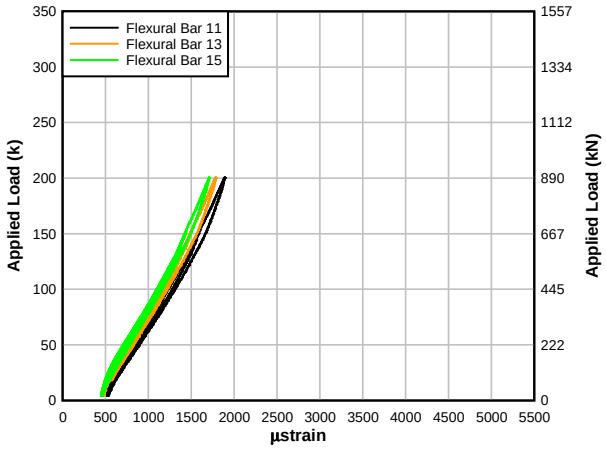

Fig. A.65 – Specimen T.45.Ld3.(5) load-flexural bar location 1 strain (ext. stirrup test)

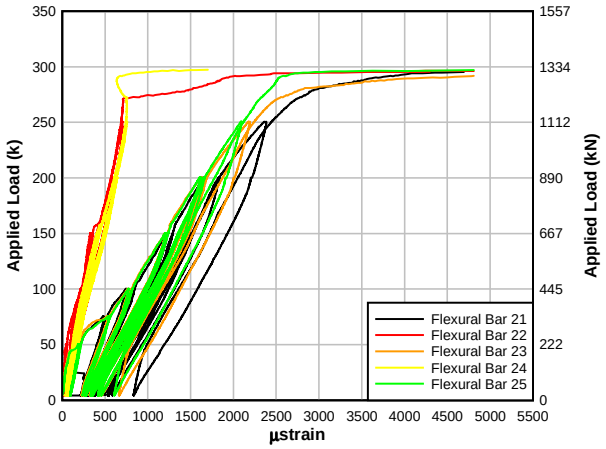

Fig. A.66 – Specimen T.45.Ld3.(5) load-flexural bar location 2 strain (failure test)

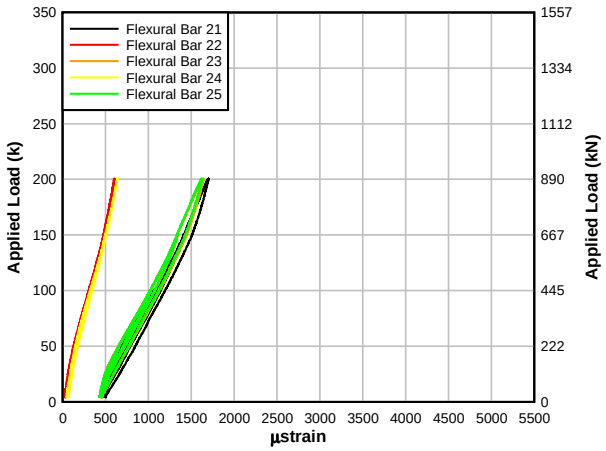

Fig. A.67 – Specimen T.45.Ld3.(5) load – flexural bar location 2 strain (baseline test)

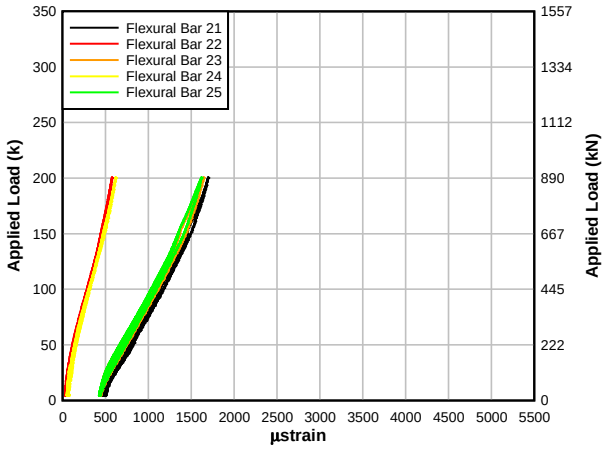

Fig. A.68 – Specimen T.45.Ld3.(5) load-lexural bar location 2 strain (ext. stirrup test)

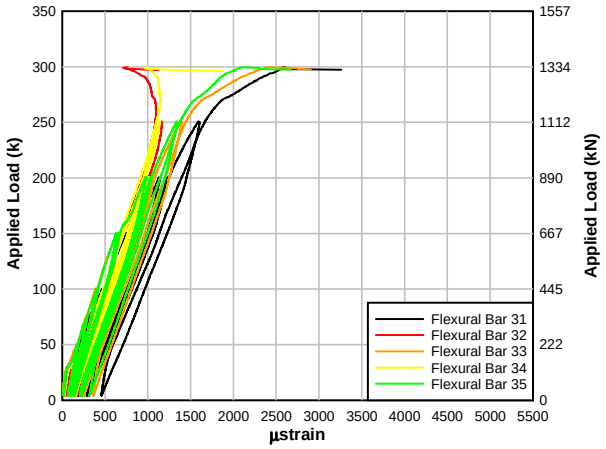

Fig. A.69 – Specimen T.45.Ld3.(5) load-flexural bar location 3 strain (failure test)

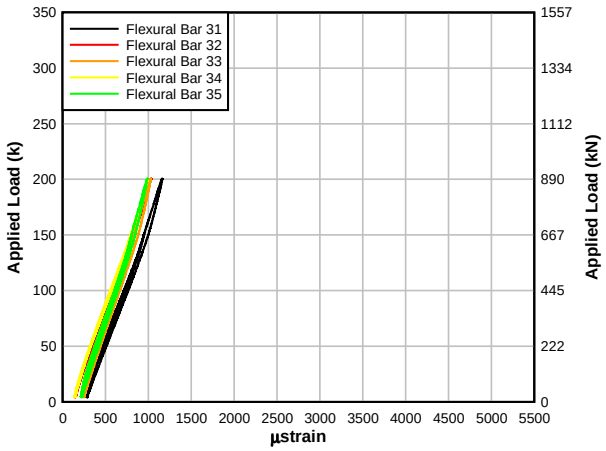

Fig. A.70 – Specimen T.45.Ld3.(5) load-flexural bar location 3 strain (baseline test)

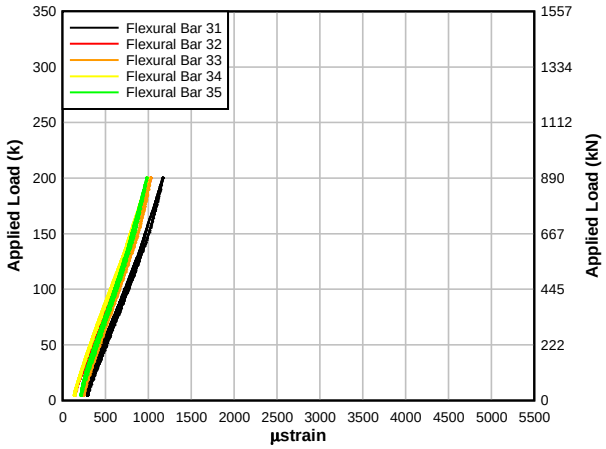

Fig. A.71 – Specimen T.45.Ld3.(5) load-flexural bar location 3 strain (ext. stirrup test)

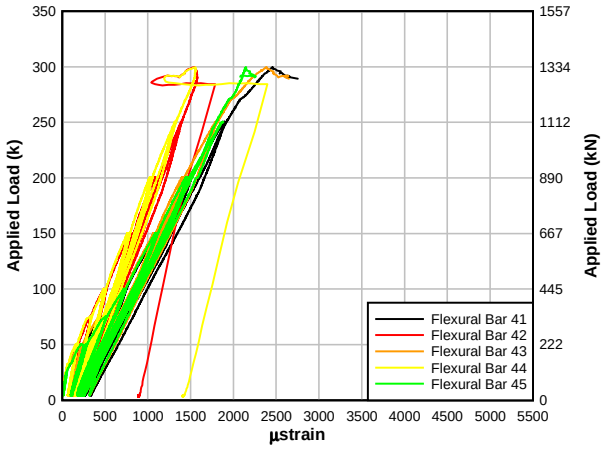

Fig. A.72 – Specimen T.45.Ld3.(5) load-flexural bar location 4 strain (failure test)

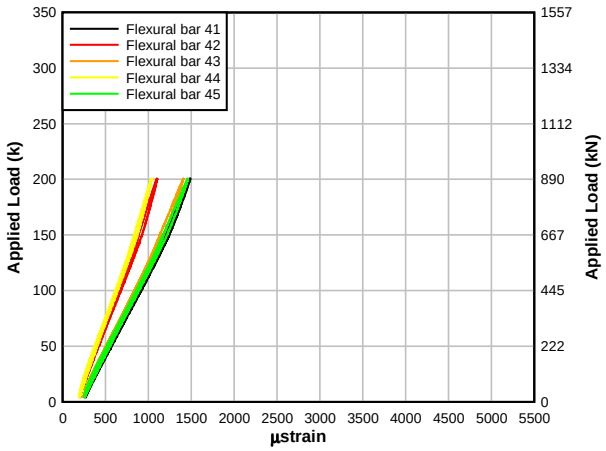

Fig. A.73 – Specimen T.45.Ld3.(5) load-flexural bar location 4 strain (baseline test)

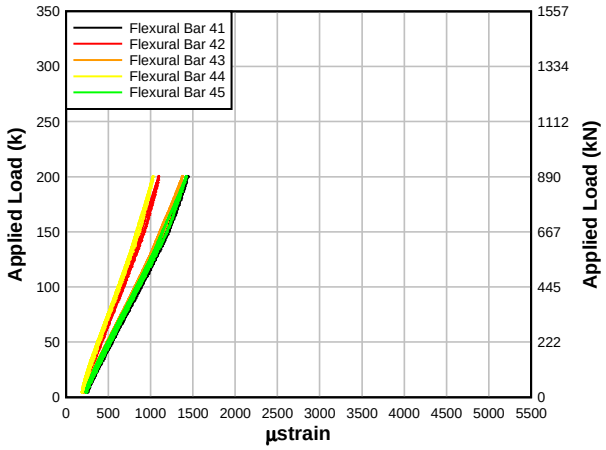

Fig. A.74 – Specimen T.45.Ld3.(5) load-flexural bar location 4 strain (ext. stirrup test)

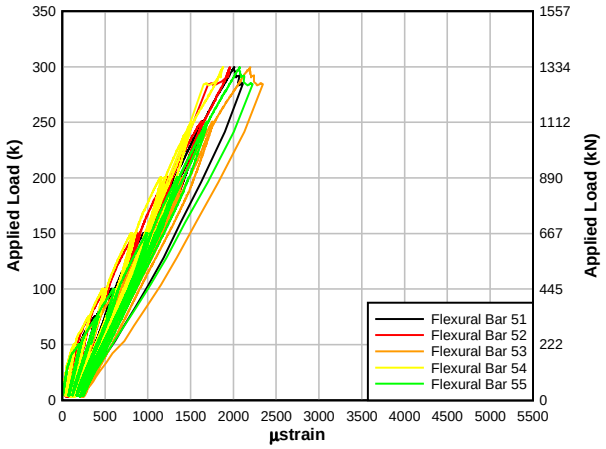

Fig. A.75 – Specimen T.45.Ld3.(5) load-flexural bar location 5 strain (failure test)

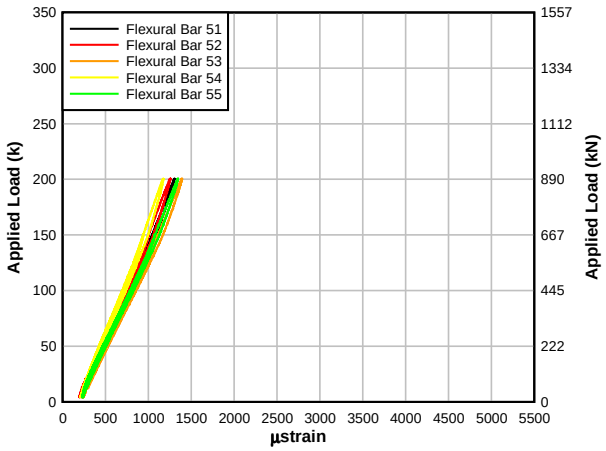

Fig. A.76 – Specimen T.45.Ld3.(5) load-flexural bar location 5 strain (baseline test)

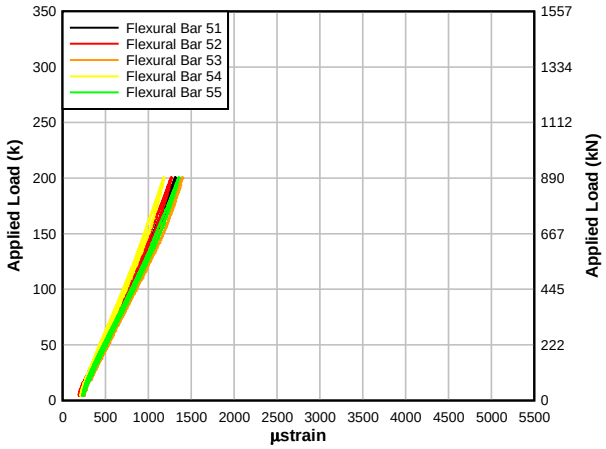

Fig. A.77 – Specimen T.45.Ld3.(5) load-flexural bar location 5 strain (ext. stirrup test)

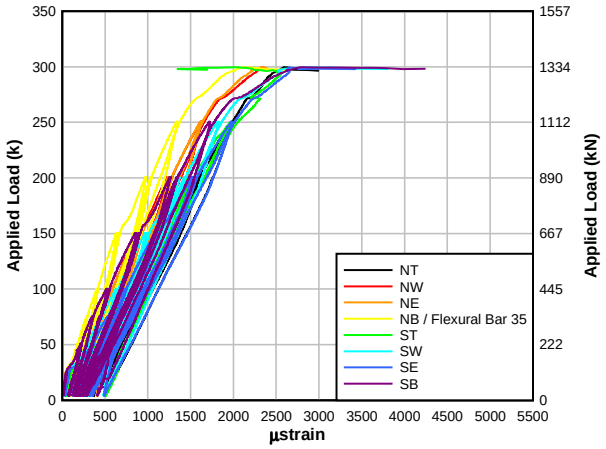

Fig. A.78 – Specimen T.45.Ld3.(5) load-dowel action stain (failure test)

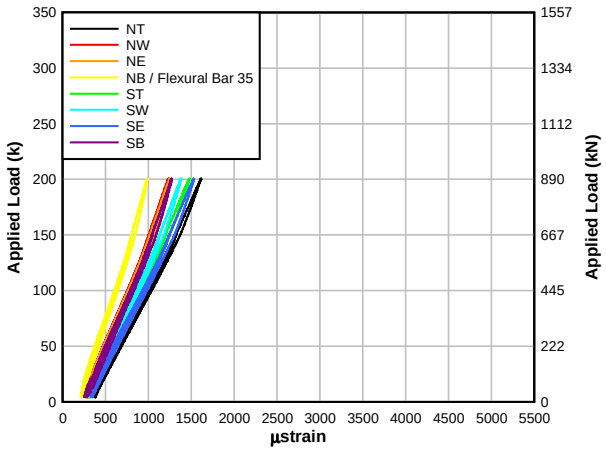

Fig. A.79 – Specimen T.45.Ld3.(5) load-dowel action stain (baseline test)

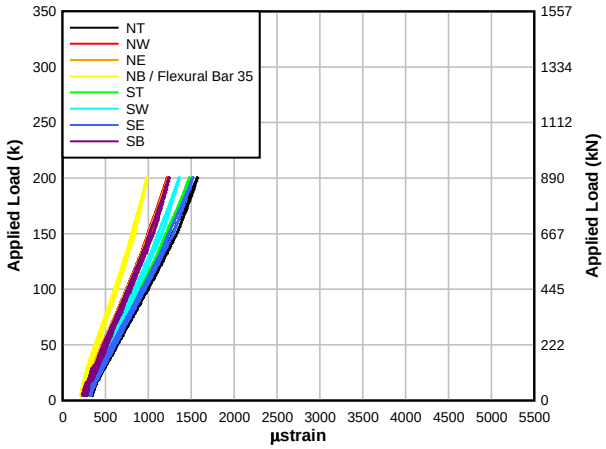

Fig. A.80 – Specimen T.45.Ld3.(5) load-dowel action stain (ext. stirrup test)

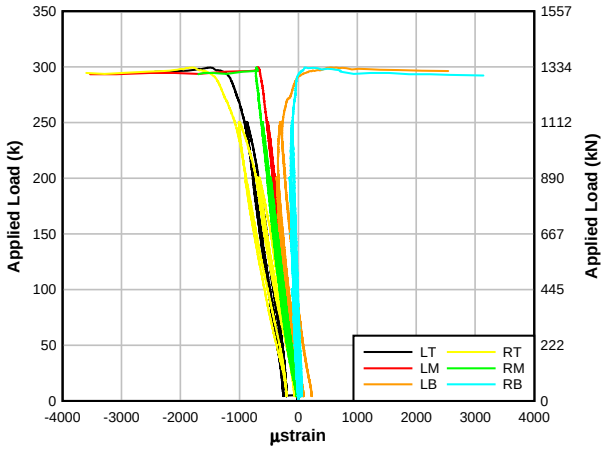

Fig. A.81 – Specimen T.45.Ld3.(5) load-concrete compression zone stain (failure test)

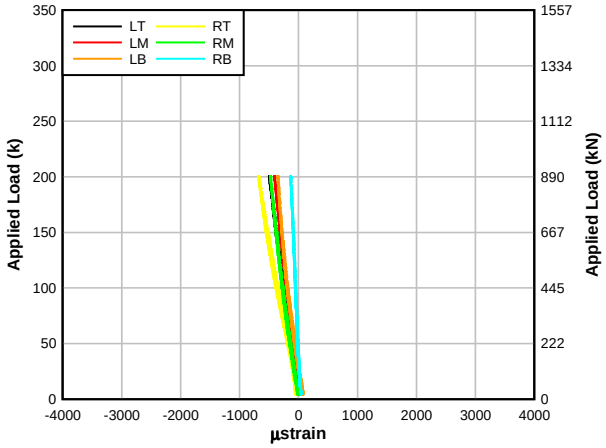

Fig. A.82 – Specimen T.45.Ld3.(5) load-concrete compression zone stain (baseline test)

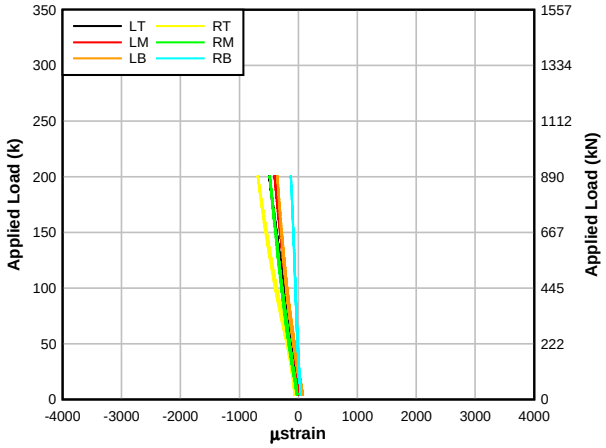

Fig. A.83 – Specimen T.45.Ld3.(5) load-concrete compression zone stain (ext. stirrup test)

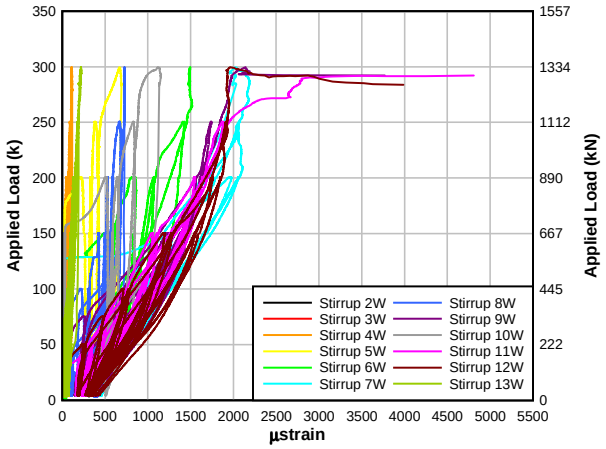

Fig. A.84 – Specimen T.45.Ld3.(5) load-west mid-height stirrup stain (failure test)

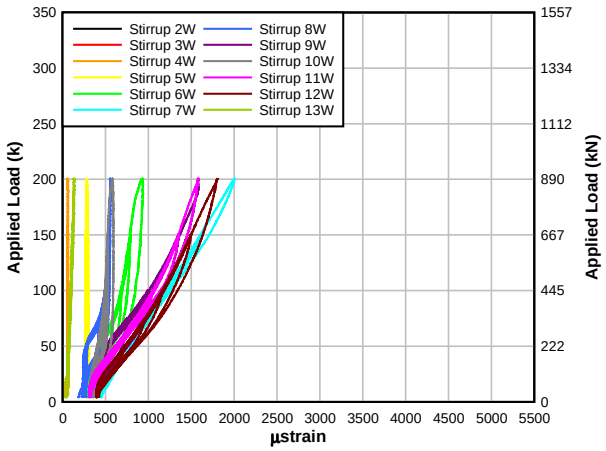

Fig. A.85 – Specimen T.45.Ld3.(5) load-west mid-height stirrup stain (baseline test)

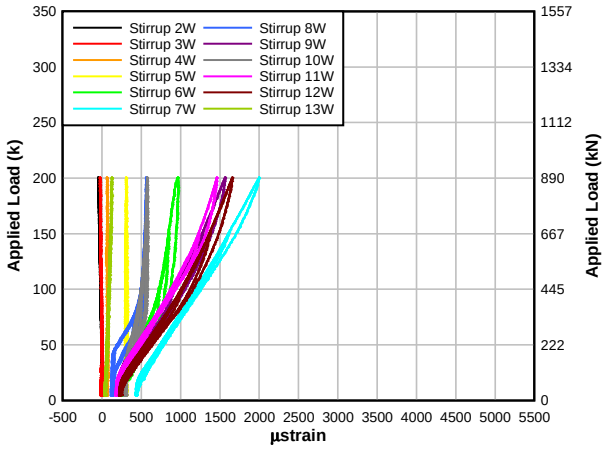

Fig. A.86 – Specimen T.45.Ld3.(5) load-west mid-height stirrup stain (ext. stirrup test)

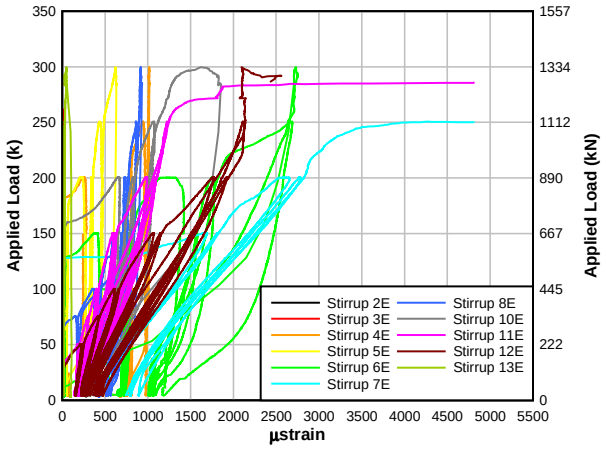

Fig. A.87 – Specimen T.45.Ld3.(5) load-east mid-height stirrup stain (failure test)

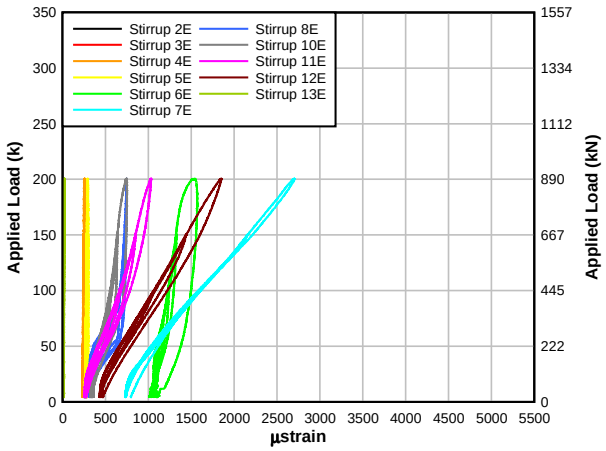

Fig. A.88 – Specimen T.45.Ld3.(5) load-east mid-height stirrup stain (baseline test)

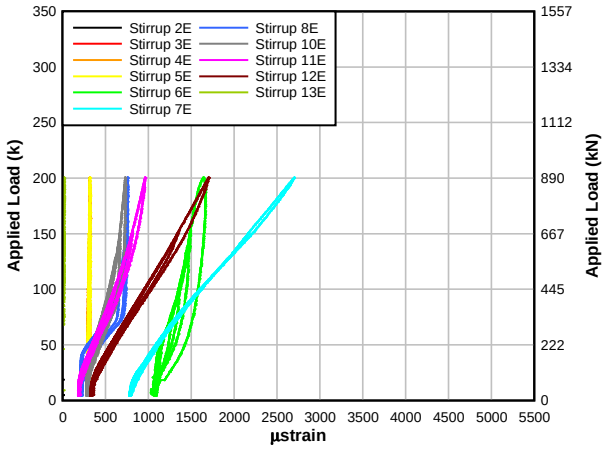

Fig. A.89 – Specimen T.45.Ld3.(4) load-east mid-height stirrup stain (ext. stirrup test)

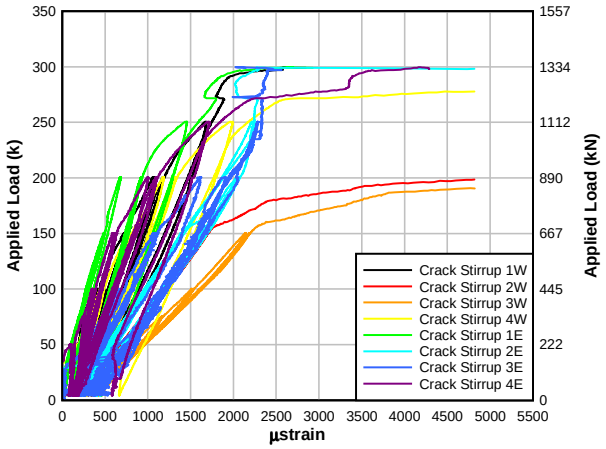

Fig. A.90 – Specimen T.45.Ld3.(5) load-preformed crack stirrup stain (failure test)

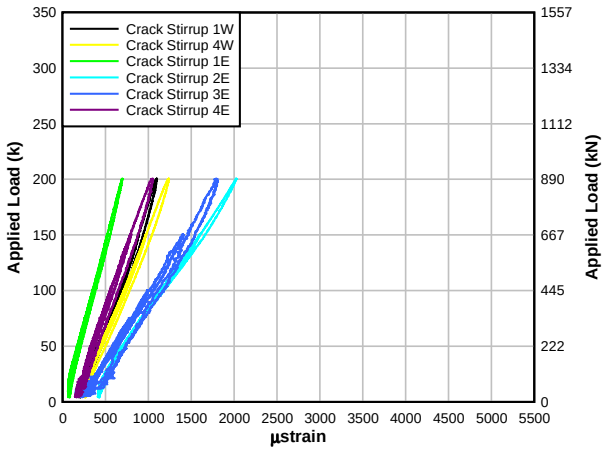

Fig. A.91 – Specimen T.45.Ld3.(5) load-preformed crack stirrup stain (baseline test)

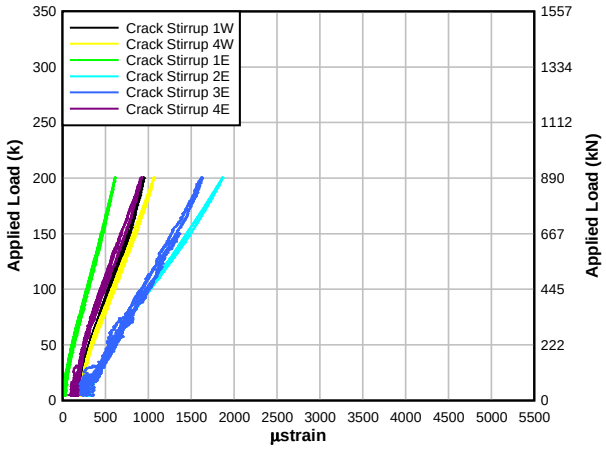

Fig. A.92 – Specimen T.45.Ld3.(5) load-preformed crack stirrup stain (ext. stirrup test)

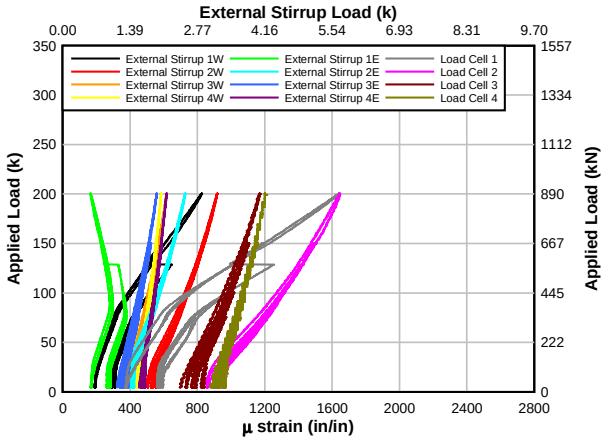

Fig. A.93 – Specimen T.45.Ld3.(5) load-external stirrup strain/load (ext. stirrup test)

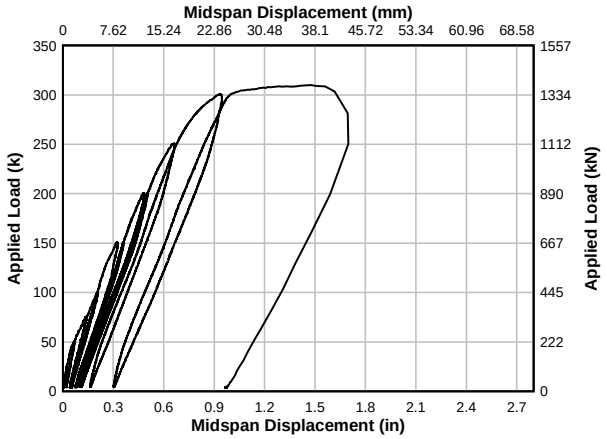

Fig. A.94 – Specimen T.60.Ld3.(5) load-midspan displacement (failure test)

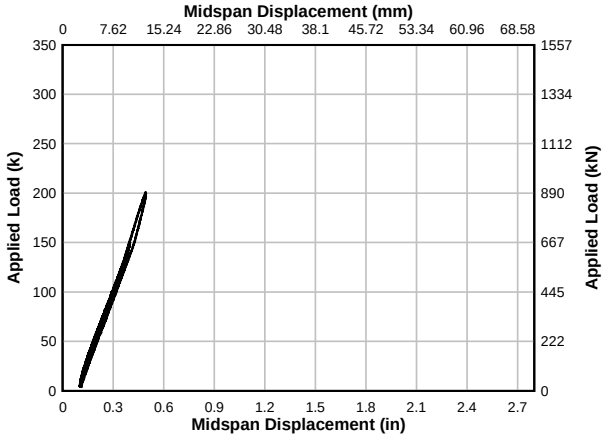

Fig. A.95 – Specimen T.60.Ld3.(5) load-midspan displacement (baseline test)

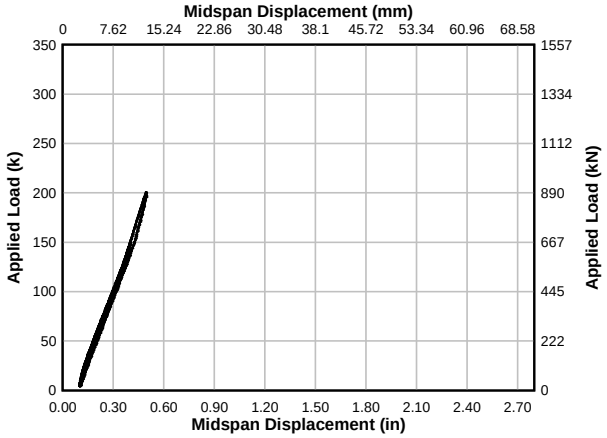

Fig. A.96 – Specimen T.60.Ld3.(5) load-midspan displacement (ext. stirrup test)

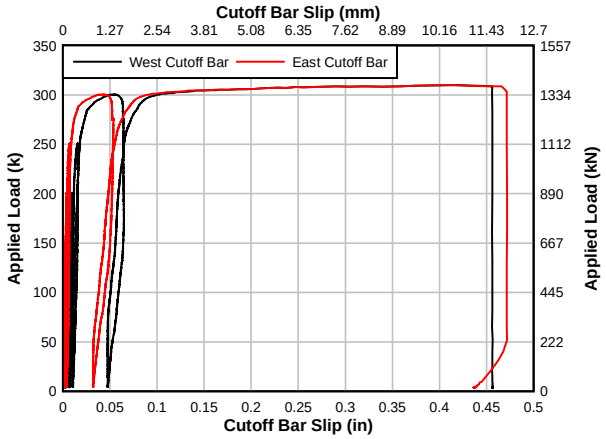

Fig. A.97 – Specimen T. 60.Ld3.(5) load-cutoff bar slip (failure test)

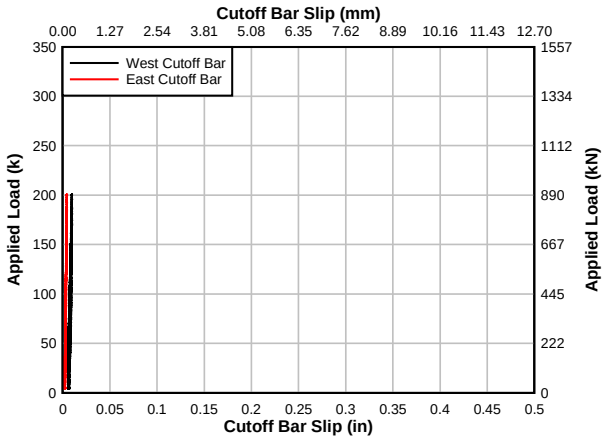

Fig. A.98 – Specimen T.60.Ld3.(5) load-cutoff bar slip (baseline test)

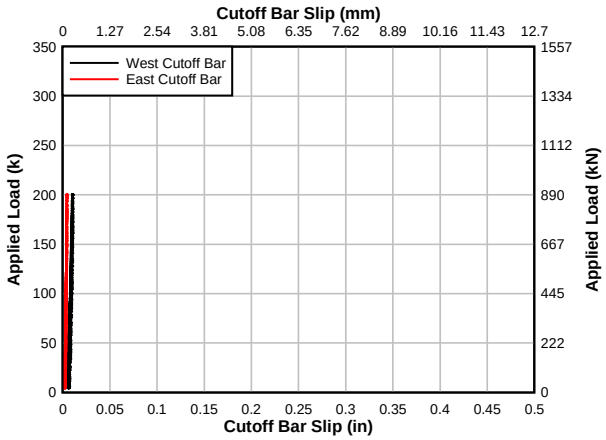

Fig. A.99 – Specimen T.60.Ld3.(5) load-cutoff bar slip (ext. stirrup test)

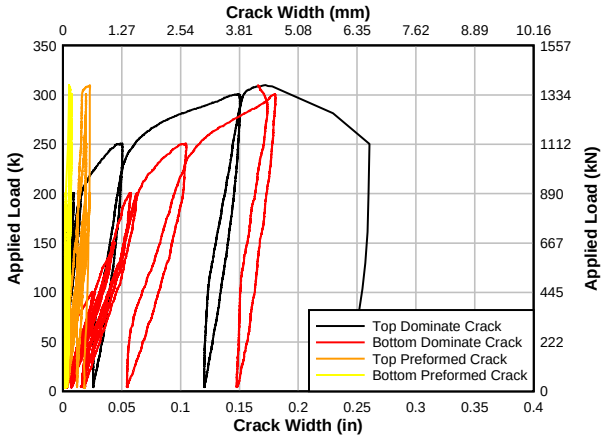

Fig. A.100 – Specimen T.60.Ld3.(5) load-crack width (failure test)

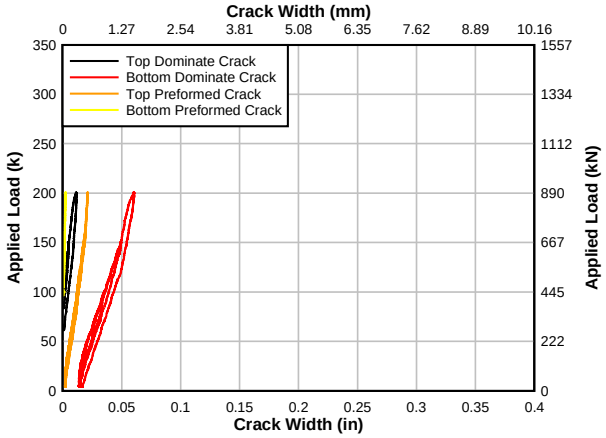

Fig. A.101 – Specimen T.60.Ld3.(5) load-crack width (baseline test)

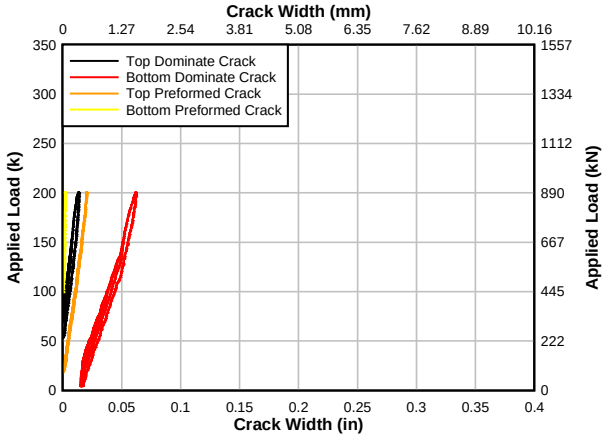

Fig. A.102 – Specimen T.60.Ld3.(5) load-crack width (ext. stirrup test)

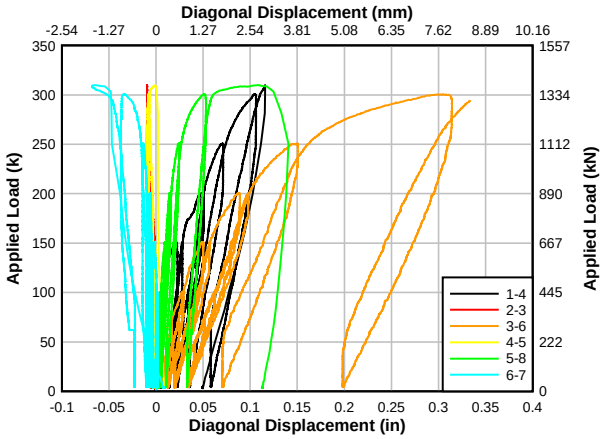

Fig. A.103 – Specimen T.60.Ld3.(5) load-diagonal displacement (failure test)

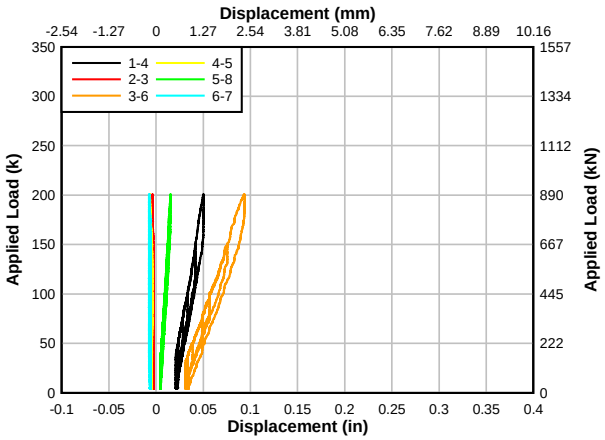

Fig. A.104 – Specimen T.60.Ld3.(5) load-diagonal displacement (baseline test)

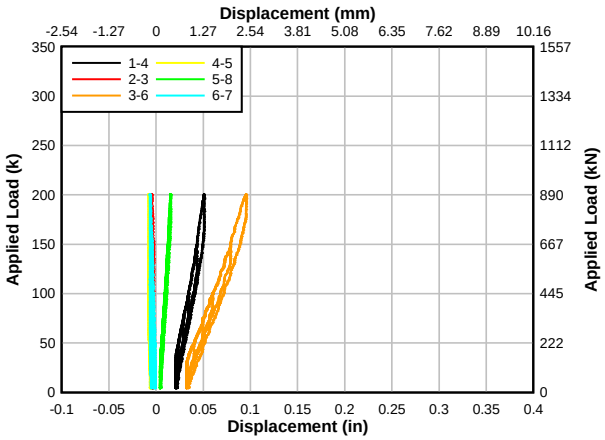

Fig. A.105 – Specimen T.60.Ld3.(5) load-diagonal displacement (ext. stirrup test)

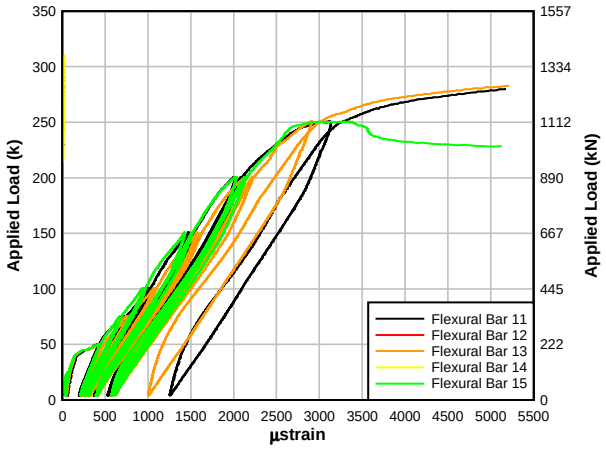

Fig. A.106 – Specimen T.60.Ld3.(5) load-flexural bar location 1 strain (failure test)

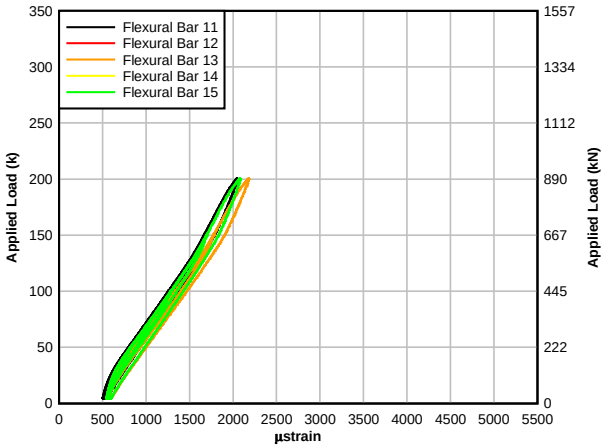

Fig. A.107 – Specimen T.60.Ld3.(5) load-flexural bar location 1 strain (baseline test)

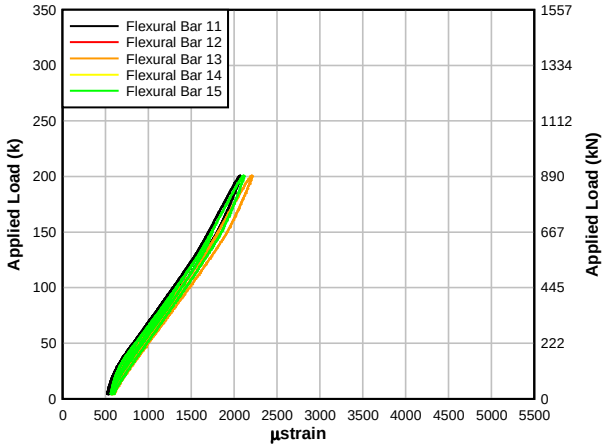

Fig. A.108 – Specimen T.60.Ld3.(5) load-flexural bar location 1 strain (ext. stirrup test)

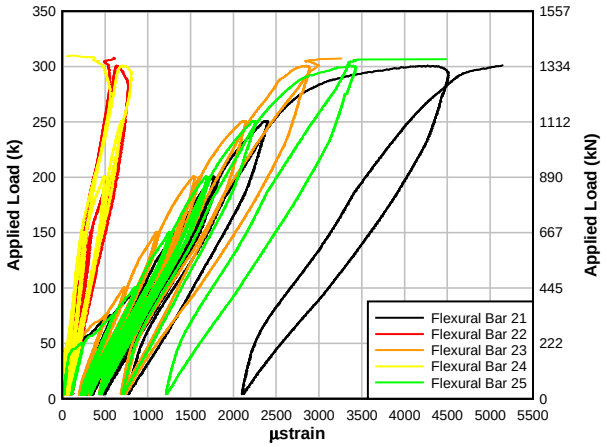

Fig. A.109 – Specimen T.60.Ld3.(5) load-flexural bar location 2 strain (failure test)

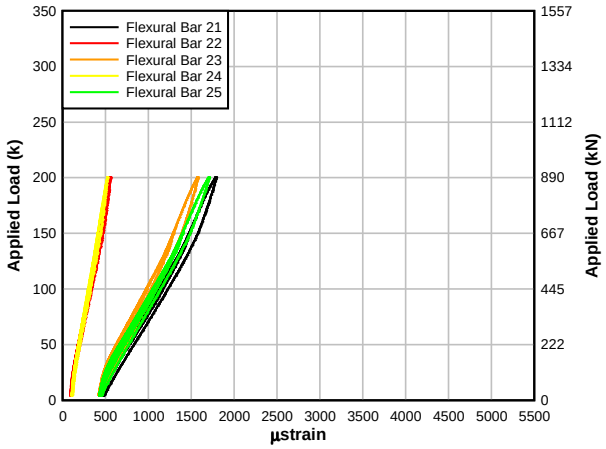

Fig. A.110 – Specimen T.60.Ld3.(5) load-flexural bar location 2 strain (baseline test)

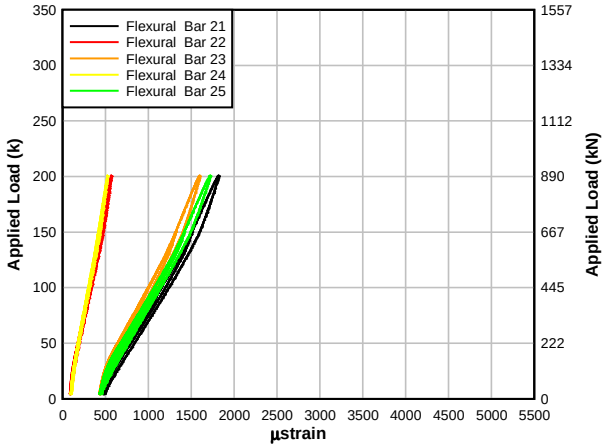

Fig. A.111 – Specimen T.60.Ld3.(5) load-flexural bar location 2 strain (ext. stirrup test)

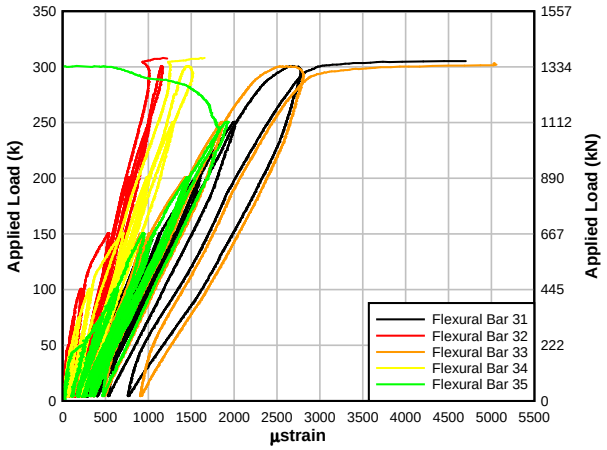

Fig. A.112 – Specimen T.60.Ld3.(5) load-flexural bar location 3 strain (failure test)

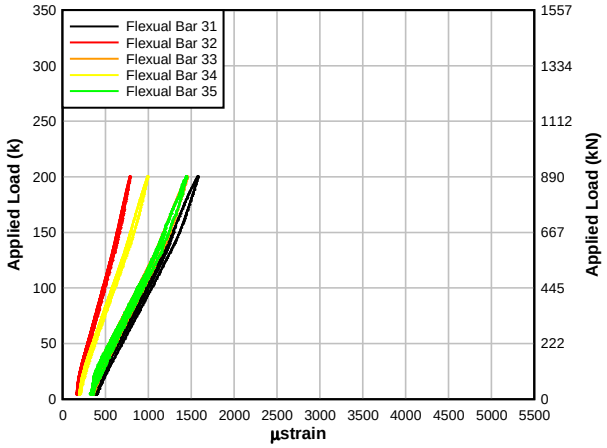

Fig. A.113 – Specimen T.60.Ld3.(5) load-flexural bar location 3 strain (baseline test)

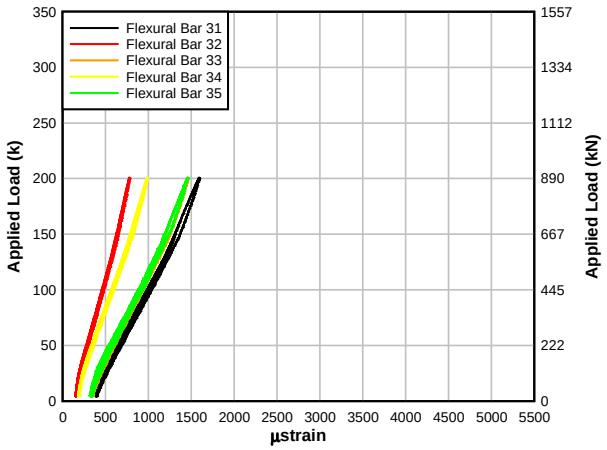

Fig. A.114 – Specimen T.60.Ld3.(5) load-flexural bar location 3 strain (ext. stirrup test)

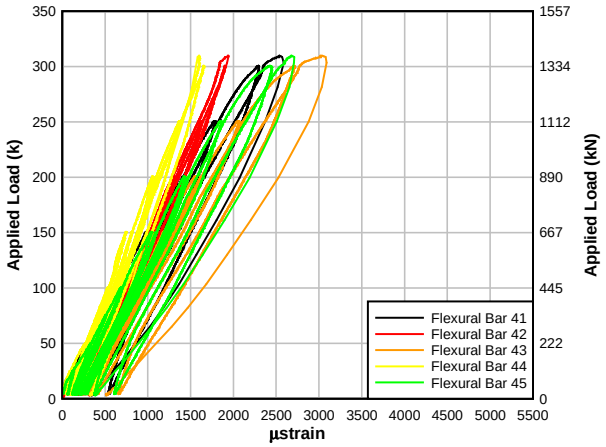

Fig. A.115 – Specimen T.60.Ld3.(5) load-flexural bar location 4 strain (failure test)

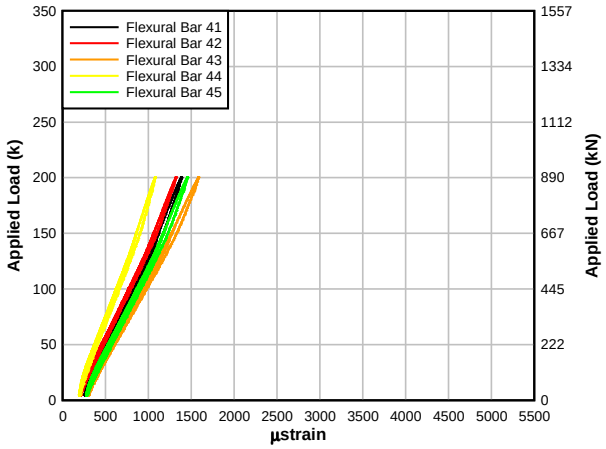

Fig. A.116 – Specimen T.60.Ld3.(5) load-flexural bar location 4 strain (baseline test)

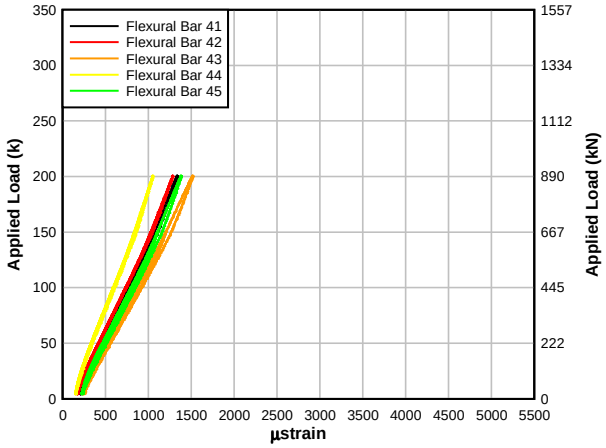

Fig. A.117 – Specimen T.60.Ld3.(5) load-flexural bar location 4 strain (ext. stirrup test)

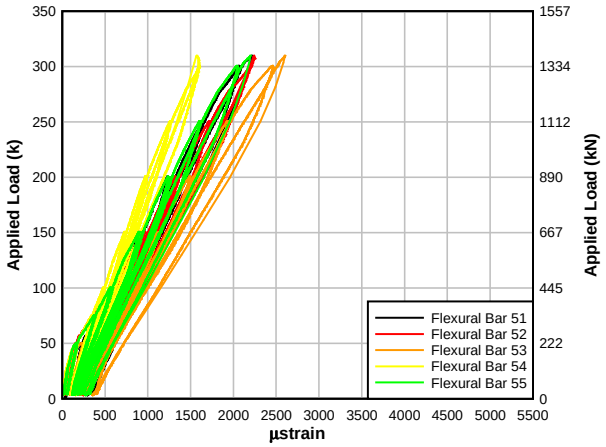

Fig. A.118 – Specimen T.60.Ld3.(5) load-flexural bar location 5 strain (failure test)

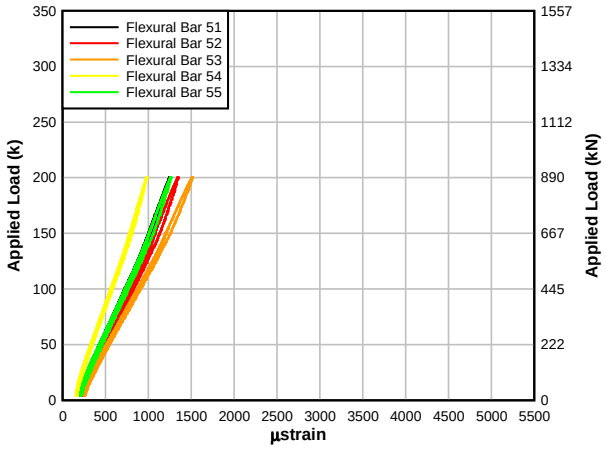

Fig. A.119 – Specimen T.60.Ld3.(5) load-flexural bar location 5 strain (baseline test)

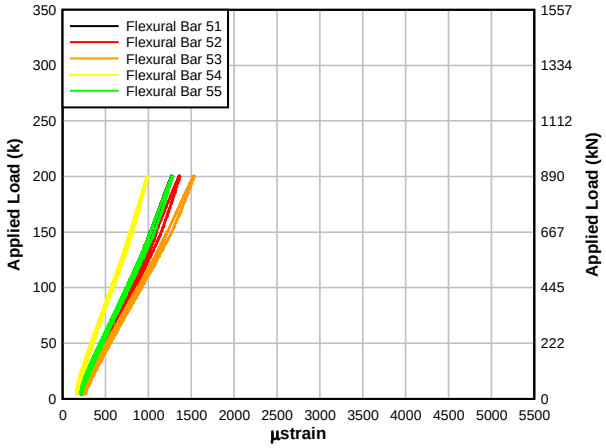

Fig. A.120 – Specimen T.60.Ld3.(5) load-flexural bar location 5 strain (ext. stirrup test)

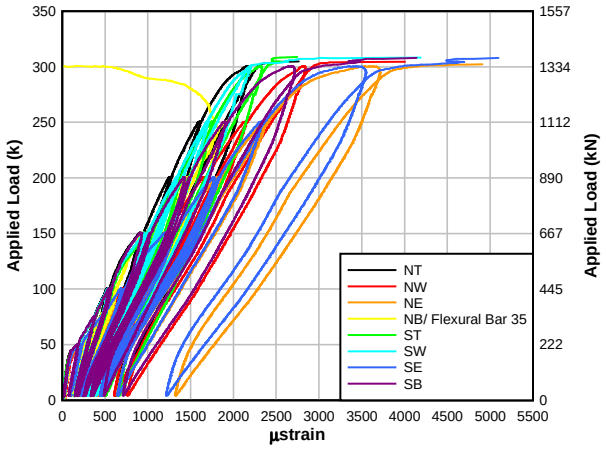

Fig. A.121 – Specimen T.60.Ld3.(5) load-dowel action stain (failure test)

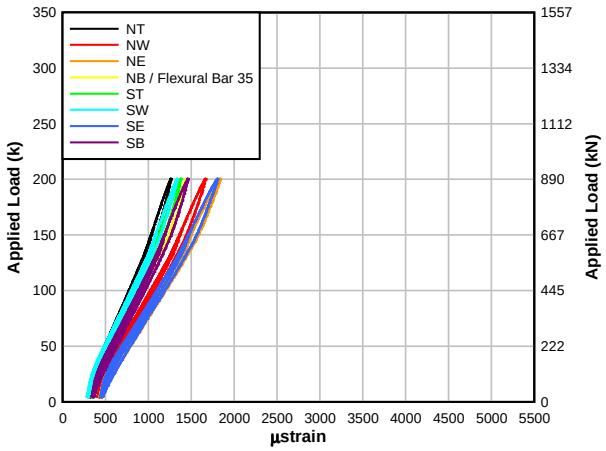

Fig. A.122 – Specimen T.60.Ld3.(5) load-dowel action stain (baseline test)

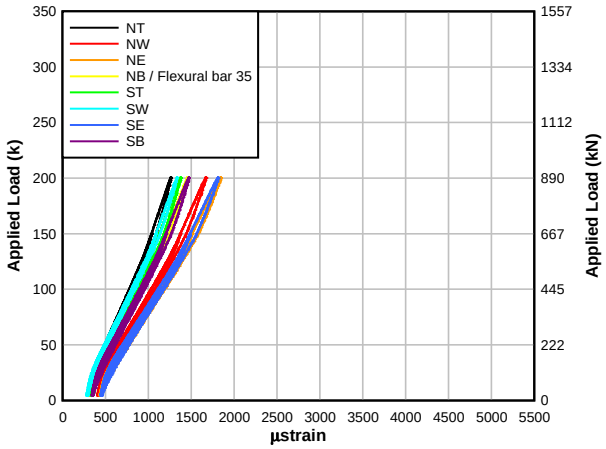

Fig. A.123 – Specimen T.60.Ld3.(5) load-dowel action stain (ext. stirrup test)

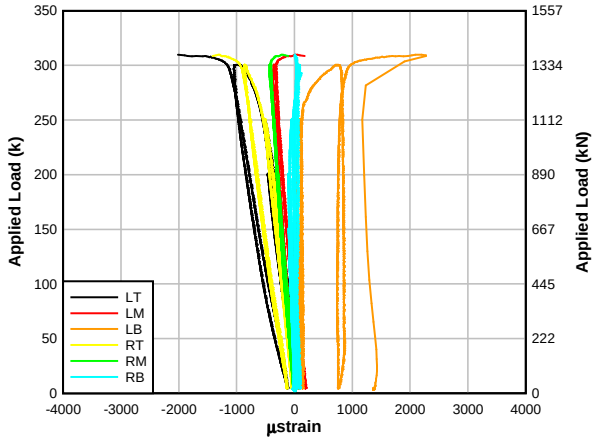

Fig. A.124 – Specimen T.60.Ld3.(5) load-concrete compression zone stain (failure test)

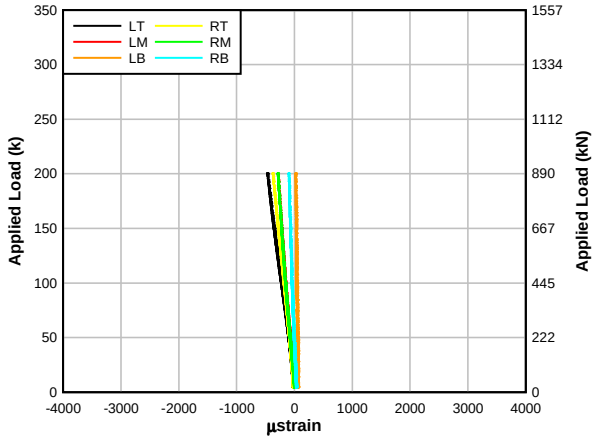

Fig. A.125 – Specimen T.60.Ld3.(5) load-concrete compression zone stain (baseline test)

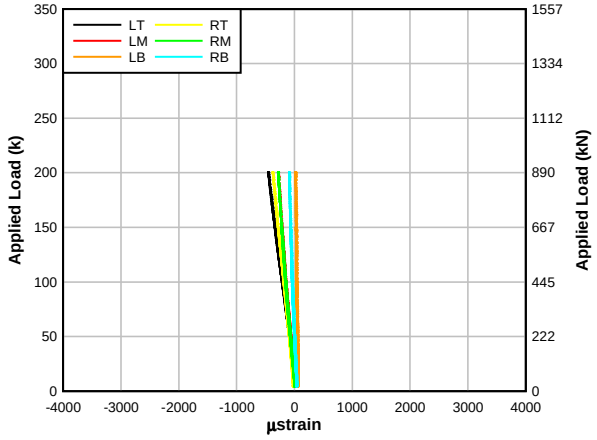

Fig. A.126 – Specimen T.60.Ld3.(5) load-concrete compression zone stain (ext. stirrup test)

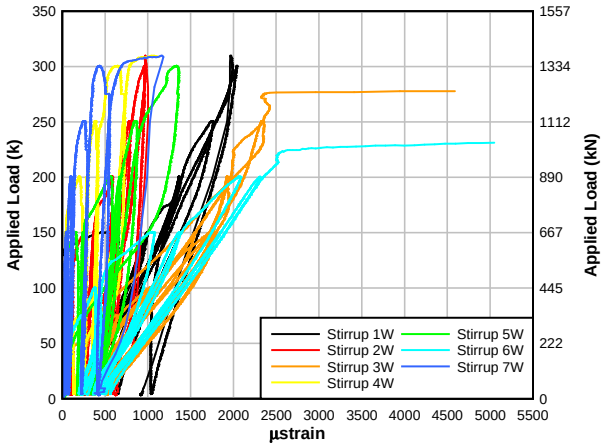

Fig. A.127 – Specimen T.60.Ld3.(5) load-west mid-height stirrup stain (failure test)

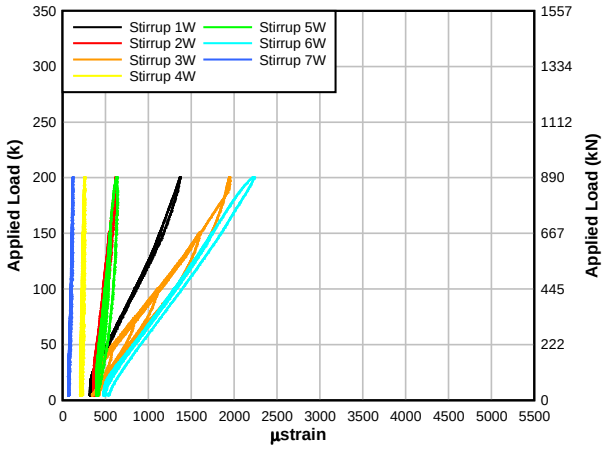

Fig. A.128 – Specimen T.60.Ld3.(5) load-west mid-height stirrup stain (baseline test)

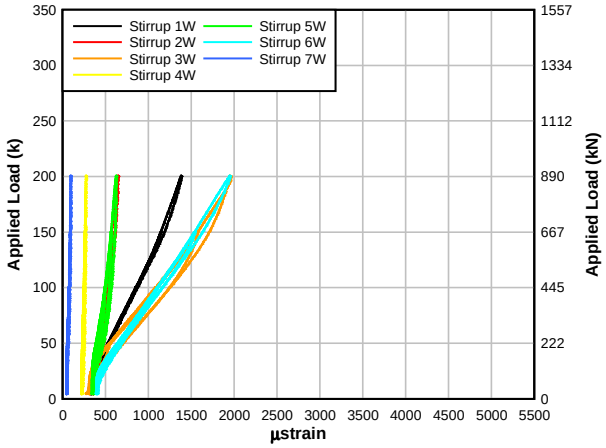

Fig. A.129 – Specimen T.60.Ld3.(5) load-west mid-height stirrup stain (ext. stirrup test)

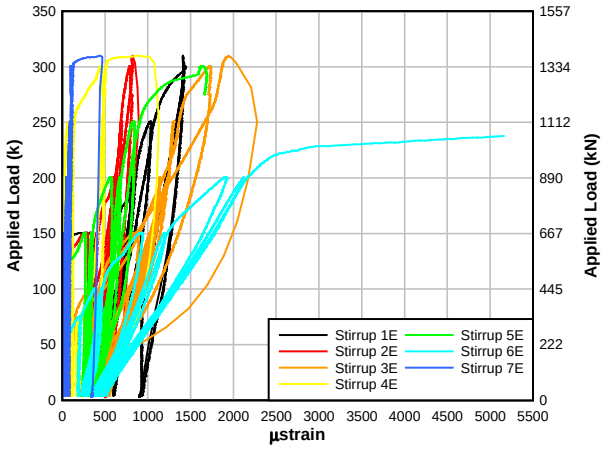

Fig. A.130 – Specimen T.60.Ld3.(5) load-east mid-height stirrup stain (failure test)

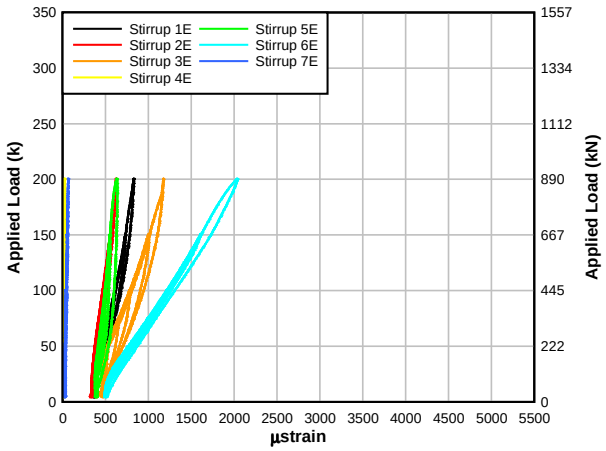

Fig. A.131 – Specimen T.60.Ld3.(5) load-east mid-height stirrup stain (baseline test)

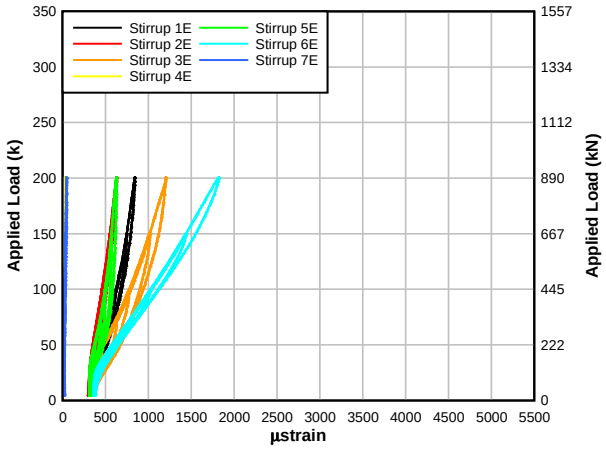

Fig. A.132 – Specimen T.60.Ld3.(5) load-east mid-height stirrup stain (ext. stirrup test)

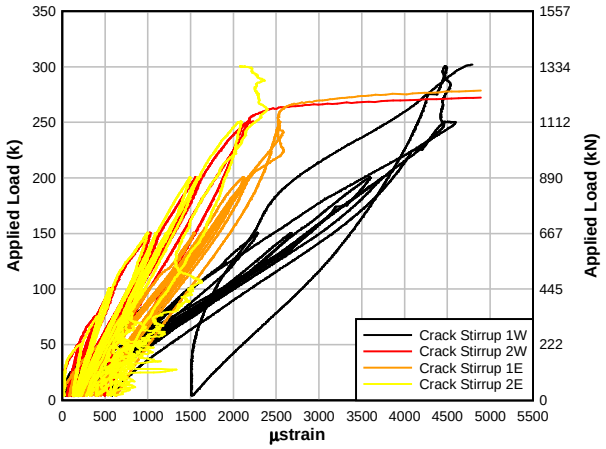

Fig. A.133 – Specimen T.60.Ld3.(5) load-preformed crack stirrup stain (failure test)

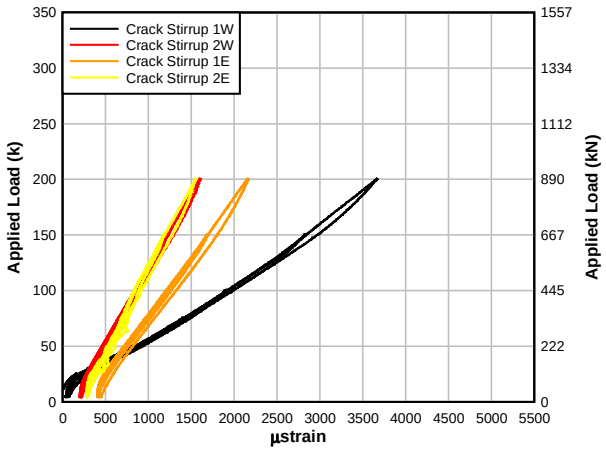

Fig. A.134 – Specimen T.60.Ld3.(5) load-preformed crack stirrup stain (baseline test)

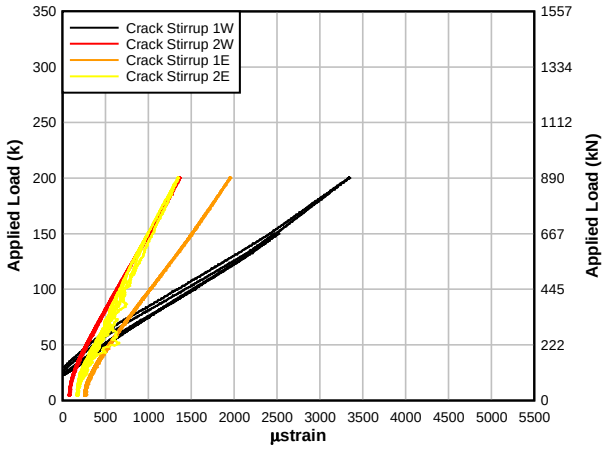

Fig. A.135 – Specimen T.60.Ld3.(5) load-preformed crack stirrup stain (ext. stirrup test)

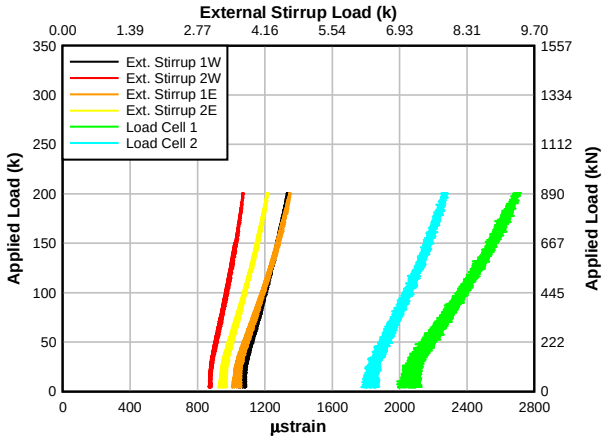

Fig. A.136 – Specimen T.60.Ld3.(5) load-external stirrup strain/load (ext. stirrup test)

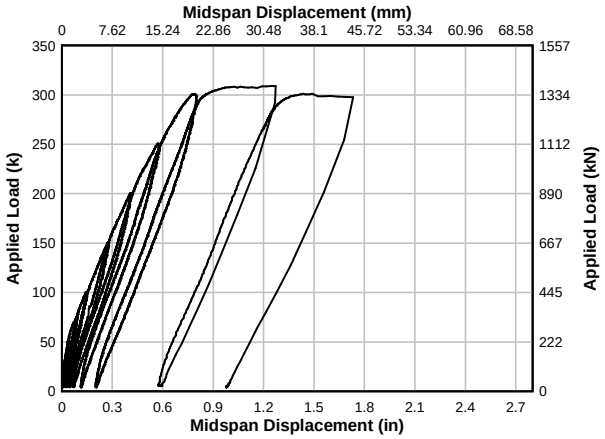

Fig. A.137 – Specimen T.0.Ld3.(5) load-midspan displacement (failure test)

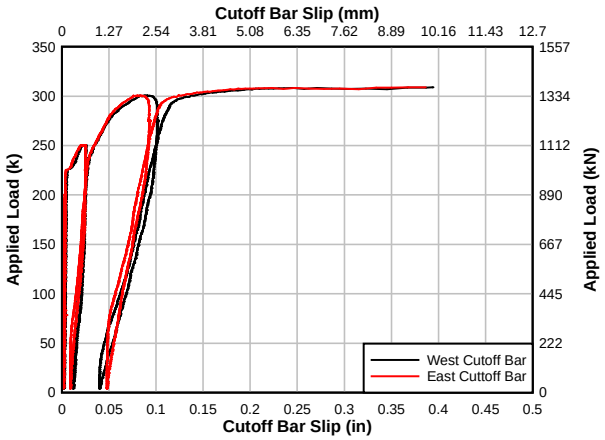

Fig. A.138 – Specimen T.0.Ld3.(5) load-cutoff bar slip (failure test)

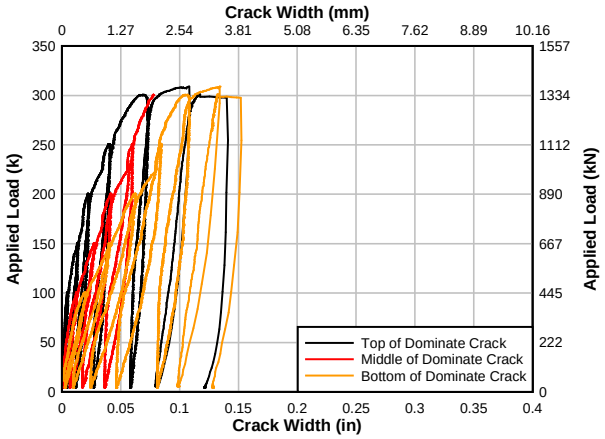

Fig. A.139 – Specimen T.0.Ld3.(5) load-crack width (failure test)

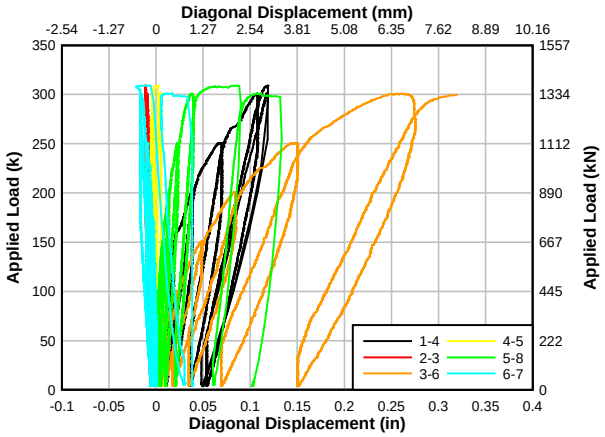

Fig. A.140 – Specimen T.0.Ld3.(5) load-diagonal displacement (failure test)

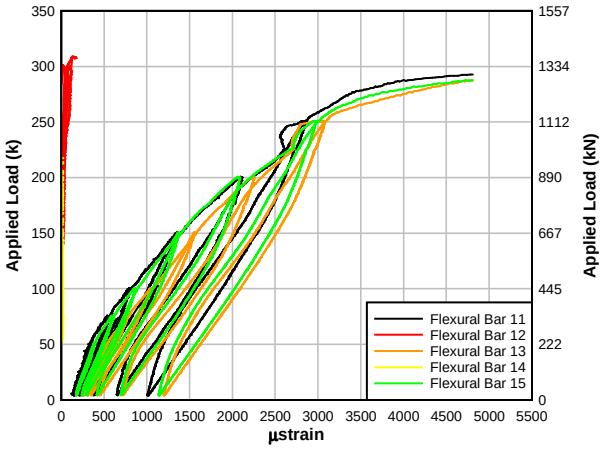

Fig. A.141 – Specimen T.0.Ld3.(5) load-flexural bar location 1 stain (failure test)

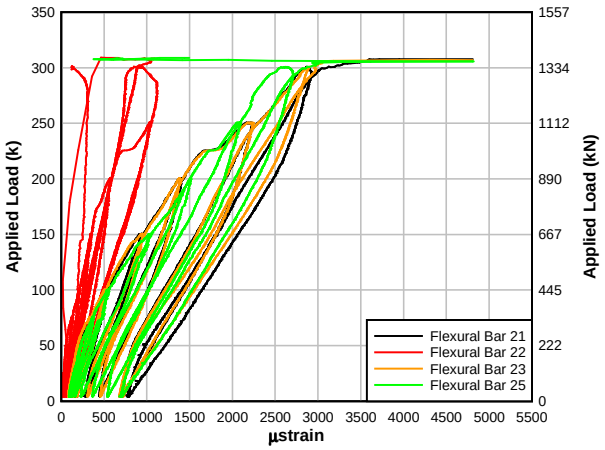

Fig. A.142 – Specimen T.0.Ld3.(5) load-flexural bar location 2 stain (failure test)

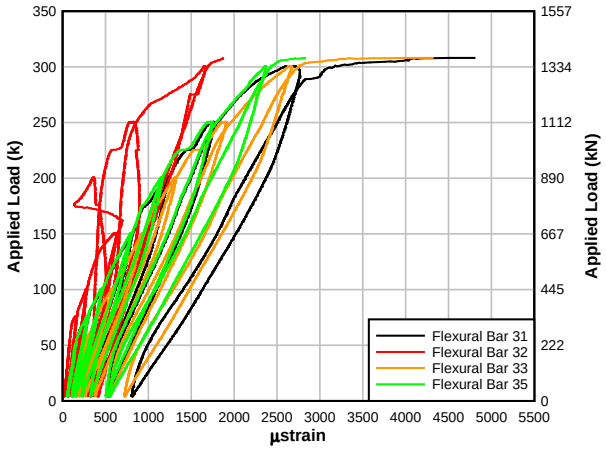

Fig. A.143 – Specimen T.0.Ld3.(5) load-flexural bar location 3 stain (failure test)

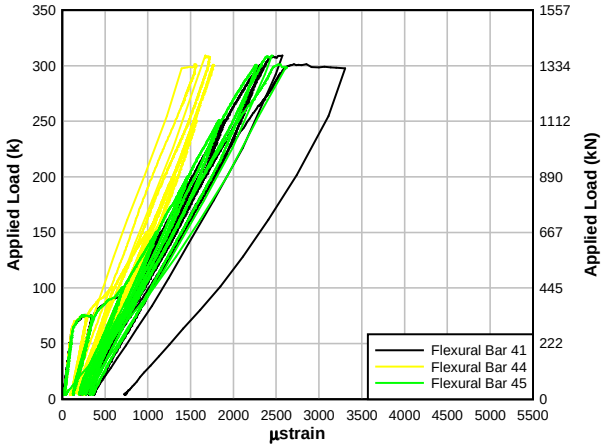

Fig. A.144 – Specimen T.0.Ld3.(5) load-flexural bar location 4 stain (failure test)

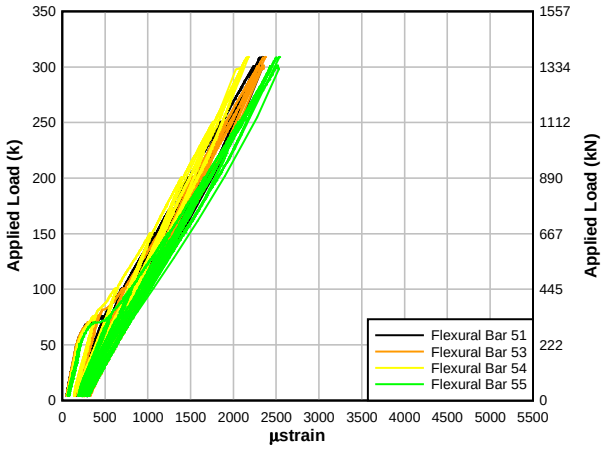

Fig. A.145 – Specimen T.0.Ld3.(5) load-flexural bar location 5 stain (failure test)

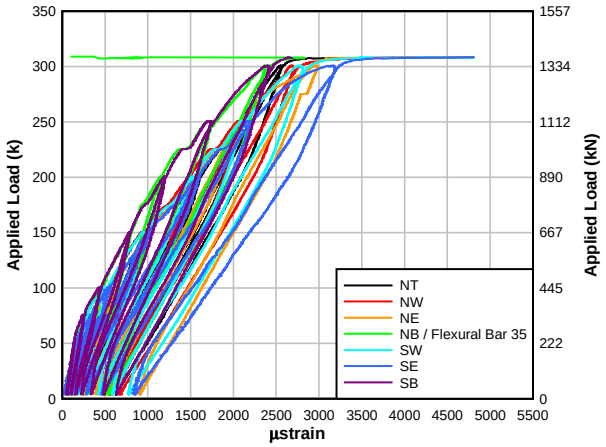

Fig. A.146 – Specimen T.0.Ld3.(5) load-dowel action stain (failure test)

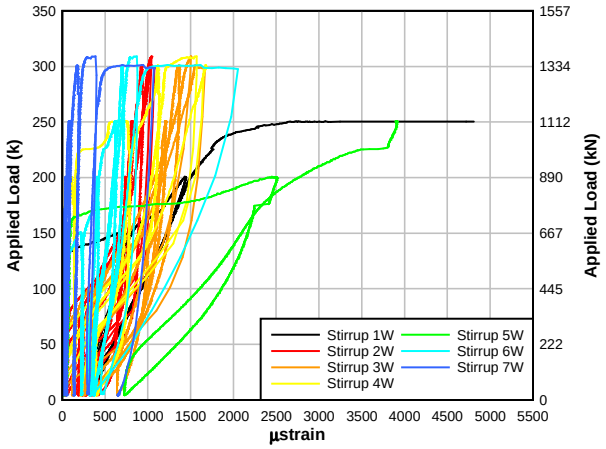

Fig. A.147 – Specimen T.0.Ld3.(5) load-west mid-height stirrup stain (failure test)

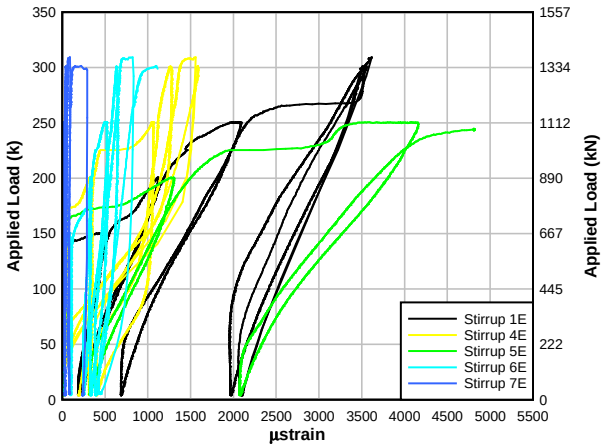

Fig. A.148 – Specimen T.0.Ld3.(5) load-east mid-height stirrup stain (failure test)

APPENDIX B – CONCRETE COMPRESSION ZONE SHEAR TRANSFER

The shear transfer in the compression zone of three of the specimens was calculated based on the experimental method described by Sherwood (2008). Just prior to failure, Sherwood applied two columns of strain gages near the head of the dominate shear crack in a reinforced concrete beam that did not have stirrups. The test program T-beams also received this pattern of gages as described in Section *3.5.2 External Sensor Array*. The experimental concrete compression shear force results are reported in Fig. 4.12 to 4.15 in Section *4.2.1 Standard Test Comparison*.

The longitudinal concrete strains, μ_x, from each column of gages were converted to flexural compressive stresses, C_x, where:

$$C_x = E_c \mu_x \qquad \text{[B.1]}$$

and where E_c is Young's Modulus for normal weight concrete and may be taken as:

$$E_c = 1820\sqrt{f_c^{'}} \qquad \text{AASHTO-LRFD C5.4.24-1} \qquad \text{[B.2]}$$

where E_c and $f_c^{'}$ are both in ksi.

Assuming a linear flexural compressive stress profile, an incremental slice of compressive stress at any height, σC_x, maybe determined as:

$$\sigma C_x = mh + c \qquad \text{[B.3]}$$

where m is the slope of the stress profile, c is the neutral axis intercept, and h is the depth at which the stresses are being considered. A depth of zero is the extreme compression fiber.

Similarly, the slice approach is used to find the change in stress across the crack at any height, $\delta\sigma C$, in the compression zone by the following calculation:

$$\delta\sigma C = \sigma C_L - \sigma C_R \quad \text{[B.4]}$$

The incremental compressive force carried by the compression zone, $\delta\Delta C$, is:

$$\delta\Delta C = \frac{\delta\sigma C_i - \delta\sigma C_{i-1}}{2}\left(h_i - h_{i-1}\right)b \quad \text{[B.5]}$$

The longitudinal shear stress transferred by each slice, δv_{cz}, is dependent on the width of the compression zone, b, and the center-to-center gage spacing, s, such that:

$$\delta v_{cz} = \frac{\delta\Delta C}{bs} \quad \text{[B.6]}$$

Therefore, the total longitudinal shear stress between the top of the beam and the slice in questions, $\Sigma\delta v_{cz}$, is:

$$\sum \delta v_{cz_n} = \sum_{i=0}^{n} \delta v_{cz_n} \quad \text{[B.7]}$$

Via statics, the longitudinal shear stress must be equal to the vertical shear stress. Therefore, the vertical shear stress transferred at each slice may be converted to a vertical shear force, δV_{cz}, using the section geometry in the following equation:

$$\delta V_{cz} = \frac{\sum \delta v_{cz_n} - \sum \delta v_{cz_{n-1}}}{2}\left(h_i - h_{i-1}\right)b \quad \text{[B.8]}$$

The total vertical concrete compression shear force, V_{cz}, is the summation of the incremental vertical shear forces:

$$V_{cz} = \sum_{i=0}^{x} \delta V_{cz_i} \quad \text{[B.9]}$$

APPENDIX C – LONGITUDINAL REINFORCEMENT DOWEL ACTION

The determination of the longitudinal reinforcement dowel action was adapted from the method used to calculate the concrete compression zone shear transfer as described in Appendix B. The experimental longitudinal reinforcing bar dowel action results are reported in Fig. 4.12 to 4.15 in Section *4.2.1 Standard Test Comparison*.

The longitudinal reinforcement strains, μ_x, from each column of gages were converted to flexural tensile stresses, T_x, where:

$$T_x = E_s \mu_x \qquad [C.1]$$

and where E_s is Young's Modulus equal to 200,000 MPA (29,000 ksi) for steel.

Assuming a linear flexural tensile stress profile, an incremental slice of tensile stress at any height, σT_x, may be determined as:

$$\sigma T_x = mh + c \qquad [C.2]$$

where m is the slope of the stress profile, c is the neutral axis intercept, and h is the depth at which the stresses are being considered. A depth of zero is the top of the reinforcing bar.

Similarly, the slice approach is used to find the change in stress across the crack at any height, $\delta\sigma T$, in the reinforcing bar by the following calculation:

$$\delta\sigma T = \sigma T_L - \sigma T_R \qquad [C.3]$$

The incremental tensile force carried by the reinforcing steel, $\delta \Delta T$, is:

$$\delta\Delta T = \frac{\delta\sigma T_i - \delta\sigma T_{i-1}}{2}\left(h_i - h_{i-1}\right)\frac{\delta b_i - \delta b_{i-1}}{2} \qquad [C.4]$$

The longitudinal shear stress transferred by each slice, δv_d, is dependent on the average width of the reinforcing bar for the slice in question, b_i, and the center-to-center gage spacing, s, such that:

$$\delta v_{cz} = \frac{\delta \Delta T}{(\delta b)\, s} \qquad [C.5]$$

Therefore, the total longitudinal shear stress between the top of the reinforcing bar and slice in question, $\Sigma \delta v_d$, is:

$$\sum \delta v_{d_n} = \sum_{i=0}^{n} \delta v_{d_n} \qquad [C.6]$$

Via statics, the longitudinal shear stress must be equal to the vertical shear stress. Therefore, the vertical shear stress transferred at each slice may be converted to a vertical shear force, δV_d, using the section geometry in the following equation:

$$\delta V_d = \frac{\sum \delta v_{d_n} - \sum \delta v_{d_{n-1}}}{2} (h_i - h_{i-1}) \frac{\delta b_i - \delta b_{i-1}}{2} \qquad [C.7]$$

The total dowel action shear force, V_d, for one fully developed flexural bar is the summation of the incremental vertical shear forces such that:

$$V_d = \sum_{i=0}^{x} \delta V_{d_i} \qquad [C.8]$$

The total dowel action of all of the flexural bars is a scaled value based on the effective area of flexural steel.

APPENDIX D – DESIGN SHEAR CAPACITY CALCULATIONS

D.1 ACI 318-08 American Building Code for Structural Concrete

As determined in Chapter 11 of the ACI 318-08 design code, the nominal shear capacity, V_n, is the sum of the shear carried by the concrete, V_c, and stirrups, V_s:

$$V_n = V_c + V_s \qquad \text{ACI 318-08 11.2} \qquad [D.1]$$

The concrete shear capacity depends on the concrete strength, f_c', in psi, web width, b_w, in inches and distance from the extreme compression fiber to the centroid of the longitudinal tension reinforcement, d, in inches. Therefore, V_c is:

$$V_c = 2\sqrt{f_c'}\,b_w d \qquad \text{ACI 318-08 11.3} \qquad [D.2]$$

When considering vertical stirrups:

$$V_s = \frac{A_v f_{yt} d}{s} \qquad \text{ACI 318-08 11.15} \qquad [D.3]$$

where the provided area of shear reinforcement, A_v is in in^2, the stirrup yield strength, f_{yt}, is in psi, and the stirrup spacing, s, is in inches. The provided area of steel reinforcement shall be no less than:

$$A_{v,\min} = 0.75\sqrt{f_c'}\,\frac{b_w s}{f_{yt}} \qquad \text{ACI 318-08 11.13} \qquad [D.4]$$

and $0.75\sqrt{f_c'}$ shall not be less than 50.

Section 11.5.5 of ACI 318-08 limits stirrup spacing to not exceed $d/2$ or 610 mm (24 in.), whichever is less. Furthermore, where V_s exceeds $4\sqrt{f_c'}\,b_w d$, the minimum stirrup spacing is reduced to $d/4$ or 305 mm (12 in.), whichever is less.

D.2 AASHTO-LRFD Bridge Design Specifications

As determined in Section 5.8.3.3 of the AASHTO-LRFD, the nominal shear capacity, V_n, is the lesser of:

$$V_n = V_c + V_s + V_p \qquad \text{AASHTO-LRFD 5.8.3.3-1} \quad [D.5]$$

$$V_n = 0.25 f_c^{'} b_v d_v + V_p \qquad \text{AASHTO-LRFD 5.8.3.3-2} \quad [D.6]$$

Unlike the ACI 318-08 equations, AASHTO-LRFD takes into account the shear carried by prestressing strains, V_p, in addition to that carried by the concrete, V_c, and the stirrup, V_s. Note that the concrete strength is in psi, effective web width, b_v, is in inches, and the effective shear depth, d_v, is taken as 90% of the distance between the extreme compressive fiber and the centroid of the flexural reinforcing steel reported in inches.

The concrete and steel shears are calculated using a method called Modified Compression Field Theory. The theory recognizes that the more shear a beam carries at a given cross-section the less moment it can resist and vice versa. The theory also considers what effect the presence of a diagonal crack has on the capacity through the use of a β term and an θ term, with β being a factor which indicates the ability of a diagonal crack to transmit tension across the crack and θ being the diagonal crack angle. Values for these terms may be found in Tables 5.8.3.4.2-1 and 5.8.3.4.2-2 of the AASHTO-LRFD code. The equations for calculating V_C and V_s are:

$$V_c = 0.0316 \beta \sqrt{f_c^{'}} b_v d_v \qquad \text{AASHTO-LRFD 5.8.3.3-3} \quad [D.7]$$

and

$$V_s = \frac{A_v f_y d_v \cot\theta}{s} \qquad \text{AASHTO-LRFD C5.8.3.3-1} \quad [D.8]$$

where the stirrup spacing, *s*, is in inches and the stirrup yield strength, f_y,is in ksi. The area of stirrup reinforcing steel, A_v, in in^2, shall not be taken less than:

$$A_v \geq 0.0316\sqrt{f_c'}\,\frac{b_v s}{f_y} \qquad \text{AASHTO-LRFD 5.8.2.5-1} \quad [D.9]$$

Determining V_C and V_s is an iterative process requiring Eq. [D.5] to equal Eq. [D.6].

APPENDIX E – DESIGN MOMENT CAPACITY CALCULATIONS

E.1 ACI 318-08 American Building Code for Structural Concrete

Section 10.2 of ACI 318-08 outlines the flexural theory design assumptions. These assumptions are: (1) plane sections remain plane; (2) the strain in the concrete and reinforcement are equal at the same level; (3) stresses in the concrete and reinforcement can be determined from the materials' stress-strain curves; (4) the tensile strength of the concrete is ignored; (5) the concrete is assumed to fail at a limiting strain of 0.003; and (6) the concrete compressive stress block may be assumed to be rectangular. Further, the specimens examined in this thesis are all tension-control beams; meaning the reinforcement in the extreme layer of tensile steel has a strain of 0.005.

Ignoring the presence of the compression steel and assuming the flexural steel yields, the nominal moment capacity, M_n, at a cross-section is:

$$M_n = T\left(d - \frac{a}{2}\right) \qquad [E.1]$$

where T is the tensile capacity of the reinforcing bars calculated as:

$$T = A_s f_y \qquad [E.2]$$

where f_y is the steel yield stress, and A_s is the cross-sectional area of flexural reinforcing steel scaled to reflect the developed percentage of the reinforcing bar at that cross section. Additionally, d is the depth between the extreme compressive fiber and the centroid of the flexural reinforcement, and the effective depth of the Whitney stress block, a, is:

$$a = \frac{A_s f_s}{0.85 f_c' b} \qquad \text{ACI 318-08 Sec. 10.2.7.1} \qquad [E.3]$$

The assumption that the tensile steel yields must be checked. If the extreme tensile strain, ε_t, is greater than 0.005, then the section is tension controlled:

$$\varepsilon_t = 0.003\left(\frac{d_t - c}{c}\right) \qquad \text{[E.4]}$$

where d_t is the depth of the extreme tensile fiber, and c is the depth from the neutral axis to the extreme compression fiber determined as:

$$c = \frac{a}{\beta_1} \qquad \text{[E.4]}$$

where β_1, is for f_c' values between 4000 and 8000 psi:

$$\beta_1 = 1.05 - 0.05\frac{f_c'}{1000} \qquad \text{[E.5]}$$

but shall not be greater than 0.85 or less than 0.65.

In accordance with ACI 318-08 Chapter 10, minimum steel requirements were also checked.

$$A_{s,\min} = \frac{3\sqrt{f_c'}}{f_y} b_w d \qquad \text{ACI 318-08 10.3} \qquad \text{[E.6]}$$

but not less than $(200 b_w d) / f_y$.

E.2 AASHTO-LRFD Bridge Design Specifications

The nominal moment capacity, M_n, for girders without prestressing strands and when h_f is less than a is:

$$M_n = A_s f_s \left(d_s - \frac{a}{2} \right) - A_s' f_s' \left(d_s' - \frac{a}{2} \right) + 0.85 f_c' (b - b_w) h_f \left(\frac{a}{2} - \frac{h_f}{2} \right)$$ AASHTO-LRFD 5.7.3.2.2-1 [E.7]

where the A_s and A_s' are the area of the tensile and compressive steel respectively; f_s and f_s' are the tensile and compressive steel stresses respectively; and f_c' is the concrete compressive strength. The cross-sectional area of flexural reinforcing steel, A_s, is scaled to reflect the developed percentage of the reinforcing bar at that cross section. The height of the flange is defined as h_f . The width of the flange and web are b and b_w respectively. The locations of the centroid of the tensile and compressive steel measured from the extreme compression fiber are d_s and d_s' respectively. The effective depth of the Whitney stress block, a, is defined as:

$$a = c\beta_1$$ AASHTO-LRFD Sec. 5.7.3.2.2 [E.8]

where

$$c = \frac{A_s f_s - A_s' f_s'}{0.85 f_c' \beta_1 b}$$ AASHTO-LRFD 5.7.3.1.2-4 [E.9]

and where β_1 for f_c' values between 4.0 and 8.0 ksi is determined as:

$$\beta_1 = 1.05 - 0.05 f_c'$$ AASHTO-LRFD Sec. 5.7.2.2 [E.10]

but shall not be greater than 0.85 or less than 0.65.

When a is less than h_f, Eq. [E.7] reduces to:

$$M_n = A_s f_s \left(d_s - \frac{a}{2} \right) - A_s' f_s' \left(d_s' - \frac{a}{2} \right)$$ [E.11]

APPENDIX F – CONSTITUTIVE MODELS USED IN NLFEA

The information present in this appendix describes the material and behavioral models implemented in the nonlinear finite element analyses using VecTor2.

F.1 Concrete Compression Pre-Peak Response

The pre-peak response of the concrete was defined using the Hognestad parabola as shown in Fig. F.1. The parabola is defined as:

$$f_{ci} = -f_p \left[2\left(\frac{\varepsilon_{ci}}{\varepsilon_p}\right) - \left(\frac{\varepsilon_{ci}}{\varepsilon_p}\right)^2 \right] < 0 \quad \text{for} \quad \varepsilon_{ci} < 0 \qquad [F.1]$$

where f_p and ϵ_p are peak compressive stress and strain, respectively.

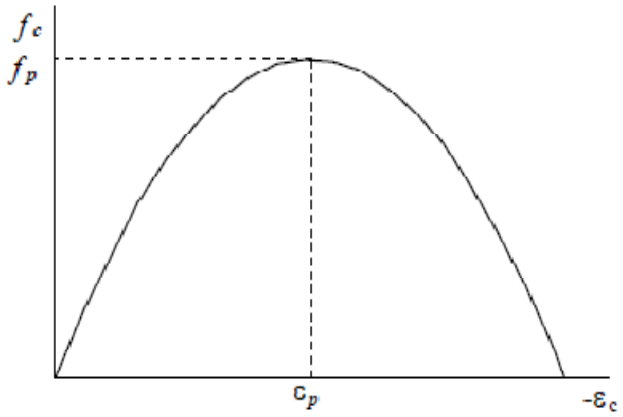

Fig. F.1 – Hognestad parabolic concrete compression response (Vecchio and Wong, 2002)

F.2 Concrete Compression Post-Peak Response

The Modified Park-Kent post-peak response model accounts for the increased concrete strength and ductility due to transverse reinforcement confinement as shown in Fig. F.2. The Modified Park-Kent model is defined as:

$$f_{ci} = -\left[f_p + Z_m f_p \left(\varepsilon_{ci} - \varepsilon_p \right) \right] \quad \text{or} \quad -0.2 f_p \quad \text{for} \quad \varepsilon_{ci} < \varepsilon_p < 0 \qquad \text{[F.2]}$$

where

$$Z_m = \frac{0.5}{\frac{3 + 0.29\left|f_c^{'}\right|}{145\left|f_c^{'}\right| - 100} \text{x} \frac{\varepsilon_o}{-0.002} + \left(\frac{\left|f_{lat}\right|}{170} \right)^{0.9} + \varepsilon_p} \qquad \text{[F.3]}$$

where ϵ_o is the concrete compressive strain, and f_{lat} (MPa) is the summation of principal stress, acting transversely to the direction under consideration:

$$f_{lat} = f_{c1} + f_{c2} + f_{c3} - f_{ci} \leq 0 \qquad \text{[F.4]}$$

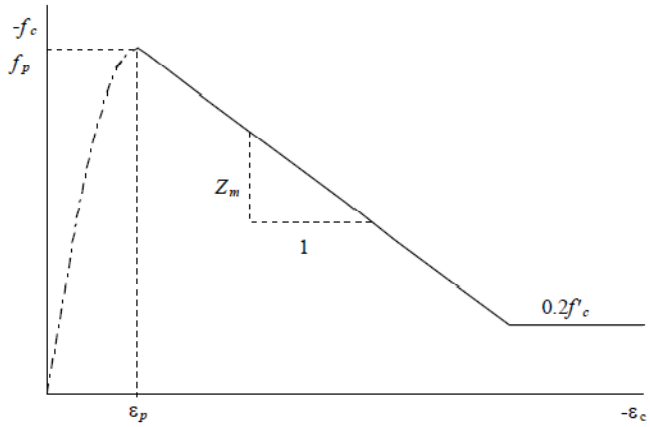

Fig. F.2 – Modified Park-Kent post-peak concrete compression response (Vecchio and Wong, 2002)

F.3 Concrete Compression Softening

Compression softening refers to the reduction of compression strength and stiffness due to transverse cracking and tensile straining. VecTor2 reduces the compressive strength, f_p, and corresponding strain, ϵ_p, using a β_d factor. The Vecchio 1992-A (e1/e2-Form) model was used for this analysis as shown in Fig. F.3. The β_d factor is determined as:

$$\beta_d = \frac{1}{1 + C_s \cdot C_d} \leq 1 \qquad [F.5]$$

$$C_d = \begin{cases} 0 & \text{if} \quad r < 0.28 \\ 0.35\left(r - 0.28\right)^{0.80} & \text{if} \quad r > 0.28 \end{cases} \qquad [F.6]$$

$$r = \frac{-\varepsilon_{c1}}{\varepsilon_{c2}} \leq 400 \qquad [F.7]$$

$$C_s = \begin{cases} 0 & \text{if shear slip is not considered} \\ 0.55 & \text{if shear slip is considered} \end{cases} \qquad [F.8]$$

$$f_p = \beta_d f_c' \qquad [F.9]$$

$$\varepsilon_p = \beta_d \varepsilon_o \qquad [F.10]$$

where C_d is the strain softening factor, C_s is the shear slip factor, ε_{c1} is the principal tensile strain, and ε_{c2} is the principal compression strain.

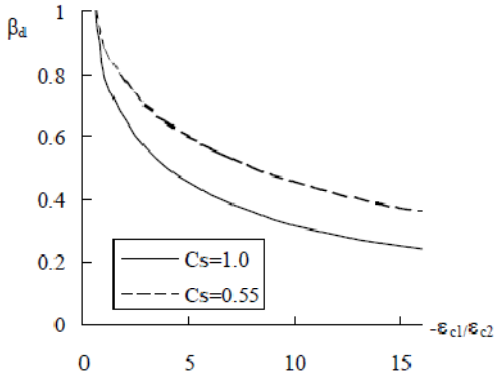

Fig. F.3 – Vecchio 1992-A compression softening model (Vecchio and Wong, 2002)

F.4 Concrete Tension Stiffening

Prior to cracking the response is assumed to be linear-elastic, as follows:

$$f_{c1} = E_c \varepsilon_{c1} \quad \text{for} \quad 0 < \varepsilon_{c1} < \varepsilon_{cr} \qquad [F.11]$$

where

$$\varepsilon_{cr} = \frac{f_{cr}}{E_c} \qquad [F.12]$$

ε_{cr} is the cracking strain, E_c is the initial tangent stiffness of concrete, ε_{c1} is the principal tensile strain, and f_{cr} is the cracking stress of concrete.

"Tension stiffening" refers to the phenomenon of cracked concrete still carrying tension stress between cracks through bond action. The Bentz tension stiffening model defines the average concrete tensile stress-strain response curve as:

$$f_{c1}^{\ a} = \frac{f_{cr}}{1+\sqrt{3.6m\ \varepsilon_{c1}}} \quad \text{for} \quad 0 < \varepsilon_{cr} < \varepsilon_{c1} \qquad [F.13]$$

where the bond parameter, *m*, reflects the ratio of the concrete area bonded to the search of the reinforcement that is tributary to the concrete.

F.5 Concrete Tension Softening

"Tension softening" is a phenomenon of concrete referring to the gradual decrease of tensile stress after cracking rather than an abrupt disappearance of tensile stress. VecTor2 assumes the average post-cracked concrete tensile stress to be the larger of the concrete tensile stress due to tension stiffening, $f_{c1}^{\ b}$, and the average concrete tensile stress due to tension stiffening.

For this analysis, VecTor2 uses a linear tension softening base curve shown in Fig. F.4, and determined from:

$$f_{c1}^{b} = f_{cr}\left[1-\frac{(\varepsilon_{c1}-\varepsilon_{cr})}{(\varepsilon_{ch}-\varepsilon_{cr})}\right] \geq 0 \quad \text{for} \quad \varepsilon_{cr} < \varepsilon_{c1} \qquad [F.14]$$

$$\varepsilon_{ch} = \frac{2G_f}{L_r \cdot f_{cr}} \quad \text{for} \quad 1.1\varepsilon_{cr} < \varepsilon_{ch} < 10\varepsilon_{cr} \qquad [F.15]$$

where ε_{ch} is the characteristic strain, G_f is the fracture energy with an assigned value of 75 N/m, and L_r is the distance over which the crack is assumed to be uniformly distributed, and assigned a value of half the crack spacing.

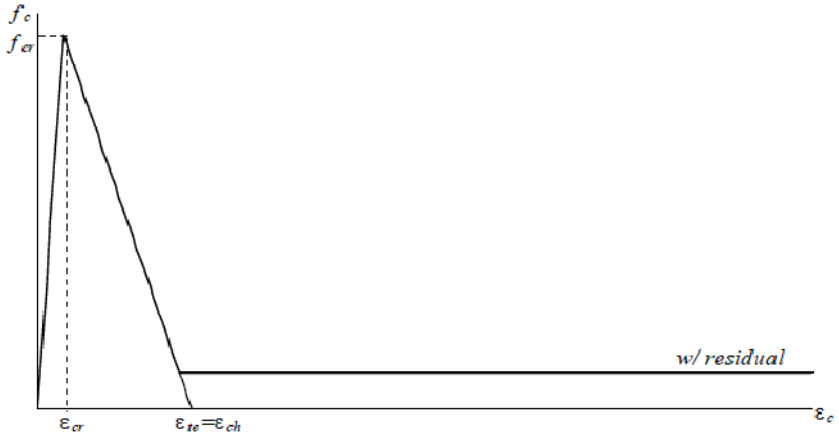

Fig. F.4 – VecTor2 linear tension softening response (Vecchio and Wong, 2002)

F.6 Concrete Confinement Strength

To account for the enhanced strength and ductility of confined concrete, VecTor2 uses a strength enhancement factor, β_1, modify the uniaxial compressive strength, f_c', and the corresponding strain, ϵ_o, to determine the peak compressive strength, f_p', and the corresponding strain, ϵ_p, as follows:

$$f_p = \beta_d \beta_1 f_c' \qquad [F.16]$$

$$\varepsilon_p = \beta_d \beta_1 \varepsilon_o \qquad [F.17]$$

where β_d accounts for compression softening.

The Kupfer/Richart model was to calculated the strength enhancement factor. The model is a combination of work conducted by Kupfer and Richart. For the direction of largest compressive stress, f_{c3}, β_1 is calculated as:

$$\beta_l = \left[1 + 0.92\left(\frac{f_{c2}}{f_c'}\right) - 0.76\left(\frac{f_{c2}}{f_c'}\right)^2\right] + 4.1\left(\frac{f_{cl}}{f_c'}\right) \quad \text{for} \quad f_{c2} < f_{c1} < 0 \qquad \text{[F.18]}$$

where

$$f_n = -\left(f_{c2} - f_{c1}\right) > 0 \qquad \text{[F.19]}$$

$$f_{c1} = -f_{c1} > 0 \qquad \text{[F.20]}$$

The calculation for determining the strength enhancement factor for the other compressive stress directions is similar.

F.7 Concrete Dilation

VecTor2 calculates Poisson's ratio for concrete in tension as:

$$\nu_{12} = \nu_{21} = \begin{cases} \nu_o & \text{for} \quad 0 < \varepsilon_{c1} < \varepsilon_{cr} \\ \nu_o\left(1 - \dfrac{\varepsilon_{c1}}{2\varepsilon_{cr}}\right) \geq 0 & \text{for} \quad \varepsilon_{cr} < \varepsilon_{c1} \end{cases} \qquad \text{[F.21]}$$

where ν_o is the initial Poisson's ratio.

For concrete in compression, the Kupfer was used. Fig. F.5 shows the nonlinear behavior of Poisson's ratio, and Posisson's ratio is defined as:

$$\upsilon_{ij} = \begin{cases} \nu_o & \text{for} \quad -0.5\varepsilon_p < \varepsilon_{cj} < 0 \\ \nu_o \left[1 + 1.5 \left(\dfrac{-2\varepsilon_{cj}}{\varepsilon_p} - 1 \right)^2 \right] \le 0.5 & \text{for} \quad \varepsilon_{cj} < -0.5\varepsilon_p \end{cases} \qquad \text{[F.22]}$$

where ϵ_p is the strain corresponding to the peak compressive stress.

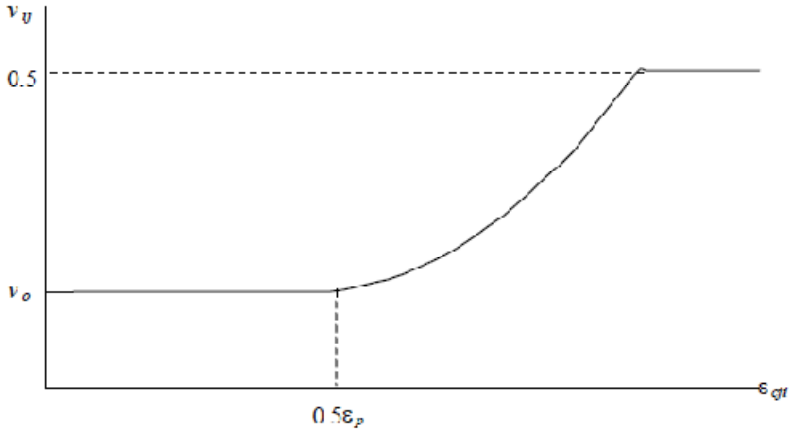

Fig. F.5 – Kupfer variable Poisson's ratio model (Vecchio and Wong, 2002)

F.8 Concrete Cracking

The Mohr-Coulomb criterion was used to determine the concrete cracking strength, f_{cr}, as:

$$f_{cr} = f_{cru} \left(\frac{1 + f_{c3}}{f_c'} \right) \quad \text{for} \quad 0.20\, f_t' \le f_{cr} \le f_t' \qquad \text{[F.23]}$$

where

$$f_{c3} = \begin{cases} -f_c' \left[2\left(\frac{\varepsilon_{c3}}{\varepsilon_o}\right) - \left(\frac{\varepsilon_{c3}}{\varepsilon_o}\right)^2 \right] & for \quad \varepsilon_{c3} < \varepsilon_o < 0 \\ -f_c' & for \quad \varepsilon_o < \varepsilon_{c3} < 0 \\ 0 & for \quad 0 < \varepsilon_{c3} \end{cases} \qquad [F.24]$$

$$f_{cru} = f_c' \frac{2c \cdot \cos\phi}{2\cos\phi} \qquad [F.25]$$

$$c = f_c' \frac{1 - \sin\phi}{2\cos\phi} \qquad [F.26]$$

where c is the cohesion, and ϕ is the angle of friction with an assigned value of 37°.

The local shear stress at the crack surface, v_{ci}^{max}, was limited based on the crack check equation from Modified Compression Field Theory (Vecchio and Collins, 1986), and the work of Walraven (1981). v_{ci}^{max} is defined as:

$$v_{ci}^{\max} = \frac{\sqrt{f_c'}}{0.3 + 24w/(a+26)} \qquad [F.27]$$

where w is the crack spacing (mm), and a is the maximum aggregate size (mm).

F.9 Concrete Slip Distortions

Concrete slip distortions were determined using the model proposed by Vecchio and Lai The slip along the crack, δ_s, is computed as:

$$\delta_s = \delta_s^* \sqrt{\frac{\psi}{1-\psi}} \le 2w \qquad [F.28]$$

where

$$\delta_s^* = \frac{0.5 v_{ci\max} + v_{co}}{1.8 w^{-0.8} + \left(0.234 w^{-0.707} - 0.20\right) f_{cc}} \quad \text{[F.29]}$$

$$\psi = \frac{v_{ci}}{v_{ci\max}} \quad \text{[F.30]}$$

$$v_{ci\max} = \frac{\sqrt{f_c'}}{0.31 + 24 w / (a + 16)} \quad \text{[F.31]}$$

$$v_{co} = \frac{f_{cc}}{30} \quad \text{[F.32]}$$

where v_{ci} is the local shear stress on the crack, w is the average crack width, a is the maximum aggregate size, v_{co} implements an initial offset in the crack shear-slip relationship, and f_{cc} (MPa) is the concrete cube strength, taken as $1.2 f_c'$.

F.10 Concrete Hysteretic Response

The plastic offset, nonlinear loading/unloading model was used to define the hysteretic response of the concrete. This model incorporates elements from the concrete hysteresis model proposed by Vecchio and Ramsberg-Osgood formulation.

The concrete stress f_c, when unloading in compression to a strain of ϵ_c is:

$$f_c = f_{cm} + E_c \left(\varepsilon_c - \varepsilon_{cm}\right) + \frac{E_c \left(\varepsilon_c - \varepsilon_{cm}\right)^{N_c}}{N_c \left(\varepsilon_c^p - \varepsilon_{cm}\right)^{N_c - 1}} \quad \text{for } 1 \le N_c \le 20 \quad \text{[F.33]}$$

where ϵ_c^p is the current plastic offset strain, ϵ_{cm} is the maximum previously attained compress strain, f_{cm} is the corresponding stress. N_c is the Ramsberg-Osgood power term representing the deviation from linear elasticity computed as:

$$N_c = \frac{E_c\left(\varepsilon_c^p - \varepsilon_{cm}\right)}{f_{cm} + E_c\left(\varepsilon_c^p - \varepsilon_{cm}\right)} \qquad [F.34]$$

When N_c does not fall between one and twenty, f_c is:

$$f_c = E_c\left(\varepsilon_c - \varepsilon_c^p\right) \quad \text{for } N_c \le 1 \text{ or } 20 \le N_c \qquad [F.35]$$

The concrete stress, f_c, when unloading in tension is:

$$f_c = f_{tm} - E_c\left(\varepsilon_{tm} - \varepsilon_c\right) + \frac{E_c\left(\varepsilon_{tm} - \varepsilon_c\right)^{N_t}}{N_c\left(\varepsilon_{tm} - \varepsilon_c^p\right)^{N_t - 1}} \quad \text{for } 1 \le N_t \le 20 \qquad [F.36]$$

where ϵ_c^p is the current plastic offset strain, ϵ_{tm} is the maximum previously attained tensile strain, f_{tm} is the corresponding stress. N_t computed as:

$$N_t = \frac{E_c\left(\varepsilon_{tm} - \varepsilon_c^p\right)}{E_c\left(\varepsilon_{tm} - \varepsilon_c^p\right) - f_{tm}} \qquad [F.37]$$

When N_t does not fall between one and twenty, f_c is:

$$f_c = E_c\left(\varepsilon_c - \varepsilon_c^p\right) \quad \text{for } N_t \le 1 \text{ or } 20 \le N_t \qquad [F.38]$$

F.11 Steel Reinforcement Stress-Strain Response

For ductile steel reinforcement, VecTor2 uses a trilinear stress-strain response as shown in Fig. F.6. The reinforcement stress, f_s, is determined as follows:

$$f_s = \begin{cases} E_s\varepsilon_s & \text{for} \quad |\varepsilon_s| \le \varepsilon_y \\ f_y & \text{for} \quad \varepsilon_y < |\varepsilon_s| \le \varepsilon_{sh} \\ f_y + E_{sh}\left(\varepsilon_s - \varepsilon_{sh}\right) & \text{for} \quad \varepsilon_{sh} < |\varepsilon_s| \le \varepsilon_u \\ 0 & \text{for} \quad \varepsilon_u < |\varepsilon_s| \end{cases} \qquad [F.39]$$

$$\varepsilon_u = \varepsilon_{sh} + \frac{\left(f_u - f_y\right)}{E_{sh}} \qquad [F.40]$$

where ϵ_s is the reinforcement strain, ϵ_y is the yield strain, ϵ_{sh} is the strain at the onset of strain hardening, ϵ_u is the ultimate strain, E_s is the elastic modulus, E_{sh} is the strain hardening modulus, f_y is the yield strength, and f_u is the ultimate strength.

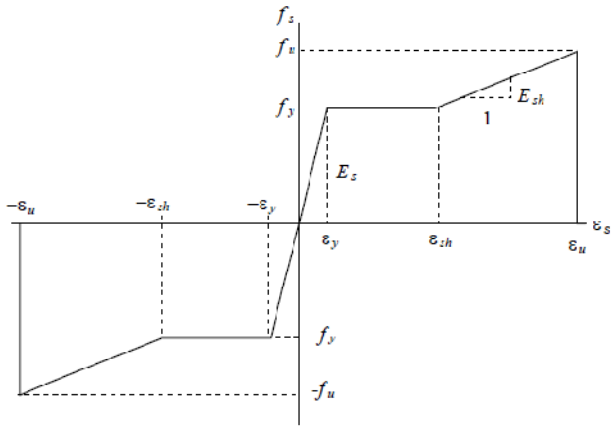

Fig. F.6 – Ductile steel reinforcement stress-strain response (Vecchio and Wong, 2002)

F.12 Steel Reinforcement Dowel Action

Dowel action occurs at crack locations when the flexural steel must resist the shear force. In beams with light transverse reinforcement, the dowel action force may be significant. The Tassios Model for dowel action shear force, $V_{d,}$ due to a relative displacement, δ_s, is:

$$V_d = E_s I_z \lambda^3 \delta_s \leq V_{du} \qquad [F.41]$$

where the area moment of inertia of the reinforcement, I_z, is:

$$I_z = \frac{\pi d_b^4}{64} \qquad [F.42]$$

where λ compares the stiffness of the concrete to the stiffness of the reinforcement and is calculated as:

$$\lambda = \sqrt[4]{\frac{k_c d_b}{4 E_s I_z}} \qquad [F.43]$$

where k_c is the stiffness of notional concrete foundation and determined as follows:

$$k_c = \frac{127 c \sqrt{f_c^{'}}}{d_b^{2/3}} \qquad [F.44]$$

c is experimentally defined as 0.8 and refers to the bar spacing.

$$c = 0.8 \qquad [F.45]$$

Lastly, the ultimate dowel force, V_{du}, describes the plastic hinging of the reinforcement and crushing of the surrounding concrete. V_{du} is calculated as:

$$V_{du} = 1.27 d_b^2 \sqrt{f_c^{'} f_y} \qquad [F.46]$$

F.13 Bond Model

The confined and unconfined bond stress-slip relationship proposed by Eligehausen is shown in Fig. F.7. The confined stress-slip relationship is defined as:

$$\tau = \begin{cases} \tau_{p1}\left(\Delta / \Delta_{p1}\right)^{\alpha} & \text{for } \Delta \le \Delta_{p1} \\ \tau_{p2} & \text{for } \Delta \le \Delta_{p1} \\ \tau_{p2} - \left[\dfrac{\left(\Delta - \Delta_{p2}\right)}{\left(\Delta_{p3} - \Delta_{p2}\right)}\left(\tau_{p2} - \tau_{pf}\right)\right] & \text{for } \Delta_{p1} < \left|\Delta\right| \le \Delta_{p2} \\ \tau_{pf} & \text{for } \Delta_{p3} < \Delta \end{cases} \qquad [F.47]$$

where

$$\tau_{pl} = \left(20 - \frac{d_b}{4}\right)\sqrt{\frac{f_c^{'}}{30}} \qquad [F.48]$$

$$\tau_{p2} = \tau_{p1} \qquad [F.49]$$

$$\tau_{pf} = \left(5.5 - 0.07\frac{S}{H}\right)\sqrt{\frac{f_c^{'}}{27.6}} \quad [F.50]$$

$$\Delta_{p1} = \sqrt{\frac{f_c^{'}}{30}} \quad [F.51]$$

$$\Delta_{p2} = 3.0\,mm \quad [F.52]$$

$$\Delta_{p3} = S \quad [F.53]$$

$$\alpha = 0.4 \quad [F.54]$$

The unconfined stress-slip relationship is defined as:

$$\tau = \begin{cases} \tau_{s1}\left(\Delta / \Delta_{p1}\right)^{\alpha} & \text{for } \Delta \le \Delta_{s1} \\ \tau_{s2} & \text{for } \Delta \le \Delta_{s1} \\ \tau_{s2} - \left[\dfrac{\left(\Delta - \Delta_{s2}\right)}{\left(\Delta_{s3} - \Delta_{s2}\right)}\left(\tau_{s2} - \tau_{sf}\right)\right] & \text{for } \Delta_{s1} < \left|\Delta\right| \le \Delta_{s2} \\ \tau_{sf} & \text{for } \Delta_{s3} < \Delta \end{cases} \quad [F.55]$$

where

$$\tau_{s1} = 0.748\sqrt{\frac{f_c^{'} c}{d_b}} \le \tau_{p1} \quad [F.56]$$

$$\tau_{s2} = \tau_{s1} \quad [F.57]$$

$$\tau_{sf} = 0.234\sqrt{\frac{f_c^{'} c}{d_b}} \le \tau_{sf} \quad [F.58]$$

$$\Delta_{s1} = \Delta_{pl} \exp\left[\frac{1}{\alpha}\ln\left(\frac{\tau_{s1}}{\tau_{p1}}\right)\right] \quad [F.59]$$

$$\Delta_{s2} = \Delta_{p2} \quad [F.60]$$

$$\Delta_{s3} = \Delta_{p3} \quad [F.61]$$

When the anticipated confinement pressure is somewhere between the unconfined and confined cases, a confinement pressure coefficient, β, is used to linearly interpolate between the unconfined and confined cases, where β is defined as:

$$\beta = \frac{\sigma}{7.5} \qquad 0 \le \beta \le 1 \qquad \text{(in MPa)} \qquad [5.62]$$

where σ is the anticipated confinement pressure in MPa. When a confinement stress factor, β, is defined, the bond stress-slip relationship is:

$$\tau = \begin{cases} \tau_{sp1}\left(\Delta / \Delta_{sp1}\right)^{\alpha} & \text{for} \quad \Delta \le \Delta_{sp1} \\ \tau_{sp1} - \left[\dfrac{\left(\Delta - \Delta_{sp2}\right)}{\left(\Delta_{sp3} - \Delta_{sp2}\right)}\left(\tau_{sp2} - \tau_{spf}\right)\right] & \text{for} \quad \Delta_{sp1} < \left|\Delta\right| \le \Delta_{sp2} \\ \tau_{sp2} - \left[\dfrac{\left(\Delta - \Delta_{sp2}\right)}{\left(\Delta_{sp3} - \Delta_{sp2}\right)}\left(\tau_{sp2} - \tau_{spf}\right)\right] & \text{for} \quad \Delta_{sp2} < \Delta \le \Delta_{sp3} \\ \tau_{spf} & \text{for} \quad \Delta_{sp3} < \Delta \end{cases} \qquad [F.63]$$

where

$$\tau_{sp1} = \tau_{s1} + \beta\left(\tau_{p1} - \tau_{s1}\right) \qquad [F.64]$$

$$\tau_{sp2} = \tau_{sp1} \qquad [F.65]$$

$$\tau_{spf} = \tau_{s1} + \beta\left(\tau_{pf} - \tau_{sf}\right) \qquad [F.66]$$

$$\Delta_{sp1} = \Delta_{s1} + \beta\left(\Delta_{p1} - \Delta_{s1}\right) \ge \Delta_{s1} \qquad [F.67]$$

$$\Delta_{sp2} = \Delta_{p2} \qquad [F.68]$$

$$\Delta_{sp3} = \Delta_{p3} \qquad [F.69]$$

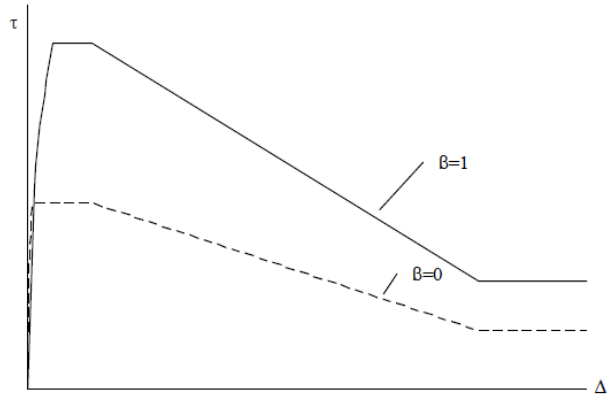

Fig. F.7 – Eligehausen bond stress-slip response (Vecchio and Wong, 2002)